

When will we have
a Zika vaccine? *p. XXX*

Global virus epidemic in
honeybees *pp. 554 & 594*

Forest influence on
climate *pp. 597 & 600*

Science

\$15
5 FEBRUARY 2016
sciencemag.org

AAAS

Regulating hair growth

The control of stem
cells in hair follicles

pp. 559, 575, & 613

CONTENTS



564

Good riddance to race in research?

5 FEBRUARY 2016 • VOLUME 351 • ISSUE 6273

NEWS

IN BRIEF

540 News at a glance

IN DEPTH

543 THE RACE FOR A ZIKA VACCINE IS ON
Researchers see many approaches—but vaccine likely will take years *By J. Cohen*

544 RISKY REACTOR FUEL TO LINGER

Getting highly enriched uranium out of research reactors will stretch to at least 2035, U.S. study concludes *By A. Cho*

545 GOOD GRADES FOR GERMANY'S PROJECT TO BUILD AN IVY LEAGUE HERE

The Excellence Initiative is on the right track, a panel says *By G. Vogel*

546 KAROLINSKA TO REOPEN INQUIRY INTO SURGEON'S WORK

Television documentary raises new questions about Paolo Macchiarini's trachea implants *By G. Vogel*

547 JAPANESE SATELLITE TARGETS THE X-RAY UNIVERSE

Galaxy cluster gases, active galactic nuclei, and supernova remnants on ASTRO-H agenda *By D. Normile*

548 CALLING ALL FAILED REPLICATION EXPERIMENTS

New journal will publish methods, data, and results *By J. Kaiser*

FEATURES

549 WHAT MAKES DARPA TICK?

The stellar reputation of this small but mighty defense agency rests on the unparalleled clout of its program managers *By J. Mervis*

553 Biology came late, and arrived with a bang

By J. Mervis

INSIGHTS

PERSPECTIVES

554 THE MITE THAT JUMPED, THE BEE THAT TRAVELED, THE DISEASE THAT FOLLOWED

Global expansion and trade contributed to the declining health of honeybees *By E. M. Villalobos*
▶ REPORT P. 594

556 THROTTLING BACK THE HEART'S MOLECULAR MOTOR

A small molecule inhibits mutated forms of myosin that cause cardiac hypertrophy *By D. M. Warshaw*
▶ REPORT P. 617

558 ADDRESSING AN ANTIFERROMAGNETIC MEMORY

Antiferromagnets could form a stable and robust platform for future spintronic technology *By C. Marrows*
▶ REPORT P. 587

559 AGING, ALOPECIA, AND STEM CELLS

Intrinsic epigenetic status and extrinsic environmental factors affect hair follicle stem cells *By M. Lei and C.-M. Chuong*
▶ RESEARCH ARTICLE P. 575; REPORT P. 613

561 NANOPARTICLES MEET THEIR STICKY ENDS

Hierarchical DNA structures direct the crystallization of gold nanoparticles *By A. R. Tao*
▶ REPORTS PP. 579 & 582

562 ICE SHEET IN PERIL

Radar data reveal how sensitive the Greenland Ice Sheet is to long-term climatic changes *By C. S. Hvidberg*
▶ REPORT P. 590

564 TAKING RACE OUT OF HUMAN GENETICS

Engaging a century-long debate about the role of race in science *By M. Yudell et al.*
▶ PODCAST

566 ALFRED GILMAN (1941–2015)

A Nobel laureate's work on G proteins illuminated how signals are transmitted into cells *By M. Simon*

BOOKS ET AL.

567 BREAD WINE CHOCOLATE

By S. Sethi, reviewed by C. Kemp

568 THE MOST WANTED MAN IN CHINA

By F. Lizhi, reviewed by I. A. Lerch

LETTERS

569 EDITORIAL RETRACTION

By M. McNutt

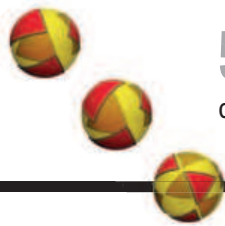
569 SOCIAL COST OF CARBON: DOMESTIC DUTY

By A. Fraas et al.

Science Staff	538
New Products	622
Information for Authors	624
Science Careers	626



Superhot gas in Andromeda, a prime target for the new ASTRO-H x-ray satellite.



561, 579, & 582

Golden lattices stitched by DNA



608

An enzyme that defends bacteria



569 FALSE POSITIVES ARE STATISTICALLY INEVITABLE

By R. D. Fricker Jr.

570 PSYCHOSOCIAL FACTORS KEY TO HEALTHY AGING

By T. D. Cosco

RESEARCH

IN BRIEF

571 From *Science* and other journals

REVIEW

574 BATTERIES

Why do batteries fail? *M. R. Palacín and A. de Guibert*

REVIEW SUMMARY; FOR FULL TEXT:

dx.doi.org/10.1126/science.1253292

RESEARCH ARTICLE

575 STEM CELLS

Hair follicle aging is driven by transepidermal elimination of stem cells via COL17A1 proteolysis
H. Matsumura et al.

RESEARCH ARTICLE SUMMARY; FOR FULL TEXT:

dx.doi.org/10.1126/science.aad4395

► PERSPECTIVE P. 559; REPORT P. 613

REPORTS

576 SUPERCONDUCTIVITY

Nematicity in stripe-ordered cuprates probed via resonant x-ray scattering
A. J. Achkar et al.

MATERIALS SCIENCE

579 Transmutable nanoparticles with reconfigurable surface ligands
Y. Kim et al.

582 Diamond family of nanoparticle superlattices *W. Liu et al.*

► PERSPECTIVE P. 561

587 SPINTRONICS

Electrical switching of an antiferromagnet *P. Wadley et al.*

► PERSPECTIVE P. 558

590 ICE SHEETS

Holocene deceleration of the Greenland Ice Sheet *J. A. MacGregor et al.*

► PERSPECTIVE P. 562

594 HONEYBEE DISEASE

Deformed wing virus is a recent global epidemic in honeybees driven by *Varroa* mites *L. Wilfert et al.*

► PERSPECTIVE P. 554; PODCAST

597 FOREST MANAGEMENT

Europe's forest management did not mitigate climate warming *K. Naudts et al.*

► REPORT P. 600

600 CLIMATE CHANGE

Biophysical climate impacts of recent changes in global forest cover
R. Alkama and A. Cescatti

► REPORT P. 597

604 CANCER THERAPEUTICS

Allele-specific inhibitors inactivate mutant KRAS G12C by a trapping mechanism *P. Lito et al.*

608 STRUCTURAL BIOLOGY

Structures of aminoarabinose transferase ArnT suggest a molecular basis for lipid A glycosylation

V. I. Petrou et al.

613 STEM CELLS

Foxc1 reinforces quiescence in self-renewing hair follicle stem cells

L. Wang et al.

► PERSPECTIVE P. 559;

RESEARCH ARTICLE P. 575

617 HEART DISEASE

A small-molecule inhibitor of sarcomere contractility suppresses hypertrophic cardiomyopathy in mice *E. M. Green et al.*

► PERSPECTIVE P. 556

DEPARTMENTS

539 EDITORIAL

Strength in members

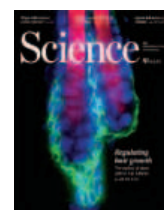
By Rush Holt

630 WORKING LIFE

Retire the letter of reference

By Rima Wilkes

ON THE COVER



Immunofluorescence image showing hair follicles in a resting stage. An old hair (right) is accompanied by a new hair (left), which awaits growth initiation signals.

When the resting follicular stem cells are triggered to self-renew, they also transiently activate a gene network to limit cell division. Understanding these dynamic mechanisms will help to harness multipotent stem cells for regenerative medicine. See page 613. A second paper (page 575) describes how DNA damage triggers stem cell depletion and hair loss.
Image: L. Wang and R. Yi

SCIENCE (ISSN 0036-8075) is published weekly on Friday, except the last week in December, by the American Association for the Advancement of Science, 1200 New York Avenue, NW, Washington, DC 20005. Periodicals mail postage (publication No. 484460) paid at Washington, DC, and additional mailing offices. Copyright © 2016 by the American Association for the Advancement of Science. The title SCIENCE is a registered trademark of the AAAS. Domestic individual membership and subscription (51 issues): \$165 (\$74 allocated to subscription). Domestic institutional subscription (51 issues): \$152; Foreign postage extra: Mexico, Caribbean (surface mail) \$55; other countries (air assist delivery) \$89. First class, airmail, student, and emeritus rates on request. Canadian rates with GST available upon request. GST #R1254 88122. Publications Mail Agreement Number 1069624. Printed in the U.S.A. Change of address: Allow 4 weeks. Surface postage; bulk rates on request. Authorization to photocopy: Send change of address to AAAS, P.O. Box 96178, Washington, DC 20090-6178. Single-copy sales: \$15.00 current issue, \$20.00 back issue prepaid includes surface postage; bulk rates on request. Authorization to photocopy: material for internal or personal use under circumstances not falling within the fair use provisions of the Copyright Act is granted by AAAS to libraries and other users registered with the Copyright Clearance Center (CCC) Transactional Reporting Service, provided that \$35.00 per article is paid directly to CCC, 222 Rosewood Drive, Danvers, MA 01923. The identification code for Science is 0036-8075. Science is indexed in the Reader's Guide to Periodical Literature and in several specialized indexes.

Editor-in-Chief Marcia McNutt

Executive Editor Monica M. Bradford **News Editor** Tim Appenzeller

Managing Editor, Research Journals Katrina L. Kelner

Deputy Editors Barbara R. Jasny, Andrew M. Sugden(UK), Valda J. Vinson, Jake S. Yeston

Research and Insights

SR. EDITORS Caroline Ash(UK), Gilbert J. Chin, Lisa D. Chong, Julia Fahrenkamp-Uppenbrink(UK), Pamela J. Hines, Stella M. Hurlley(UK), Paula A. Kiberstis, Marc S. Lavine(Canada), Kristen L. Mueller, Ian S. Osborne(UK), Beverly A. Purnell, L. Bryan Ray, Guy Riddiough, H. Jesse Smith, Jelena Stajic, Peter Stern(UK), Phillip D. Szuromi, Sacha Vignieri, Brad Wible, Nicholas S. Wigginton, Laura M. Zahn **ASSOCIATE EDITORS** Brent Grocholski, Keith T. Smith **ASSOCIATE BOOK REVIEW EDITOR** Valerie B. Thompson **ASSOCIATE LETTERS EDITOR** Jennifer Silks **CHIEF CONTENT PRODUCTION EDITOR** Cara Tate **SR. CONTENT PRODUCTION EDITORS** Harry Jach, Lauren Kmeck **CONTENT PRODUCTION EDITORS** Jeffrey E. Cook, Chris Filialetau, Cynthia Howe, Barbara P. Ordway, Catherine Wolner **SR. EDITORIAL COORDINATORS** Carolyn Kyle, Beverly Shields **EDITORIAL COORDINATORS** Joi S. Granger, Lisa Johnson, Anita Wynn **PUBLICATIONS ASSISTANTS** Aneera Dobbins, Jeffrey Hearn, Dona Mathieu, Le-Toya Mayne Flood, Shannon McMahon, Scott Miller, Caitlyn Phillips, Jerry Richardson, Rachel Roberts(UK), Alice Whaley(UK), Brian White **EXECUTIVE ASSISTANT** Anna Bashkirova **ADMINISTRATIVE SUPPORT** Janet Clements(UK), Lizanne Newton(UK), Maryrose Madrid, John Wood(UK)

News

NEWS MANAGING EDITOR John Travis **INTERNATIONAL EDITOR** Richard Stone **DEPUTY NEWS EDITORS** Daniel Clery(UK), Robert Coontz, Elizabeth Culotta, David Grimm, David Malakoff, Leslie Roberts **CONTRIBUTING EDITOR** Martin Enserink(Europe) **SR. CORRESPONDENTS** Jeffrey Mervis, Elizabeth Pennisi **NEWS WRITERS** Adrian Cho, Jon Cohen, Jennifer Couzin-Frankel, Carolyn Gramling, Eric Hand, Jocelyn Kaiser, Catherine Maticic, Jeff Servick, Robert F. Service, Erik Stokstad(Cambridge, UK), Emily Underwood **INTERNS** Hanae Armitage, Nala Rogers **CONTRIBUTING CORRESPONDENTS** Michael Balter(Paris), John Bohannon, Ann Gibbons, Mara Hvistendahl, Sam Kean, Eli Kintisch, Kai Kupferschmidt(Berlin), Andrew Lawler, Christina Larson(Beijing), Mitch Leslie, Charles C. Mann, Eliot Marshall, Virginia Morell, Dennis Normile(Shanghai), Heather Pringle, Tania Rabesandratana(London), Gretchen Vogel(Berlin), Lizzie Wade(Mexico City) **CAREERS** Donisha Adams, Rachel Bernstein(Editor) **COPY EDITORS** Julia Cole, Dorie Chevien, Jennifer Levin (Chief) **ADMINISTRATIVE SUPPORT** Jessica Williams

Executive Publisher

Interim Publisher Bill Moran **Chief Digital Media Officer** Rob Covey

BUSINESS OPERATIONS AND PORTFOLIO MANAGEMENT DIRECTOR Sarah Whalen **PRODUCT DEVELOPMENT DIRECTOR** Will Schweitzer **PRODUCT DEVELOPMENT ASSOCIATE** Hal Moore **BUSINESS SYSTEMS AND FINANCIAL ANALYSIS DIRECTOR** Randy Yi **MANAGER OF FULFILLMENT SYSTEMS** Neal Hawkins **SYSTEMS ANALYST** Nicole Mehmedovich **ASSISTANT DIRECTOR, BUSINESS OPERATIONS** Eric Knott **MANAGER, BUSINESS OPERATIONS** Jessica Tierney **BUSINESS ANALYST** Cory Lipman **FINANCIAL ANALYST** Robert Clark **RIGHTS AND PERMISSIONS ASSISTANT DIRECTOR** Emilie David **PERMISSIONS ASSOCIATE** Elizabeth Sandler **RIGHTS, CONTRACTS, AND LICENSING ASSOCIATE** Lili Kiser

MARKETING DIRECTOR Elise Swinehart **ASSOCIATE DIRECTOR OF ACQUISITION AND RETENTION** Julianne Wielga **MARKETING ASSOCIATE** Elizabeth Sattler **SR. MARKETING EXECUTIVE** Jennifer Reeves **ASSOCIATE DIRECTOR, CREATIVE SERVICES** Tzeitel Sorrosa **ART ASSOCIATE** Seil Lee **JR. ART ASSOCIATE** Kim Huynh **ASSISTANT COMMERCIAL EDITOR** Selby Frame **MARKETING PROJECT MANAGER** Angelissa McArthur **PROGRAM DIRECTOR, AAAS MEMBER CENTRAL** Peggy Mihelich **FULFILLMENT SYSTEMS AND OPERATIONS** membership@aaas.org **MANAGER, MEMBER SERVICES** Pat Butler **SPECIALISTS** Terrance Morrison, Latasha Russell **MANAGER, DATA ENTRY** Mickie Napoleoni **DATA ENTRY SPECIALISTS** Brenden Aquilino, Fiona Giblin

INTERIM DIRECTOR, SITE LICENSING Will Schweitzer **PUBLISHER RELATIONS MANAGER** Catherine Holland **PUBLISHER RELATIONS, EASTERN REGION** Keith Layson **PUBLISHER RELATIONS, WESTERN REGION** Ryan Rexroth **SALES RESEARCH COORDINATOR** Aiesha Marshall **MANAGER, SITE LICENSE OPERATIONS** Iqo Edim **SENIOR PRODUCTION SPECIALIST** Robert Koepke **SENIOR OPERATIONS ANALYST** Lana Guo **FULFILLMENT ANALYST** Judy Lillibridge **ASSOCIATE DIRECTOR, MARKETING** Christina Schlecht **MARKETING ASSOCIATES** Thomas Landreth, Isa Sesay-Bah

WEB TECHNOLOGIES SR. DEVELOPER Chris Coleman **DEVELOPERS** Dan Berger, Jimmy Marks, Ryan Jensen **SR. PROJECT MANAGER** Trista Smith **PROJECT MANAGER** Nick Fletcher

DIGITAL MEDIA DIRECTOR OF ANALYTICS Enrique Gonzales **DIGITAL REPORTING ANALYST** Eric Hossinger **SR. WEB PRODUCER** Sarah Crespi **WEB PRODUCER** Alison Crawford **VIDEO PRODUCER** Nguyen Nguyen **SOCIAL MEDIA PRODUCER** Brice Russ

DIRECTOR OF OPERATIONS PRINT AND ONLINE Elizabeth Harman **DIGITAL/PRINT STRATEGY MANAGER** Jason Hillman **QUALITY TECHNICAL MANAGER** Marcus Spiegler **PROJECT ACCOUNT MANAGER** Tara Kelly **DIGITAL PRODUCTION MANAGER** Lisa Stanford **ASSISTANT MANAGER** DIGITAL/PRINT Rebecca Doshi **SENIOR CONTENT SPECIALISTS** Steve Forrester, Antoinette Hodal, Lori Murphy, Anthony Rosen **CONTENT SPECIALISTS** Jacob Hedrick, Kimberley Oster

DESIGN DIRECTOR Beth Rakouskas **DESIGN EDITOR** Marcy Atarod **SENIOR DESIGNER** Garvin Grullón **DESIGNER** Chrystal Smith **GRAPHICS MANAGING EDITOR** Alberto Cuadra **SENIOR SCIENTIFIC ILLUSTRATORS** Chris Bueckl, Katharine Sutliff **SCIENTIFIC ILLUSTRATOR** Valerie Altounian **SENIOR ART ASSOCIATES** Holly Bishop, Nathalie Cary, Preston Huey **PHOTOGRAPHY MANAGING EDITOR** William Douthitt **PHOTO EDITORS** Leslie Blizard, Christy Steele

DIRECTOR, GLOBAL COLLABORATION, CUSTOM PUBLICATIONS, ADVERTISING Bill Moran **EDITOR, CUSTOM PUBLISHING** Sean Sanders: 202-326-6430 **ASSISTANT EDITOR, CUSTOM PUBLISHING** Tianna Hicklin: 202-326-6463 **ADVERTISING MARKETING MANAGER** Justin Sawyers: 202-326-7061 **science_advertising@aaas.org** **ADVERTISING SUPPORT MANAGER** Karen Foote: 202-326-6740 **ADVERTISING PRODUCTION OPERATIONS MANAGER** Deborah Tompkins **SR. PRODUCTION SPECIALIST/GRAPHIC DESIGNER** Amy Hardcastle **SR. TRAFFIC ASSOCIATE** Christine Hall **SALES COORDINATOR** Shirley Young **ASSOCIATE DIRECTOR, COLLABORATION, CUSTOM PUBLICATIONS/CHINA/TAIWAN/KOREA/SINGAPORE** Ruolei Wu: +86-186 0082 9345, rwu@aaas.org **COLLABORATION/CUSTOM PUBLICATIONS/JAPAN** Adarsh Sandhu + 81532-81-5142 asandhu@aaas.org **EAST COAST/E. CANADA** Laurie Faraday: 508-747-9395, FAX 617-507-8189 **WEST COAST/W. CANADA** Lynne Stickrod: 415-931-9782, FAX 415-520-6940 **MIDWEST** Jeffrey Dembski: 847-498-4520 x3005, Steven Loerch: 847-498-4520 x3006 **UK EUROPE/ASIA** Roger Goncalves: TEL/FAX +41 43 243 1358 **JAPAN** Katsuyoshi Fukamizu(Tokyo): +81-3-3219-5777 kfukamizu@aaas.org **CHINA/TAIWAN** Ruolei Wu: +86-186 0082 9345, rwu@aaas.org

WORLDWIDE ASSOCIATE DIRECTOR OF SCIENCE CAREERS Tracy Holmes: +44 (0) 1223 326525, FAX +44 (0) 1223 326532 tholmes@science-int.co.uk **CLASSIFIED** advertise@sciencecareers.org **U.S. SALES** Tina Burks: 202-326-6577 **Nancy Toema**: 202-326-6578 **EUROPE/ROW SALES** Sarah Lelarge **SALES ASSISTANT** Kelly Grace **Japan** Hiruyuki Mashiki(Kyoto): +81-75-823-1109 hmashiki@aaas.org **CHINA/TAIWAN** Ruolei Wu: +86-186 0082 9345 rwu@aaas.org **MARKETING MANAGER** Allison Pritchard **MARKETING ASSOCIATE** Aimee Aponte

AAAS BOARD OF DIRECTORS **RETIRING PRESIDENT, CHAIR** Gerald R. Fink **PRESIDENT** Geraldine (Geri) Richmond **PRESIDENT-ELECT** Barbara A. Schaal **TREASURER** David Evans Shaw **CHIEF EXECUTIVE OFFICER** Rush D. Holt **BOARD** Bonnie L. Bassler, May R. Berenbaum, Carlos J. Bustamante, Stephen P.A. Forde, Claire M. Fraser, Michael S. Gazzaniga, Laura H. Greene, Elizabeth Loftus, Mercedes Pascual

SUBSCRIPTION SERVICES For change of address, missing issues, new orders and renewals, and payment questions: 866-434-AAAS (2227) or 202-326-6417, FAX 202-326-1065. Mailing addresses: AAAS, P.O. Box 96178, Washington, DC 20090-6178 or AAAS Member Services, 1200 New York Avenue, NW, Washington, DC 20005

INSTITUTIONAL SITE LICENSES 202-326-6730 **REPRINTS:** Author Inquiries 800-635-7181 **COMMERCIAL INQUIRIES** 803-359-4578 **PERMISSIONS** 202-326-6765, permissions@aaas.org **AAAS Member Services** 202-326-6417 or http://membercentral.aaas.org/discussions

Science serves as a forum for discussion of important issues related to the advancement of science by publishing material on which a consensus has been reached as well as including the presentation of minority or conflicting points of view. Accordingly, all articles published in Science—including editorials, news and comment, and books reviews—are signed and reflect the individual views of the authors and not official points of view adopted by AAAS or the institutions with which the authors are affiliated.

INFORMATION FOR AUTHORS See pages 678 and 679 of the 6 February 2015 issue or access www.sciencemag.org/about/authors

SENIOR EDITORIAL BOARD

Gary King, *Harvard University*; Susan M. Rosenberg, *Baylor College of Medicine*; Ali Shilatifard, *Northwestern University Feinberg School of Medicine*

BOARD OF REVIEWING EDITORS

 (Statistics board members indicated with S)

Adriano Aguzzi, *U. Hospital Zürich*
Takuzo Aida, *U. of Tokyo*
Leslie Aiello, *Wenner-Gren Foundation*
Judith Allen, *U. of Edinburgh*
Sonia Altizer, *U. of Georgia*
Sebastian Amigorena, *Institut Curie*
Kathryn Anderson, *Memorial Sloan-Kettering Cancer Center*
Meinrat O. Andreae, *Max-Planck Inst. Mainz*
Paola Arlotta, *Harvard U.*
Johan Auwerx, *EPFL*
David A. Axelsen, *U. of Chicago*
Clare Baker, *University of Cambridge*
Jordi Bascompte, *University of Zurich*
Facundo Batista, *London Research Inst.*
Ray H. Baughman, *U. of Texas, Dallas*
David Baum, *U. of Wisconsin*
Carlo Beenakker, *Leiden U.*
Kamran Behnia, *ESPCI-ParisTech*
Yasmine Belkaid, *NIH, NIH*
Philip Benfey, *Duke U.*
May Berenbaum, *U. of Illinois*
Gabriele Bergers, *U. of California, San Francisco*
Bradley Bernstein, *Massachusetts General Hospital*
Peer Bork, *EMBL*
Bernard Bourdon, *École Normale Supérieure de Lyon*
Chris Bowler, *École Normale Supérieure*
Ian Boyd, *U. of St. Andrews*
Emily Brodsky, *U. of California, Santa Cruz*
Ron Brookmeyer, *U. of California, Los Angeles (S)*
Christian Büchel, *U. Hamburg-Eppendorf*
Joseph A. Burns, *Cornell U.*
Carter Tribley Butts, *U. of California, Irvine*
György Buzsáki, *New York U. School of Medicine*
Bianche Capel, *Duke U.*
Mats Carlsson, *U. of Oslo*
Ib Chorkendorff, *U. of Denmark*
David Clapham, *Children's Hospital Boston*
Joel Cohen, *Rockefeller U., Columbia U.*
James J. Collins, *MIT*
Robert Cook-Deegan, *Duke U.*
Lisa Coussens, *Oregon Health & Science U.*
Alan Cowman, *Walter & Eliza Hall Inst.*
Robert H. Crabtree, *Yale U.*
Roberta Croce, *Vrije Universiteit*
Janet Currie, *Princeton U.*
Jeff L. Dangl, *U. of North Carolina*
Tom Daniel, *U. of Washington*
Frans de Waal, *Emory U.*
Stanislas Dehaene, *Collège de France*
Robert Desimone, *MIT*
Claude Desplan, *New York U.*
Dennis Discher, *U. of Pennsylvania*
Gerald W. Dorn II, *Washington U. School of Medicine*
Jennifer A. Doudna, *U. of California, Berkeley*
Bruce Dunn, *U. of California, Los Angeles*
William Dunphy, *Caltech*
Christopher Dye, *WHO*
Todd Ehlers, *U. of Tuebingen*
David Ehrhardt, *Carnegie Inst. of Washington*
Tim Elston, *U. of North Carolina at Chapel Hill*
Gerhard Ertl, *Fritz-Haber-Institut, Berlin*
Barry Everitt, *U. of Cambridge*
Ernst Fehr, *U. of Zurich*
Anne C. Ferguson-Smith, *U. of Cambridge*
Michael Feuer, *The George Washington U.*
Toren Finkel, *NHLBI, NIH*
Kate Fitzgerald, *U. of Massachusetts*
Peter Fratzl, *Max-Planck Inst.*
Elaine Fuchs, *Rockefeller U.*
Daniel Geschwind, *UCLA*
Karl-Heinz Glassmeier, *TU Braunschweig*
Ramon Gonzalez, *Rice U.*
Julia R. Greer, *Caltech*
Elizabeth Grove, *U. of Chicago*
Nicolas Gruber, *ETH Zurich*
Kip Guy, *St. Jude's Children's Research Hospital*
Taekjip Ha, *U. of Illinois at Urbana-Champaign*
Christian Haass, *Ludwig Maximilians U.*
Michael Hasselmo, *Boston U.*
Martin Heimann, *Max-Planck Inst. Jena*
Yka Helariutta, *U. of Cambridge*
James A. Hendler, *Rensselaer Polytechnic Inst.*
Janet G. Hering, *Swiss Fed. Inst. of Aquatic Science & Technology*
Kai-Uwe Hinrichs, *U. of Bremen*
David Hodell, *U. of Cambridge*
David Holden, *Imperial College*
Lora Hooper, *UT Southwestern Medical Ctr. at Dallas*
Tamas Horvath, *Yale University*
Raymond Huey, *U. of Washington*
Auke Ijpeert, *EPFL Lausanne*
Steven Jacobsen, *U. of California, Los Angeles*
Stephen Jackson, *U. of Arizona*
Kai Johnsson, *EPFL Lausanne*
Peter Jonas, *Inst. of Science & Technology (IST) Austria*
Matt Kaebberlein, *U. of Washington*
William Kaelin Jr., *Dana-Farber Cancer Inst.*
Daniel Kahne, *Harvard U.*
Daniel Kammen, *U. of California, Berkeley*
Masashi Kawasaki, *U. of Tokyo*
Ny S. Kim, *Seoul National U.*
Joel Kingsolver, *U. of North Carolina at Chapel Hill*
Robert Kingston, *Harvard Medical School*
Etienne Kochkin, *École Normale Supérieure*
Alexander Kolodkin, *Johns Hopkins U.*
Thomas Langer, *U. of Cologne*
Mitchell A. Lazar, *U. of Pennsylvania*
David Lazer, *Harvard U.*
Thomas Lecuit, *IBDM*
Virginia Lee, *U. of Pennsylvania*
Stanley Lemon, *U. of North Carolina at Chapel Hill*
Ottoline Leyser, *Cambridge U.*
Wendell Lim, *U.C. San Francisco*
Marcia C. Linn, *U. of California, Berkeley*
Jianguo Liu, *Michigan State U.*
Luis Liz-Marzan, *CIC bioGUNE*
Jonathan Losos, *Harvard U.*
Ke Lu, *Chinese Acad. of Sciences*
Christian Lüscher, *U. of Geneva*
Laura Machesky, *CRUK Bealson Inst. for Cancer Research*
Anne Magurran, *U. of St. Andrews*
Oscar Marin, *CSIC & U. Miguel Hernández*
Charles Marshall, *U. of California, Berkeley*
C. Robertson McClung, *Dartmouth College*
Graham Medley, *U. of Warwick*
Tom Misteli, *NCI*
Yasushi Miyashita, *U. of Tokyo*
Mary Ann Moran, *U. of Georgia*
Richard Morris, *U. of Edinburgh*
Alison Murray-Reif, *NC State U. (S)*
Thomas Murray, *The Hastings Center*
Daniel Neumar, *U. of California, Berkeley*
Kitty Nijmeijer, *U. of Twente*
Pär Nordlund, *Karolinska Inst.*
Hela Nowotny, *European Research Advisory Board*
Ben Oken, *MIT*
Joe Orenstein, *U. of California Berkeley & Lawrence Berkeley National Lab*
Harry Orr, *U. of Minnesota*
Andrew Oswald, *U. of Warwick*
Steve Palumbi, *Stanford U.*
Jane Parker, *Max-Planck Inst. of Plant Breeding Research*
Giovanni Parmigiani, *Dana-Farber Cancer Inst. (S)*
John H. J. Petrini, *Memorial Sloan-Kettering Cancer Center*
Samuel Pfaff, *Salk Institute for Biological Studies*
Joshua Plotkin, *U. of Pennsylvania*
Albert Polman, *FOM Institute AMOLF*
Philippe Poulin, *CNRS*
Jonathan Pritchard, *Stanford U.*
David Randall, *Colorado State U.*
Felix Rey, *Institut Pasteur*
Trevor Robbins, *U. of Cambridge*
Jim Roberts, *Fred Hutchinson Cancer Research Ctr.*
Barbara A. Romanowicz, *U. of California, Berkeley*
Amy Rosenzweig, *Northwestern University*
Mike Ryan, *U. of Texas, Austin*
Mitsunori Saitou, *Kyoto U.*
Shimon Sakaguchi, *Kyoto U.*
Miquel Salmeron, *Lawrence Berkeley National Lab*
Jürgen Sandkühner, *Medical U. of Vienna*
Alexander Schier, *Harvard U.*
Vladimir Shaltov, *Purdue U.*
Robert Siliciano, *Johns Hopkins School of Medicine*
Denis Simon, *Arizona State U.*
Uri Simonsohn, *U. of Pennsylvania*
Alison Smith, *John Innes Centre*
Richard Smith, *U. of North Carolina (S)*
John Speakman, *U. of Aberdeen*
Allan C. Spradling, *Carnegie Institution of Washington*
Jonathan Sprent, *Garvan Inst. of Medical Research*
Eric Steig, *U. of Washington*
Paula Stephan, *George State U. and National Bureau of Economic Research*
Molly Stevens, *Imperial College London*
V. S. Subrahmanian, *U. of Maryland*
Ira Tabas, *Columbia U.*
Sarah Teichmann, *Cambridge U.*
John Thomas, *North Carolina State U.*
Shubha Tole, *Tata Institute of Fundamental Research*
Christopher Tyler-Smith, *The Wellcome Trust Sanger Inst.*
Herbert Virgin, *Washington U.*
Bert Vogelstein, *Johns Hopkins U.*
Cynthia Volkert, *U. of Göttingen*
Douglas Wallace, *Dalhousie U.*
David Wallace, *Weizmann Inst. of Science*
Ian Walmsey, *U. of Oxford*
Jane-Ling Wang, *U. of California, Davis (S)*
David A. Wardle, *Swedish U. of Agric. Sciences*
David Waxman, *Fudan U.*
Jonathan Weissman, *U. of California, San Francisco*
Chris Wikle, *U. of Missouri (S)*
Ian A. Wilson, *The Scripps Res. Inst. (S)*
Timothy D. Wilson, *U. of Virginia*
Rosemary Wyse, *Johns Hopkins U.*
Jan Zaenen, *Leiden U.*
Kenneth Zaret, *U. of Pennsylvania School of Medicine*
Jonathan Zehr, *U. of California, Santa Cruz*
Len Zou, *Children's Hospital Boston*
Maria Zuber, *MIT*

BOOK REVIEW BOARD

David Bloom, *Harvard U.*; Samuel Bowring, *MIT*; Angela Creager, *Princeton U.*; Richard Swedner, *U. of Chicago*; Ed Wasserman, *DuPont*

Strength in members

A year ago on this page, I described some of the challenges that science faces in cultivating support from the society it serves. Stepping in as the new Chief Executive Officer of the American Association for the Advancement of Science (AAAS, the publisher of *Science*), my editorial asked, “Why science? Why AAAS?” My thoughts about the nature and service of science and the mission and goals of AAAS—the world’s largest general science membership organization—have since been focusing on new and revitalized efforts that will continue to make AAAS the principal voice for science. A great example of this will be the AAAS Annual Meeting next week in Washington, DC (11 to 16 February), where we will bring together diverse leading voices from around the world to discuss how “Global Science Engagement” can move society toward a secure future.

The annual meeting reflects, in many respects, how AAAS has always advanced science in the world, in countless ways, large and small: by guiding teachers, educating legislators, conducting international studies, illuminating vexing public issues, and upholding principles of fairness, openness, and reason. The organization has been doing these things for more than a century and a half, and today’s more than 100,000 members make it possible for AAAS to continue to show the public the beauty and cultural enrichment found in science, the power of evidence-based thinking, and the practicality of policies that integrate good science.

And yet, I am often struck by how few people know about the work of AAAS. Some readers of this editorial are AAAS members and may know about the important work of the organization, but probably most readers are not members, accessing *Science* through institutional subscriptions at their worksites. Even those who are members often think of themselves as subscribers only and forget that they belong to an organization that is a powerful force for science, engineering, and tech-

nology in the world. Indeed, the influence of AAAS has been potent: from helping to create the U.S. National Science Foundation soon after World War II, to forging the foundation for modern education reform; from convening the Science and Human Rights Coalition, to successfully advocating for a U.S. national forest service and the scientific management of resources; from funding the legal defense in the 1925 Scopes trial on teaching evolution, to challenging today’s politically motivated interference in research in climate change and in social and behavioral sciences, and denouncing legislated restrictions on the study of gun violence as a public health issue.

Moving forward, AAAS will continue its outspoken presence on issues of the day. We will also work with other science and engineering societies to raise the standards of the practice and application of science around the world, as well as annually place nearly 300 Ph.D.-level scientists in fellowships in various departments of the U.S. federal government. We will, with the Kavli Foundation, recognize excellence in science journalism with the most prestigious annual awards.

And through various activities, including publication of the journal *Science and Diplomacy*, AAAS will focus the world’s attention on the role that science plays in international relations.

These and other accomplishments of AAAS, too numerous to describe here, can be attributed to one important factor: its members. The numbers, strength, and wisdom of its members (many practicing scientists or engineers, many not) provide a tremendous driving force. Because AAAS values members so much, the organization is undertaking new initiatives to build, and better engage with, our network of members and fellows, so that together we can champion the mission of AAAS.

I encourage scientists and all those interested in science to join AAAS and become part of an organization that will continue to advance science for human welfare.

– Rush Holt



Rush Holt is Chief Executive Officer of AAAS and Executive Publisher of *Science*. E-mail: rholt@aaas.org



“..AAAS [is] the world’s largest general science membership organization..”

“I will put it into my syllabus that the class is not open to students carrying guns. I may wind up in court. I’m willing to accept that possibility.”

Nobel Prize–winning physicist Steven Weinberg of the University of Texas, Austin, pledging opposition last week to a state law allowing concealed weapons on campus.

IN BRIEF



Scientists lose fight for California bones

These rare ancient skeletons from California are likely to be reburied without scientific study, after the U.S. Supreme Court declined to hear a court case about them last week. The remains, which were discovered in 1976 on the grounds of the University of California (UC), San Diego, date to about 9000 years ago, making them among the oldest in North America. They could shed light on the still murky peopling of the continent and on the possible coastal lifestyle of some of the earliest Americans. However, a local Native American tribe, the Kumeyaay, declared rights to the bones, saying that the remains had been found on their ancient lands. UC officials agreed to give the remains to the tribe for likely reburial, but three UC scientists sued the university system to allow scientific analyses, particularly ancient DNA studies, to determine the remains’ relationship to living tribes (<http://scim.ag/Calibones>). “We just wanted to study the remains,” said UC Berkeley paleoanthropologist Tim White, one of the plaintiffs. California courts ruled against the scientists in 2013, based on a legal technicality involving the Kumeyaay’s status as a sovereign nation. Now that the Supreme Court has declined to reopen the case, the UC system is expected to give the bones to the Kumeyaay, perhaps as soon as the end of February.

AROUND THE WORLD

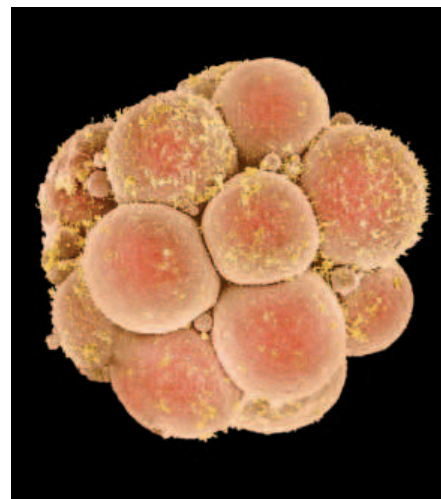
Twisty stellarator hits its stride

GREIFSWALD, GERMANY | German Chancellor Angela Merkel this week kicked off real fusion research on the country’s new reactor Wendelstein 7-X by flicking the switch to fill the reactor with hydrogen plasma. W7-X is a stellarator, a fusion reactor with a strange, twisty shape that researchers hope will keep the superhot gas inside more stable than traditional doughnut-shaped “tokamaks” do (*Science*, 23 October 2015, p. 369). Nineteen years and €1 billion in the making, W7-X started operation last November, producing a plasma of helium gas. But hydrogen is required for the reactor’s ultimate goal: to get the gas so hot that its atoms fuse together. The rate of actual fusion

reactions with plain hydrogen will be very low, however; to up that rate and produce more energy, the plain hydrogen will eventually have to be replaced with its more reactive isotope deuterium. Future reactors will use a yet more reactive mix of deuterium and tritium.

Scientist can edit human embryos

LONDON | Developmental biologist Kathy Niakan has received permission from U.K. authorities to modify human embryos using CRISPR/Cas9 gene-editing technology. Niakan, who works at the Francis Crick Institute in London, applied for permission to use the technique in studies to better understand the role of key genes during the first few days of human embryo development. The debate about



A U.K. researcher has gotten a green light to modify human embryos (pictured, 4 days after fertilization).

the ethics of editing embryonic genomes has raged for several years; critics say studies such as Niakan's could be the first step toward "designer babies" or even eugenics. The Human Fertilisation and Embryology Authority (HFEA), which grants licenses for work with human embryos, sperm, and eggs in the United Kingdom, approved Niakan's application at a meeting of HFEA's license committee on 14 January. The minutes of that meeting state that "[o]n balance, the proposed use of CRISPR/Cas9 ... was a justified technical approach to obtaining research data about gene function from the embryos used." <http://scim.ag/Niakanperm>

Scholars call to free scientist

TEHRAN | More than 300 scholars, including seven Nobel laureates, have signed a letter dated 27 January that calls on Iran to release a jailed chemist. An Iranian court last year sentenced Mohammad Rafiee, a chemist retired from the University of Tehran, to 6 years in prison for "spreading propaganda against the regime" and other crimes. In June 2014, Rafiee posted on his website a lengthy analysis endorsing Iran's efforts to reach a nuclear deal with the United States and other nations. The move came shortly after Iran's president, Hassan Rouhani, had challenged Iranian intellectuals to publicly back his support for a deal. "Why are the professors silent?" Rouhani had asked. Last week, the U.S. State Department said in a statement that it considers Rafiee "to be a political prisoner ... and would call for his release, as we do for other political prisoners in Iran." <http://scim.ag/Iranchemist>

\$1 billion for cancer moonshot

WASHINGTON, D.C. | The White House plans to spend \$1 billion to jump-start Vice President Joe Biden's moonshot to cure cancer. The initiative will include \$195 million for new activities at the National Institutes of Health (NIH) this year. The White House also plans to ask for \$755 million in its fiscal year 2017 budget request to be released on 9 February, mostly for NIH and the rest for the U.S. Food and Drug Administration. The moonshot will ramp up efforts in cancer prevention, early detection, immunotherapy, tumor genomics, data sharing, and pediatric cancer. It will also include a new fund for high-risk, high-reward research. The National Cancer Institute will assemble a blue-ribbon panel to begin guiding the effort.



The Hive at the Milan Expo in Italy in 2015.

Kew Gardens to host *The Hive*

A twisting structure meant to evoke a swarm of bees is set to alight at the Royal Botanic Gardens, Kew, in the United Kingdom this summer. *The Hive*, an installation that was originally part of the U.K. Pavilion at the 2015 Milan Expo in Italy, was designed by artist Wolfgang Buttress and inspired by U.K. research into the health of bees, bee communication, and the role of bees in the global food chain. Visitors will enter the 17-meter-tall aluminum structure through a wildflower meadow, and will then be surrounded by hundreds of LED lights and a swell of music, buzzes, and pulses that increases as they move toward its center. The structure—which won dozens of awards at the expo—is set to arrive in June.

NEWSMAKERS

Obokata has her say in new book

Disgraced stem cell researcher **Haruko Obokata** is telling her story. In a book out last week, she describes how the discovery of stimulus-triggered acquisition of pluripotency (STAP) cells unraveled and shifts much of the blame to another researcher. The STAP method, reported in two 2014 papers in *Nature*, promised an easy way to create pluripotent cells for future medical treatments. Investigations by RIKEN, Japan's network of national laboratories where Obokata worked, concluded that the papers contained falsified data and that the supposed STAP cells in her laboratory were actually embryonic stem cells. RIKEN fired her, the *Nature* papers were retracted, and one co-author committed suicide. In *Ano Hi (That Day)*, Obokata claims there is still evidence that STAP cells exist but says the pressures of the

investigations and media attention kept her from replicating her experiments. She also says a senior colleague, Teruhiko Wakayama, now at the University of Yamanashi, provided the cells used in the experiments, but that she was left to take the blame for the cell line mix-up. Obokata says she still admires Charles Vacanti, of Harvard Medical School in Boston, in whose lab she started work on STAP cells as a postdoc.

FINDINGS

Bumping up baby microbiomes

When delivered by cesarian section, a baby's "microbiome"—the trillions of bacteria in the body—is different from that of infants who travel through mom's birth canal. These differences have been linked to more asthma, obesity, and allergies, although the details remain controversial.

Now, a new study examines whether rubbing mom's vaginal bacteria over a newborn delivered by C-section could alter the microbial makeup. Scientists placed sterile gauze in four mothers' vaginas for an hour before their scheduled C-sections, then rubbed the gauze over each baby right after delivery. Fourteen other babies, some born vaginally and some by C-section, acted as controls. Over the next 30 days, the team sampled bacteria on the babies' mouths, anuses, and skin. Among treated babies, the microbiome shifted somewhat toward that of the average vaginally born baby, the team reports this week in *Nature Medicine*. In particular, they observed enrichments in *Lactobacillus* bacteria and *Bacteroides*, both diminished in babies born by C-section. The authors say they are now enrolling dozens more babies for a larger scale and longer term test. <http://scim.ag/biomebabies>

Pacific oysters reproduce less when they've ingested microplastics, a lab study shows.

**Microplastics hurt oyster reproduction**

Eating, for an oyster, is pretty simple: Take water in, keep the tasty plankton, spit water out. But increasingly, the mollusks are getting an unwelcome additive: tiny pieces of plastic ranging from a few micrometers to a millimeter in size. Over time, the human-produced plastic—derived from anything from clothing to industrial processes—washed into the oceans breaks down into smaller and smaller pieces. Now, a new laboratory-based study shows that when Pacific oysters are exposed to these so-called microplastics, they ingest as much as 69% of 6-micrometer particles added to water. The microplastics end up in the oysters' guts and disrupt their digestion or hormone systems, ultimately causing them to invest less energy in reproduction. Female oysters exposed to microplastics made 38% fewer eggs, and males made sperm that were 23% slower. Plus, they had fewer offspring, which were themselves slower to reach maturity.

BY THE NUMBERS

82,000

Number of deaths worldwide that could be prevented each year by making breastfeeding nearly universal for infants and young children (*The Lancet*).

99%

Fraction of U.S. coastal waters in which contaminants in fish tissue pose a threat to predator fish, birds, and wildlife, according to a new report by the U.S. Environmental Protection Agency. Selenium is the primary culprit, likely boosted by pollution such as agricultural runoff and sewage.

\$54,600

List price for a 12-week course of Merck & Co.'s newly approved hepatitis C drug Zepatier; that's much less than the listed price of similar drug regimens from AbbVie (\$83,300) and Gilead Sciences (\$94,500).



INFECTIOUS DISEASE

The race for a Zika vaccine is on

Researchers see many approaches—but a vaccine likely will take years

By Jon Cohen

Less than a year ago, Zika seemed trivial for anyone to bother developing countermeasures. The mosquito-borne virus was racing through the Southern Hemisphere, but, at worst, it appeared to cause a mild fever and rash. No longer: On 1 February the World Health Organization (WHO) declared the “extraordinary” cluster of microcephaly and other neurological complications that have now been linked to Zika a “public health emergency of international concern.” And vaccinemakers, big and small, have begun the race to head it off. They have a good shot at success, several experts say, but they caution that vaccine development requires years of testing.

Isolated in 1947, Zika first caused serious concern in May 2015 after it arrived in South America and suspicions grew that infection during pregnancy might be causing brain-damaging microcephaly in babies. The link, WHO Director-General Margaret Chan in Geneva, Switzerland, stresses, is “strongly suspected though not yet scientifically proven”—as is a potential connection to Guillain-Barré syndrome, which can cause a temporary paralysis in adults. With viral spread increasing, a vaccine is now a top priority.

Vaccine pioneer Stanley Plotkin of the University of Pennsylvania predicts “a straight-

forward developmental pathway” for a vaccine. He notes that Zika belongs to the flavivirus family, and vaccines exist for several of its relatives, including dengue, yellow fever, and Japanese encephalitis. “I don’t see any technical issues such as the ones that obviously exist for vaccines against HIV, tuberculosis, and many other agents,” says Plotkin, who consults with several vaccinemakers.

Still, “there are many puzzles,” says Thomas Monath, a virologist who studied Zika in wild monkeys in Nigeria in the 1970s and is now the chief scientific officer at NewLink Genetics in Devens, Massachusetts, which helped develop a promising Ebola vaccine. For Zika, one unknown is whether infection leads to lifelong protection—a key feature of diseases for which vaccines are most effective, such as yellow fever. Another question is whether natural or vaccine-induced immunity against other related viruses—particularly yellow fever—could offer a measure of “cross protection,” which might confuse efforts to evaluate Zika vaccines. Nor have researchers yet established a much-needed monkey model to enable comparisons of candidate vaccines.

Monath, who has developed vaccines against several flaviviruses, says NewLink will pursue a traditional strategy that inactivates, or kills, the virus with a chemical so it cannot replicate in the body. He thinks an inactivated vaccine has the best chance of

Jorge Kalil (holding box), director of Brazil’s Butantan Institute, says his team hopes to make a Zika vaccine by mimicking a strategy used for the related dengue virus.

winning regulatory approval as a product that pregnant women might use.

At the nonprofit Butantan Institute in São Paulo, Brazil, however, immunologist and director Jorge Kalil is betting that a weakened, live vaccine can be safe and potentially more effective than killed virus. His team plans to exploit a technology that researchers at the U.S. National Institute of Allergy and Infectious Diseases (NIAID) used to make a dengue vaccine, which Butantan licensed and is now testing in an efficacy trial. To weaken that virus, researchers deleted genes so it can copy itself but not cause disease. “Perhaps we can attenuate the Zika virus by using the same deletions of the same sites,” Kalil says, noting that Butantan likely would partner with NIAID to develop its vaccine. The Brazilian institute has a key advantage: Unlike almost every other nonprofit in the world that does vaccine research, it has an industrial-scale manufacturing plant—last year the institute cranked out 40 million doses of influenza vaccine—so it might be able to supply enough product for Brazil without needing help from big pharma.

NIAID Director Anthony Fauci in Bethesda, Maryland, says his institute has a “head start” with a different technology it

used to make an experimental vaccine for West Nile, another flavivirus. The manufacturing process begins with a circular “plasmid” of DNA that holds key viral genes. When it is inserted into bacterial cells, they produce “viruslike particles” that are similar to an inactivated vaccine, because they cannot copy themselves. (The West Nile vaccine worked well in early human studies, but NIAID could not find a commercial partner to take it forward.)

Inovio Pharmaceuticals of Plymouth Meeting, Pennsylvania, boasts it already has an experimental Zika vaccine containing nothing more than a plasmid made of Zika genes. With the help of an electrical zap on the skin, the plasmid goes directly into human cells, which then make Zika proteins that stimulate the immune system. CEO Joseph Kim says his team already has begun tests in mice. But although researchers can quickly make such simple DNA vaccines, they have lost their luster over the past 20 years because they have not triggered strong immune responses. “There are people very knowledgeable in the field who have lost faith in this technology,” Kim concedes. “I want to prove that this technology is viable and perhaps the best option for these types of outbreaks.”

The small Jenner Institute in Oxford, U.K., is putting the Zika surface protein into harmless chimpanzee adenoviruses, which serve as a “vector”—an approach similar to one used in GlaxoSmithKline’s Ebola vaccine, which was tested during the West African epidemic. Vaccinemakers Protein Sciences of Meriden, Connecticut, and Hawaii Biotech of Honolulu—which both specialize in producing viral proteins in insect cell lines—also have projects underway.

Predicting when a vaccine will come to market is a mug’s game, but NIAID’s Fauci thinks animal studies could be completed in a few months and small human studies to evaluate safety and immune responses could begin by the end of 2016. Even if a promising candidate surfaces, large-scale efficacy trials are probably years away, he says. Getting a vaccine approved and supplying millions of doses could take the resources of a major manufacturer. Of the four big pharma companies that make vaccines, only Sanofi Pasteur of Lyon, France—which produces all three existing flavivirus vaccines—has launched a Zika program, though the others say they are watching the field closely.

As a stopgap measure for pregnant women, Kalil says Butantan hopes to produce a protective serum, which the institute already makes for several diseases, by injecting Zika virus into horses and harvesting the antibodies the animals make. “This would take a little over a year,” Kalil says. “That’s the best timeline—if you’re very, very optimistic.” ■

NUCLEAR NONPROLIFERATION

Risky reactor fuel to linger

Getting highly enriched uranium out of research reactors will stretch to at least 2035, U.S. study concludes

By **Adrian Cho**

Since 1978, the United States and other nations have been pushing to eliminate the use of highly enriched uranium (HEU)—which a terrorist or rogue nation could use to make a bomb—as fuel in dozens of civilian research reactors around the world. But achieving that goal will take far longer than previously hoped, according to a study from the National Academies of Sciences, Engineering, and Medicine. Experts had once hoped to eliminate HEU fuel by 2018, but 2035 is more realistic, the 28 January report concludes.

“Clearly there have been unexpected challenges, both technical and nontechnical,” says Julia Phillips, a former vice president of Sandia National Laboratories in Albuquerque, New Mexico, and chairperson of the panel that wrote the report, which Congress requested in 2012.

Research reactors are relatively small facilities that focus on materials science, reactor design, and the production of medical isotopes. That work generally requires fluxes of neutrons higher than those produced in commercial power reactors. Whereas power reactors make do with uranium enriched to about 4% of the fissile isotope U-235, research reactors run on uranium that is more highly enriched, in some cases to about 90%—the level of weapons-grade uranium.

Globally, the civilian research stock of HEU—uranium enriched to at least 20%—totals 60 tons, enough to make roughly 1000 bombs, and nonproliferation experts worry that it may be less secure than far bigger military supplies. Since the 1970s, dozens of civilian research reactors have either closed or converted to safer low enriched uranium (LEU), including 28 since 2009. That leaves 74 similar reactors that are still using, or

plan to use, HEU. “The long and short of it is that the easy conversions have been made,” Phillips says.

On the technical side, nuclear scientists and engineers have struggled to develop adequate replacement fuels based on LEU. To maintain the needed neutron fluxes, the fuels need a high density of uranium. Researchers in Europe and Asia are developing a so-called dispersion fuel, in which granules of a uranium molybdenum alloy are embedded within an aluminum matrix. In con-

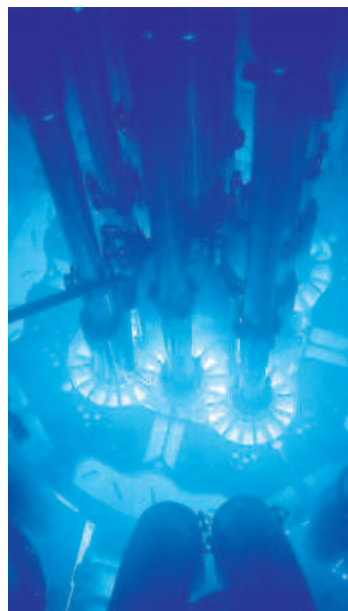
trast, the United States is developing a “monolithic” fuel that consists of a single ribbon of uranium-molybdenum alloy clad in aluminum. Development of both fuels will likely take another 12 to 17 years, the report estimates.

On the nontechnical side, Russia has expressed little interest in converting its 32 research reactors. “This is not a priority with the Russian government,” says William Tobey, a panel member and nonproliferation expert at Harvard University.

The report makes seven recommendations, including engaging Russia in greater collaboration and planning for facilities to replace the

eight aging U.S. civilian research reactors. Most controversially, as an interim step it calls for converting those reactors to a somewhat less enriched form of HEU. The United States has designated 20 tons of 93% enriched weapons-grade uranium for civilian research. The report recommends diluting that supply to 45% enrichment and using it until LEU fuel is available.

That’s a bad idea, says Alan Kuperman, a political scientist at the University of Texas, Austin. Using 45% enriched HEU would perpetuate commerce in HEU and undermine efforts to develop LEU fuel, he says. Simply put, Kuperman says, “it’s incredibly stupid from a policy perspective.” ■



The core of the Advanced Test Reactor at the Idaho National Laboratory holds 43 kilograms of highly enriched uranium.



Ludwig Maximilian University of Munich is one of Germany's top schools.

RESEARCH FUNDING

Good grades for Germany's project to build an Ivy League

The Excellence Initiative is on the right track, a panel says

By **Gretchen Vogel**, in Berlin

A decade ago, amid worries that its universities were unable to keep up with the global academic elite, Germany embarked on a radical experiment: The government poured €4.6 billion into a plan to strengthen research at select universities and create its own version of the Ivy League. The Excellence Initiative, as it was called, ran counter to a long egalitarian tradition in German higher education; critics warned that focusing on the top would also create a tier of second-rate schools.

That hasn't happened, an international committee concludes in a report published on 29 January. The panel was convened by the Joint Science Conference (GWK), which includes federal and state science ministers of research, education, and finance. The report concludes that the initiative had "very positive" effects and should continue, although with some important changes. "It has set the system on the right path," says physicist Dieter Imboden of ETH Zurich in Switzerland, who chaired the commission.

Most German politicians had already concluded as much. Opposition to the idea of rewarding excellence has softened in recent years, and in December 2014, GWK committed to setting up a follow-up program after the initiative ends in 2017. The report's rec-

ommendations will help shape the successor.

Germany's universities are run and funded by the 16 *Länder*, or states, but the Excellence Initiative added a layer of federal money to challenge universities to specialize in areas where they might excel. The program had three categories. Graduate schools, still fairly rare in Germany 10 years ago, competed to receive up to €2.5 million a year. So-called "excellence clusters" were eligible for up to €8 million a year "to promote top-level research," often linking researchers from multiple universities and Max Planck institutes or Helmholtz centers. In addition, "institutional strategies" gave universities extra funds to help ensure that the other two components were successful over the long term. The program has sprouted a range of new projects—from the Erlangen Graduate School in Advanced Optical Technologies and the Center for Regenerative Therapies in Dresden to the Center for Integrated Protein Science in Munich.

So far, none of them have propelled Germany into the higher echelons of university rankings, which are dominated by the United States and the United Kingdom. In the annual table produced by Jiao Tong University in Shanghai, China, the best German school is Heidelberg University at 46th place. Still, the initiative "has made the German university system more dynamic and has become a tangible symbol of the will to improve the

international competitiveness of German universities," the panel concludes. "That such a small amount of money can bring about so much movement and genuinely bring about a competitive spirit ... I did not expect that when the whole thing started," says Gerhard Casper, former president of Stanford University in Palo Alto, California, now the president of the American Academy here and a member of the panel.

The worries about a growing divide haven't panned out, because even the universities that didn't do well came up with plans to focus and build on their areas of strength, the panel says, sometimes with grant money found elsewhere. "Everywhere we looked there were positive effects," says vice-chair Elke Lütjen-Drecoll, an anatomist and professor emeritus at Friedrich-Alexander University Erlangen-Nürnberg.

The panel recommends changes for the next phase, however. Graduate schools have become common at research universities and can be dropped from the program; funding for research clusters should become more flexible to allow for smaller projects, especially in the humanities, and to allow for collaborations between geographically distant partners. Perhaps most controversial, the panel suggests scrapping the "institutional strategies"; instead, the 10 top universities—ranked by award-winning professors, European Research Council grants, and other accolades—should receive an extra €15 million per year for 7 or 8 years. Rewarding past achievements instead of good plans will avoid "window dressing promises" by universities and relieve the pressure to apply for grants, Imboden says.

To award a new round of competitive grants by 2018, GWK would have to agree on the main program outlines by April, so that Chancellor Angela Merkel and the ministers-president of the *Länder* can give their final approval in June. That schedule is too tight, says the Imboden commission, which recommends extending current funding for two more years, until 2019.

Although creating an academic elite is no longer a taboo, there is widespread concern that overall spending on Germany's universities is simply too low. The commission points out that the number of students has grown much faster than the number of professors or overall funding. Imboden urged politicians to keep in mind that the world's top universities each spend significantly more than €1 billion a year. The roughly €500 million annually available under Germany's program is "respectable," he said, "but if you want to compete with Stanford, it's a small sum." ■



Paolo Macchiarini gave eight patients an artificial windpipe.

SCIENTIFIC MISCONDUCT

Karolinska to reopen inquiry into surgeon's work

Television documentary raises new questions about Paolo Macchiarini's trachea implants

By Gretchen Vogel

A chilling TV documentary is causing new trouble for Italian star surgeon and former media darling Paolo Macchiarini. Last summer, the Karolinska Institute (KI) in Stockholm dismissed charges that Macchiarini had misrepresented the success of his pioneering trachea implants in a series of scientific papers. But a three-part series by Swedish public television channel SVT, aired in January, suggests that he didn't fully inform his patients about the risks of his operations. Most of them died, including at least one who was not seriously ill before the surgery.

In an email to *Science*, Macchiarini wrote the series "was a gross misrepresentation of fact," and that he can't comment further at the moment. But KI, where Macchiarini is a senior researcher, says it may reopen its investigation against him. "We've seen footage in SVT's documentary that is truly alarming, and I empathise deeply with the patients and their relatives," Anders Hamsten, KI's vice-chancellor, said in a statement last week.

The film has also raised questions about the way Hamsten and other administrators at KI, Sweden's most prestigious university

and home of the selection committee for the Nobel Prize in Physiology or Medicine, have handled the scandal. "I am concerned that it will affect the trust that we have from the public, for Sweden as a prominent research nation, and for the Karolinska Institute," Sweden's minister for higher education and research, Helene Hellmark Knutsson, told *Science*. The chairman of the institute's board of directors, Lars Leijonborg, says he expects the board to approve an independent inquiry into KI's 5-year relationship with Macchiarini this week.

Macchiarini replaced missing or damaged windpipes with an artificial trachea made of a polymer scaffold "seeded" with the patients' own stem cells, which were supposed to grow into living tissue. Between 2011 and 2014, he conducted three such transplants at Karolinska University Hospital, four in cooperation with the Kuban State Medical University in Krasnodar, Russia, as part of a formal clinical trial, and one—on a toddler born without a trachea—in Illinois.

In 2014, colleagues at KI alleged that Macchiarini's papers made his transplants seem more successful than they were, omitting serious complications. Two patients treated at Karolinska died, and a third has been in intensive care since receiving

a trachea in 2012. The Illinois patient also died, as did three patients in Russia. Bengt Gerdin, a professor emeritus of surgery at Uppsala University in Sweden who investigated the charges at KI's request, concluded in May 2015 that differences between published papers and lab records constituted scientific misconduct. But Hamsten rejected that conclusion based on additional material Macchiarini submitted later.

The documentary shows footage of a patient who says Macchiarini reassured him before the surgery that experiments had been done on pigs, when in fact none had taken place. It also follows the wrenching story of the first patient in Krasnodar. A 33-year-old woman, she was living with a tracheostomy that she said caused her pain, but her condition was not life-threatening. The film suggests that she wasn't fully aware of the risks of the operation, and that Macchiarini and his colleagues knew about problems with the implant before the surgery. The patient's first implant failed, and she received a second one in 2013. She died in 2014.

The fact that a relatively healthy patient underwent Macchiarini's experimental procedure caused consternation in Sweden. "The information that has emerged in the documentaries on the ethical nature of these operations is new to Professor Hamsten," the university said in a statement. The operations, if they occurred as shown in the documentary, would never have been approved at KI, the university says.

However, Macchiarini was open about his plan to include patients who didn't have life-threatening conditions in the Krasnodar trial. At KI, "[w]e were allowed to do this type of transplantation only in extreme cases," he told *Science* 3 years ago. "The clinical study for the first time gives us a chance to include patients who are not in such critical shape" (*Science*, 19 April 2013, p. 266).

KI says that it is also investigating the allegation, made in a *Vanity Fair* story last month, that Macchiarini included incorrect information on his CV. (That article focused on Macchiarini's past relationship with Benita Alexander, an NBC News producer; among other things, Alexander says Macchiarini convinced her that he had operated on several heads of state and that he would marry her in a ceremony officiated by Pope Francis.)

Macchiarini's appointment as a visiting professor at KI ended in October 2015; in November 2015, the institute gave him a 1-year contract as a senior researcher. That decision, like many others in the Macchiarini affair, is now likely to come under scrutiny as the new investigations get underway. ■

SPACE SCIENCE

Japanese satellite targets the x-ray universe

Galaxy cluster gases, active galactic nuclei, and supernova remnants on ASTRO-H agenda

By Dennis Normile

A bus-sized satellite due to go into orbit next week promises to open a view of some of the most tumultuous corners of the universe. The 12 February launch of the x-ray observatory ASTRO-H from Japan's Tanegashima Space Center will give astronomers a long-awaited opportunity to track the superheated gases, glowing in x-rays, that surge from black holes, swirl within galaxy clusters, and abound in supernova remnants.

"It's going to open up a new branch of x-ray astronomy," says Andrew Fabian, a theoretical astrophysicist at the University of Cambridge in the United Kingdom, who is a member of the ASTRO-H science working group. Whereas previous x-ray missions were tuned to image point sources such as black holes and neutron stars, ASTRO-H is built to analyze the x-rays emanating from large, diffuse celestial structures. ASTRO-H "is going to be spectacular," says Graziella Branduardi-Raymont, an astrophysicist at University College London, who works on the European Space Agency's XMM-Newton x-ray observatory, an older, complementary mission.

It has been a long time coming. A launch rocket failure sent Japan's ASTRO-E x-ray satellite crashing into the Pacific in 2000. The replacement mission, Suzaku, lost a key instrument to equipment troubles several weeks after its 2005 launch. As a result, "there hasn't been a major new x-ray observatory since 1999," when XMM-Newton and NASA's Chandra X-ray Observatory took flight, Fabian says.

A joint Japanese Aerospace Exploration Agency (JAXA) and NASA project, ASTRO-H fields a team of 240 scientists from 60 institutions in Japan, North America, and Europe. For JAXA's Institute of Space and Astronautical Science (ISAS), it is the biggest collaboration ever, says project manager Tadayuki Takahashi in Tokyo. The spacecraft is packed with six cutting-edge telescopes and instruments to catch and analyze soft x-rays, hard x-rays, and gamma rays.

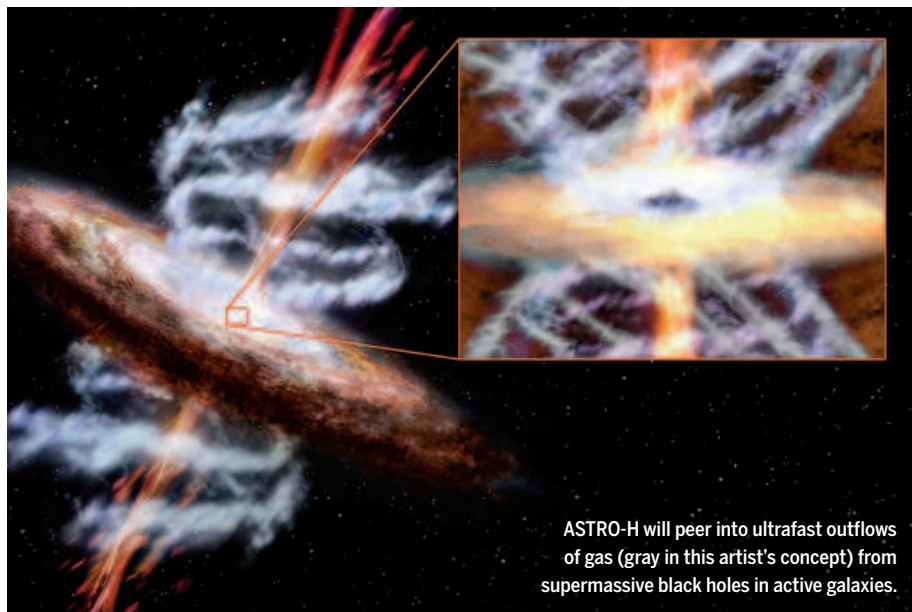
Scientists are most excited about the mission's soft x-ray spectrometer (SXS)—a kind of instrument that was also aboard JAXA's two earlier, ill-fated x-ray observatories. At its heart is a calorimeter that determines the energy of each incoming x-ray photon by measuring how it raises the temperature of

an absorbing material. This technique gives SXS 30 times the resolution of previous detectors, Takahashi says. The calorimeter must be kept at just 0.05° above absolute zero, which requires a sophisticated cooling system. But its dramatically better resolution, particularly at high energies, will be "transformational," Fabian says, illuminating details in celestial objects only hinted at by current detectors.

One observational target is the gas captured within galaxy clusters. "Most of the gas in the universe is not formed into stars. It lies between galaxies and is difficult to see," Fabian explains. The gravitational pull of galaxy clusters squeezes the gas and heats

AGNs. ASTRO-H promises to bring their blurred pictures into focus, providing details on the outflow velocity and dynamics. Studying these winds might help unravel why "the mass of a galaxy is found to be closely correlated with the mass of the central supermassive black hole," says Ken Pounds, an astrophysicist at University of Leicester in the United Kingdom.

The mission could also clear up an ongoing controversy about mysterious emissions at 3.55 kilo-electron volts that x-ray satellites have spotted emanating from Andromeda and other galaxies. The radiation could be due to dark matter particles annihilating one another, but there are other



ASTRO-H will peer into ultrafast outflows of gas (gray in this artist's concept) from supermassive black holes in active galaxies.

it to temperatures of millions of degrees, causing it to emit x-rays. By observing the gas in exquisite detail, ASTRO-H's SXS will reveal the chemical elements it contains and trace its violent movement within the cluster. Such data, Fabian says, should provide insights into how the universe gradually built up its chemical element inventory and what role interstellar gases play in star and galaxy formation.

Takahashi is particularly looking forward to training ASTRO-H's scopes on active galactic nuclei (AGNs), fountains of energy powered by the supermassive black holes in the hearts of distant galaxies. He says Suzaku and XMM-Newton have glimpsed evidence of ultrafast outflows of gas from

possibilities. Masahiro Takada, a cosmologist at the University of Tokyo's Kavli Institute for the Physics and Mathematics of the Universe, says that if swirling gases are producing the emissions, there would be a rotational motion signature; a signal from dark matter annihilation would not have any rotational component. ASTRO-H's resolution "allows us to make a direct test of the dark matter signal hypothesis," Takada says.

"There's just a zillion other things," on the ASTRO-H agenda, Fabian says. But scientists involved say the most important findings may come as complete surprises. "We have many good reasons why we need ASTRO-H, but my hope is that we can find something new that nobody expects," Takahashi says. ■

BIOMEDICAL RESEARCH

Calling all failed replication experiments

New journal will publish methods, data, and results

By Jocelyn Kaiser

The biotech company Amgen and prominent biochemist Bruce Alberts have created a new online journal that aims to lift the curtain on often-hidden results in biomedicine: failed efforts to confirm other groups' published papers. Amgen is seeding the publication with reports on its own futile attempts to replicate three studies in diabetes and neurodegenerative disease and hopes other companies will follow suit.

The contradictory results—along with successful confirmations—will be published by F1000Research, an open-access, online-only publisher. Its new *Preclinical Reproducibility and Robustness* channel, launched on 4 February, will allow both companies and academic scientists to share their replications so that others will be less likely to waste time following up on flawed findings, says Sasha Kamb, senior vice president for research at Amgen in Thousand Oaks, California. The aim is “to help improve the self-correcting nature of science to benefit society as a whole, including those of us trying to create new medicines.”

Alberts, a former *Science* editor-in-chief and National Academy of Sciences president who is at the University of California, San Francisco, says the journal will be a place for data that other journals often aren't interested in publishing because replication efforts lack novelty. “The whole idea is to lower the energy barrier for people doing this,” Alberts says.

A growing number of retractions—a few linked to fraud—have helped stir concerns about irreproducible results. Amgen itself raised the alarm 4 years ago when one of its scientists, who had recently left the firm, co-authored a commentary in *Nature* announcing that Amgen researchers could replicate just six of 53 landmark cancer biology studies. Bayer had published a similar analysis a few months earlier. The Amgen report drew criticism, however, because the company did not release any data or even reveal which studies it examined. (The former Amgen scientist, C. Glenn Begley, said one reason was confidentiality agreements with some of the original authors.)

The new channel, in contrast, will publish both methods and data from the replication attempts. “I do think it's proper

to show data and let people decide for themselves, and that's the plan here,” says Kamb, who joined forces with Alberts after they attended a retreat on integrity in science early last year.

Putting the contradictory data out in the open will “force the original authors to clarify [the discrepancies],” Alberts says. “Maybe it was correct, but the original



“I do think it's proper to show data and let people decide for themselves, and that's the plan here.”

Sasha Kamb, Amgen

description of what they did was flawed.” Publishing the data will also give the replicators credit for the time they've spent, he and Kamb say.

Amgen chose the three papers initially highlighted on the site not because they were particularly noteworthy, but because the company's scientists were ready to write them up, Kamb says. In one study, Amgen was not able to confirm a 2012 report in *Science* that a cancer drug, bexarotene, could clear β -amyloid plaques and reverse cognitive problems associated with Alzheimer's disease in mice. Four other groups had already questioned the findings in technical comments in *Science*. But Kamb says Amgen's contribution, which uses a different

tool molecule to test bexarotene's purported mechanism, adds “another very large brick.”

Amgen also reports that it failed to confirm a 2010 *Nature* study finding that blocking an enzyme called Usp14 helped cells degrade toxic proteins involved in Alzheimer's and amyotrophic lateral sclerosis. The Amgen work “raises questions about the utility of Usp14 as a therapeutic target for neurodegenerative disease,” Kamb says. In their third paper, Amgen scientists report that a genetic flaw in a commercially available mouse model that lacks the gene for the protein Gpr21 led both an earlier Amgen team and an academic lab to erroneously report that Gpr21 influences body weight and glucose metabolism. (Amgen gave reporters summaries of the three studies on the condition that they not contact the original authors until after the new channel launched.)

Like other F1000Research “channels,” the new journal will first post the raw manuscripts, then invite peer reviews that will be added with the reviewers' names. F1000Research charges author fees of \$150–\$1000 per paper depending on length. If the papers are accepted after peer review, they will be indexed in PubMed and “become part of the record,” Alberts says.

The project joins other efforts to promote reproducibility. The nonprofit Center for Open Science headed by psychologist Brian Nosek of the University of Virginia in Charlottesville is working with contract labs to replicate experiments from up to 50 high-impact papers in cancer biology. The project contacts the papers' original authors for input on protocols and will also invite them to peer review the results before they are published in the open-access journal *eLife*. Such consultation has “social and cultural value,” Nosek says, but he doesn't see it as a requirement and supports the new channel.

National Institutes of Health (NIH), Deputy Director Lawrence Tabak in Bethesda, Maryland, says NIH is also “supportive of” the new channel and is “encouraged by Amgen's leadership role.” Microbiologist Arturo Casadevall of Johns Hopkins University in Baltimore, Maryland, is a fan as well, but he cautions that a failed confirmation doesn't always mean the original findings were incorrect. Ideally the original authors will “try to understand the variables” that led to different conclusions, he says. ■



Downloaded from on February 4, 2016

WHAT MAKES DARPA TICK?

The stellar reputation of this small but mighty defense agency rests on the unparalleled clout of its program managers

By Jeffrey Mervis

In 2005, mathematician Ben Mann was pondering the fundamentals of life. Physical scientists had a bevy of fundamental equations that explained how the world worked. Biologists had nothing of the sort. What would happen, Mann wondered, if some of the best minds in math and biology were challenged to find such laws?

It wasn't an idle question. Mann was a new program manager at the Defense Advanced Research Projects Agency (DARPA) in Arlington, Virginia, an arm of the U.S. military renowned for pursuing seemingly wild ideas. Unlike at most other research agencies, where starting something new can require overcoming major bureaucratic hurdles, the only person Mann had to persuade

Mathematician Benjamin Mann, at home in Austin, was at DARPA from 2004 to 2010.

at DARPA before launching his quest for fundamental laws of biology—dubbed FunBio—was then-DARPA Director Tony Tether.

To Mann's delight, Tether quickly said yes. "Biology seemed to me just one accidental discovery after another," recalls Tether, an



DARPA developed the technology behind the F-117A, the first in a series of stealth aircraft that have revolutionized aerial warfare.

electrical engineer with deep roots in the defense community. “Ben thought he could make some headway.”

Founded in 1958 in the aftermath of Sputnik, DARPA’s job is to make sure the U.S. military holds a technological edge over its enemies. Over the decades since, it has earned a reputation for using out-of-the-box thinking to solve what defense officials like to call “DARPA-hard” problems. “The public gives DARPA \$3 billion a year, in round numbers, and every decade out pops an Internet, or synthetic biology, or carbon nanotubes, or another significant technology,” says Zach Lemnios, the Pentagon’s chief technology officer during the first Obama administration.

Lemnios also could have mentioned DARPA’s role in inventing stealth aircraft, pilotless drones, and laser-guided weapons, and nurturing the materials science and computer science communities. Its successes have inspired lawmakers to create a spate of imitators that try to duplicate DARPA’s free-wheeling approach, including the Intelligence Advanced Research Projects Activity (IARPA) and the Advanced Research Projects Agency-Energy (ARPA-E).

Such efforts inevitably raise a core question: What makes DARPA tick? The answer, say dozens of people who have worked for or with DARPA, is its cadre of program managers—people like Ben Mann—who enjoy a combination of autonomy, authority, and ample resources that is rare in government.

DARPA’s roughly 100 program manag-

ers are the agency’s “secret sauce,” says Lemnios, who now heads global research at IBM in Yorktown Heights, New York. They largely decide which projects DARPA tackles, says Craig Fields, who spent 15 years at the agency before becoming its director in 1989. “Is there a program manager around who wants to do it?” Fields says. “If not, it’s not going to happen.”

Mann, who will be 68 in April, says his 6-year stay at DARPA “was the most intellectually romantic period of my life. I felt that Daddy had given me the keys to the car to work in the best interests of the country.”

HOW MANN got his hands on those keys, and the way he drove the car, says a lot about how DARPA operates. After earning his Ph.D. from Stanford University in Palo Alto, California, in 1975, Mann spent the next quarter-century as an academic, with stops at Harvard University; Clarkson University in Potsdam, New York; and the University of New Mexico, Albuquerque. Twice he earned tenure. But job security didn’t keep him rooted. “I have the patience of an unstable subatomic particle,” Mann says.

His research specialty also contributed to his restlessness. “I’m an algebraic topologist, a field that was booming in the 1920s and 1930s,” he explains. “But by the time I got into it, it had become very technical. It’s like 10-meter Olympic diving, where you get points for style and degrees of difficulty.” Reviewers also penalized researchers who struck out in a new direc-

tion, Mann notes, damning them with such comments as “it’s not nearly as elegant as what you had been doing.”

That conservatism prompted Mann to look outside academia, and in 1999 he joined the National Science Foundation (NSF) as a program manager in its mathematics division. But the September 2001 terrorist attacks prompted another re-evaluation. He felt the surprise attacks had demonstrated that government officials “were looking at data the wrong way” and that his field could help them see things more clearly.

Personal factors were also at play. “My father was a World War II veteran and he was very upset by 9/11,” Mann recounts. “After he passed away in 2002, I felt I wanted to do something about it.”

Mann’s first step on the road to DARPA was helping run a joint, NSF-DARPA research program that used geometrically inspired algorithms to better describe complex 3D images. Ultimately, Mann’s counterpart at DARPA, mathematician Douglas Cochran, ended up recruiting him to the agency. Cochran had come to DARPA in 2000, on leave from Arizona State University, Tempe. Term limits are standard at DARPA, and on Cochran’s first day, his boss had told him to put finding a successor at the top of his to-do list.

When Cochran met Mann a few years later, he decided he’d make an ideal DARPA program manager. Mann “has tons of energy and interests, he’s very creative, and he’s obsessive to the point of being compulsive in trying to figure out how all the pieces fit together,” Cochran says.

After Cochran made his pitch, Mann didn’t hesitate. “They say you go to DARPA if you have something you absolutely have to do, and you can’t get it done anywhere else,” Mann says. “My *raison d’être* was to take math that other people thought was totally useless and show that it was applicable to the military.”

MANN ARRIVED at DARPA in June 2004 on a 2-year appointment with an option for renewal, like most program managers at the \$2.9 billion agency. That heavy reliance on temporary employees stands out among government agencies. The biggest U.S. research funder, the National Institutes of Health (NIH), has career employees managing its \$31 billion budget. At NSF, visiting scientists play an essential role in managing the agency’s \$7.3 billion research portfolio, but just one-third of its roughly 500 program officers are “rotators.”

DARPA officials believe that short stints keep the pressure on program managers to get things done. “My badge had an expiration date,” Mann says, “and I felt the clock

was always ticking.” But there are downsides to DARPA’s approach.

The agency loses up to a quarter of its front-line staff every year. A lack of institutional memory can result in duplicative efforts. And because staff “are generally recruited by existing program managers” or identified by a previous program manager, Cochran says, DARPA runs the risk of becoming something of an old boys’ club. “Someone ... brings in a friend, who brings in two friends, and pretty soon you have a self-perpetuating circle,” he notes.

That process might contribute to the extreme gender imbalance among DARPA program managers, who are 95% men, according to a recent roster. The agency’s current upper management—including the heads of the agency’s six top-level offices and their deputies—is slightly less skewed, with 10 men and four women. And the two directors appointed by the Obama administration—Regina Dugan in 2009 and Arati Prabhakar in 2012—are the only women to lead the agency in its 68-year history. (A quarter-century earlier, Prabhakar was also the first woman to manage one of DARPA’s top-level offices, in microelectronics.)

Inbreeding can also affect DARPA’s research agenda, Cochran says, when new program managers tap into the same network of researchers as their predecessors. “It’s possible for program managers to rotate,” he says, “but for DARPA to [continue funding] the usual suspects.”

The easiest way to freshen DARPA’s talent pool is to head off in a new direction. And DARPA’s culture made it much easier for Mann to plow new ground than it was at NSF.

For starters, NSF program managers rarely get the chance to jump-start a new research program; most of the agency’s budget is already committed to ongoing projects. In addition, NSF’s mission is to support entire disciplines, so program officers can’t place too many of their chips on one bet. In contrast, DARPA encourages its managers to take informed risks. “If I had brought my NSF mentality to DARPA, I would have failed,” Mann says.

Mann’s place within DARPA’s relatively flat bureaucratic structure also encouraged creativity. He worked for the Defense Sciences Office, often called “DARPA’s DARPA” because it has the broadest remit, and many of its projects start out as blue-sky adventures. (Three other offices are charged with developing technologies in specific areas, such as computing or biology, and two work with the military to adopt those technologies.)

Nor did Mann have to worry that a good idea would struggle for funding. Whereas many government research heads fret about

budgets that don’t at least keep pace with inflation, past DARPA directors are surprisingly blasé about the agency’s finances. “I never really felt constrained by money,” Tether says. “I was more constrained by ideas.” In fact, aerospace engineer Verne (Larry) Lynn, DARPA’s director from 1995 to 1998, says he successfully lobbied Congress to shrink his budget after the Clinton administration had boosted it to “dangerous levels” to finance a short-lived technology re-investment program. “When an organization becomes bigger, it becomes more bureaucratic,” Lynn told an interviewer in 2006.

Mann’s first proposal was to explore a field known as topological data analysis (TDA). Topology is the study of shapes; TDA rests on the idea that data have shape, and that their shape can reveal information that could not be gleaned with traditional analyses.

Mann’s interest in TDA dated from his graduate years at Stanford under James Milgram. He had befriended another of Milgram’s students, Gunnar Carlsson, who went on to develop TDA. Mann believed the field was ripe for a harvest, and it meshed with his post-9/11 urge to improve

pose ourselves to risk, because that’s how you get impact.”

Once TDA was approved, Mann was free to exploit another notable DARPA feature: a program manager’s near-absolute power to assemble a research team. Agency veterans say the prospect of becoming a funding czar is a powerful recruiting tool. In 1988, applied physicist Jane (Xan) Alexander was contemplating an academic career when she was recruited by Prabhakar. “She told me: ‘You don’t want to go to a university, where you’ll have graduate students working for you. If you come to DARPA, you’ll have professors working for you,’” recalls Alexander, who stayed 14 years and eventually became the agency’s deputy director.

To lead the TDA project, Mann tapped Carlsson, who had returned to Stanford in 1991. Within 6 months, Carlsson’s team produced an eye-catching success, discovering patterns in a data set that nobody had seen before. “That was a really big deal,” Mann explains. “It showed that the method was clearly applicable to use on many other massive data sets.”

The result convinced Tether to fund TDA

Two different ways to fund research

Although Defense Advanced Research Projects Agency (DARPA) program managers typically are on board for only a few years, they enjoy a degree of autonomy, flexibility, and authority unique among their colleagues at U.S. research agencies. Here’s how DARPA’s grantsmaking process generally differs from that at the National Science Foundation (NSF), which also relies heavily on short-termers to manage its research portfolio.

	DARPA	NSF
How much money is available?	Open-ended, but enough to complete the project	Fixed program budget
Who comes up with the idea?	Program managers must create and sell their projects.	Program officers inherit activities but can propose new initiatives.
Who can apply?	Program managers reach out to potential applicants, shape teams.	Most proposals come in over the transom on regular cycles.
How are proposals reviewed?	Program managers judge quality.	Panels assign scores based on scientific merit and broader impacts of proposed research.
Who makes the call?	Program managers pick winners with a firm goal in mind.	Top-ranked proposals usually get funded, but external factors also play a role. Scientific merit drives process.
How is the grant managed?	Program managers stay in close touch, enforcing milestones and making changes as needed.	Grantees have free rein to follow the science.

the government’s capacity to analyze data.

Mann knew his TDA proposal wouldn’t be scrutinized and scored by peer-review panels, as it might at NSF or NIH. Nor would the final decision be made by consensus. Once his idea passed muster with his office head, its next—and final—stop was the DARPA director.

“We don’t have a voting process,” Prabhakar explains. “Voting is really good to reduce risk. But I actually want us to ex-

pose ourselves to risk, because that’s how you get impact.”

AT FIRST GLANCE, FunBio might seem to have little to do with improving the efficacy of the U.S. military. But Mann hoped that discovering fundamental laws of biology might eventually help the military safeguard the health of its troops. And, more broadly, FunBio reflected DARPA’s long-standing interest in basic research that has

no obvious immediate application, but the tantalizing prospect of an enormous payoff down the road.

To be sure, DARPA's spending on basic research—known as 6.1 funding, after its line number in the Pentagon's budget—is small compared with its spending on more applied research (6.2) and technology development (6.3). In 2015, DARPA spent just 12% of its budget—or about \$350 million—on basic research. Typical projects total just a few million or tens of millions of dollars spread over up to 5 years. Yet DARPA's 6.1 investments can be a boon to a field. For example, Cochran says that a DARPA program to explore concepts in fundamental mathematics that he began—and Mann inherited—was at the time the government's largest single investment in pure mathematics.

It's not just the money that appeals to some grantees. There's also the lure of taking a gamble. Tim Buchman, director of the critical care center at Emory University's medical school in Atlanta, had two reactions in early 2005 when Mann invited him, out of the blue, to join FunBio: "That's a crazy idea," he said. "Count me in."

For his part, Tether would sometimes remind Mann that he had high hopes for FunBio. "You'd better come back with $F=ma$," Tether would growl, referring to Newton's second law of motion.

DESPITE ITS REPUTATION as a wild-idea factory, DARPA will ultimately be judged on its contribution to U.S. military superiority. But the best way to measure the agency's success or failure is the subject of perennial debate.

One challenge for DARPA is that it doesn't make new weapons and technologies. Instead, Alexander says, "it takes on the risky thing, and makes it real enough that the next guy will invest in it." That next guy may be a branch of the military, which then awards a contract to manufacture the weapon. Or a company may decide to incorporate the technology into a product for the commercial and/or military sector.

A study of 10 recent DARPA advanced technology projects by the Government Accountability Office (GAO), the watchdog arm of Congress, has added fuel to the debate. Five projects made a successful "transition" to military or commercial use, the December 2015 report concluded, including efforts to create new ship coatings to resist biofouling and to build an advanced radio system for the military.

GAO didn't address whether that 50% success rate was good or bad. But it did find that a technology was more likely to be adopted if the military or the commercial

sector had asked for it. And it said DARPA is doing an "inadequate" job of preparing program managers for the task of finding users for their products.

Pentagon officials took exception to that finding, which included a recommendation for additional training in making such transitions. The "relatively short tenure" of program managers doesn't allow for such training, they wrote in a response.

Former DARPA officials say GAO's metrics ignore how new technologies are devel-

"Is there a program manager around who wants to do it? If not, it's not going to happen."

Craig Fields, former DARPA director

oped. "You tie DARPA's hands if you say that it's never allowed to do a 6.3 program unless the services [have] already signed up," Alexander says, echoing the views of several past DARPA directors. "You'd never have had drones. The point is to develop a technology that will be a serious disruption to the status quo."

Mann applied his own metrics for measuring the success of his programs. (There were ultimately seven, all in basic research.) "My ideal program would run for 3 to 4 years, take the technical excuses off the table, and create a community of users, be it in [the military], academia, or industry, [and] preferably all three," he says. "I think most of my programs did that."

The TDA program, for example, ultimately spawned research groups at several research universities. It also paved the way for Ayasdi, a software firm that Carlsson and a former student founded in 2008 to help scientists make better use of massive data sets. The startup, based in Menlo Park, California, has grown to more than 100 employees, and last fall Carlsson retired from Stanford to spend full time at the company. DARPA considers Ayasdi such a success story that it invited Carlsson to give the kickoff talk at a 3-day conference held last fall to show off its programs and attract new researchers into the fold.

FunBio hasn't generated a commercial success like Ayasdi. But 2 years into the project, theoretical physicist Michael Deem of Rice University in Houston, Texas, did come up with a new way of describing a dynamical biological system. Deem found that environmental forces can induce a change in "modularity," which measures how a large system is built from well-defined pieces.

Deem then joined forces with Buchman to test whether this discovery might have clinical applications. In one NIH-funded study, they applied the model to predicting how cardiac patients on respirators would respond if asked to breathe on their own. The goal, the researchers explained in a 2013 paper, is to develop automated interventions that could save the life of an "off-trajectory" patient by anticipating "what will happen five minutes from right now."

That goal may never be reached, Buchman concedes. "It's a big stretch to go from finding a fundamental law to asking if it's safe to do something at the bedside, without having a human being actually think about it first," he says. But Simon Levin, an evolutionary biologist at Princeton University and principal investigator on the FunBio project, says that it has made a significant impact on the rapidly growing field of complex systems biology.

"Ben's approach allowed us to do science that both explored really novel areas and also exploited that knowledge to tackle specific problems," Levin says. "NSF or NIH grants don't usually let you do both things."

CRITICS OF DARPA say its top-down, go-for-broke culture can give short shrift to the ethical and moral implications of the agency's research. DARPA's role in developing the chemical defoliant Agent Orange during the Vietnam War is one glaring example, they say. A more recent instance is Total Information Awareness, a program launched after the 9/11 attacks to analyze communications among millions of Americans; it was quickly shut down following a public outcry. And a recent book billed as "an uncensored history" of the agency suggests that DARPA's sizable investments in improving the interface between humans and computers for prosthetic and robotic devices are really intended to create supersoldiers and mind-control systems—a suggestion DARPA officials reject.

The agency's relative autonomy has also allowed it to promote research far outside the scientific mainstream. Tether, for example, admits to a fondness for sonofusion, a controversial scheme for harnessing cavitating bubbles to spark nuclear fusion. Under his 8-year watch, DARPA spent millions of dollars annually on a sonofusion program based on little more than Tether's conviction that "there was something there." He admits that "I kept it under the radar."

Even a theoretical mathematician like Mann has been criticized for overreaching. At a 2007 DARPA conference, Mann laid out "23 challenges" in mathematics—a tribute to a list of 23 problems that math-

ematics legend David Hilbert presented at The International Congress of Mathematicians in Paris in 1900, which heavily influenced the field for the next century. Some researchers accused Mann of hubris, and others saw a veiled attempt to get mathematicians to do the military's bidding.

Looking back, Mann acknowledges that the idea "might have offended some mathematicians." His goal, he says, was simply to tell the community "what I wanted to see happen if I was going to stay [at DARPA

for] another 5 years."

That didn't come to pass. Mann left DARPA in 2010 after Dugan became the first DARPA director chosen by the Obama administration. "I had too much of Tony [Tether]'s DNA on me, and Regina pulled the plug on everything I was doing," he says. "But that's OK. I don't blame her for wanting to do something different."

Mann became a vice president at Ayasdi, where he stayed for 5 years before resigning last summer. Now living in Austin, he con-

sults for DARPA and other clients.

Some talented scientists and engineers may be uncomfortable with having their discoveries used in waging war, Mann admits. Still, the agency's unique approach to research, and its unusual way of deploying program managers, has made it an important part of the U.S. scientific landscape. "It woke up my thinking, like Rip van Winkle," Mann says. "DARPA at its worst is catastrophic. But DARPA at its best, there's nothing like it." ■

Biology came late, and arrived with a bang *By Jeffrey Mervis*

After the Cold War ended, U.S. military leaders began to worry that rogue states might wage bioterrorism attacks on both U.S. soldiers and civilian populations. That new threat exposed a significant hole in the Defense Advanced Research Projects Agency's (DARPA's) portfolio: the life sciences.

Remarkably, the agency didn't hire its first biologist until 1990. But over the next quarter-century it made up for lost time, and in June 2014 DARPA put the life sciences on an equal footing with other disciplines by creating the Biological Technologies Office (BTO).

Arriving late has allowed DARPA to take advantage of the stunning advances in biology over the past 50 years without losing sight of its unique mission. "We're not in the business of dealing with all of human health," says DARPA Director Arati Prabhakar in Arlington, Virginia. "We're going to look for specific opportunities that connect to national security."

There is no shortage of targets. "One area is about restoring brains and bodies, because that's part of what our warfighters deserve," she explains. The havoc wrought by improvised explosive devices in Iraq and Afghanistan, for example, has led to a program on revolutionizing prosthetics that has attracted widespread media coverage. Similarly, concerns about bioterrorism spawned major initiatives for detecting and diagnosing potentially lethal agents as well as developing medical countermeasures, including new vaccines and therapeutics. A third area is synthetic biology, in which biology becomes a platform upon which to build new molecules and materials.

Those challenges, Prabhakar says, have forced the agency to rethink its



Hazmat firefighters in Las Vegas, Nevada, train for the possibility of bioterrorism, a threat that required DARPA to beef up its scant expertise in the life sciences.

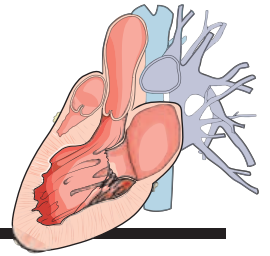
traditional approach to developing new technologies. "When we engineers think about building a system, we think about sensors that interact with the physical world, about hardware and software," she explains. "And if we're really smart we think about the human being in the loop. Right now we don't design with biology in mind. But imagine if biology were part of the design palette in the same way that mechanical and electronic and information technologies are now."

Although the BTO staff is just one-third the size of the microelectronics and the computing/information sciences offices, that's a major step up for the field from when aerospace engineer Verne (Larry) Lynn became director in 1995. "We had just a little bit of biology knowledge, enough to be dangerous but not enough to do much," Lynn recalled

in a 2006 interview.

That changed in a hurry. Biology became a major focus during Lynn's 2.5-year tenure, and the agency's annual investment in biodefense skyrocketed, from \$20 million to \$180 million.

The rapid scale-up also required senior managers to run programs well outside their areas of expertise. "The office head was a chemist, and I was a physicist by training," recalls Jane (Xan) Alexander, then-deputy director of the Defense Sciences Office, which housed the agency's fledgling biodefense programs. "We both had strong backgrounds in materials and electronics. So we ended up flipping a coin to see who would handle biology. And I spent a long time getting up to speed." A quarter-century later, the existence of BTO suggests that's not a problem anymore. ■



No larger than a pinhead in size, a female *V. destructor* uses a worker bee as transport and food source.

PERSPECTIVES

ECOLOGY

The mite that jumped, the bee that traveled, the disease that followed

Global expansion and trade contributed to the declining health of honeybees

By Ethel M. Villalobos

European honeybees are among the best-studied and most widely recognized insect species in the world. Originally kept for honey production, they have become the flagship species for pollination and large-scale

agriculture. Since large colony losses were reported across the United States in 2006, researchers have investigated the myriad factors that contribute to the decline in honeybee populations. In particular, the aptly named *Varroa destructor* mite (see the photo) and the deformed wing virus (DWV) have been clearly linked to colony

collapse (1). On page 594 of this issue, Wilfert *et al.* use a phylogeographic analysis to examine the evolutionary origin and mechanisms for the global spread of the DWV (2).

Based on molecular data from 17 countries and 32 geographical regions, the authors confirm that DWV is an endemic

PHOTO: MATT BERTONE

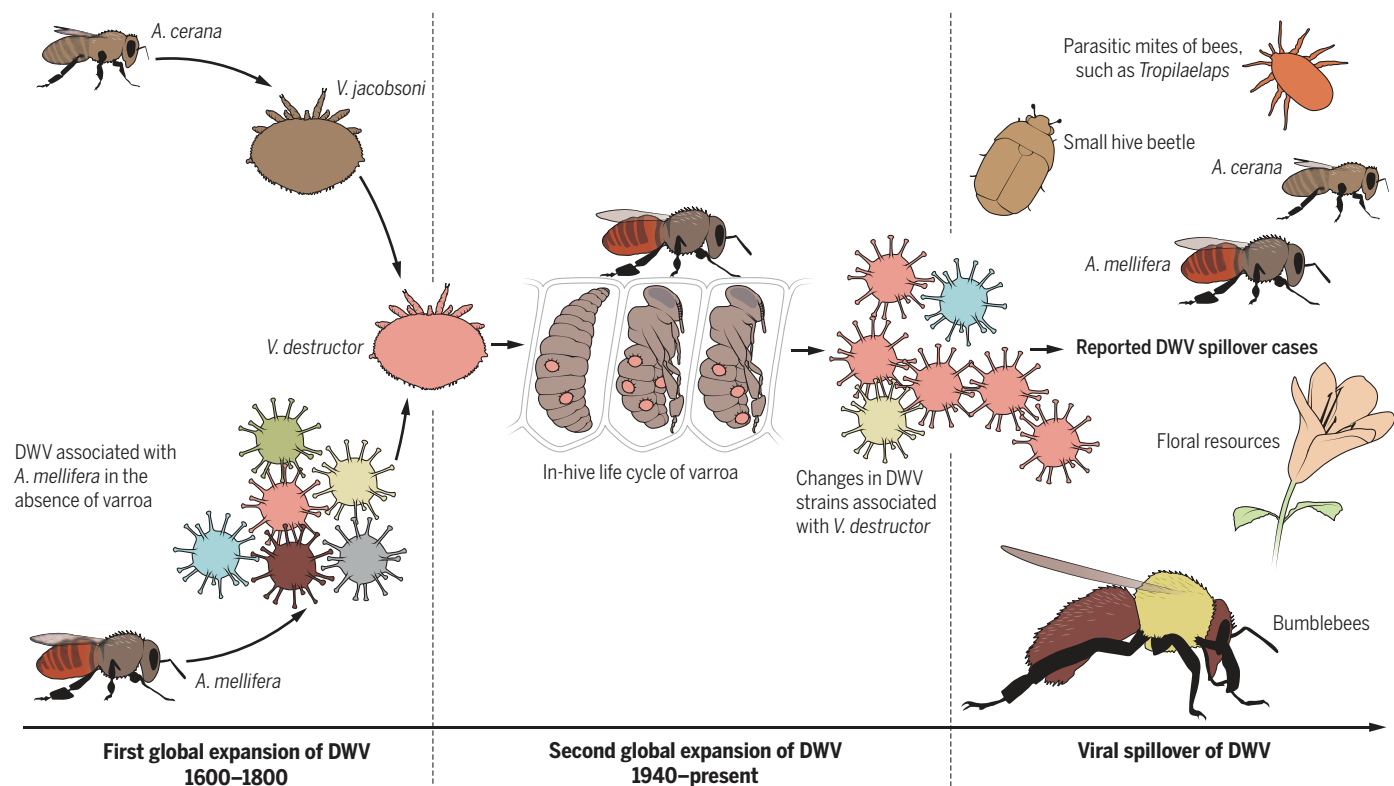
pathogen of the European honeybee, *Apis mellifera* (see the figure). Thus, the recent honeybee decline associated with DWV constitutes the reemergence of a previously existing disease of *A. mellifera*. This reemergence was facilitated by the spread of the new vector *V. destructor* and by human transport of honeybee colonies from Europe and North America to other geographical regions.

The DWV epidemic is part of a global trend of disease reemergence affecting a diverse range of organisms. In the past 20 years, an increase in viral diseases of vegetable crops has greatly affected productivity worldwide. This change was driven by

both of these haplotypes are now grouped under *V. destructor* (4). This novel vector-host relationship was mediated by human introduction of European honeybees to central and southeastern Asia, bringing these two closely related bee species (5) into contact.

Martin *et al.* (1) have shown that the arrival of *V. destructor* on previously varroa-free islands in Hawaii led to a rapid reduction in DWV strain diversity, coupled with a dramatic increase in virulence. Wilfert *et al.* (2) now track the historical global movements of DWV and show that in the recent past, the virus has spread to multiple hosts. Cross-species infections and viral

As with the viral-whitefly association (3), the role of humans in the global spread of the European honeybee, the varroa mite, and DWV is undeniable. The first expansion of the honeybee's range began in the early 1600s and continued until the late 1800s. Honeybee colonies were transported on slow-moving cargo ships, packed in iceboxes to simulate winter months and slow their metabolism (8). The second large wave of expansion occurred in the past 75 years, promoted by the development of large-scale modern agriculture (see the figure). Wilfert *et al.* use 20th-century samples to reconstruct the origin and migration rates of the DWV during this second wave and correlate the virus expan-



Global spread. As shown by Wilfert *et al.*, factors driving the global reemergence of DWV, an endemic pathogen of the European honeybee, include human-mediated movement of managed bees, adaptation of a vector mite to a novel host, and changes in the viral population. The first global movement involved managed bees without the vectoring mite. The second, more recent, event occurred after the varroa mite had come into contact with DWV. The increased viral levels and pathogenicity of DWV in the presence of *V. destructor* appear to be linked to a viral spillover to floral resources and a number of arthropod species, including native solitary and social bees.

the spread of an insect vector, the whitefly, *Bemisia tabaci*, and the human transport of infected plants (3). In the case of the European honeybee and *V. destructor*, natural genetic variation in the brood parasite *Varroa jacobsoni* facilitated its jump from the Asian honeybee (*Apis cerana*) to the European honeybee (*A. mellifera*). Two haplotypes derived from *V. jacobsoni* have adapted to reproduction on *A. mellifera*;

reemergence are more likely to occur if the virus is a “generalist” that can recognize a range of cell receptors and invade a diversity of tissues and hosts (6, 7). According to Wilfert *et al.* (2), three viral fragments of the DWV (*rdrp*, *vp3*, and *lp*) show little host specificity, a trait that would favor global expansion. The data provide solid evidence for transmission of DWV from the ancestral host, *A. mellifera*, to *V. destructor*, as well as to novel hosts, such as *Tropilaelaps clarea* (another Asian honeybee mite) and bumblebees.

tion with global patterns of mite distribution. Europe and North America are clearly the main centers for transmission of DWV to other areas of the world. Varroa-free areas, such as Australia and some islands in Hawaii, show weaker migration rates of DWV due to geographical isolation, reduced trade, and restrictions on the import of live honeybees to these regions.

Knowledge of the history and ecology of new diseases provides a framework in which to understand the origins, effect, and possible strategies for pathogen control.

Wilfred *et al.* provide such a tool by combining molecular data, geography, and a time line for the global dispersion of DWV and *V. destructor*. The high levels of DWV due to mite-related transmission (9) affect not only honeybees, but also possibly other insects that may come into contact with the virus (10) and food resources they share (10, 11). DWV has been detected in various insect groups that play dramatically different ecological roles, including insect predators and scavengers, pollinators, and pest species that live inside the colony (10).

The increased prevalence of DWV in infected colonies, combined with the high density of colonies in certain regions, creates a favorable environment for the virus to spread. The global snapshot provided by Wilfert *et al.* suggests that certain geographic areas have unique ecological conditions that may shed light on the evolution of the DWV and the host-vector relationship. South America, for example, hosts a hybrid of the European and the African honeybee, *Apis scutellata*, which shows genetic differences in immune responses and a greater tendency to remove brood infected by varroa from the hive (5). The overlapping ranges of *A. mellifera* and *A. cerana* in Southeast Asia provide an opportunity to compare noncoding RNAs that may be related to antiviral activity (12).

Finally, three master variants of DWV—type A, type B, and the newly discovered master variant type C—may produce recombinants, compete with each other within the host colony, and differ in virulence levels (7). The few remaining varroa-free refugia provide a unique opportunity to study the numerous master strains that exist without the vector's input. In-depth studies of virus, vector, and host populations in diverse geographical regions will help to understand how viruses spread to new hosts and adapt to new environments. ■

REFERENCES AND NOTES

1. S. J. Martin *et al.*, *Science* **336**, 1304 (2012).
2. L. Wilfert *et al.*, *Science* **351**, 594 (2016).
3. J. Navas-Castillo *et al.*, *Annu. Rev. Phytopathol.* **49**, 219 (2011).
4. D. L. Anderson, J. W. H. Trueman, *Exp. Appl. Acarol.* **24**, 165 (2000).
5. A. Wallberg *et al.*, *Nat. Genet.* **46**, 1081 (2014).
6. A. Moya *et al.*, *Nat. Rev. Microbiol.* **2**, 279 (2004).
7. G. J. Mordecai, L. Wilfert, S. J. Martin, I. M. Jones, D. C. Schroeder, *ISME J.* **10**, 1038/ismej, 2015.178 (2015).
8. E. Crane, *The World History of Beekeeping and Honey Hunting* (Routledge, New York, 1999).
9. Y. P. Chen *et al.*, *Appl. Environ. Microbiol.* **71**, 436 (2005).
10. R. Singh *et al.*, *PLOS ONE* **5**, e14357 (2010).
11. D. P. McMahon *et al.*, *J. Anim. Ecol.* **84**, 615 (2015).
12. M. Jayakodi *et al.*, *BMC Genom.* **16**, 680 (2015).

ACKNOWLEDGMENTS

I thank W. Haines, L. Brettell, E. Shelly, and C. Tarutani for comments that improved the manuscript and J. Wright for his expert assistance with the graphics.

10.1126/science.aaf0938

HEART DISEASE

Throttling back the heart's molecular motor

A small molecule inhibits mutated forms of myosin that cause cardiac hypertrophy

By David M. Warshaw

A young athlete collapses and dies during competition. Autopsy reveals an enlarged heart with thickened walls in which the cardiac muscle cells are in disarray and surrounded by fibrotic tissue. Until 1990, the cause of such sudden death was unknown. This devastating condition, called familial hypertrophic cardiomyopathy (HCM), was eventually linked to a mutation in myosin (1), the heart's molecular motor. Today, more than 300 separate HCM-causing mutations have been identified throughout the myosin molecule. On page 617 of this issue, Green *et al.* (2) describe a small molecule that binds to myosin and inhibits its activity, delaying the onset and progression of the disease in a mouse model. The study offers hope that a “simple” remedy for HCM may be possible.

Myosin is an adenosine triphosphatase (ATPase) enzyme that cyclically interacts with cytoskeletal actin filaments to convert chemical energy—through its hydrolysis of ATP—into force and motion that powers the heart's pumping action. Muscle cells of the heart shorten by the sliding of actin filaments past myosin filaments in the sarcomere, the cell's smallest contractile unit. Each myosin filament is composed of ~300 myosin molecular motors that generate power through their interaction with actin (see the figure). Mutation in the human β -cardiac myosin gene (*MYH7*) results in the amino acid substitution of arginine at position 403 with glutamine (R403Q) in the molecular motor. With 50% of R403Q patients dying by age 35 (3), understanding the molecular basis of the mutation's primary insult to the myosin motor's power-generating capacity has been a matter of vigorous debate.

Initially, it was proposed that a loss in myosin power output was the causative factor of HCM, and that remodeling of the heart was

a failed compensatory response (4, 5). To address this question, a mouse model of HCM was generated in which the animal develops a hypertrophied heart and dies suddenly when physically challenged—outcomes resulting from a single R403Q allele, as occurs in humans (6). Mice homozygous for R403Q die within 7 days of birth, emphasizing the devastating impact of this mutation (6). Analysis of pure mutant α -cardiac myosin (which is 92% identical in its wild-type primary sequence to human β -cardiac myosin) isolated from the hearts of these mutant mice revealed that the motor protein had twice the force- and motion-generating capacity compared to normal myosin (in a simplified in vitro model of cardiac contraction), and also had equally enhanced ATPase activity (7). These characteristics raise the potential for excessive ATP utilization and, consequently, boost energy demand, which could signal hypertrophic remodeling (8). These gains of function for the mutant form of myosin

should not have been surprising, given that clinical measures of cardiac performance describe the HCM heart as hyperdynamic (9). Many of the mutations discovered in myosin's motor domain have a tendency toward enhanced

mechanical and/or ATPase capacities (10)—specifically, the R403Q, R453C, and R719W mutations studied by Green *et al.*, in which arginine (R) at position 403, 453, and 719 is substituted with glutamine (Q), cysteine (C), and tryptophan (W), respectively.

In some patients with HCM, surgical thinning of the septal wall between the right and left ventricle can reduce the thickened wall's encroachment on the left ventricle's outflow tract (11); for severe cases, cardiac transplantation may be the only option. With 1 in 500 individuals having HCM, a far less invasive intervention is desirable. Green *et al.* tested the hypothesis that if HCM mutations lead to enhanced myosin power production, then early intervention using small-molecule inhibitors of myosin power generation should prevent hypertrophy. MyoKardia, a company founded by four authors of the Green *et al.* study, developed such a small-molecule in-

“...a ‘simple’
remedy for HCM
may be possible.”

Molecular Physiology and Biophysics, Cardiovascular Research Institute, University of Vermont, Burlington, VT 05405, USA. E-mail: david.warshaw@med.uvm.edu

hibitor (MYK-461). Green *et al.* observed that the small molecule reduced both myosin's power generation, as measured in isolated rodent cardiac muscle fibers, and ATPase rate. The authors tested two protocols for administering MYK-461 (via drinking water) to HCM (i.e., R403Q, R453C, and R719W) mice: at age 8 to 15 weeks before detectable cardiac hypertrophy, myocyte disarray, and fibrosis; and at age 30 to 35 weeks, once cardiac remodeling has occurred. Amazingly, early, chronic drug administration effectively prevented the development of hypertrophy, muscle cell disarray, and fibrosis, and diminished both hypertrophic and profibrotic gene expression. However, these dramatic and positive effects were seen only with early drug administration, but not observed in the older HCM mice once the pathologic cardiac remodeling

occurred. Whether the benefits of early intervention last if MYK-461 treatment is halted, or instead unleash the hypertrophic program has yet to be determined.

Mutations to virtually every contractile protein of the heart can lead to HCM (10); most notably, cardiac myosin-binding protein-C (cMyBP-C), which serves as a "brake" to limit myosin power production through its interactions with both myosin and actin (12). Mutations in cMyBP-C are a leading cause of HCM and compromise cMyBP-C braking action (13), resulting in increased myosin power production. Enhanced cardiac contractility is a recurrent theme (10), suggesting that the myocardium is finely tuned to myosin's normal steady-state stress levels (force/unit area of muscle). By analogy, placing the engine of an Indy race car (i.e., mutant myo-

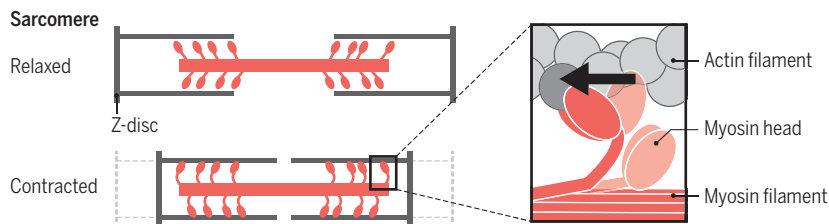
sin) in a stock car chassis (i.e., the heart's connective tissue matrix) could lead to internal stress and structural damage; for the heart, this amounts to inducing cardiac fibrosis and muscle cell disarray that are characteristic of HCM patients. If enhanced sarcomeric power production is the driving signal for cardiac hypertrophy, then simply throttling back the myosin engine with a small-molecule inhibitor may be a generalized approach to deal with the vast array of contractile protein mutations (e.g. actin, troponin, tropomyosin, cMyBP-C).

Interestingly, mutations in some of the same cardiac contractile proteins lead to dilated cardiomyopathy (DCM), where thin ventricular walls are almost incapable of pumping blood. In stark contrast to HCM mutations, myosin mutant forms S532P and F764L (in which serine at position 532 and phenylalanine at position 764 are replaced by proline and leucine, respectively) that cause DCM have diminished power production and ATPase activity (14). Could early intervention with small-molecule activators of cardiac myosin power production effectively treat genetic DCM? The myosin activator omecamtiv mecarbil is now in phase 2 clinical trials for treating human heart failure (15).

Early identification of HCM and DCM mutations could rely on family genetic history or a more ethically challenging agenda of genetically screening segments of the population. Perhaps genetic cardiomyopathies will be best served by a taking a daily pill to suppress the genetic programs that may lead to sudden death. Maybe gene therapy based on the use of clustered regular interspaced short palindromic repeats (CRISPR) technology will be commonplace in the future. Only time will tell, but Green *et al.* suggest that basic science can push clinical treatments from managing symptoms to correcting a defect. ■

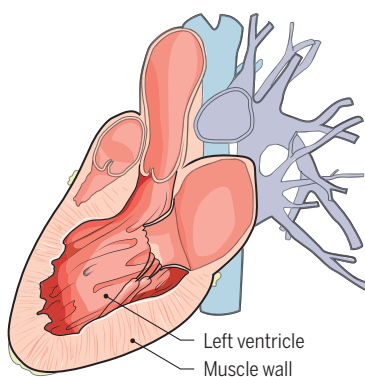
Myosin and muscle contraction

Myosin generates power that moves actin filaments in the sarcomere, in turn contracting muscle cells. Mutations in myosin that increase this capacity cause hypertrophic cardiomyopathy (HCM).



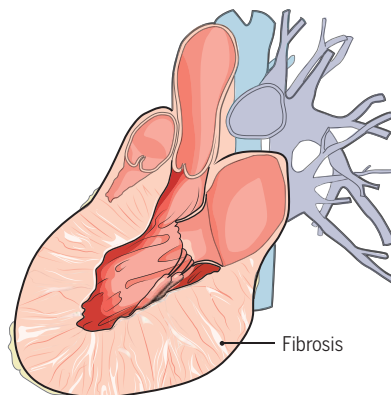
Young HCM patient

Genetic predisposition but no pathology yet



Older HCM patient

Genetic predisposition and pathology seen



Myosin inhibitor treatment

No disease
Hyperdynamic muscle contraction not occurring
Discontinue treatment
?

No change
Hyperdynamic muscle contraction persists
Heart failure

Targeting myosin. Mutations in myosin that increase power generation lead to hypertrophic cardiomyopathy (HCM). In a mouse model of HCM, early intervention with a small-molecule inhibitor of myosin reverses the disease (hypothetical patient scenario is shown). Such intervention could simplify treatment and become a generalized approach to control many contractile protein mutations that lead to HCM, or the use of myosin activators for dilated cardiomyopathy (DCM). DCM is characterized by less power production by myosin, heart muscle atrophy, and heart failure.

REFERENCES

1. A. A. Geisterfer-Lowrance *et al.*, *Cell* **62**, 999 (1990).
2. E. M. Green *et al.*, *Science* **351**, 617 (2016).
3. N. D. Epstein *et al.*, *Circulation* **86**, 345 (1992).
4. G. Cuda *et al.*, *J. Clin. Invest.* **91**, 2861 (1993).
5. E. B. Lankford *et al.*, *J. Clin. Invest.* **95**, 1409 (1995).
6. A. A. Geisterfer-Lowrance *et al.*, *Science* **272**, 731 (1996).
7. M. J. Tyska *et al.*, *Circ. Res.* **86**, 737 (2000).
8. H. Ashrafian *et al.*, *Trends Genet.* **19**, 263 (2003).
9. M. D. Klein *et al.*, *Am. J. Cardiol.* **15**, 773 (1965).
10. J. R. Moore *et al.*, *Circ. Res.* **111**, 375 (2012).
11. J. A. Dearani *et al.*, *Nat. Clin. Pract. Cardiovasc. Med.* **4**, 503 (2007).
12. M. J. Previs *et al.*, *Science* **337**, 1215 (2012).
13. S. P. Harris *et al.*, *Circ. Res.* **108**, 751 (2011).
14. E. P. Debold *et al.*, *Am. J. Physiol. Heart Circ. Physiol.* **293**, H284 (2007).
15. F. I. Malik *et al.*, *Science* **331**, 1439 (2011).

ACKNOWLEDGMENTS

This work is supported by NIH grants to D.M.W. (HL059408, HL126909).

APPLIED PHYSICS

Addressing an antiferromagnetic memory

Antiferromagnets could form a stable and robust platform for future spintronic technology

By Christopher Marrows

Spintronics (1) is one of the most commercially successful nanotechnologies. The invention of the giant-magnetoresistance spin valve (2) revolutionized the magnetic recording industry, enabling the immensely cheap, high-density disk drive storage on which the data centers that support our insatiable demand for cloud computing, social networking, and video sharing technologies rely. The combination of magnetic tunneling junctions (3) and spin-transfer torque (STT) (4) has brought about the prospect of magnetic random-access memory (MRAM), written using STT, as a way to provide nonvolatile storage that can be written and operated using extremely low power. Such technologies have just entered the marketplace. Even more energy-efficient writing is possible using the recently discovered spin-orbit torque (SOT) (5). All

of these technologies use ferromagnets—the type of magnetic materials that “stick to the fridge” because they possess a magnetic moment—to store the data; the direction of that magnetic moment (“north” or “south”) represents the 0 or 1 of a digital bit. In both STT and SOT, the flow of a spin-polarized electrical current exerts torques on the magnetic moments to affect the change in magnetization direction that writes this bit. On page 587 of this issue, Wadley *et al.* (6) show that a hitherto exotic class of magnetic materials, antiferromagnets, are candidates for an entirely new type of spintronic memory.

The antiferromagnets were described by Louis Néel, in his 1970 Nobel lecture, as being theoretically interesting but technologically useless. This is because the magnetic moments on each atomic site, rather than all pointing in the same direction as in a ferromagnet, alternate in direction. This means that antiferromagnetic order is difficult to detect externally, as there is no net magnetization to measure, and even more difficult to manipulate, as there is

Stable switching. The flow of an electrical current reorients the alternating antiferromagnetic (AF) moments to lie across the direction of electron flow. Two different states, at right angles to each other, can be used to represent the “0” or “1” of a bit of digital data.

almost no response to the application of a magnetic field. Unless one is a connoisseur, with sophisticated techniques such as neutron diffraction at hand, these materials appear to be nonmagnetic. To date, the sole technological application of antiferromagnets has been the stabilization of the magnetization in the reference layer of spin valves and magnetic tunnel junctions, finding a commercial market almost 30 years after Néel’s lecture. Although there is only one way for all the magnetic moments to point in the same direction, there is a rich variety of interesting ways in which spins can alternate in direction on a three-dimensional crystal lattice.

Wadley *et al.* have built on the previous theoretical insight that some of these ways of alternating have a very special property: that the flow of an electrical current can exert alternating torques on the alternating moments, rigidly rotating the whole spin structure to alternate along a different direction (7) (see the figure). Having already demonstrated the growth of an appropriate material (8), CuMnAs, in a thin film suitable for fabricating microelectronic devices by the usual planar processing methods, and knowing that the different directions of the alternating moments give rise to slightly different electrical resistances (9), the stage is set for the breakthrough reported

“...data stored in such a memory will be stable against any attempt (planned or accidental) to externally wipe it...”

here: an antiferromagnetic device into which a digital bit can be written and read electrically and stored without power, in a way that is insensitive to magnetic fields.

This is what Wadley *et al.* have now demonstrated. By patterning an eight-armed “Union Jack” device from their CuMnAs film, they have all the electrical contacts needed to rotate the alternating spin structure in the device back and forth by 90° into a pair of stable states, and then subsequently detect these rotations electrically. Furthermore, they have used synchrotron-based x-ray microscopy to directly visualize the rotations in the magnetic order,

School of Physics and Astronomy, University of Leeds, Leeds LS2 9JT, UK. E-mail: c.h.marrows@leeds.ac.uk

confirming the nature of the electrical signals that are read out in their devices. As expected, there is almost no sensitivity to applied magnetic fields. All this was performed at room temperature.

This breakthrough reveals fertile ground for new spintronics device concepts based on antiferromagnets. The lack of magnetic moment and concomitant insensitivity to fields means that data stored in such a memory will be stable against any attempt (planned or accidental) to externally wipe it with a magnetic field. The devices can also be packed arbitrarily densely on a chip without fear of their disturbing one another's state. Because antiferromagnets display resonances in the terahertz frequency range, versus gigahertz for ferromagnets, they offer the prospect of extremely fast operation.

However, major obstacles to a competitive memory technology remain. The device presented by Wadley *et al.* produces a very small readout signal, but this problem could be ameliorated by using a tunnel-junction readout technique, where it is already known that the readout signals can be large (10). Such a vertical device geometry could also help to increase memory cell density in an array architecture; at the moment, the "Union Jack" lateral geometry will occupy a prohibitively large footprint. Solving these problems will entail some interesting device engineering projects. Of more fundamental interest is the slow relaxation of the antiferromagnetic order into its rotated state, which sometimes requires many pulses, each of tens of milliseconds, to induce the full resistance change. Determining whether current-driven dynamics can truly happen at terahertz frequencies remains an outstanding challenge. Nonetheless, identifying this promising class of antiferromagnets that can display this remarkable behavior is a breakthrough that will be seized upon by many other laboratories, not least because these effects are predicted in other materials systems (11). Given the vast number of antiferromagnets, it is unlikely that the optimal material has been discovered at this early stage. The search is now on to find it. ■

REFERENCES

1. A. Hoffmann, S. Bader, *Phys. Rev. Appl.* **4**, 047001 (2015).
2. B. Dieny *et al.*, *Phys. Rev. B* **43**, 1297(R) (1991).
3. J. S. Moodera *et al.*, *Phys. Rev. Lett.* **74**, 3273 (1995).
4. J. A. Katine *et al.*, *Phys. Rev. Lett.* **84**, 3149 (2000).
5. L. Liu *et al.*, *Science* **336**, 555 (2012).
6. P. Wadley *et al.*, *Science* **351**, 587 (2016).
7. J. Železný *et al.*, *Phys. Rev. Lett.* **113**, 157201 (2014).
8. P. Wadley *et al.*, *Nat. Commun.* **4**, 2322 (2013).
9. X. Marti *et al.*, *Nat. Mater.* **13**, 367 (2014).
10. B. G. Park *et al.*, *Nat. Mater.* **10**, 347 (2011).
11. V. M. T. S. Barthem, *Nat. Commun.* **4**, 2892 (2013).

10.1126/science.aad8211

STEM CELLS

Aging, alopecia, and stem cells

Intrinsic epigenetic status and extrinsic environmental factors affect hair follicle stem cells

By Mingxing Lei,^{1,2} and Cheng-Ming Chung^{1,3}

Many tissues turn over during adult life, and declines in this process are associated with the progression of aging. Whether renewal is continual (as in the intestinal villi) or episodic (as in hair follicles), it is mainly attributed to somatic stem cells. One fundamental question is whether a decline of tissue renewal reflects the lifelong accumulation of external insults or the internal progression of a clock within stem cells? On pages 613 and 575 of this issue, Wang *et al.* (1) and Matsuura *et al.* (2), respectively, gain insight into this phenomenon by examining hair follicle growth and aging.

Slowing down aging and moving toward regenerative medicine requires understanding fundamental principles of tissue renewal. If intrinsic changes in stem cells play a major role, the basis for their use to prevent aging weakens. If environmental factors play a dominant role, rebuilding stem cell niches or modifying the global body environment will be important.

The hair follicle is an excellent model for studying regeneration because the follicle contains stem cells that can be activated cyclically, reflected in the growing (anagen) and resting (telogen) phases of the hair cycle (3, 4) (see the second figure). The longer the growth phase, the longer the hair. Thus, the vitality of stem cells, reflected in the duration of the growth phase, is a measurable capacity. Because hair can show different phenotypes in different life stages and in different anatomical locations (5), it provides a highly accessible window to peek into

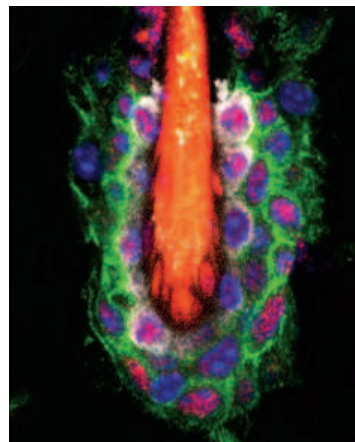
the cellular and molecular basis of stem cell activity in growth and aging. Indeed, androgenetic alopecia (hair loss) is a common sign of aging.

During cyclic quiescence and activation, hair follicle stem cells (HFSCs) in resting phase constantly "sum up" the input of activators and inhibitors. When total activators become dominant, the follicle enters growth phase (4–6). The secreted proteins bone morphogenetic protein (BMP) and Wnt display competing inhibitor and activator activities, respectively, leading to stem cell quiescence (telogen) or entrance into hair growth (anagen). Yet the internal status of stem cells determines the response to these external factors (7, 8). For example, deletion of DNA methyltransferase-1 (DNMT1) from the epidermis (in mice) decreases the probability

of successful stem cell activation in every hair cycle, leading to progressive alopecia (9). This indicates that an intrinsic mechanism affecting the epigenetic landscape is involved in the response of HFSCs to external factors. As well, transcription factors such as LIM homeobox 2 (Lhx2), transcription factor 3/4 (TCF3/4), SRY-box 9 (Sox9), Tbox 1 (Tbx1), and nuclear factor of activated T cells, cytoplasmic 1 (Nfatc1) are critical to HFSC properties, and their absence results in accelerated entry into

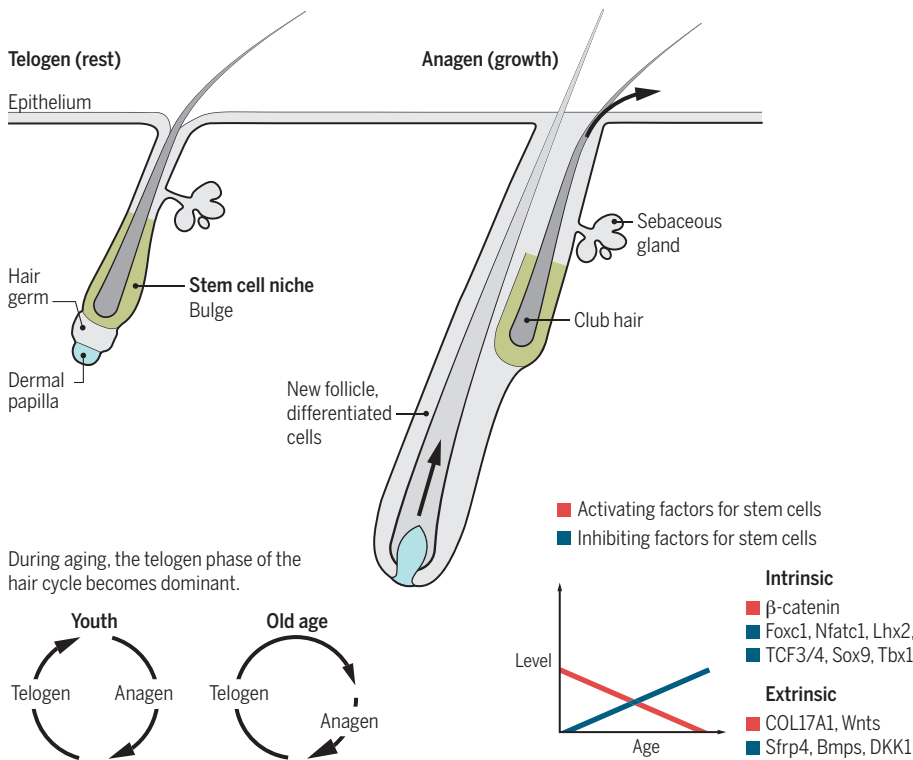
the hair growth cycle (10).

In androgenetic alopecia, hair fibers become shorter, thinner, and fewer as thick terminal scalp hairs are gradually replaced by fine vellus hairs. Yet in the early stages of this condition, HFSCs appear generally normal; a failure in their activation to form hair germ cells was the problem (11). Hair germ arises from activated HFSCs and migrate out of the bulge during early catagen to support the generation of a new hair. This suggests that the environment affects HFSCs. Such effects are not limited to the intrafollicle niche (the bulge); they also include the extrafollicular dermal environment and body hormone



Hair follicle. The Foxc1 transcription factor (magenta) is present in stem cells (green) and their niche (white) during self renewal.

¹Department of Pathology, Keck School of Medicine, University of Southern California, Los Angeles, CA, USA. ²"111" Project Laboratory of Biomechanics and Tissue Repair, College of Bioengineering, Chongqing University, Chongqing, China. ³Integrative Stem Cell Center, China Medical University, Taichung, Taiwan. E-mail: cmchung@usc.edu



Hair growth and aging. Renewal capacity of the hair cycle decreases with aging. Intrinsic and extrinsic factors affect hair follicle stem cells. During aging, there is a shift from an activator-dominant to an inhibitor-dominant environment.

status (12). In aged mice, secreted factors in the intradermal adipose tissue that inhibit Wnt signaling [e.g., dickkopf wnt signaling pathway inhibitor 1 (DKK1) and secreted frizzled-related protein 4 (Sfrp4)] are present in a wider dermal region and persist for long amounts of time, thus blocking activation of hair growth and decreasing hair regeneration ability. The aging phenotype of the skin of an old mouse was partially rescued when transplanted into the dermal environment of a young mouse (13). Thus, the control of hair cycling during aging is likely affected by both intrinsic stem cell properties and extrinsic environmental factors. We need to learn more about how these different regulatory compartments interact to control HFSC activation.

The downstream effectors of dynamic histone modifications during hair cycling are considered to be good candidates for driving epigenetic change. Among these effectors is the transcription factor forkhead box C1 (Foxc1) (8). Wang *et al.* show in mice that Foxc1 is expressed dynamically in HFSCs during hair cycling (see the first figure). It is absent during telogen (when stem cells are quiescent) but is expressed throughout the entire bulge when the next new hair cycle is initiated. Reducing Foxc1 expression in the basal hair follicle layer, where stem cells are located, resulted in a shortened telogen phase and loss of the old hair. Its absence in

the suprabasal bulge caused a loss of club hairs (as new hair is formed, the hair fiber from the previous cycle—the club hair—is pushed upward in the follicle and eventually out). These results indicate that Foxc1 promotes HFSC quiescence and also maintains the niche structure. Wang *et al.* also show that genes that maintain HFSC quiescence are down-regulated in the HFSCs of mice lacking Foxc1. Chromatin immunoprecipitation (ChIP) sequencing and assay for transposase-accessible chromatin (ATAC) sequencing data revealed that several genes controlling HFSC quiescence contain Foxc1 binding sites in their promoter or enhancer regions. Remarkably, these include genes encoding Bmp and Nfatc1, factors that suppress HFSC activation. The findings push our understanding of hair cycle control from the morphogen level to an epigenetic level.

Extracellular matrix is a major component of the follicle stem cell niche. Among the matrix constituents, type XVII collagen is required to maintain both HFSCs and melanocyte stem cells (14). But how is the homeostasis of type XVII collagen regulated? Matsumura *et al.* show that during repetitive hair cycling, HFSCs accumulate DNA damage, which leads to proteolysis of type XVII collagen. They found that aging dorsal skin proceeds in a stepwise manner (in the mouse). Gene ontology analyses showed

that genes involved in the DNA damage response are enriched in aged HFSCs, implying the accumulation of DNA damage during aging. Aged HFSCs produce ELA2/neutrophil elastase (ELANE) and other proteases that degrade COL17A1, the alpha chain constituent of type XVII collagen. Without COL17A1, HFSCs lose their self-renewal property and differentiate into an epidermal lineage. Thus, Matsumura *et al.* reveal an explicit mechanism for how aging-related DNA damage in HFSCs loops back to alter the stem cell microenvironment. Maintaining COL17A1 in the skin protected HFSCs against aging and reduced hair loss in mice. The study links DNA damage with changes of key extracellular matrix components in the stem cell niche, resulting in altered stem cell fate, depletion of stem cell numbers, reduction of organ size (miniature hairs), and reduced hair numbers. This finding also raises the possibility of rejuvenating HFSCs, because the microenvironment is seemingly easier to modulate than the HFSCs themselves.

Tissue regenerative ability after wound-healing also declines during aging. In large wound-induced follicle neogenesis, new follicles form in addition to the regeneration of hair from the original follicles. However, this ability declines gradually with aging (15). Hair regeneration in aging persons is hormone-dependent and region-specific. Androgens suppress hair growth in the scalp but enhance hair growth in beards and eyebrows (5). The findings of Wang *et al.* and Matsumura *et al.* should facilitate a multidimensional understanding of stem cell regulation and management during aging. It may also provide some hope for restoring hair growth in people with alopecia. ■

REFERENCES AND NOTES

1. L. Wang *et al.*, *Science* **351**, 613 (2016).
2. H. Matsumura *et al.*, *Science* **351**, aad4395 (2016).
3. Y. C. Hsu, E. Fuchs, *Nat. Rev. Mol. Cell Biol.* **13**, 103 (2012).
4. E. Kandyba *et al.*, *Proc. Natl. Acad. Sci. U.S.A.* **110**, 1351 (2013).
5. C. M. Chuong *et al.*, *Physiology* **27**, 61 (2012).
6. V. Greco *et al.*, *Cell Stem Cell* **4**, 155 (2009).
7. V. A. Botchkarev, M. R. Gdula, A. N. Mardaryev, A. A. Sharov, M. Y. Fessing, *J. Invest. Dermatol.* **132**, 2505 (2012).
8. W. H. Lien *et al.*, *Cell Stem Cell* **9**, 219 (2011).
9. J. Li *et al.*, *J. Invest. Dermatol.* **132**, 2681 (2012).
10. B. E. Keyes *et al.*, *Proc. Natl. Acad. Sci. U.S.A.* **110**, E4950 (2013).
11. L. A. Garza *et al.*, *J. Clin. Invest.* **121**, 613 (2011).
12. M. V. Plikus *et al.*, *Nature* **451**, 340 (2008).
13. C. C. Chen *et al.*, *J. Invest. Dermatol.* **134**, 2086 (2014).
14. S. Tanimura *et al.*, *Cell Stem Cell* **8**, 177 (2011).
15. M. Ito *et al.*, *Nature* **447**, 316 (2007).

ACKNOWLEDGMENTS

C.-M.C. is supported by NIH grants AR42177 and AR60306. M.L. is supported by Fundamental Research Funds for the Central Universities (106112015CDJRC231206), Special Funding for Postdoctoral Research Projects in Chongqing (Xm2015093), and a fellowship from the China Scholarship Council (2011605042). We thank R. Widelitz, L. Yang, and T. Yang for discussion.

10.1126/science.aaf1635

Nanoparticles meet their sticky ends

Hierarchical DNA structures direct the crystallization of gold nanoparticles

By **Andrea R. Tao**

The first studies showing that DNA could be grafted onto the surfaces of metal nanoparticles (NPs) (1, 2) provided a glimpse into the potential of using genetic material to program NP assembly. With major advances in DNA nanotechnology (3, 4) in the subsequent years, researchers have just begun to harness the molecular and nanoscale precision that DNA offers in the construction of ordered three-dimensional (3D) NP superlattices. In this issue, two studies show how hierarchically structured DNA imparts valency and symmetry to spherical gold NPs that are otherwise chemically and geometrically isotropic. On page 582, Liu *et al.* (5) demonstrate the rational assembly of NPs into diamond and diamond-family superlattices using DNA origami linkers. On page 579, Kim *et al.* (6) demonstrate how DNA hairpins serve as addressable NP linkers that can be activated or deactivated with chemical precision.

The use of DNA in NP coatings enables clear distinctions to be made between aggregation versus directed assembly in the formation of NP clusters. Early on, researchers found that spherical solid-state NPs could spontaneously form 3D superlattices resembling the close-packed crystal structures adopted by hard spheres (7). In these close-packed forms, NP crystallization is driven by nonspecific Lennard-Jones-type interparticle interactions. Modifying the NP surface with DNA introduces chemical specificity so that interparticle interactions can be precisely and discretely tuned by programming the number of base-pair interactions involved in NP binding. DNA serves as a chemical handle for manipulating NP arrangements beyond the close-packed structures observed in aggregating systems. The studies by Liu *et al.* and Kim *et al.* take this control one step further by engineering the macromolecular structure of DNA.

Liu *et al.* devise a strategy to crystallize gold NPs into non-close-packed superlattices typically adopted by covalent solids such as diamond and silicon (see the figure, panel A). In their method, rigid polyhedral DNA origami cages serve both to encapsulate gold NPs and as supramolecular cages that bind NPs

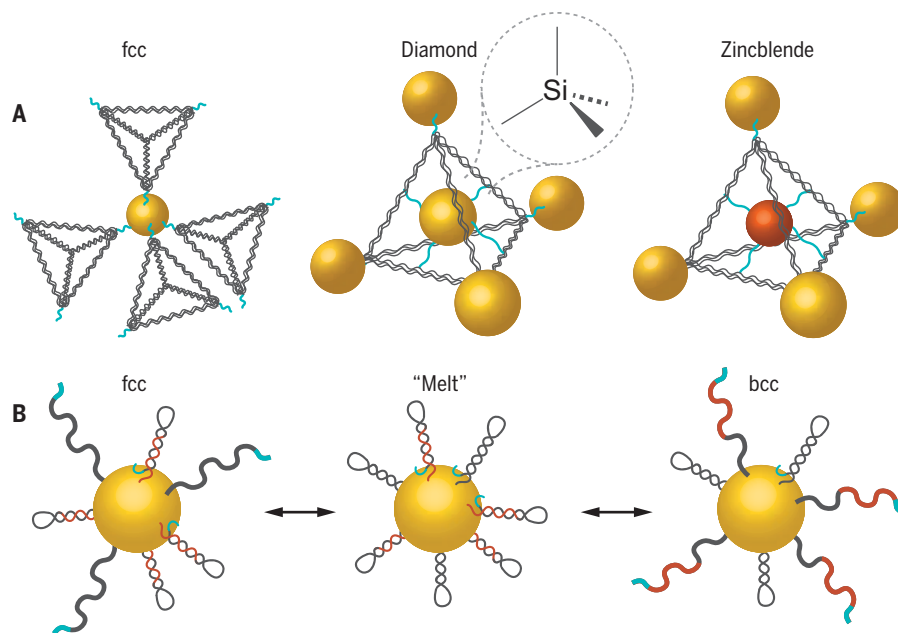
together via hierarchical 3D DNA structures. Using methods pioneered by Rothemund (8), Liu *et al.* take single-stranded DNA and fold it into an open-faced tetrahedron that is held together by short oligonucleotide segments or “staples.” Each edge of the tetrahedron—the architectural struts of the cage—is composed of a rigid 10-helix DNA bundle 36 nm in length. The outer surface of the DNA origami cage is functionalized with a DNA sequence that is available for hybridization, also known as a “sticky” strand, and that is programmed to bind to gold NPs functionalized with complementary oligonucleotide strands.

In their simplest implementation, the sticky strands direct crystallization of gold NPs into face-centered cubic (fcc) superlattices in which the NPs are loosely spaced. Small-angle x-ray spectroscopy (SAXS) and electron microscopy verified that the DNA cage served as tetravalent linkers between NPs. Each NP supports coordination to four DNA cages, which is determined by the binding footprint of the DNA cage projected onto the spherical NP surface. For a NP with a diameter of 14.5 nm, each tetrahedron vertex covers ~12.2% of the NP surface, and tetrahe-

dral NP-to-cage coordination offers the most efficient space packing.

To form a diamond superlattice, the inner surface of the DNA cage is also functionalized with sticky DNA strands, enabling the encapsulation of one or more guest NPs within the origami linker. When these guest NPs are identical to those located at the tetrahedron vertices, SAXS data indicate that a diamond superlattice formed. When the guest particles NPs are smaller or composed of NP dimers, zincblende-type superlattices formed.

Hierarchical DNA ligands not only enable exquisite control over the spatial organization of solid-state NPs in superlattices, but can also be used to actively toggle between different superlattice structures. Kim *et al.* show how gold NPs can be encoded with the ability to disperse or recrystallize in response to chemical cues by functionalizing them with DNA hairpin ligands—loopy DNA strands that form when the opposite ends of a single-stranded DNA chain possess complementary sequences and that can open and close upon hybridization. The tail of the DNA hairpin is programmed with a sticky end to facilitate interparticle binding (see the figure,



Nanoparticle-DNA building blocks for artificial materials. Modifying NPs with sticky DNA strands that are ready to hybridize enables nanoscale crystallization. (A) Building blocks composed of 3D DNA tetrahedra and gold NPs lead to diamondlike superlattice structures. (B) Gold NPs functionalized with hairpin DNA ligands are programmed to exhibit a martensitic transition between face-centered and body-centered cubic superlattices.

Department of NanoEngineering, University of California San Diego, La Jolla, CA 92093-0448, USA. E-mail: atao@ucsd.edu

panel B). When the hairpin is closed, the sticky end is protected and NP assembly is effectively deactivated. The hairpin is opened by adding a complementary oligonucleotide called an effector, which unfolds the hairpin by forming a double-stranded DNA segment that straightens out the loop, activating NP assembly.

Kim *et al.* enabled superlattice toggling by grafting the surface of 10- to 20-nm-diameter gold NPs with two different types of hairpin ligands that operate in an orthogonal manner: one with a self-complementary sticky end and one with a non-self-complementary sticky end. Previous demonstrations from the same research group showed that NPs bound with self-complementary DNA favor crystallization into an fcc superlattice, whereas NPs bound with non-self-complementary sticky ends favor crystallization into a body-centered cubic (bcc) superlattice. No evidence of crystallization when both types of hairpin ligands are closed was seen with SAXS. When the self-complementary strands are activated, the NPs assemble into an fcc superlattice; when the non-self-complementary hairpins are activated, the NPs assemble into a bcc superlattice.

The superlattice structure can be toggled back and forth between fcc and bcc in a matter of minutes by adding the appropriate activating and deactivating effectors simultaneously, and this scheme can be extended to more complex structures. For example, NP assemblies can be toggled between bcc and AlB₂-type superlattices by modulating NP type, ligand density, and ligand length.

The work of Liu *et al.* and Kim *et al.* represents a major advance in engineering NPs as atom-like building blocks. However, the immediate extension of these DNA constructs to solid-state nanomaterials beyond gold NPs is hindered foremost by the lack of established surface chemistries between DNA and other inorganic materials. There may also be size and scale limitations to DNA-guided assembly because NPs may experience strong van der Waals forces that dominate over any chemical anisotropy imparted by DNA ligands, linkers, and scaffolds. Nonetheless, DNA nanotechnology remains an attractive and potentially disruptive strategy for the construction of new and undiscovered materials. ■

REFERENCES

1. C. A. Mirkin *et al.*, *Nature* **382**, 607 (1996).
2. A. P. Alivisatos *et al.*, *Nature* **382**, 609 (1996).
3. A. V. Pinheiro *et al.*, *Nat. Nanotechnol.* **6**, 763 (2011).
4. C.-H. Lu, B. Willner, I. Willner, *ACS Nano* **7**, 8320 (2013).
5. W. Liu *et al.*, *Science* **351**, 582 (2016).
6. Y. Kim *et al.*, *Science* **351**, 579 (2016).
7. B. L. V. Prasad, C. M. Sorensen, K. J. Klabundec, *Chem. Soc. Rev.* **37**, 1871 (2008).
8. P. W. K. Rothmund, *Nature* **440**, 297 (2006).

10.1126/science.aae0455



CRYOSPHERE

Ice sheet in peril

Radar data reveal how sensitive the Greenland Ice Sheet is to long-term climatic changes

By **Christine S. Hvidberg**

Earth's large ice sheets in Greenland and Antarctica are major contributors to sea level change. At present, the Greenland Ice Sheet (see the photo) is losing mass in response to climate warming in Greenland (1), but the present changes also include a long-term response to past climate transitions. On page 590 of this issue, MacGregor *et al.* (2) estimate the mean rates of snow accumulation and ice flow of the Greenland Ice Sheet over the past 9000 years based on an ice sheet-wide dated radar stratigraphy (3). They show that the present changes of the Greenland Ice Sheet are partly an ongoing response to the last deglaciation. The results help to clarify how sensitive the ice sheet is to climate changes.

One of the great challenges in estimating the future evolution and mass loss of the Greenland Ice Sheet is to determine the present flow properties of the ice sheet. The ice sheet is monitored by numerous instruments to provide knowledge of ice thickness, surface velocity, and current mass balance changes. However, key properties such as ice viscosity remain poorly constrained, as do sliding and melting rates at the base of

the ice sheet. These properties change over time because warmer surface temperatures are slowly heating up the deeper layers of the ice sheet and because ice from the current interglacial period (the Holocene, which began 11,700 years ago) gradually replaces older and softer ice from the last glacial period.

Direct observations of ice temperature and anisotropic flow properties (4, 5) are available at only a few deep ice core sites on the Greenland Ice Sheet. However, additional information is contained in the internal structure of the ice sheet, which can be detected with radar stratigraphy. The radar layers are isochrones: past surfaces buried by subsequent layers of snow and deformed as ice flows from the interior toward the margins (see the figure). The radar layer depths record the combined effects of external and internal forcings, providing valuable constraints on ice flow history and past accumulation rates.

In their study, MacGregor *et al.* use a comprehensive dated radar stratigraphy that they have recently constructed from radio echosounding data from the Greenland Ice Sheet collected between 1993 and 2013 (3). They dated the stratigraphy by matching radar layers with ice core records at intersections with ice core sites (3), thereby determining the depth-age structure of the ice sheet. In the current study, the authors focused on the

Centre for Ice and Climate, Niels Bohr Institute, University of Copenhagen, 2100 Copenhagen, Denmark. E-mail: ch@nbi.ku.dk



depth-age distribution of layers younger than 9000 years. Using a one-dimensional ice flow model, they determined the mean thinning rate and accumulation rate for the past 9000 years that provide the best fit between modeled and observed depth-age scales. This approach is similar to that used to determine accumulation rates from ice core records. The resulting mean accumulation rates during the past 9000 years are generally higher in most of Greenland than the modern model-based accumulation rates.

A previous reconstruction of Greenland accumulation rates over the past 400 years based on ice cores and climate models showed the accumulation rate to be sensi-

Ice, ice everywhere. Although it looks immutable, the Greenland Ice Sheet continuously flows toward the sea. Radio data help to understand how this flow changes in response to climatic changes. The photo shows the ice sheet close to the Ilulissat Icefjord.

tive to past temperature (6). Deep ice cores confirm this finding further back in time into the last glacial (7). Warm climate approximately 9000 to 5000 years ago (4) may have been accompanied by higher accumulation rates; this might explain why the mean accumulation rates for the past 9000 years are higher than present-day modeled accumulation rates. The reconstructed mean Holocene accumulation rate reported by MacGregor *et al.* extends existing observation-based maps of past accumulation rates further back in time and covers a large fraction of the Greenland Ice Sheet. The results are highly relevant for constraining models of past ice sheet evolution.

MacGregor *et al.* also derived a map of mean Holocene surface velocity. They first calculated the balance velocity field corresponding to the mean Holocene accumulation rate—that is, the depth-averaged horizontal ice velocities needed to balance the accumulation rates. They then used a simplified model of internal deformation to convert balance velocities to surface velocities. Comparison of the reconstructed mean surface velocities with modern surface velocities observed from space revealed an apparent modern deceleration of the Greenland Ice Sheet. This is an interesting and surprising finding.

The authors argue that the higher mean Holocene accumulation rates relative to

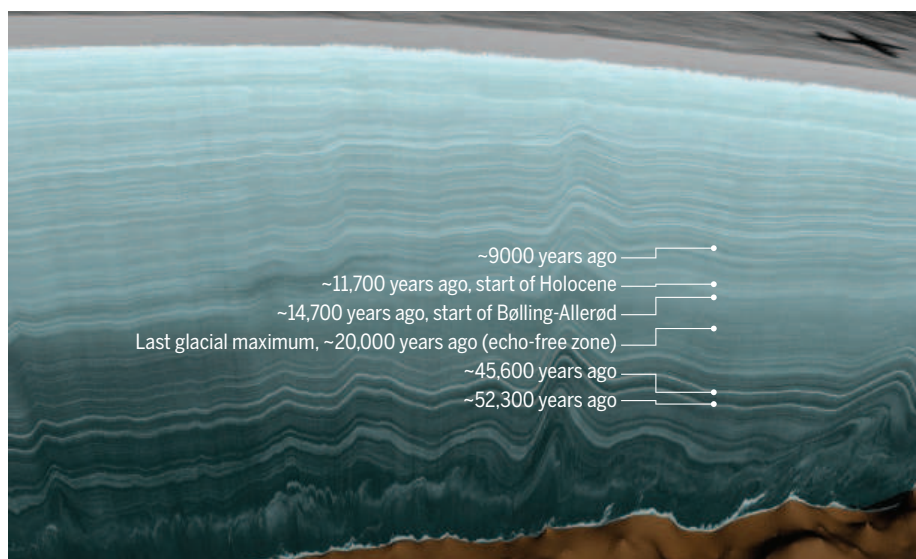
modern climate model results can only partly explain the deceleration. They propose that changes in ice dynamics have also contributed to the deceleration, mainly because of a general hardening of the ice sheet as glacial ice is being replaced by Holocene ice. Glacial ice contains more impurities than interglacial ice and is softer than ice deposited during the Holocene. The dynamic response to this gradual hardening may be effective for tens of thousands of years after the climate transition at the end of the last glacial period (8), and it affects estimates of future mass loss from the Greenland Ice Sheet.

However, the one-dimensional ice flow model used to derive the 9000-year mean accumulation rate is simplified and does not correct for variations of accumulation rate along the flow direction. MacGregor *et al.* argue that the local model is suitable because it contains many relatively young layers that reflect local conditions. Nonetheless, future work should account for upstream corrections to ensure that low accumulation rates in the ice sheet's interior do not propagate with the flow and affect the resulting accumulation rates at lower elevations (9). Thinning of the Greenland Ice Sheet during the Holocene (10) would have affected the ice flow and thinning of layers, but the effect was probably minor over the past 9000 years (7). Future work may benefit from more sophisticated methods to account for vertical thinning and nonsteady conditions.

The termination of the last ice age 11,700 years ago was a large and abrupt climate transition that still continues to affect the Greenland Ice Sheet. Future research should explore in more detail the possible effects of ice rheology changes on local and regional ice dynamics. A general hardening of the Greenland Ice Sheet could increase the long-term resilience of the ice sheet if global warming proceeds. The Greenland Ice Sheet reacts to climate changes on short and long time scales. Better constraining the long-term response is crucial for improved future projections of its contribution to sea level change. ■

REFERENCES

1. J. A. Church *et al.*, in *Climate Change 2013: The Physical Science Basis. Contribution of Working Group I to the Fifth Assessment Report of the Intergovernmental Panel on Climate Change*, T. F. Stocker *et al.*, Eds. (Cambridge Univ. Press, 2013), pp. 1137–1177.
2. J. A. MacGregor *et al.*, *Science* **351**, 590 (2016).
3. J. A. MacGregor *et al.*, *J. Geophys. Res.* **120**, 212 (2015).
4. D. Dahl-Jensen *et al.*, *Science* **282**, 268 (1998).
5. NEEM members, *Nature* **493**, 489 (2013).
6. J. E. Box *et al.*, *J. Clim.* **26**, 3919 (2013).
7. V. Gkinis, S. B. Simonsen, S. L. Buchardt, J. W. C. White, B. M. Vinther, *Earth Planet. Sci. Lett.* **405**, 132 (2014).
8. N. Reeh, *Nature* **317**, 797 (1985).
9. L. T. Nielsen, N. B. Karlsson, C. S. Hvidberg, *Ann. Glaciol.* **56**, 70 (2015).
10. B. M. Vinther *et al.*, *Nature* **461**, 385 (2009).



How an ice sheet flows. The radar data in this figure are from a flight made by Operation IceBridge across the Greenland Ice Sheet on 2 May 2011. The thicknesses and shapes of the layers provide insight into how past climatic changes have affected—and continue to affect—the ice sheet's flow. On the basis of such radar stratigraphy data, MacGregor *et al.* show that over the past 9000 years, ice sheet flow has been faster than it is today.

ILLUSTRATION: ADAPTED FROM NASA SCIENTIFIC VISUALIZATION STUDIO BY P. HUEY/SCIENCE

SCIENCE AND SOCIETY

Taking race out of human genetics

Engaging a century-long debate about the role of race in science

By Michael Yudell,^{1*} Dorothy Roberts,²
Rob DeSalle,³ Sarah Tishkoff²

In the wake of the sequencing of the human genome in the early 2000s, genome pioneers and social scientists alike called for an end to the use of race as a variable in genetic research (1, 2).

Unfortunately, by some measures, the use of race as a biological category has increased in the postgenomic age (3). Although inconsistent definition and use has been a chief problem with the race concept, it has historically been used as a taxonomic

POLICY categorization based on common hereditary traits (such as skin color) to elucidate the relationship between our ancestry and our genes. We believe the use of biological concepts of race in human genetic research—so disputed and so mired in confusion—is problematic at best and harmful at worst. It is time for biologists to find a better way.

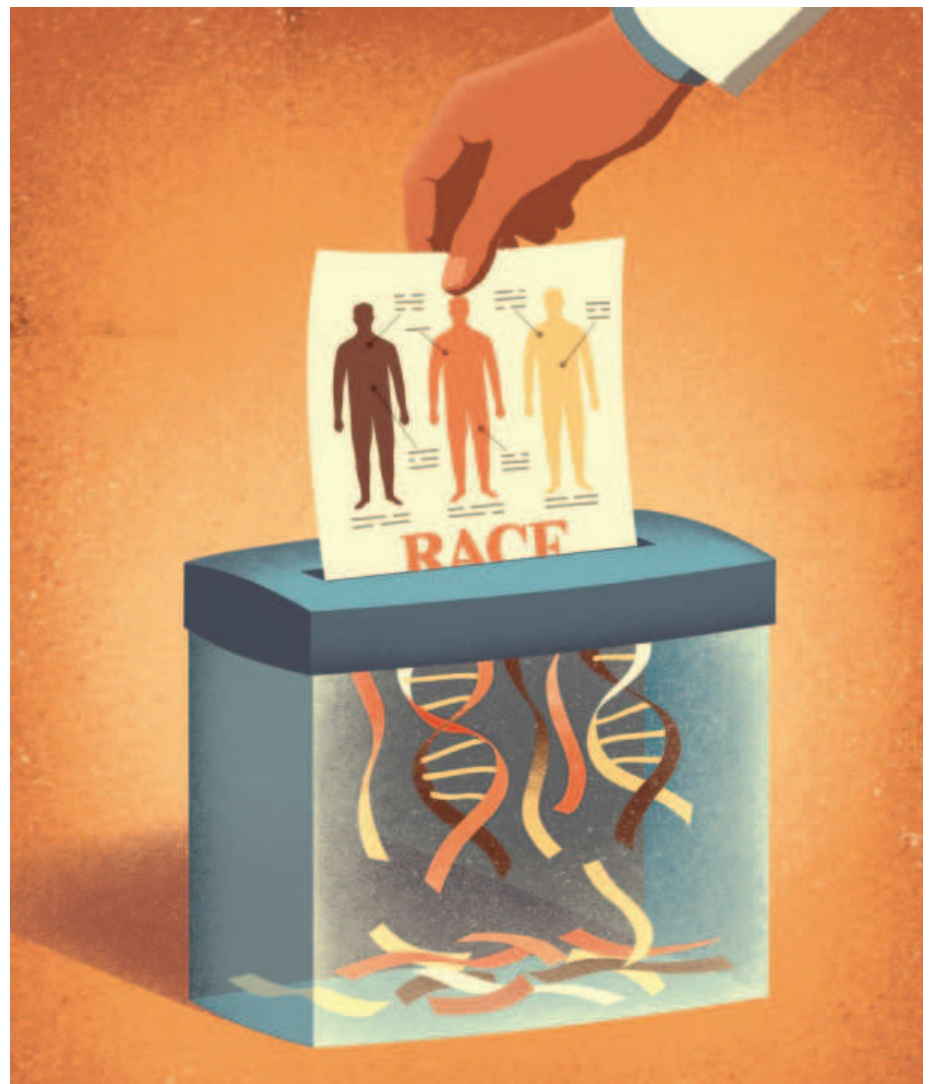
Racial research has a long and controversial history. At the turn of the 20th century, sociologist and civil rights leader W. E. B. Du Bois was the first to synthesize natural and social scientific research to conclude that the concept of race was not a scientific category. Contrary to the then-dominant view, Du Bois maintained that health disparities between blacks and whites stemmed from social, not biological, inequality (4). Evolutionary geneticist Theodosius Dobzhansky, whose work helped reimagine the race concept in the 1930s at the outset of the evolutionary synthesis, wrestled with many of the same problems modern biologists face when studying human populations—for example, how to define and sample populations and genes (5). For much of his career, Dobzhansky brushed aside criticism of the race concept, arguing that the problem with race was not its scientific use, but its nonscientific misuse. Over time, he grew disillusioned, concerned that scientific study of human diversity had “floundered in confusion and misunderstanding” (6). His transformation from defender to detractor of the race concept in biology still resonates.

Today, scientists continue to draw wildly different conclusions on the utility of the race

concept in biological research. Some have argued that relevant genetic information can be seen at the racial level (7) and that race is the best proxy we have for examining human genetic diversity (8, 9). Others have concluded that race is neither a relevant nor accurate way to understand or map human genetic diversity (10, 11). Still others have argued that race-based predictions in clinical settings, because of the heterogeneous nature of racial groups, are of questionable use (12), particularly as the prevalence of admixture increases across populations.

Several meetings and journal articles have called attention to a host of issues, which include (i) a proposed shift to “focus

on racism (i.e., social relations) rather than race (i.e., supposed innate biologic predisposition) in the interpretation of racial/ethnic ‘effects’” (13); (ii) a failure of scientists to distinguish between self-identified racial categories and assigned or assumed racial categories (14); and (iii) concern over “the haphazard use and reporting of racial/ethnic variables in genetic research” (15) and a need to justify use of racial categories relative to the research questions asked and methods used (6). Several academic journals have taken up this last concern and, with mixed success, have issued guidelines for use of race in research they publish (16). Despite these concerns, there have been no



¹Drexel University, Philadelphia, PA 19104, USA. ²University of Pennsylvania, Philadelphia, PA 19104, USA. ³American Museum of Natural History, New York, NY 10024, USA.
*Corresponding author. E-mail: myudell@drexel.edu

systematic attempts to address these issues and the situation has worsened with the rise of large-scale genetic surveys that use race as a tool to stratify these data (17).

It is important to distinguish ancestry from a taxonomic notion such as race. Ancestry is a process-based concept, a statement about an individual's relationship to other individuals in their genealogical history; thus, it is a very personal understanding of one's genomic heritage. Race, on the other hand, is a pattern-based concept that has led scientists and laypersons alike to draw conclusions about hierarchical organization of humans, which connect an individual to a larger pre-conceived geographically circumscribed or socially constructed group.

Unlike earlier disagreements concerning race and biology, today's discussions generally lack clear ideological and political antipodes of "racist" and "nonracist." Most contemporary discussions about race among scientists concern examination of population-level differences between groups, with

"...the use of biological concepts of race in human genetic research...is problematic at best and harmful at worst."

the goal of understanding human evolutionary history, characterizing the frequency of traits within and between populations, and using an individual's self-identified ancestry to identify genetic risk factors of disease and to help determine the best course of medical treatments (6).

If this is what race in contemporary scientific and medical practice is about, then why should we be concerned? One reason is that phylogenetic and population genetic methods do not support a priori classifications of race, as expected for an interbreeding species like *Homo sapiens* (11, 18). As a result, racial assumptions are not the biological guideposts some believe them to be, as commonly defined racial groups are genetically heterogeneous and lack clear-cut genetic boundaries (10, 11). For example, hemoglobinopathies can be misdiagnosed because of the identification of sickle-cell as a "Black" disease and thalassemia as a "Mediterranean" disease (10). Cystic fibrosis is underdiagnosed in populations of African ancestry, because it is thought of as a "White" disease (19). Popular misinterpretations of the use of race in genetics also continue to fuel racist beliefs, so much so that, in 2014, a group of leading human population geneticists publicly refuted

claims about the genetic basis of social differences between races (20). Finally, the use of the race concept in genetics, an issue that has vexed natural and social scientists for more than a century, will not be obviated by new technologies. Although the low cost of next-generation sequencing has facilitated efforts to sequence hundreds of thousands of individuals, adding whole-genome sequences does not negate the fact that racial classifications do not make sense in terms of genetics.

More than five decades after Dobzhansky called on biologists to develop better methods for investigating human genetic diversity (21), biology remains stuck in a paradox that reflects Dobzhansky's own struggle with the race concept: both believing race to be a tool to elucidate human genetic diversity and believing that race is a poorly defined marker of that diversity and an imprecise proxy for the relation between ancestry and genetics. In an attempt to resolve this paradox and to improve study of human genetic diversity, we propose the following.

Scientific journals and professional societies should encourage use of terms like "ancestry" or "population" to describe human groupings in genetic studies and should require authors to clearly define how they are using such variables. It is preferable to refer to geographic ancestry, culture, socioeconomic status, and language, among other variables, depending on the questions being addressed, to untangle the complicated relationship between humans, their evolutionary history, and their health. Some have shown that substituting such terms for race changes nothing if the underlying racial thinking stays the same (22, 23). But language matters, and the scientific language of race has a considerable influence on how the public (which includes scientists) understands human diversity (24). We are not the first to call for change on this subject. But, to date, calls to rationalize the use of concepts in the study of human genetic diversity, particularly race, have been implemented only in a piecemeal and inconsistent fashion, which perpetuates ambiguity of the concept and makes sustained change unfeasible (16). Having journals rationalize the use of classificatory terminology in studying human genetic diversity would force scientists to clarify their use and would allow researchers to understand and interpret data across studies. It would help avoid confusing, inconsistent, and contradictory usage of such terms.

Phasing out racial terminology in biological sciences would send an important message to scientists and the public alike: Historical racial categories that are treated as natural and infused with notions of superiority and inferiority have no place in biology. We acknowledge that using race as a political or social category to study racism and

its biological effects, although fraught with challenges, remains necessary. Such research is important to understand how structural inequities and discrimination produce health disparities in socioculturally defined groups.

The U.S. National Academies of Sciences, Engineering, and Medicine should convene a panel of experts from biological sciences, social sciences, and humanities to recommend ways for research into human biological diversity to move past the use of race as a tool for classification in both laboratory and clinical research. Such an effort would bring stakeholders together for a simple goal: to improve the scientific study of human difference and commonality. The committee would be charged with examining current and historical usage of the race concept and ways current and future technology may improve the study of human genetic diversity; thus, they could take up Dobzhansky's challenge that "the problem that now faces the science of man [sic] is how to devise better methods for further observations that will give more meaningful results" (21). Regardless of where one stands on this issue, this is an opportunity to strengthen research by thinking more carefully about human genetic diversity. ■

REFERENCES AND NOTES

1. F. Collins, *Nat. Genet.* **36** (suppl.), S13 (2004).
2. M. W. Foster, R. R. Sharp, *Nat. Rev. Genet.* **5**, 790 (2004).
3. P. A. Chow-White, S. E. Green Jr., *Int. J. Commun.* **7**, 556 (2013).
4. W. E. B. Du Bois, *The Health and Physique of the Negro American* (Publ. no. 11, Atlanta Univ. Publications, Atlanta, GA, 1906).
5. T. Dobzhansky, *Genetics and the Origin of Species* (Columbia Univ. Press, New York, 1937).
6. M. Yudell, *Race Unmasked: Biology and Race in the 20th Century* (Columbia Univ. Press, New York, 2014).
7. E. G. Burchard et al., *N. Engl. J. Med.* **348**, 1170 (2003).
8. Y. Banda et al., *Genetics* **200**, 1285 (2015).
9. C. E. Powe et al., *N. Engl. J. Med.* **369**, 1991 (2013).
10. D. Roberts, *Fatal Invention: How Science, Politics, and Big Business Re-Created Race in the Twenty-First Century* (The New Press, New York, 2012).
11. D. Serre, S. Pääbo, *Genome Res.* **14**, 1679 (2004).
12. P. C. Ng, Q. Zhao, S. Levy, R. L. Strausberg, J. C. Venter, *Clin. Pharmacol. Ther.* **84**, 306 (2008).
13. J. S. Kaufman, R. S. Cooper, *Am. J. Epidemiol.* **154**, 291 (2001).
14. T. R. Rebbeck, P. Sankar, *Cancer Epidemiol. Prev.* **14**, 2467 (2005).
15. L. M. Hunt, M. S. Megyesi, *J. Med. Ethics* **34**, 495 (2008).
16. A. Smart, R. Tutton, P. Martin, G. T. H. Ellison, R. Ashcroft, *Soc. Stud. Sci.* **38**, 407 (2008).
17. G. Lettre et al., *PLoS Genet.* **7**, e1001300 (2011).
18. K. Bremer, H. E. Wanntorp, *Syst. Biol.* **28**, 624 (1979).
19. C. Stewart, M. S. Pepper, *Genet. Med.* (2015).
20. G. Coop et al., *New York Times*, 8 August 2014, p. B6.
21. T. Dobzhansky, *Mankind Evolving: The Evolution of the Human Species* (Yale Univ. Press, New Haven, CT, 1962).
22. S. M. Fullerton, J. H. Yu, J. Crouch, K. Fryer-Edwards, W. Burke, *Hum. Genet.* **127**, 563 (2010).
23. L. Braun, E. Hammonds, *Soc. Sci. Med.* **67**, 1580 (2008).
24. W. C. Byrd, M. W. Hughey, *Ann. Am. Acad. Pol. Soc. Sci.* **661**, 1 (2015).

ACKNOWLEDGMENTS

All authors contributed equally to the conceptualization of this paper. M.Y. wrote the first draft and revised it based on comments from coauthors. Special thanks to E. Arana for research assistance.

10.1126/science.aac4951

RETROSPECTIVE

Alfred Gilman (1941-2015)

A Nobel laureate's work on G proteins illuminated how signals are transmitted into cells

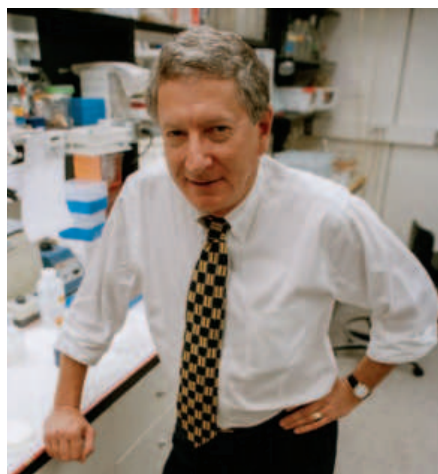
By Melvin Simon

Alfred Goodman Gilman died on 23 December, after a protracted battle with pancreatic cancer. We lost an extraordinary scientist, academic leader, and “*mensh*.” Al pioneered our understanding of the biochemical mechanisms that drive signal transduction and (with Martin Rodbell) shared the 1994 Nobel Prize in Physiology or Medicine for his role in the discovery of heterotrimeric guanine nucleotide-binding proteins (G proteins). He went on to describe the basic design of G protein-mediated cellular signaling circuits that regulate an enormous number of physiological responses and are the targets of a large fraction of today's drugs.

Al was born into the scientific community. His father was an accomplished research pharmacologist, department chairman, and coauthor of a major pharmacology textbook. Al followed in his father's footsteps. After receiving his BS in biochemistry from Yale University, Al pursued an MD-Ph.D. at Case Western Reserve University in Cleveland, Ohio, where he worked under Ted Rall and became intrigued with the mechanism of cellular signaling and the role of the enzyme adenylyl cyclase and its product cyclic adenosine 3',5'-monophosphate (AMP). As a postdoctoral fellow at the U.S. National Institutes of Health, he developed a sensitive assay for cyclic AMP and moved on to a faculty position at the University of Virginia Medical School in Charlottesville, where he returned to the issue of cellular signaling. The problem was that hormones were known to bind to specific receptors on the outside of the cell and to activate the enzyme adenylyl cyclase inside the cell. But how did the information regarding the receptor-binding event get communicated to the enzyme? Martin Rodbell showed that the connection between the two required the nucleotide guanosine 5'-triphosphate (GTP) and possibly a third protein component. However, the most straightforward resolution of the issue was to separate each of the possible components and to reconstitute the system. At the time, this was a herculean task, but it was accom-

plished by Al and his postdoctoral fellow Elliot Ross. Other members of the lab, including Paul Sternweis and John Northrup, finished the job by purifying the G protein and studying its nucleotide-binding and GTPase activity.

In 1981, Al moved to Texas to chair the pharmacology department at the University of Texas (UT) Southwestern Medical Center in Dallas and to understand the mechanism of information processing by G-protein circuits. The hypothesis was that the circuit was driven by a series of consecutive conformational changes in protein structure alternatively stabilized by GDP or GTP. Taking the most straightforward approach, Al's group was amazingly successful in producing the proteins and complexes required for x-ray



diffraction analysis and in collaborating with outstanding crystallographers. Highly informative pictures of the structural changes in signaling intermediates at the atomic level emerged. Even the cantankerous adenylyl cyclase yielded some of its intimate secrets. During evolution, nature used elements and variations of the G-protein paradigm to solve a multitude of information processing problems by circuit design. Thus, there are hundreds of genes specifying G protein-coupled membrane receptors, dozens of homologous genes that code for the components of G proteins, and G-protein regulators that increase or decrease the amplitude of the signal, as well as many gene families representing targeted effectors. G-protein signaling circuits are integral to almost every physiological

function. In his Nobel lecture Al wrote, “The complexity of the cellular switchboard thus appears sufficiently vast to permit each cell (type) to design a highly customized signaling repertoire by expression of a relatively modest number of modular components.” He went on to predict that, “With this information in hand, we will be able to complete our understanding of the wiring diagram of the signaling switchboard in each type of cell.” In 1997, Al initiated the conversation about a project to deduce the nature of the wiring diagram. He called on me, Henry Bourne, and others working in various signaling systems. We spoke about a consortium of laboratories with an advisory group that would coordinate the research project and the development of analytical tools and reagents. The Alliance for Cellular Signaling was born in 2000. There were enormous problems, and Al was a remarkable leader and administrator. We were making headway, but all of the necessary technology wasn't yet available. We were just too early. Today, the process is beginning again in a more dispersed fashion with better tools under the rubric of systems biology.

Al Gilman did it all. As chairman, he built an outstanding department of pharmacology in Dallas. His research opened the cellular signaling field. His work on the mechanism of signal transduction continues to provide a basis for new drug design and development. He was Dean of the medical school at UT Southwestern Medical Center in Dallas and a member of the Board of Directors of the Eli Lilly pharmaceutical company. His students populate some of the best pharmacology and biochemistry departments in the country, and he was a founder, together with his former student Leonard Schleifer, of Regeneron, which is on its way to becoming a major pharmaceutical company. Al even published his own retrospective (*Annual Review of Pharmacology and Toxicology*, 2012). It is a wonderful review written in his engaging style.

I didn't get to know Al's family well. However, I admired how his wife Kathy cared for him in the last months of his life. She and Al set up, in their home, what Al called the “off-shore faculty club annex.” Once or twice a week at a designated hour, friends and former students would drop by, make themselves a drink, and visit with Al. He loved engaging in conversation about science, sports, or the ways of the world with a congenial, mildly lubricated group of colleagues. In addition to his scientific prowess, intellectual acuity, administrative ability, and fierce integrity, Al was a charming and delightful friend. We will sorely miss him. ■

Division of Biology and Biological Engineering, California Institute of Technology, Pasadena, CA 91125, USA.
E-mail: simonm@caltech.edu

10.1126/science.aaf2848



"Monodiets of megacrops" are replacing the rich diversity of foods we once consumed.

AGRICULTURE

Losing our taste for diversity

An emphasis on consistency and durability over variety and flavor has left many of our favorite foods in peril

By **Christopher Kemp**

In the 1960s, Homero Castro, an Ecuadorian agronomist, was desperately striving to produce a new variety of cacao—the plant that serves as the source of the world's chocolate. There was a lot at stake. Fungi were devastating Ecuador's local "Nacional" varieties of cacao. By the 1920s, more than 70% of the country's crops had been lost. Then, in 1965, on his 51st attempt, Castro hit the jackpot.

As Simran Sethi writes in *Bread Wine Chocolate*, Castro's variant, known as CCN-51, is robust. It gives high yields and is resistant to fungal attack. In many locations, it has replaced Nacional completely. The only problem is that it doesn't taste particularly good. But, as Sethi explains, depending on whom you ask, the actual taste of CCN-51 is not necessarily relevant.

Sethi, a journalist and former NBC News correspondent, uses *Bread Wine Chocolate*

to explore the loss of biodiversity worldwide and its long-reaching—and often unnoticed—effects on the foods we eat. "I counted 21 kinds of potato chips," she writes, after a trip to the grocery store, "but in the produce aisle, I found only five types of potatoes."

Almost every historic fruit and vegetable once grown in the United States is gone. "According to the Food and Agriculture Organization of the United Nations (FAO), 95 percent of the world's calories now come from 30 species," Sethi writes. "Of 30,000 edible plant species, we cultivate about 150." The reason: The modern food system is not driven by taste but instead by factors like consistency, predictability, low cost, and high yield. The same features that enabled the worldwide distribution of once-exotic foods like coffee and chocolate have now so drastically altered how those products are made that we risk losing them altogether.

Brimming with information and amply footnoted, *Bread Wine Chocolate* is a revelation throughout. Who knew, for example, that chocolate is a fermented food? Or that the fruit of a coffee plant looks like a cherry?

Bread Wine Chocolate

The Slow Loss of Foods We Love

Simran Sethi

HarperOne, 2015. 352 pp.



The book is divided into six sections devoted to different foods: the bread, wine, and chocolate of the title as well as beer, coffee, and octopus. In each, Sethi travels to the points of origin, meets producers, and takes a discerning look at how that food has changed. In Ecuador, she meets cacao farmers and scoops the sweet innards from cacao pods harvested from the plant. She meets coffee roasters in New Zealand; brewers in England who are trying to resurrect long-dead beers; and the Ethiopian farmers who grow coffee cherry in wild, tangled forests. Each section includes tasting guides—such as a wine aroma wheel—that help readers explore the food under discussion, as well as instructions on tasting its different varieties.

The Cavendish banana—the most widely grown of the 1000 varieties in existence—will soon be gone, rendered extinct by a fungus that is spreading slowly, inexorably, across the tropics. The subtle, fragrant qualities of Nacional cacao will be gone too, replaced by CCN-51. Wild Ethiopian coffee, which is alive with unexpected and complex flavor profiles not found in coffees grown elsewhere, will be gone also, because during slumps in the coffee market, Ethiopian coffee farmers actually end up paying to grow their crop. One day, they will give up and grow khat, a leafy stimulant they can sell to their neighbors for a higher price.

But all is not lost. The Svalbard Global Seed Vault on the Norwegian island of Spitsbergen near the North Pole stores the seeds of 865,000 plant varieties. The U.S. Department of Agriculture's National Clonal Germplasm Repository in Davis, California, houses around 6000 different grape vines, including more wild Greek grape species than are found in Greece. The National Collection of Yeast Cultures in Norwich, England, holds more than 4000 strains of yeast. These biodiversity banks and others represent one potential way to ensure that unique food crops are preserved for future generations.

Another way we can promote biodiversity is by selecting fair-trade coffee and artisanal chocolate and paying more for it, writes Sethi. After reading her excellent book, that is the least I'm willing to do.

10.1126/science.aad9077

The reviewer is at the Department of Translational Science and Molecular Medicine, Michigan State University, Grand Rapids, MI 49503, USA. E-mail: cjtemp@gmail.com

SCIENCE LIVES

Public enemy

Physicist Fang Lizhi recounts his clashes with the Chinese regime and his role in the Tiananmen Square protests

By Irving A. Lerch

Four years after his death, one of the most important figures of the Chinese scientific establishment has given us a first-person account of growing to manhood and eminence in revolutionary China. *The Most Wanted Man in China* is both a memoir and a personal testament of Fang Lizhi—a renowned scientist, humane scholar, political activist, intractable enemy of authoritarian government, and courageous advocate of human rights. And, unusual for this grim subject, it is a tale told with humor as well as deep introspection.

Beijing, where Fang was born, was relatively calm during the Japanese occupation and the Chinese Civil War. Then the Japanese presence was replaced by the Kuomintang (KMT). Fang's transformation to political awareness coincided with the rise of Mao Zedong, the Communist revolutionary who founded the People's Republic of China (PRC) in 1949. "The tide turned toward the Communists on the ideological battlefield even before it did on the physical battlefields," Fang writes. "... [S]ympathies came much less from the discovery of new truth than from a wish to jettison a moribund regime."

By 1948, defying KMT authorities, Fang had joined the Communist Federation of Democratic Youth and remained active during his student days in Peking University. On graduation, Fang was appointed to do research in nuclear physics—an elite specialty. Yet within a few years, he would be expelled from his Eden in the wake of Mao's "Anti-Rightist" crusade, having been identified as a potential reactionary troublemaker.

In 1957, Fang was exiled to labor in the rural fields of China. He would return and be banished again multiple times over the next two decades, perhaps targeted for helping to draft a critical letter to Party Central—criticism invited by the Party but designed to identify potential dissidents. The enlistment

of Chinese intellectuals in their own suppression was so successful that none could emerge as a heroic figure capable of capturing public sentiment or leadership.

Fang appreciated the resilience of his fellow laborers. During his exile to the Xishan coal mines, he recalled one miner's response to demands for greater productivity: "Sixty cents of pay buys sixty cents of work."

Fang soon learned that party proscriptions extended to the kinds of scientific inquiry that could be pursued. The precedent set by



Beijing residents survey the damage from the Tiananmen Square demonstrations.

the Soviet Union was to discourage the study of modern science in adherence with Marxist principles, an approach that foundered on the shoals of reality after World War II. With the enlistment of scientists in the nuclear program, Stalin was forced to promote talented physicists like Andrei Sakharov, who became "heroes of the revolution." Mao knew that all he needed were faceless technicians to build his bomb.

Forced to abandon his early research (*I*), Fang turned to astrophysics and soon began publishing on cosmology. The authorities took notice and hastened to slam the door. Their criticism was redolent with unintended humor: "The model of an expanding universe 'seeks to establish that the capitalist system not only cannot be overcome but will continue indefinitely to expand.'"

By 1979, Fang was considered "rehabilitated," and in 1984 he became vice president of the University of Science and Technology of China (USTC). He did not have to wait long to be engulfed in another altercation.

At an astronomy meeting in the Vatican, the International Center for Relativistic As-

The Most Wanted Man in China
My Journey from Scientist to
Enemy of the State

Fang Lizhi; translation and
afterword by Perry Link

Henry Holt, 2016. 352 pp.



trophysics (ICRA) was organized, and Fang lost no time in enlisting his institution. It was an important coup for Chinese science. Not only would USTC be a founding member of a prestigious international program, it would benefit further from the gift of a telescope. However, a poisonous cloud of suspicion rose from Beijing, where authorities were mistrusting and intolerant of international initiatives that originated outside of the city. This suspicion eventually enveloped USTC's membership in the ICRA and would engulf Fang.

In December 1985, USTC students took to the streets, demanding democratic elections to the district council. The authorities yielded, igniting new fervor and agitation. Fang and several colleagues tried to dampen the students' ardor, to no avail. In 1987, Premier Deng Xiaoping ordered Fang's expulsion from the Party, and both he and USTC president Guan Weiyan were fired.

In the winter of 1989, Fang wrote a letter to Deng Xiaoping noting that the year marked the 40th anniversary of the found-

ing of the PRC and the 70th anniversary of the May Fourth Movement. "In order to capture the spirit of these occasions in the best possible way, I sincerely propose that you announce a general amnesty, specifically to include all political prisoners," he concluded. This letter would be cited by the authorities as the principal cause of the student demonstrations that incited the government to use military force, which resulted in the massacre in Tiananmen Square.

Fang would eventually continue his fight for human rights in the United States, where he pursued theoretical astrophysics at the University of Arizona in Tucson. His death 4 years ago at the age of 76 deprived the world of an eloquent voice in the advocacy of human rights, but his expulsion from China allowed that voice to be heard around the world.

REFERENCES AND NOTES

1. Fang had already amassed a distinguished bibliography of articles in other fields of physics despite his difficulties with the authorities—difficulties that led to efforts to expunge his name from publications or replace his name with a pseudonym.

The reviewer is emeritus director of international scientific affairs at the American Physical Society, College Park, MD 20740, USA. E-mail: ialerch@verizon.net

Edited by Jennifer Sills

Editorial retraction

ON 7 MAY 2004, *Science* published the Report “RNA-mediated metal-metal bond formation in the synthesis of hexagonal palladium nanoparticles” by Lina A. Gugliotti, Daniel L. Feldheim, and Bruce E. Eaton (1). After an investigation by the U.S. National Science Foundation’s (NSF’s) Office of Inspector General, NSF did not find that the authors’ actions constituted misconduct. NSF nonetheless concluded that they “were a significant departure from research practices” and “a misrepresentation of data on which a conclusion was based” (2). In response to the NSF ruling, author Feldheim sent wording for a correction to *Science*. However, the Editors do not think a correction is appropriate given the concerns raised by the Inspector General’s report about what evidence was available to support the authors’ assertions at the time the paper was published. Hence, *Science* is issuing this Retraction instead. Author Gugliotti could not be reached for her concurrence in this matter. Authors Feldheim and Eaton do not agree to this Retraction.

Marcia McNutt

Editor-in-Chief

REFERENCES

1. L.A. Gugliotti, D.L. Feldheim, B.E. Eaton, *Science* **304**, 850 (2004).
2. NSF Office of Inspector General, Closeout Memorandum (www.nsf.gov/oig/case-closeout/A06110054.pdf).

Social cost of carbon: Domestic duty

THE NATIONAL ACADEMIES of Sciences have assembled a committee to review the economic aspects of climate change in order to better estimate the social cost of carbon (SCC) (1). The SCC is an estimate in dollars of the long-term damage caused by a one-ton increase in global carbon emissions in a given year. Although the SCC oversimplifies a dauntingly complex reality, agreement on an SCC is necessary for cost-effective emissions controls (2). A key question is whether the SCC should reflect social costs to the United States or the entire world.

In 2013, an interagency group established the current federal SCC values—\$43 per metric ton of CO₂ in 2020 assuming a 3% discount rate—based on the estimated



Cost-effective emissions controls depend on calculating the domestic and global social costs of carbon.

global SCC (3). Regulatory agencies use this global SCC as the sole summary measure of the value of reducing greenhouse gas emissions and compare it with estimates of domestic costs. This approach conflicts with long-standing federal regulatory policy directing agencies to issue regulations only upon a “reasoned determination” that the benefits “justify” the costs (4–6). A decision to issue a regulation with substantial domestic costs based on a finding that benefits to foreigners “justify” such costs would be irregular at best. Even with explicitly stated altruistic or strategic motivations (7), analyses that present only global benefits of regulations to reduce U.S. emissions would be misleading.

The federal government has a duty to inform Americans about the reductions in domestic climate damages that may result from federal regulation. The current approach of reporting only the global benefits neglects that duty. The National Academies of Sciences should refocus regulatory analysis of U.S. regulations on their domestic effects by recommending the use of a domestic SCC and supporting separate reporting of estimates of effects beyond the United States.

Art Fraas,¹ Randall Lutter,^{2,1*} Susan Dudley,³ Ted Gayer,⁴ John Graham,⁵ Jason F. Shogren,⁶ W. Kip Viscusi⁷

¹Resources for the Future, Washington, DC 20036, USA. ²Frank Batten School of Leadership and Public Policy, University of Virginia, Charlottesville, VA 22904, USA. ³Regulatory Studies Center, The George Washington University, Washington, DC 20052, USA. ⁴Brookings Institution, Washington, DC 20036, USA. ⁵School of Public and Environmental Affairs, Indiana University, Bloomington, IN 47402, USA. ⁶University of Wyoming, Laramie, WY 82071, USA. ⁷Vanderbilt Law School, Vanderbilt University, Nashville, TN 37203, USA.

*Corresponding author. E-mail: Lutter@rff.org

REFERENCES

1. Board of Environmental Change and Society, *Assessing Approaches to Updating the Social Cost of Carbon* (The National Academies, Washington, DC, 2015–2016); <https://www8.nationalacademies.org/cp/projectview.aspx?key=49733>.
2. S. E. Dudley, B. Mannix, *Federalist Soc.* **Engage** **15**, 1 (2014).
3. Interagency Working Group on Social Cost of Carbon, *Technical Support Document: Social Cost of Carbon for Regulatory Impact Analysis Under Executive Order 12866* (White House, Washington, DC, 2013); <http://1.usa.gov/18ftAsH>.
4. T. Gayer, W. K. Viscusi, “Determining the proper scope of climate change benefits” (Brookings Institution, Washington, DC, 2014); www.brookings.edu/~media/research/files/papers/2014/06/04-determining-proper-scope-climate-change-benefits-gayer/04_determining_proper_scope_climate_change_benefits.pdf.
5. Executive Order No. 13563, *76 Fed. Reg.* 3821 (2011).
6. Executive Order No. 12866, *58 Fed. Reg.* 51735 (1993).
7. W. Pizer *et al.*, *Science* **346**, 1189 (2014).

False positives are statistically inevitable

IN HIS NEWS story “Reproducibility in psychology” (18 December 2015, p. 1459), J. Bohannon reports on the progress researchers in the field of psychology have made in implementing the practice of reproducing experimental results. He points out that preregistration—a procedure in which researchers first specify their hypotheses and methods and then publish the results of their analyses regardless of outcome—has helped achieve reproducibility goals. This type of methodology can help minimize poor statistical practices, such as doing multiple tests on data and only reporting those that are statistically significant. However, Bohannon’s conclusion that “[i]f everyone followed that protocol, false positives might all but disappear from journals” is a bit overstated.

In the absence of poor statistical practice and pressures to find and publish statistically significant results, the rate of false-positive results should correspond to the experimenter’s choice of test significance level, typically denoted as α . For a statistical test in which the conventional choice of $\alpha = 0.05$ is used, one would expect 5% of experiments to generate spurious “significant” results, and the probability of independently reproducing a false-positive experiment result at the same significance level is $0.05 \times 0.05 = 0.0025$. Under these conditions, this means we can expect that one-quarter of one percent of the experiments will have a false-positive result in the original experiment as well as a false positive in the reproduced experiment, thus seemingly confirming the original erroneous result.

Although this seems like a very small chance, leading to the suggestion that false positives “might all but disappear,”

the observed number of false positives is also a function of the number of scientific publications, which by one estimate in 2006 was 1.35 million articles (1). Others have estimated that the scientific output may double every 10 years (2). If correct, there could be 2.7 million or so scientific papers published in 2016.

So, imagine if half of all papers published in 2016 (about 1.35 million) contained the results of exactly one statistical test conducted at a significance level of $\alpha = 0.05$, and if every one of those tests was reproduced, then we would expect to observe around 3375 “confirmed” spurious results ($0.0025 \times 1,350,000 = 3375$). Of course, that is much better than the 67,500 false positives in the original papers ($0.05 \times 1,350,000$), but it is rather larger than “all but disappear.”

Reproducibility is clearly important, and we should support and encourage those who promote it—across all fields, not just psychology—as a crucial part of the scientific enterprise. In particular, moving away from publication standards based solely on the statistical significance of a single experiment or a single set of observed data to those based on evidence that observed

results can be reproduced is a critical change that we must make in the academic publishing culture. However, we must also recognize that, even within the most careful and rigorous experimental framework, erroneous conclusions are always possible. We should thus always maintain a healthy skepticism when assessing study results.

R. D. Fricker Jr.

Department of Statistics, Virginia Polytechnic Institute and State University, Blacksburg, VA 24061, USA. E-mail: rf@vt.edu

REFERENCES

1. P. O. Larson, M. von Ins, *Scientometrics* **84**, 575 (2010).
2. D. J. de S. Price, *Little Science, Big Science* (Columbia Univ. Press, New York, 1963).

Psychosocial factors key to healthy aging

I READ WITH great interest M. Kaeberlein *et al.*'s Review “Healthy aging: The ultimate preventative medicine” (4 December 2015, p. 1191). I agree that going beyond a disease-specific focus and “directly targeting aging” will be beneficial. However, Kaeberlein *et al.* focus on the biomedical aspects of this

challenge. The psychosocial components of aging should not be overlooked.

In a recent systematic review of qualitative studies examining what older adults considered to be “successful aging,” interviewees most commonly mentioned, and deemed most important, psychosocial components, such as social engagement, positive perspective, and personal growth (1). Just as it is important to go beyond a disease-specific focus to facilitate healthy aging, it is important to go beyond a strictly biomedical focus and to examine the ways in which psychosocial strengths can be fostered and quality of life improved. Augmenting models of translational geroscience to include psychosocial aspects of aging, such as social and emotional aging and resilience, will provide a more comprehensive perspective on aging. In addition to adding years to one's life, we must also work to add life to those years.

Theodore D. Cosco

MRC Unit for Lifelong Health and Ageing at University College London, London, WC1B 5JU, UK. E-mail: tdcosco@cantab.net

REFERENCE

1. T. D. Cosco, A. M. Prina, J. Perales, B. Stephan, C. Brayne, *BMJ Open* **3**, e002710 (2013).

REVIEW SUMMARY

BATTERIES

Why do batteries fail?

M. R. Palacín* and A. de Guibert

BACKGROUND: We are all familiar with the importance of mobile power sources (automobile batteries, cell phone batteries, etc.) and their seeming tendency to malfunction at just the wrong moment. All batteries show performance losses during their service lives that involve a progressive decrease in capacity (loss of autonomy) and increase in internal resistance, leading to voltage decay and loss of power. Battery aging phenomena evolve at substantially different rates depending on storage or usage conditions (temperature, charge/discharge rates, and voltage operation limits) and are specific to each battery chemistry. The study of the origin of such processes is important for battery calendar-life predictions, but this research is complex to carry out because it involves field trials as well as extrap-

olation from accelerated tests using suitable models.

ADVANCES: Electrification of automotive transportation and renewable energy integration constitute two imperative pathways toward reduction of gas emissions and global warming. These incur challenges in terms of energy storage technologies, for which batteries emerge as a versatile and efficient option. Durability is critical per se in such large-scale applications and also has a direct impact in terms of cost. As a result, efforts toward understanding the mechanisms of battery degradation have intensified in recent years.

Aging and failure mechanisms result from various interrelated processes taking place at diverse time scales, hence their complete

elucidation is a very challenging target. Battery operation upon each charge/discharge cycle should ideally only involve changes in the phases present at both electrodes and modification of their physical properties. However, all battery components can interact with one another to some extent, contributing to a convoluted system of interrelated physicochemical processes in which the influences of temperature and charge/discharge rate are decisive.

Although interactions between the active materials and the electrolyte are largely responsible for aging upon storage, cycling generally

ON OUR WEB SITE

Read the full article at <http://dx.doi.org/10.1126/science.1253292>

damages electrode active materials' reversibility because of the mechanical stresses induced by the structural changes taking place. Although both mechanisms are often considered as additive, interactions may occur and some additional factors (such as temperature) have an impact on both. Moreover, the variety of possible parasitic reactions is enhanced by the number of chemical elements present in the cell; this number is lowest for Pb/acid batteries (redox processes involve lead at both electrodes and current collectors are also made of lead) and highest for lithium-ion batteries, which can also comprise a larger variety of subtechnologies depending on the active materials used.

Overall, the current available knowledge on these matters results from a vast combination of experimental and modeling approaches and has greatly benefited from the progressive improvement of available materials science characterization tools.

OUTLOOK: The requirements for battery long-term stability are extremely stringent, and hence the advent of batteries with optimized calendar and cycle life will only be triggered by a full understanding of the ways in which the different systems fail. Thorough studies involving both testing and monitoring of real or model cells under different environments and/or postmortem studies using a wide range of experimental techniques coupled to modeling approaches are crucial to the complete elucidation of aging and failure mechanisms. Such knowledge is vital to developing reliable, realistic operation models, which in turn will synergistically contribute to the development of batteries with optimized calendar life. This is currently a research priority in the field that is expected to yield substantial progress in the years to come. ■



Performance degradation is common to all battery technologies. Failure and gradual performance degradation (aging) are the result of complex interrelated phenomena that depend on battery chemistry, design, environment (temperature), and actual operation conditions (discharge rate, charge protocol, depth of discharge, etc.). Knowledge of such processes is crucial for the widespread deployment of large-scale battery applications such as transportation and the electric grid.

The list of author affiliations is available in the full article online.

*Corresponding author. E-mail: rosa.palacin@icmab.es

Cite this paper as M. R. Palacín, A. de Guibert, *Science* 351, 1253292 (2016). DOI: 10.1126/science.1253292

REVIEW

BATTERIES

Why do batteries fail?

M. R. Palacín^{1*} and A. de Guibert²

Battery failure and gradual performance degradation (aging) are the result of complex interrelated phenomena that depend on battery chemistry, design, environment, and the actual operation conditions. The current available knowledge on these matters results from a vast combination of experimental and modeling approaches. We explore the state of the art with respect to materials as well as usage (temperature, charge/discharge rate, etc.) for lead-acid, nickel-cadmium, nickel–metal hydride, and lithium-ion chemistries. Battery diagnosis strategies and plausible developments related to large-scale battery applications are also discussed.

Energy storage is a key enabler for modern life. A large spectrum of storage technologies exists today, with wide variation in terms of maturity, amount of energy stored, speed of release (power), efficiency, durability, and cost. Batteries occupy a privileged position in this landscape, as they are highly versatile: Cells can be manufactured in a wide range of sizes that can also be assembled into packs if necessary. Countless technologies could be developed a priori by coupling different pairs of electrodes based on any favored redox reaction. Nonetheless, more than 200 years after Volta's invention, only a few systems have been considered to fulfill all requirements to enable practical development and a mere handful of them are commercially important. Their historical evolution in terms of performance has seen a few disruptive events, such as the patents of the Pb/acid battery in France (Planté, Faure) and Ni-based technologies in Sweden and the United States (Jüngner, Edison) at the turn of the 20th century, and most recently the commercialization of Li-ion technology in Japan (Sony) in 1991.

The versatility of batteries has enabled their use in widely diverse domains of application, from miniaturized devices to large-scale storage plants. The total size of the global battery market accounted for \$54 billion (U.S.) in 2013, with 5% average growth per year between 1990 and 2013. Lithium-ion technology is the most popular at present, with an equivalent to about 38,000 MWh of storage being commercialized in 2013. The proportion used in portable electronics far exceeds that used in alternative or emerging applications such as hybrid and electric vehicles (sometimes known as xEVs). The largest part of the ~1.8 million vehicles sold in 2013 use Ni–metal hydride (Ni/MH) batteries, with Li-ion batteries accounting for roughly

500,000 vehicles (and corresponding to 3500 MWh) (1). Stationary energy storage involves the use of large batteries, and even if it is expected to grow concomitant with renewable energy penetration (2), its present capacity is only 1170 MWh of battery storage, of which ~40% consists of Li-ion batteries. Growth expectations in all sectors are derived from diverse converging forecasts, with an estimated global market by 2020 close to \$32 billion for Li-ion technology alone.

Despite this success, the requirements for long-term battery stability are extremely stringent. As a consequence, a battery's performance is ultimately always modified (degraded) during its lifetime. Users are familiar with this phenomenon even if they are seldom aware of its causes, as they are often specific to each battery technology and are rarely addressed globally. The present paper aims to fill this void.

At first glance, any battery operation may seem extremely straightforward, based on a combination of two redox semi-reactions as taught in high school chemistry class. Yet an intrinsically complex and evolving system exists behind this apparent simplicity. Aside from the requirements for “active” electrode materials and an electrolyte that makes ionic transport possible, practical performance is enabled by alternative “inactive” components such as current collectors (metal foil, grid, foam, etc.), separators (glass fiber or polymeric microporous film in which the electrolyte is embedded), conductive additives (typically metals, inorganic conducting compounds, or different types of carbon), and often some sort of polymeric binder (Fig. 1A). All these contribute to battery function by maintaining the electrode's electronic and mechanical integrity. In addition, batteries are often designed for a particular application, and there is usually a trade-off between the maximum power output possible and the maximum stored energy. Indeed, cells designed for high power output require low internal resistance and low electrode polarization, accomplished by thin electrodes of high surface area. Thus, the inert current collectors, separators, etc., constitute a higher fraction of the mass and volume, and the stored energy density

decreases by comparison to energy-optimized cell designs.

Battery operation upon each charge/discharge cycle brings about a change in the phases present at both electrodes and modification of their physical properties. Ideally, such processes should be fully reversible and should exclusively involve the active materials. However, all battery components can interact with one another to some extent, contributing to a convoluted system of interrelated physicochemical processes, which are dependent on many factors. Some of them are related to practical operation conditions such as charge/discharge rate or temperature.

Basics of battery operation

The chemical energy stored in a battery is the product of capacity and voltage, and is primarily determined by the cell chemistry and electrode materials. Usually, the open-circuit voltage is considered together with the discharge capacity to a certain cutoff voltage. These are not absolute, independent measures; they are heavily affected by electrode kinetics, and thus they depend on discharge rate and temperature (3). The fundamentals of the most commercially relevant rechargeable battery systems (4) are given in Table 1.

The maximum electric energy that can be delivered by the electrode active materials depends on the change in free energy ΔG of the chemical reaction involved (Table 1). Upon operation, irreversible energy losses occur because batteries exhibit an intrinsic internal resistance (R): Joule heating (I^2R) and ohmic drop (IR drop). These losses are all related to the current flowing through the cell (I , the charge/discharge rate), which is usually expressed in terms of C/n rate, where n is the time (in hours) to achieve the cell capacity (C). As the current drain of the battery is increased, losses increase and the amount of energy recovered is reduced. In contrast, at extremely low current drains, energy can approach theoretical expected values. This explains, for instance, why a primary battery used to its end-of-life (EoL) in a high-drain application (e.g., camera flash) can subsequently be used to power a quartz clock, requiring much lower current.

The operation of Pb/acid cells involves major structural reorganization of the electrode active materials, with dissolution and reprecipitation of lead sulfate or lead dioxide at each cycle. In the case of Ni-based batteries, the Cd electrode also involves a dissolution-precipitation mechanism, whereas the reaction at the MH electrode takes place in the solid state. For the Ni(OH)₂ positive electrode active material, a solid-state redox reaction involves reversible de-insertion of H⁺ from the layered crystal structure with concomitant modification of its stacking sequence (5). Lithium-ion batteries operate through reversible (usually topotactic) insertion of Li ions in the structure of both electrode materials; the most common materials are graphite for the negative electrode and layered transition metal oxides or lithium iron phosphate for the positive electrode (Table 1). Materials operating through alternative redox mechanisms enabling higher

¹ALISTORE-ERI European Research Institute, Institut de Ciència de Materials de Barcelona (ICMAB-CSIC) Campus UAB, E-08193 Bellaterra, Catalonia, Spain. ²SAFT Research Department, 111 Boulevard Alfred Daney, 33074 Bordeaux, France.

*Corresponding author. E-mail: rosa.palacin@icmab.es

energy densities have been intensively investigated (6) but have not yet reached the commercial stage.

The electrolyte is ideally a chemically inert medium that simply impregnates both electrodes and the separator to enable ionic transport. Aqueous electrolytes (either acid or alkaline) are used in “traditional” battery technologies such as Pb/acid, Ni/Cd, and Ni/MH. These are, however, unstable at the operation potentials of Li-ion batteries, and a mixture of organic solvents (commonly alkylcarbonates) is used, typically with 1 M LiPF₆ dissolved. This adds some complexity to the picture, because the electrochemistry in these media is much less developed. The energy separation of the lowest unoccupied molecular orbital and the highest occupied molecular orbital of the electrolyte (LUMO and HOMO, respectively; Fig. 1B) determines the thermodynamic cell’s electrochemical stability window.

The electrolyte is crucial in generating stable electrode/electrolyte interfaces and thus plays a key role in cycle life (defined as the number of

charge/discharge cycles that a battery can sustain while keeping a given percentage of its initial capacity, usually 80%, set as EoL). For the case of Li-ion technology, electrolyte solvents are unstable below ~0.8 V versus Li⁺/Li and above ~4.5 V versus Li⁺/Li in the presence of the electrode materials, which are strongly reducing/oxidizing. Consequently, electrolyte solvent degradation reactions take place at the electrode/electrolyte interfaces, which often also involve the electrolyte salt and water impurity traces. The resulting insoluble products form a solid protective passivation layer adhering to the surface of the negative electrode (termed the solid-electrolyte interphase, or SEI) (7–9). An interphase is also formed at the surface of the positive electrode, sometimes called the surface layer (SL) to distinguish it from the one formed at the negative electrode. Thus, cell operation is made possible through proper passivation of both electrode surfaces, which enables successful operation of the electrolytes outside their thermodynamic stability windows (10). However, overcharge (supply of charge in excess of that

required by electrode materials) will still lead to side reactions, such as irreversible electrolyte decomposition (11) with gas generation.

In aqueous technologies, the operating voltage is limited by water decomposition; the Pb/acid battery voltage is higher than that of Ni-based technologies, owing to a much higher hydrogen overvoltage. Overcharging leads to water electrolysis with formation of oxygen at the positive electrode that can diffuse to the negative electrode and recombine by reduction at its surface. Thus, effective battery designs enabling rapid transport of oxygen and recombination efficiencies close to 100% provide overcharge protection and enhanced safety (12, 13).

Battery degradation and failure

Although battery operation should ideally entail the reversible redox reactions mentioned above, involving exclusively electrode active materials (or some electrolyte components for Pb/acid and Ni/Cd; Table 1), the real situation is much more complex, and additional physicochemical processes

Fig. 1. Schematics of typical battery cell and example of energy levels involved. (A) Architecture of a cell with composite electrodes. (B) Illustration of the energy levels involved in a Li-ion electrochemical cell. The dashed red, blue, and green lines correspond to the chemical potential of Li in the negative electrode, the chemical potential of Li in the positive electrode, and a typical placement for the voltage window of the electrolyte, respectively. V_{oc} , open-circuit voltage of the cell; μ , chemical potential. [(B) adapted with permission from (57)]

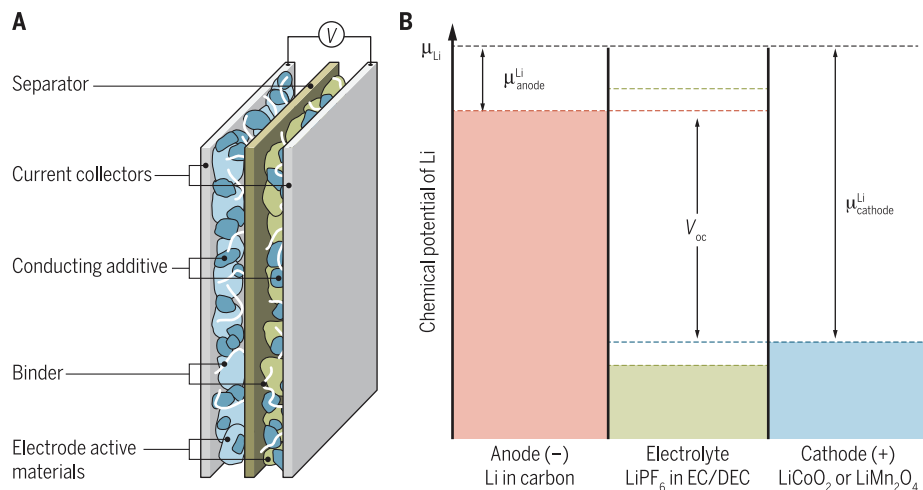


Table 1. Chemical reactions and performance figures of merit for commercially relevant rechargeable battery technologies.

Technology	Electrolyte	Overall reaction	Cell voltage (V)	Specific energy (Wh/kg)	Operating temperature (°C)
Pb/acid	Sulfuric acid (aq.)*	$\text{Pb} + \text{PbO}_2 + 2\text{H}_2\text{SO}_4 \rightarrow 2\text{PbSO}_4 + 2\text{H}_2\text{O}$	2.04	30	-25 to +50
Ni/Cd	Alkali hydroxide (aq.)†	$2\text{NiOOH} + \text{Cd} + 2\text{H}_2\text{O} \rightarrow 2\text{Ni(OH)}_2 + \text{Cd(OH)}_2$	1.3	50	-40 to +60
Ni/MH‡	Alkali hydroxide (aq.)†	$\text{NiOOH} + \text{MH}_x \rightarrow \text{Ni(OH)}_2 + \text{MH}_{1-x}$	1.35	65	-20 to +60
Li ion	LiPF ₆ (organic solvents)	$\text{Li}_{1-x}\text{MO}_2 + \text{Li}_x\text{C}_6 \rightarrow \text{LiMO}_2 + 6\text{C}$	3.6§	150 to 270	-30 to +60¶
Li polymer#	Li salt** (polyethyleneoxide)	$x\text{Li} + \text{V}_2\text{O}_5 \rightarrow \text{Li}_x\text{V}_2\text{O}_5^{\dagger\dagger}$	3	140	60 to 100

*The electrolyte (sulfuric acid, $d = 1.27 \text{ g/cm}^3$) and electrolyte solvent (water) participate in the reaction, being consumed during discharge and regenerated upon charge.

†Typically a mixture of KOH, NaOH, and LiOH with overall concentration 4.5 to 8 M. NaOH and LiOH are added to improve chargeability through increase of the oxygen release overpotential. ‡The anode is an alloy, most frequently AB₅, where A is a rare earth (mostly mischmetal to limit cost) and B is Ni, Co, Mn, and/or Al. §With graphite (C) anode and layered transition metal oxide cathode such as LiCoO₂ (LCO), LiNi_{0.8}Co_{0.15}Al_{0.05}O₂ (NCA), LiNi_{1/3}Mn_{1/3}Co_{1/3}O₂ (NMC 1/1/1), or other compositions containing Ni, Mn, and Co, which exhibit more stable crystal structures upon lithium de-insertion and thus larger capacity. Alternative cathodes such as LiMn₂O₄ (LMO) or LiFePO₄ (LFP) yield cell potentials of 3.6 V and 3.2 V, respectively, and somewhat (15%) reduced energy densities due to lower specific capacity and lower voltage, respectively.

¶The lower figure corresponds to industrial long-life batteries; the higher figure applies to low-power, limited-life batteries for portable applications. ¶¶Can reach somewhat expanded low or high limits in particular applications with specifically designed batteries. #Not to be confused with Li-ion chemistry with liquid electrolyte embedded in a polymer, sometimes commercially (and misleadingly) denoted “polymer Li-ion.” **Commonly LiN(CF₃SO₂)₂ (usually denoted LiTFSI). ††More recently, LiFePO₄ has also been introduced as positive electrode material without major change in performance.

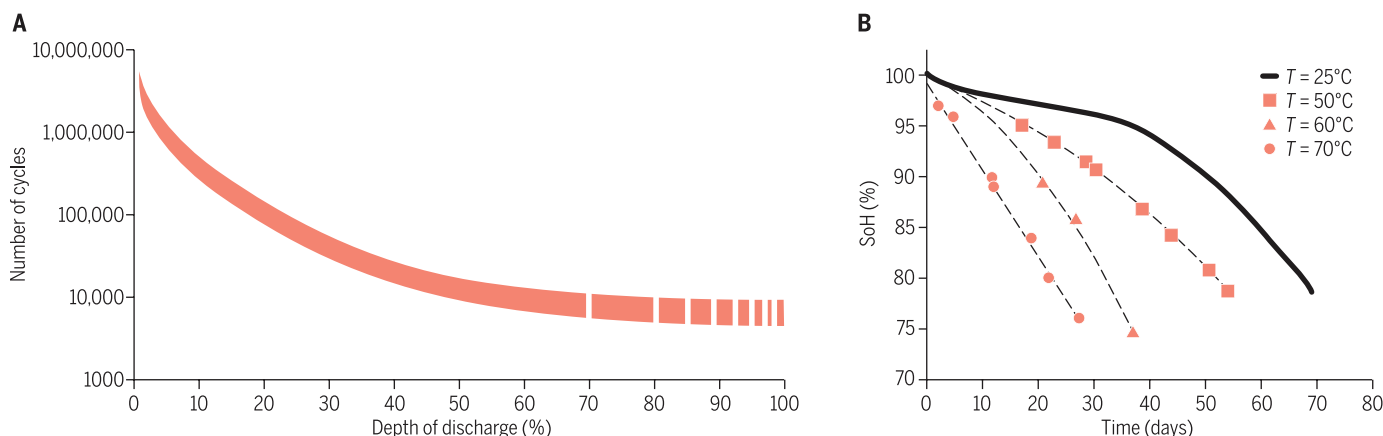


Fig. 2. Influence of depth of discharge and temperature on battery performance degradation. (A) Cycle life as a function of DoD for Li-ion cells operating at 25°C. (B) State of health (SoH, defined as the discharge capacity of an aged cell relative to the discharge capacity of the same cell when it was new) as a function of time for Li-ion cells cycling at a rate of 1C at different temperatures. [Adapted with permission from (17)]

occur that may involve any battery component. These are obviously dependent on battery chemistry, with the number of possible parasitic reactions being enhanced by the number of chemical elements active or present in the cell. This number is lowest for Pb/acid batteries (redox processes involve lead at both electrodes, and current collectors are also made of lead) and highest for Li-ion batteries, which can also comprise a larger variety of subtechnologies depending on the active materials used (Table 1). The type and extent of such reactions is also affected by the environment (temperature) and conditions of use [discharge rate, charge protocol, depth of discharge (DoD), etc.] throughout the battery lifetime. For example, batteries used in uninterrupted power supply (UPS) units remain in float condition (compensating any self-discharge of the battery by constant charge at very low current) and are normally subjected to a limited number of cycles during their life, whereas pure hybrid electric vehicles usually operate at low DoD but in a partial state of charge, and batteries in fully electric vehicles or portable electronics function at high DoD (or charge-depleting mode).

The above-mentioned side reactions can cause phenomena leading to sudden failure (cell drying, short circuit, thermal runaway) or can manifest indirectly via a large variety of symptoms that contribute to battery “aging” with progressive performance degradation to EoL (14). Sudden failure is often encountered in Pb/acid 12-V SLI (starting, lighting, and ignition) six-cell batteries used to start vehicle internal combustion engines. This may happen on cold winter mornings, as when an aged battery with decreased power and enhanced-viscosity electrolyte is unable to start an engine that uses a higher-viscosity motor oil. Yet it can also take place in hot climates, as when temperature-enhanced corrosion causes grid short circuits or disconnection. The study of the origin of such processes is important for battery calendar-life predictions, but such research necessarily involves either field trials or extrapolations from accelerated tests using suitable models (15). Moreover, Li-ion battery

designs are not always optimized to provide the longest possible calendar life. Although this is the case for large batteries used in industrial applications, smaller ones used in portable electronics are merely targeted to outlive the devices they power (~3 years for cell phones), and their designs are optimized for specific energy (autonomy).

The main generic manifestations of battery aging are observed both during use and upon storage: a progressive decrease in capacity (loss of autonomy) and an increase in internal resistance leading to voltage decay and loss of power. Cycling generally damages electrode active materials’ reversibility, especially at high DoD (1000 cycles at 100% DoD is a heavier duty than 10,000 cycles at 10% DoD) (Fig. 2A). This can be rationalized in terms of the mechanical stresses induced by the changes taking place at the electrode active materials as a function of state of charge (e.g., intercalation of lithium ions in a graphite electrode leads to 12% expansion of graphite along the *c* axis for a fully charged electrode). In contrast, interactions between the active materials and the electrolyte are mostly responsible for aging upon storage for Li-ion or MH electrodes. Although both mechanisms are often considered as additive, interactions may definitely occur and some additional factors (e.g., temperature) can have a substantial impact, which adds even more complexity to the scenario.

Fast operation rates involve higher losses in terms of polarization and Joule heating (and hence a temperature increase). The general trend is an increase of degradation with temperature (Fig. 2B), the cause being mostly the enhanced rate of side reactions involving electrode/electrolyte interfaces, which take place both upon cycling and upon storage. This is nicely exemplified by the results of a study dealing with SLI Pb/acid batteries sampled from 24 U.S. cities showing a strong correlation between battery service life and the number of days per year with maximum temperature above 32°C (90°F) (16). The usual way of scientifically analyzing

the influence of temperature is to assume that side reaction rates follow an Arrhenius law (i.e., they increase exponentially with *T* through a coefficient linked to an activation energy). Yet this is no easy task, as several reactions may simultaneously or successively take place, each with its own activation energy and rate constant (17).

Performance degradation through battery lifetime is common to all battery technologies and can evolve at different rates, depending on operation conditions (temperature, charge/discharge rate, and voltage operation limits). Still, aging processes are ultimately rooted in chemical reactions between battery components and are thus technology-specific. These reactions are complex and in some cases not fully elucidated. Below, we outline the currently assessed trends for the three main rechargeable battery technologies, focusing on main reactions while emphasizing aspects related to cell design or electrode technology.

Pb/acid batteries

Pb/acid batteries still constitute the largest part of the worldwide battery market share in terms of MWh (7). Aside from SLI batteries (60 million produced each year), they are also used in small traction vehicles used in airports, golf courses, industry (forklifts), motorized wheelchairs, and stationary applications to cover power backup in hospitals or emergency services and alarms, among others.

Some of the failure mechanisms for SLI batteries—by far the most common type of Pb/acid battery in use today—are simply the result of mechanical shocks (broken or damaged containers or terminals including electrolyte leakage); others depend on use (e.g., electrolyte dryout due to overcharge) and choice of design (18, 19). Positive electrode grid corrosion or fracture and loss of contact have been observed, which can be mitigated by improving corrosion resilience with the use of Pb-Ca or Pb-Ca-Sn alloys (for the negative and positive electrodes, respectively) and through control of grid microstructure to avoid grain growth in the casting process. It is also noteworthy that antimony-containing alloys

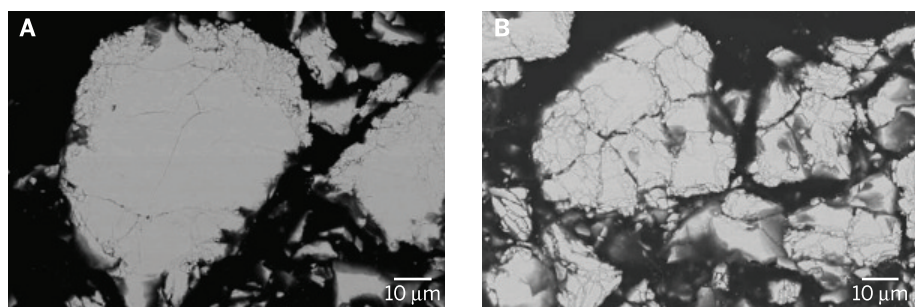


Fig. 3. Scanning electron micrographs of electrode cross sections. (A) Before cycling; (B) after 100 cycles. These images (magnification 1000 \times) show that the active material surface exposed to electrolyte is much larger on cycled cells, which in turn enhances the corrosion rate.

used in the positive electrode grids for easier castability result in corrosion and further migration of antimony ions to the negative electrode, which decreases the hydrogen overvoltage and hence results in decreased chargeability.

Loss of active material adhesion can also take place, which may lead to short-circuit after sedimentation (mud formation) unless pocket plate separators wrapping one electrode are used. The growth of large crystals of insulating lead sulfate on the negative electrode, concomitant with the decrease in sulfate concentration in the electrolyte, has also been assessed (termed “sulfation”) (20). Such crystals exhibit very slow reaction kinetics that may not enable operation. This issue can be alleviated by addition of higher amounts of carbon to the electrode to enhance electronic conductivity, but still restricts the application of Pb/acid batteries in hybrid electric vehicles (HEVs) (2).

In addition, large industrial Pb/acid batteries used in UPS or stationary applications may suffer from electrolyte stratification (development of a vertical sulfuric acid concentration gradient) (22), which can result in nonuniform usage of the active material and is mitigated by setting the battery to deliberate gassing during extended overcharge. Finally, because recombination efficiency never reaches 100%, there is a progressive loss of water and dryout of the electrolyte, which enhances recombination current and in turn heat emission, which can ultimately result in thermal runaway for valve-regulated aged batteries.

Nickel-based batteries

There are two main Ni-based battery technologies widely used in different applications: Ni/Cd and Ni/MH. Globally, Ni/Cd sales decreased by 6% per year between 2002 and 2012 while Ni/MH increased by 5% per year in the same period. Both types of battery are fabricated as small sealed cylindrical cells for portable applications and as large prismatic cells or modules for industrial applications. Although small Ni/Cd cells are no longer in use for portable devices because of the toxicity of cadmium and the difficulty of collecting them for recycling, they are still used for emergency lightning units (ELUs) as they can withstand 4 years floating at 40° to 55°C better than other chemistries. Industrial Ni/Cd batteries,

either flooded (with excess electrolyte) or needing low maintenance (occasional addition of water to compensate for electrolyte consumption), are renowned for their very long life—up to 20 years—and reliability in either cycling or standby applications. This is related to the very reversible electrochemical reactions, excellent stability of the active materials, and very small number of side reactions (which allows extremely low fading even at 100% DoD) and to the existence of commercial batteries with robust design that can withstand mechanical abuse. Small Ni/MH batteries are used in home appliances (cordless phones, toys) and are starting to be used for ELUs, whereas larger cells are used in hybrid vehicles such as trams, buses, and cars (such as the Toyota Prius), where their absence of maintenance is a key advantage compensating for their higher cost.

The operation in concentrated alkaline electrolyte in oxidizing medium (presence of oxygen when the cell is charged) leads to decomposition of organic polymers present in the cell (separator, fibers, binder) and formation of carbonates in electrolyte, which decreases its ionic conductivity and hence the performance. Moreover, alkali carbonates have a limited solubility and can precipitate, which would enhance this effect.

Degradation phenomena at the positive Ni electrode are largely dependent on the electrode technology. Indeed, the insulating character of Ni(OH)₂ (usually also alleviated by partial nickel substitution for cobalt and zinc) results in conducting additives being essential. Sintered plates are made of sintered nickel particle substrates on which the active nickel hydroxide material is deposited by chemical precipitation or by electrochemical reduction of nickel nitrate solutions. These are thus very conducting, as the active material is always in contact with the metallic substrate that also acts as current collector. Nonetheless, such electrodes are more expensive to manufacture, and they sacrifice capacity on a weight and volume basis. Alternatively, electrodes pasted on a metal foam, mesh, or sheet require the use of a plastic binder and conducting cobalt oxide and hydroxide additives, commonly added by simple mixture with the nickel hydroxide active material particles or coating their surfaces. Yet such cobalt-containing phases do chemically evolve and are irreversibly reduced

upon battery operation, which brings about a decrease in the electrode conductivity.

With respect to the cadmium negative electrode, crystal growth can be promoted at the expense of nucleation under certain cycling and storage conditions, which results in a reduced active electrochemical surface and lower efficiency. In contrast, a pulsed charging mode is associated with long rest periods that can result in the growth of cadmium particles (metallization), which may cross the separator and induce soft shorts (nonviolent short circuits perceived by the user as high self-discharge).

Degradation of the negative electrode in the Ni/MH technology takes place mainly through two related processes (23–25). These involve corrosion of the alloy active material through surface reaction with the alkaline electrolyte and further pulverization due to stresses induced in the structure by hydrogen absorption/desorption upon cycling (Fig. 3). Fracture exposes new fresh electrode surfaces and corrosion proceeds, consuming water from the electrolyte, which results in cell dryout and enhanced resistance. Therefore, Ni/MH batteries under normal use conditions exhibit the same progressive aging linked to the positive electrode, and additionally a gradual increase of the internal resistance related to corrosion of the negative electrode. Such corrosion processes can lead to insoluble (mostly metal hydroxides) or soluble products, which can then interact with the positive electrode. For instance, incorporation of aluminum into the crystal Ni(OH)₂ lattice results in an increase of the nickel oxidation potential and hence reduced charge acceptance. Aluminum content in the positive material is commonly taken as a measure to assess the corrosion level of the negative material (26).

Nickel-based batteries suffer from what is commonly termed “memory effect,” which manifests in discharge taking place at a lower potential or, if a cutoff potential for discharge is set, as a loss of discharge capacity (27). This effect results from the combination of different phenomena that are dependent on electrode technology and battery operation conditions, all entailing the modification of phase composition at the electrodes causing operation at lower potential. One phenomenon is cadmium alloying with a nickel-containing electrode substrate (sinter or foam) to form the Ni₅Cd₂₁ alloy, which is reduced at lower potential than Cd. Alternatively, the phase present in the positive electrode in the charged state (β -NiOOH, which exhibits a layered structure) can, upon overcharge in concentrated electrolyte, be transformed to the γ polymorph, which exhibits a higher nickel oxidation state and co-intercalated alkaline ions and water molecules from the electrolyte in the interlayer space. The reduction of this phase takes place at 70 to 100 mV lower potential than that of the β phase. Finally, in electrolytes containing Li⁺ ions (Table 1), exchange with protons in the positive electrode active material can take place with formation of LiNiO₂ (isostructural to β -NiOOH). Again the effect is reduction at lower

potential, which is magnified at high currents because of a difference in reaction kinetics. Finally, β -NiOOH is metastable, and proton rearrangements in the crystal structure upon prolonged storage can result in reduced electronic conductivity, which enhances ohmic polarization. Because the above-mentioned reactions are mostly reversible, the memory effect can be suppressed through a full discharge to low potential to promote full reduction of all involved phases prior to complete recharge.

Li-ion batteries

Li-ion batteries have now been in commercial production for 25 years. Their development, in parallel with the growth of the consumer electronics market, is a striking example of synergy—an application-driven product with constant research-driven improvements in performance. This has enabled diversification of the technology into several subfamilies tailored to meet application needs. The ever-increasing energy density has sometimes been outpaced by practical requirements, as for cell phones requiring continuous operation/connection and large display screens. Transport (xEV) applications are especially challenging because the energy density determines the vehicle autonomy range but safety constraints force some compromises that affect the choice of specific electrode materials, cell designs, and battery management. Lifetime performance is crucial, and U.S. Advanced Battery Council (USABC) goals involve the extension of battery life to 15 years. In this context, identification of the causes of battery degradation is critical, and research efforts in this direction have recently intensified.

Li-ion batteries under normal use conditions do exhibit progressive aging, namely gradual decrease in discharge capacity caused by growth of internal resistance, which manifests as a loss of autonomy for the powered device. Such phenomena (28–30) arise from the combination of some general mechanisms with reactions specific to the particular electrode materials used in each Li-ion battery chemistry. Although the choice is more limited on the negative electrode, enlisting almost exclusively graphite, the positive side involves a larger spectrum of compounds (Table 1).

Capacity decrease for positive electrodes is parallel to enhancement of internal resistance, except for LiFePO_4 , which exhibits lower operation voltage. This can be due to different interrelated phenomena such as decreased ionic conductivity or modification of surface properties as well as reactivity with the electrolyte. Overcharging the positive electrodes, especially those operating at higher voltage, can lead to gas release from electrolyte oxidation as well as oxygen loss from the crystal structure of layered LiMO_2 oxides. This causes both degradation of the active material and an increase in cell internal pressure. In addition, as a result of the absence of recombination mechanisms, the reaction of emitted oxygen with the electrolyte represents a safety concern. The rate of solvent

oxidation is related to the operating voltage but depends as well on the composition and surface area of the active material. Furthermore, it is also largely affected by the surface area of the carbon additives commonly used to enhance electronic conductivity in the electrode. Finally, some positive electrode active materials may also suffer from partial dissolution. This can be related to specific operation conditions (i.e., high temperature) or reactivity with HF (31), which is formed by LiPF_6 hydrolysis with trace water impurities and can be temporarily present in the cell prior to its reaction to form LiF and hydrogen at the negative electrode upon charge. Metal ions (Fe^{3+} , Mn^{2+} , Co^{3+}) present in the electrolyte can be reduced in contact with the negative electrode, damaging the SEI, and can further catalyze electrolyte decomposition.

The two major factors contributing to loss of negative electrode performance are SEI instability and lithium metal plating. Lithium deposition may occur at high charge rates (and thus high polarization, enabling the Li metal deposition potential to be reached) or low operation temperatures (16, 32). At low temperature ($<10^\circ\text{C}$), the diffusion of Li^+ ions inside the graphite structure becomes slow, and Li metal deposition on the surface of the negative electrode can take place with risk of dendrite formation and short circuit. In addition, deposited Li reacts to form its own SEI, consuming electrolyte and lowering the interface porosity, thereby creating inhomogeneities in the electrode. As a result, the cell exhibits both decreased power (due to slower kinetics) and lower capacity (due to loss of active lithium ions in the cell).

An optimal SEI (ionically conducting, electronically insulating, and mechanically resilient) that is stable both upon cycling and storage is critical to long calendar life (33–35). Typical SEI degradation pathways are partial dissolution at high temperature or crack formation due to mechanical stresses inherent to electrode operation. These result in exposure of fresh naked graphite surfaces to the electrolyte on which an additional SEI grows, consuming electrolyte and enhancing electrode resistivity. The thermal breakdown of the SEI commonly starts around 110°C , well below exothermic positive electrode degradation reactions that take place above 200°C and can ultimately yield to thermal runaway (36, 37). SEI properties are extremely composition-dependent and are thus determined by the electrolyte used. This explains why most commercial battery electrolyte formulations are complex and commonly enlist some film formation additives (such as vinylene carbonate) (38). The SEI is formed in the first battery operation cycles (commonly called formation cycles) that are the final step of the manufacturing process, and is usually accompanied by the release of gaseous decomposition products. These cycles are usually performed under specific temperature and cycling rate conditions to minimize the electrochemical capacity involved and commonly result in irreversible consumption of $\sim 15\%$ of the active lithium ions initially present in the cell. Thus, they

have a substantial impact on cell capacity balancing (i.e., optimization of the ratio between the mass loadings of the two electrodes) for optimal use of active materials and hence affect the maximum achievable cell energy density. In an ideal scenario, this capacity balance would not change over the cell life, but this is seldom strictly the case, as it is modified by most of the aging processes mentioned above (Fig. 4) (39–41). Aside from lower energy density, unbalanced cells can exhibit safety hazards due to “overcharge” of the limiting electrode, which in the case of the negative electrode will typically result in lithium metal deposition. To address this contingency, cells are in practice built with an excess of negative active material. This is a compromise strategy to enhance safety at the expense of cell energy density.

Battery monitoring and diagnosis

The users' requirement of permanent knowledge of the remaining battery autonomy (or state of charge, SoC) and state of health (SoH, a term applied to diverse battery indicators, with 100% corresponding to the battery ideal condition in absence of degradation) can only be fulfilled through adequate battery diagnosis protocols based on the identification and monitoring of critical parameters.

The simplest diagnostic system (the “magic eye”) can be found for the Pb/acid technology, in which the electrolyte density varies between the fully charged and discharged states (typically from $\sim 1.27 \text{ g/cm}^3$ to $<1.1 \text{ g/cm}^3$ in SLI batteries). It consists of three colored (green, orange, and black) small balls with different densities that are immersed in the electrolyte. Battery status is inferred through a window in the battery cover by the color of the floating ball, which is determined by the electrolyte density and thus SoC. In this case, diagnosis is achieved by human intervention, is limited to three predefined levels, and does not involve any data storage. Li-ion batteries lie at the other extreme in complexity of monitoring and diagnosis protocols. For cells using layered cathodes, the discharge curve at different temperatures is precisely known and the SoC is extrapolated from the cell voltage measured in rest periods or discharges at low current. However, more sophisticated procedures are required for LiFePO_4 , as it exhibits a flat voltage discharge curve. In all cases, sensors are typically implemented at the cell level to monitor voltage, current, and temperature. Data acquired are transferred, stored, and analyzed through a battery management system (BMS). These systems started to be developed at the beginning of the 1990s by Texas Instruments, Ericsson, and Motorola and consist of electronic cards with specifically designed diagnosis and active control algorithms based on battery operation models (42). The fabrication quality of the cells or packs, and the knowledge of their behavior in every application environment, is crucial for building reliable models that can be successfully implemented in BMSs to manage battery operation. Such models rely

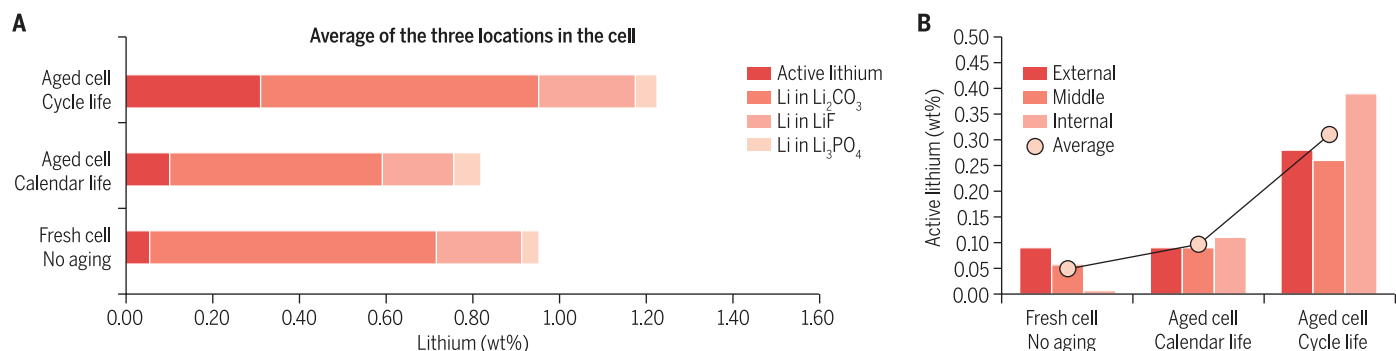


Fig. 4. Evolution of active lithium upon aging of a Li-ion cell. (A) Results of chemical analyses to determine active lithium in the negative electrodes of fresh and aged commercial Li-ion cells. Calendar life denotes 1.5 years of storage at 60°C and 60% state of charge; cycle life denotes 4200 hours of operation at 20°C with 10% DoD. Values for samples taken from the external, middle, and internal parts of the cell are given. (B) Relative quantification based on the lithium compounds actually present in the electrode. [Reprinted with permission from (39)]

on results of testing under different working conditions (temperature, discharge rate, DoD, charge protocol, etc.) and analysis of incremental capacity (43, 44) or differential voltage (45–47), and their use is compulsory to guarantee battery safety and ensure as long a cycle life as possible.

High-precision coulometry and calorimetry have recently proved to be very effective to detect side reactions contributing to performance degradation (48, 49). Yet battery aging and failure mechanisms result from various interrelated processes at diverse time scales, so their complete elucidation and understanding remains a complex and challenging target. Although researchers will take advantage of the benefits in situ and in operando techniques (50), the practical relevance of the outcome needs to be assessed as the test cells are designed to meet analytical requirements (in terms of geometry, size, etc.) and may not be representative of real batteries. Testing of aged electrodes in newly assembled cells (51) coupled to postmortem studies to probe any battery component sampled from distributed cell/electrode locations can provide critical information, especially if a wide spectrum of complementary experimental techniques is used (elemental analysis, optical and electron microscopy, diffraction, nuclear magnetic resonance, infrared, Raman, x-ray photoelectron spectroscopy, etc.) (52–56).

Overall, a smart combination of all such approaches is essential to elucidate the reaction mechanisms accounting for the observed loss in performance upon operation. This knowledge is crucial to developing reliable realistic operation models, which in turn will synergistically contribute to the development of batteries with optimized calendar life.

Conclusion

Although the growth in our understanding of the structure-property relationships of electrode materials has enabled steady progress in battery performance, especially in the case of Li-ion technology, the study of aging and failure mechanisms has developed at a much slower pace. This is mostly due to their intrinsic complexity,

as batteries are multicomponent chemical reactors that can differently evolve through their lifetime depending on their specific design, environment, and operation conditions.

Research efforts in this direction have recently intensified as a result of two different factors: (i) the progressive improvement of available experimental and modeling characterization tools coupled to the fundamental knowledge gained through materials research, and (ii) the need and opportunity for batteries to embrace larger-scale energy storage, for which durability is critical per se and also has a direct impact in application costs. Aside from progress in materials performance and tailored cell design, improvements in the understanding of the mechanisms underpinning battery degradation are required for enhanced xEV market penetration and for the widespread deployment of stationary electrical energy storage to enable a more efficient grid in the years to come.

REFERENCES AND NOTES

- C. Pillot, "Battery Market Development for Consumer Electronics, Automotive, and Industrial: Materials Requirements and Trends," presentation at China International Battery Fair (18 to 20 June 2014, Shenzhen); <http://doc.mbalib.com/view/43447d8528f67f9ec048d87d65754b9.html>.
- B. Dunn, H. Kamath, J. M. Tarascon, Electrical energy storage for the grid: A battery of choices. *Science* **334**, 928–935 (2011). doi: [10.1126/science.1212741](https://doi.org/10.1126/science.1212741); pmid: [22096188](https://pubmed.ncbi.nlm.nih.gov/22096188/)
- R. M. Dell, D. A. J. Rand, *Understanding Batteries* (RSC, Cambridge, 2001).
- D. Linden, T. B. Reddy, *Handbook of Batteries* (McGraw-Hill, New York, ed. 3, 2002).
- M. Casas-Cabanas, J. Canales-Vazquez, J. Rodríguez-Carvajal, M. R. Palacín, Deciphering the structural transformations during nickel oxyhydroxide electrode operation. *J. Am. Chem. Soc.* **129**, 5840–5842 (2007). doi: [10.1021/ja068433a](https://doi.org/10.1021/ja068433a); pmid: [17432856](https://pubmed.ncbi.nlm.nih.gov/17432856/)
- L. Croguennec, M. R. Palacín, Recent achievements on inorganic electrode materials for lithium-ion batteries. *J. Am. Chem. Soc.* **137**, 3140–3156 (2015). doi: [10.1021/ja507828x](https://doi.org/10.1021/ja507828x); pmid: [25679823](https://pubmed.ncbi.nlm.nih.gov/25679823/)
- E. Peled, C. Menahem, D. Bar Tow, A. Melman, Improved graphite anode for Lithium-ion batteries. *J. Electrochem. Soc.* **143**, L4 (1996). doi: [10.1149/1.1836372](https://doi.org/10.1149/1.1836372)
- K. Xu, A. von Cresce, Interfacing electrolytes with electrodes in Li ion batteries. *J. Mater. Chem.* **21**, 9849 (2011). doi: [10.1039/c0jm04309e](https://doi.org/10.1039/c0jm04309e)
- D. Aurbach, Review of selected electrode–solution interactions which determine the performance of Li and Li ion batteries.

- J. Power Sources* **89**, 206–218 (2000). doi: [10.1016/S0378-7753\(00\)00431-6](https://doi.org/10.1016/S0378-7753(00)00431-6)
- K. Xu, Electrolytes and interphases in Li-ion batteries and beyond. *Chem. Rev.* **114**, 11503–11618 (2014). doi: [10.1021/cr500003w](https://doi.org/10.1021/cr500003w); pmid: [25351820](https://pubmed.ncbi.nlm.nih.gov/25351820/)
- R. Fathi, J. C. Burns, D. A. Stevens, H. Ye, C. Hu, G. Jain, E. Scott, C. Schmidt, J. R. Dahn, Ultra high-precision studies of degradation mechanisms in aged LiCoO_2 /graphite Li-ion cells. *J. Electrochem. Soc.* **161**, A1572–A1579 (2014). doi: [10.1149/2.0321410jes](https://doi.org/10.1149/2.0321410jes)
- C. D. S. Tuck, Ed., *Modern Battery Technology* (Ellis Horwood, 1991).
- D. Berndt, *Maintenance-Free Batteries* (Wiley, 1997).
- M. Broussely, in *Advances in Lithium-Ion Batteries*, W. A. van Schalkwijk, B. Scrosati, Eds. (Kluwer Academic/Plenum, New York, 2002), pp. 393–432.
- J. Wang et al., Cycle-life model for graphite-LiFePO₄ cells. *J. Power Sources* **196**, 3942–3948 (2011). doi: [10.1016/j.jpowsour.2010.11.134](https://doi.org/10.1016/j.jpowsour.2010.11.134)
- H. Hoover, D. P. Boden, Failure mechanisms of lead/acid automotive batteries in service in the U.S.A. *J. Power Sources* **33**, 257–273 (1991). doi: [10.1016/0378-7753\(91\)85064-4](https://doi.org/10.1016/0378-7753(91)85064-4)
- T. Waldmann, M. Wilka, M. Kasper, M. Fleischhammer, M. Wohlfahrt-Mehrens, Temperature dependent aging mechanisms in lithium-ion batteries—a post-mortem study. *J. Power Sources* **262**, 129–135 (2014). doi: [10.1016/j.jpowsour.2014.03.112](https://doi.org/10.1016/j.jpowsour.2014.03.112)
- K. R. Bullock, Lead/acid batteries. *J. Power Sources* **51**, 1–17 (1994). doi: [10.1016/0378-7753\(94\)01952-5](https://doi.org/10.1016/0378-7753(94)01952-5)
- D. Berndt, Valve-regulated lead-acid batteries. *J. Power Sources* **100**, 29–46 (2001). doi: [10.1016/S0378-7753\(01\)00881-3](https://doi.org/10.1016/S0378-7753(01)00881-3)
- L. T. Lam, N. P. Haigh, C. G. Phyland, A. J. Urban, Failure mode of valve-regulated lead-acid batteries under high-rate partial-state-of-charge operation. *J. Power Sources* **133**, 126–134 (2004). doi: [10.1016/j.jpowsour.2003.11.048](https://doi.org/10.1016/j.jpowsour.2003.11.048)
- P. T. Moseley, D. A. J. Rand, B. Monahov, Designing lead-acid batteries to meet energy and power requirements of future automobiles. *J. Power Sources* **219**, 75–79 (2012). doi: [10.1016/j.jpowsour.2012.07.040](https://doi.org/10.1016/j.jpowsour.2012.07.040)
- D. Schulte et al., "Stratifiability index"—A quantitative assessment of acid stratification in flooded lead acid batteries. *J. Power Sources* **269**, 704–715 (2014). doi: [10.1016/j.jpowsour.2014.06.155](https://doi.org/10.1016/j.jpowsour.2014.06.155)
- P. Notten, M. Latroche, in *Encyclopedia of Electrochemical Power Sources*, J. Garche, Ed. (Elsevier, 2009), vol. 4, pp. 502–521.
- L. Le Guenne, P. Bernard, Life duration of Ni-MH cells for high power applications. *J. Power Sources* **105**, 134–138 (2002). doi: [10.1016/S0378-7753\(01\)00931-4](https://doi.org/10.1016/S0378-7753(01)00931-4)
- P. Bernard, Effects on the positive electrode of the corrosion of AB₅ alloys in nickel-metal hydride batteries. *J. Electrochem. Soc.* **145**, 456 (1998). doi: [10.1149/1.1838284](https://doi.org/10.1149/1.1838284)
- P. Leblanc, C. Jordy, B. Knosp, P. Blanchard, Mechanism of alloy corrosion and consequences on sealed nickel-metal hydride battery performance. *J. Electrochem. Soc.* **145**, 860 (1998). doi: [10.1149/1.1838358](https://doi.org/10.1149/1.1838358)
- Y. Sato, in *Encyclopedia of Electrochemical Power Sources*, J. Garche, Ed. (Elsevier, 2009), vol. 4, pp. 534–549.

28. P. Arora, R. E. White, M. Doyle, Capacity fade mechanisms and side reactions in Lithium-ion batteries. *J. Electrochem. Soc.* **145**, 3647 (1998). doi: [10.1149/1.1838857](https://doi.org/10.1149/1.1838857)
29. M. Broussely *et al.*, Main aging mechanisms in Li ion batteries. *J. Power Sources* **146**, 90–96 (2005). doi: [10.1016/j.jpowsour.2005.03.172](https://doi.org/10.1016/j.jpowsour.2005.03.172)
30. J. Vetter *et al.*, Ageing mechanisms in lithium-ion batteries. *J. Power Sources* **147**, 269–281 (2005). doi: [10.1016/j.jpowsour.2005.01.006](https://doi.org/10.1016/j.jpowsour.2005.01.006)
31. A. Blyr *et al.*, Self-discharge of $\text{LiMn}_2\text{O}_4/\text{C}$ Li-ion cells in their discharged state: Understanding by means of three-electrode measurements. *J. Electrochem. Soc.* **145**, 194 (1998). doi: [10.1149/1.1838235](https://doi.org/10.1149/1.1838235)
32. V. Zinth *et al.*, Lithium plating in lithium-ion batteries at sub-ambient temperatures investigated by in situ neutron diffraction. *J. Power Sources* **271**, 152 (2014).
33. S. Grolleau *et al.*, Calendar aging of commercial graphite/ LiFePO_4 cell—predicting capacity fade under time dependent storage conditions. *J. Power Sources* **255**, 450 (2014).
34. J. Belt, V. Utgikar, I. Bloom, Calendar and PHEV cycle life aging of high-energy, lithium-ion cells containing blended spinel and layered-oxide cathodes. *J. Power Sources* **196**, 10213–10221 (2011). doi: [10.1016/j.jpowsour.2011.08.067](https://doi.org/10.1016/j.jpowsour.2011.08.067)
35. A. H. Smith, H. M. Dahn, J. C. Burns, J. R. Dahn, Long-term low-rate cycling of $\text{LiCoO}_2/\text{graphite}$ Li-ion cells at 55°C. *J. Electrochem. Soc.* **159**, A705 (2012). doi: [10.1149/2.056206jes](https://doi.org/10.1149/2.056206jes)
36. Q. Wang *et al.*, Thermal runaway caused fire and explosion of lithium ion battery. *J. Power Sources* **208**, 210–224 (2012). doi: [10.1016/j.jpowsour.2012.02.038](https://doi.org/10.1016/j.jpowsour.2012.02.038)
37. P. E. Roth, C. J. Orendorff, How electrolytes influence battery safety. *Electrochem. Soc. Interface* **21**, 45–49 (2012).
38. S. S. Zhang, A review on electrolyte additives for lithium-ion batteries. *J. Power Sources* **162**, 1379–1394 (2006). doi: [10.1016/j.jpowsour.2006.07.074](https://doi.org/10.1016/j.jpowsour.2006.07.074)
39. S. Bourlot, P. Blanchard, S. Robert, Investigation of aging mechanisms of high power Li-ion cells used for hybrid electric vehicles. *J. Power Sources* **196**, 6841–6846 (2011). doi: [10.1016/j.jpowsour.2010.09.103](https://doi.org/10.1016/j.jpowsour.2010.09.103)
40. M. Dubarry *et al.*, Identifying battery aging mechanisms in large format Li ion cells. *J. Power Sources* **196**, 3420–3425 (2011). doi: [10.1016/j.jpowsour.2010.07.029](https://doi.org/10.1016/j.jpowsour.2010.07.029)
41. J. Wang *et al.*, Degradation of lithium ion batteries employing graphite negatives and nickel–cobalt–manganese oxide + spinel manganese oxide positives: Part 1, aging mechanisms and life estimation. *J. Power Sources* **269**, 937–948 (2014). doi: [10.1016/j.jpowsour.2014.07.030](https://doi.org/10.1016/j.jpowsour.2014.07.030)
42. L. Lu, X. Han, J. Li, J. Hua, M. Ouyang, A review on the key issues for lithium-ion battery management in electric vehicles. *J. Power Sources* **226**, 272–288 (2013). doi: [10.1016/j.jpowsour.2012.10.060](https://doi.org/10.1016/j.jpowsour.2012.10.060)
43. M. Dubarry, C. Truchot, B. Y. Liaw, Synthesize battery degradation modes via a diagnostic and prognostic model. *J. Power Sources* **219**, 204–216 (2012). doi: [10.1016/j.jpowsour.2012.07.016](https://doi.org/10.1016/j.jpowsour.2012.07.016)
44. M. Dubarry, C. Truchot, B. Y. Liaw, Cell degradation in commercial LiFePO_4 cells with high-power and high-energy designs. *J. Power Sources* **258**, 408–419 (2014). doi: [10.1016/j.jpowsour.2014.02.052](https://doi.org/10.1016/j.jpowsour.2014.02.052)
45. I. Bloom *et al.*, Differential voltage analyses of high-power, lithium-ion cells: 1. Technique and application. *J. Power Sources* **139**, 295–303 (2005). doi: [10.1016/j.jpowsour.2004.07.021](https://doi.org/10.1016/j.jpowsour.2004.07.021)
46. H. M. Dahn, A. J. Smith, J. C. Burns, D. A. Stevens, J. R. Dahn, User-friendly differential voltage analysis freeware for the analysis of degradation mechanisms in Li-ion batteries. *J. Electrochem. Soc.* **159**, A1405–A1409 (2012). doi: [10.1149/2.013209jes](https://doi.org/10.1149/2.013209jes)
47. K. Honkura, T. Horiba, Study of the deterioration mechanism of $\text{LiCoO}_2/\text{graphite}$ cells in charge/discharge cycles using the discharge curve analysis. *J. Power Sources* **264**, 140–146 (2014). doi: [10.1016/j.jpowsour.2014.04.036](https://doi.org/10.1016/j.jpowsour.2014.04.036)
48. J. C. Burns *et al.*, Predicting and extending the lifetime of Li-ion batteries. *J. Electrochem. Soc.* **160**, A1451–A1456 (2013). doi: [10.1149/2.060309jes](https://doi.org/10.1149/2.060309jes)
49. L. J. Krause, L. D. Jensen, J. R. Dahn, Measurement of parasitic reactions in Li ion cells by electrochemical calorimetry. *J. Electrochem. Soc.* **159**, A937–A943 (2012). doi: [10.1149/2.021207jes](https://doi.org/10.1149/2.021207jes)
50. P. Novák *et al.*, Advanced in situ methods for the characterization of practical electrodes. *J. Power Sources* **90**, 52–58 (2000). doi: [10.1016/S0378-7753\(00\)00447-X](https://doi.org/10.1016/S0378-7753(00)00447-X)
51. S. Brown, N. Melgren, M. Vynnycky, G. Lindbergh, Impedance as a tool for investigating aging in lithium-ion porous electrodes: II. Positive electrode examination. *J. Electrochem. Soc.* **155**, A320 (2008). doi: [10.1149/1.2832654](https://doi.org/10.1149/1.2832654)
52. J. Shim, R. Kostecky, T. Richardson, X. Song, K. A. Striebel, Electrochemical analysis for cycle performance and capacity fading of a lithium-ion battery cycled at elevated temperature. *J. Power Sources* **112**, 222–230 (2002). doi: [10.1016/S0378-7753\(02\)00363-4](https://doi.org/10.1016/S0378-7753(02)00363-4)
53. L. Bodenes *et al.*, Lithium secondary batteries working at very high temperature: Capacity fade and understanding of aging mechanisms. *J. Power Sources* **236**, 265–275 (2013). doi: [10.1016/j.jpowsour.2013.02.067](https://doi.org/10.1016/j.jpowsour.2013.02.067)
54. Y. Kobayashi *et al.*, Decrease in capacity in Mn-based/graphite commercial lithium-ion batteries: II. Nondestructive analysis by precise temperature measurement. *J. Electrochem. Soc.* **160**, A1415–A1420 (2013). doi: [10.1149/2.053309jes](https://doi.org/10.1149/2.053309jes)
55. T. Waldmann *et al.*, A mechanical aging mechanism in lithium-ion batteries. *J. Electrochem. Soc.* **161**, A1742–A1747 (2014). doi: [10.1149/2.1001410jes](https://doi.org/10.1149/2.1001410jes)
56. B. Stiaszny *et al.*, Electrochemical characterization and post-mortem analysis of aged $\text{LiMn}_2\text{O}_4/\text{NMC}/\text{graphite}$ lithium ion batteries part II: Calendar aging. *J. Power Sources* **258**, 61–75 (2014). doi: [10.1016/j.jpowsour.2014.02.019](https://doi.org/10.1016/j.jpowsour.2014.02.019)
57. B. C. Melot, J. M. Tarascon, Design and preparation of materials for advanced electrochemical storage. *Acc. Chem. Res.* **46**, 1226–1238 (2013). doi: [10.1021/ar300088q](https://doi.org/10.1021/ar300088q); pmid: [23282038](https://pubmed.ncbi.nlm.nih.gov/23282038/)

ACKNOWLEDGMENTS

We thank ALISTORE-ERI academic and industrial members for sharing fruitful discussions; P. Bernard and P. Johansson for valuable comments and critical reading of the text; and Ministerio de Ciencia e Innovación (Spain) grant MAT2014-53500-R (M.R.P.).

10.1126/science.1253292

RESEARCH ARTICLE

STEM CELLS

Hair follicle aging is driven by transepidermal elimination of stem cells via COL17A1 proteolysis

Hiroyuki Matsumura,^{1*} Yasuaki Mohri,^{1*} Nguyen Thanh Binh,^{1,2*} Hironobu Morinaga,¹ Makoto Fukuda,¹ Mayumi Ito,³ Sotaro Kurata,⁴ Jan Hoeijmakers,⁵ Emi K. Nishimura^{1†}

Hair thinning and loss are prominent aging phenotypes but have an unknown mechanism. We show that hair follicle stem cell (HFSC) aging causes the stepwise miniaturization of hair follicles and eventual hair loss in wild-type mice and in humans. In vivo fate analysis of HFSCs revealed that the DNA damage response in HFSCs causes proteolysis of type XVII collagen (COL17A1/BP180), a critical molecule for HFSC maintenance, to trigger HFSC aging, characterized by the loss of stemness signatures and by epidermal commitment. Aged HFSCs are cyclically eliminated from the skin through terminal epidermal differentiation, thereby causing hair follicle miniaturization. The aging process can be recapitulated by *Col17a1* deficiency and prevented by the forced maintenance of COL17A1 in HFSCs, demonstrating that COL17A1 in HFSCs orchestrates the stem cell-centric aging program of the epithelial mini-organ.

Tissues and organs undergo structural and functional declines due to aging (1). Many different hypotheses have been proposed to explain tissue aging as well as organism aging (2–7). Genes involved in aging phenotypes and/or organism longevity have been reported (8–11), yet the exact mechanism(s) underlying tissue aging is poorly understood.

Accumulation of DNA damage has been implicated in tissue aging (12, 13). Replication errors, reactive oxygen species, eroded telomeres, and chromosome breaks represent sources of endogenous DNA damage. Typical aging phenotypes, including hair loss and graying, are accelerated by intrinsic genomic instability in individuals with premature aging syndromes (progeroid syndromes) and their mouse models (14–16), as well as by extrinsic genomic instability such as by ionizing radiation (IR) (17, 18). Tissue decline due to genomic instability has been explained by cellular senescence or apoptosis (14, 19, 20). However, typical senescent cells are not readily induced in tissues simply with genomic instability (18), but appear in premalignant lesions such as carcinogen-induced papilloma and melanocytic nevi in the skin (21, 22). Aging-associated changes in stem

cells (stem cell aging) are currently recognized as one of the hallmarks of aging (7); however, the fates of those aged stem cells in aging tissues, the impact of DNA damage in their fate, and the roles of stem cell aging in the tissue and organ aging process are still largely unknown.

Hair follicle stem cells (HFSCs), which reside in the bulge/sub-bulge area of the hair follicle (HF), sustain cyclic hair regrowth over repeated hair cycles (23–26) (fig. S1A). It has been reported that mouse HFSCs generally do not display apparent decline (27), but with aging, hair cycle waves slow down and display imbalanced cytokine signaling in HFSCs, as well as diminished colony-forming capability in vitro (28–30). On the other hand, mammals that live longer lose their hair and HFs with age (31, 32). In this article, we describe the stepwise dynamics of mini-organ aging of HFs and provide mechanistic links from DNA damage and stem cell aging to eventual hair loss phenotype, with evidence for the existence of a tissue and organ aging program.

Aging-associated thinning hair and hair loss

The HF is a mini-organ of the skin that is specialized to grow hair (fig. S1A). To understand aging-associated hair loss in genetically defined mammals, we studied HF aging in wild-type mice. Aged C57BL/6 mice show diffuse and symmetric patterns of hair thinning on the back (Fig. 1A) that typically become apparent on the dorsal-most area of the neck and the trunk, with formation of a patchy or linear hair loss pattern and distal spreading toward the flanks (Fig. 1B). Hair thinning in C57BL/6N mice is sometimes apparent as early as 16 months after birth, but usually appears at around 18 months of age and becomes

conspicuous by 24 to 28 months. Those mice show a more advanced phenotype after hair depilation (18 to 31 months; $n = 6$ mice) (fig. S1B), indicating that cyclic hair regeneration accelerates HF aging. Notably, the areas with greatest hair loss never grow hair even with hair cycle inducers (fig. S1C), indicating that they have lost hair cycle waves. Histological analysis of the skin revealed a significant decrease of HF numbers later than 12 months of age (Fig. 1, C and D) and the miniaturization of HFs with reduction of dermal thickness (Fig. 1, C to G, and fig. S1D). We classified the chronological HF changes typically seen in affected skin areas into five different stages, judging from the level of HF miniaturization (proportional shortening of the permanent portion) and the presence or absence of dermal papillae, sebaceous glands, and the infundibulum (Fig. 1, E and F, and fig. S1E). Cyst formation was also found occasionally in the bulge/sub-bulge area of HFs, often with the loss of dermal papillae (fig. S1F). More advanced stages of HFs were found in older mice (Fig. 1G) more frequently on the dorsal-most areas with advanced hair thinning (Fig. 1, A to C, and fig. S1C). Thus, we concluded that HF aging proceeds progressively in a stepwise manner with distal advancement once homeostatic maintenance starts failing.

Stem cell dysregulation precedes HF miniaturization

To gain insight into the homeostatic machinery regulating HF aging, we hypothesized that changes in HFSCs, which generate all kinds of HF keratinocytes (23, 24, 33), may underlie the aging-associated structural and functional decline of the mini-organ. We examined the expression of HFSC markers, including CD34, S100A6 (34, 35), and keratin 15 (Krt1-15/K15) (33), using immunohistochemistry. Whereas bulge cells in young HFs expressed those markers, they were reduced in number in aged HFs (Fig. 1H and fig. S2A). This was prominently seen in areas of hair thinning and loss (HL), where HFs showed variable levels of miniaturization with reduced numbers of HFs, but were more sparse in the surrounding less-affected hairy (H) areas (Fig. 1, C and H, and fig. S2, A to F). Next, we tested the expression of key genes involved in HFSC maintenance, including LHX2, SOX9, and COL17A1 (36–39). Analysis of the signal intensity and expression-positive cell number showed that those molecules are often decreased or even undetectable in stage I and II HFs of aged mice (24 to 26 months) (Fig. 1, I to K, and fig. S2G), indicating that the down-regulation of HFSC signature molecules precedes HF miniaturization and hair loss during physiological aging. Interestingly, the distribution of the reduced level of COL17A1 was restricted to the basement membrane zone or was undetectable in those HFs (Fig. 1I). Further histological analysis of the HF aging process indicated that individual HF components are well maintained in early stage HFs, even with some reduction of HFSC marker expression, but are diminished in a stepwise, regular, and proportional manner once HFs initiate the miniaturization process with the reduction of mesenchymal

¹Department of Stem Cell Biology, Medical Research Institute, Tokyo Medical and Dental University, 1-5-45 Yushima, Bunkyo-ku, Tokyo, 113-8510, Japan. ²Department of Stem Cell Medicine, Cancer Research Institute, Kanazawa University, Kanazawa, Ishikawa 920-0934, Japan.

³Departments of Dermatology and Cell Biology, New York University School of Medicine, New York, NY, USA. ⁴Beppu Garden-Hill Clinic, Kurata Clinic, Beppu city, Oita 8740831, Japan. ⁵Department of Genetics, Cancer Genomics Center, Erasmus MC, Room Ee 722, Dr. Wytemaweg 80, 3015 CN Rotterdam, Netherlands.

*These authors contributed equally to this work. †Corresponding author. E-mail: nishscm@tmd.ac.jp

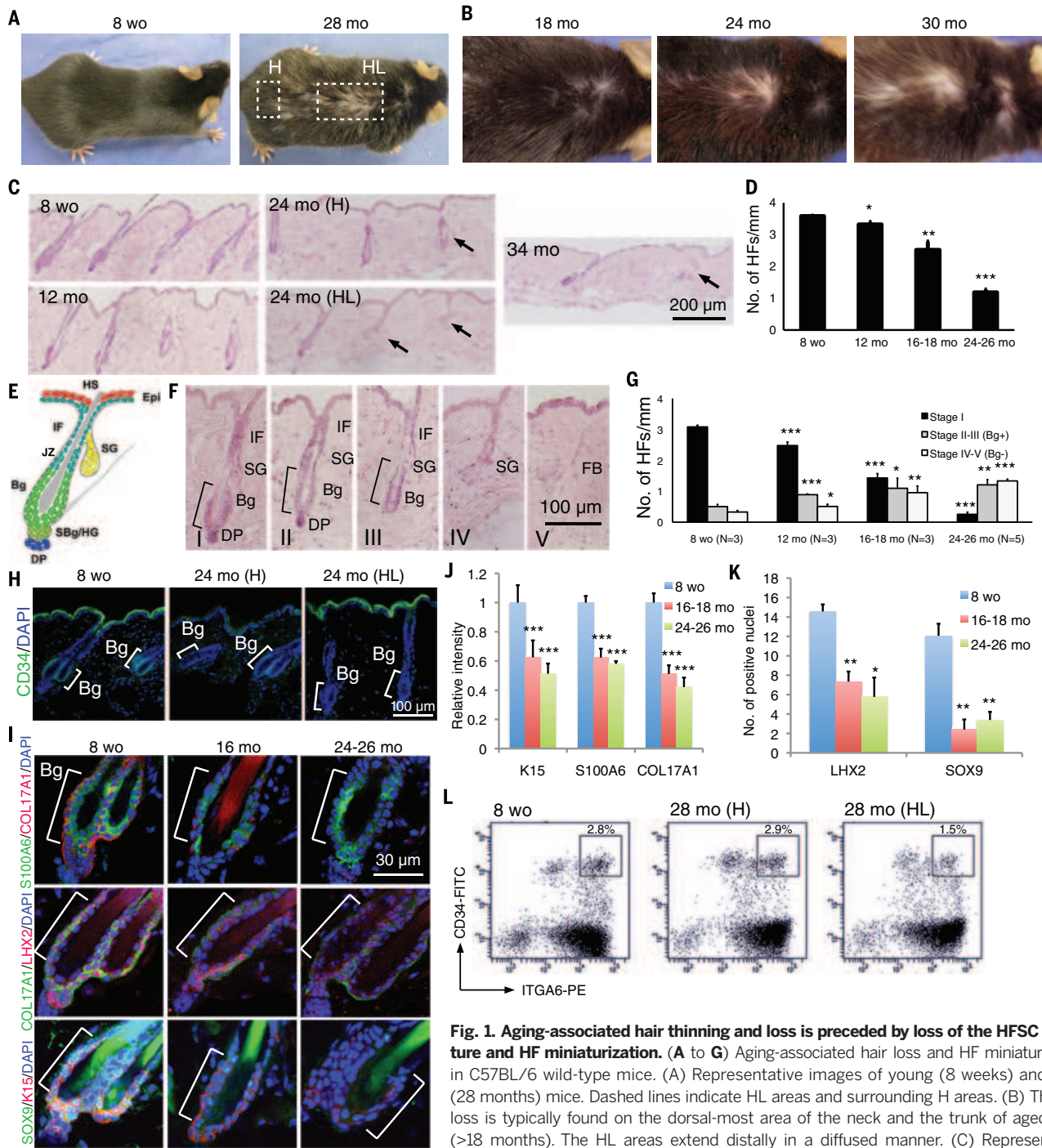


Fig. 1. Aging-associated hair thinning and loss is preceded by loss of the HFSC signature and HF miniaturization.

(A to G) Aging-associated hair loss and HF miniaturization in C57BL/6 wild-type mice. (A) Representative images of young (8 weeks) and aged (28 months) mice. Dashed lines indicate HL areas and surrounding H areas. (B) The hair loss is typically found on the dorsal-most area of the neck and the trunk of aged mice (>18 months). The HL areas extend distally in a diffused manner. (C) Representative histology of the dorsal skin from young (8 weeks), middle-aged (12 months) and aged

(24 and 34 months) wild-type mice by hematoxylin and eosin (H&E) stain. The miniaturized HF are indicated by arrows. (D) HF number per mm. (E) Simplified schematic of the HF structure at telogen phase. HS, hair shaft; IF, infundibulum; SG, sebaceous gland; JZ, junctional zone; Bg, bulge; SBg/HG, sub-bulge/hair germ; DP, dermal papilla. (F) Staging of chronological HF aging. Representative histological images at different HF stages are shown. Stage I, HF with standard structure and size; Stage II, shortened (miniaturized) HF with proportional size and structure, including DP and Bg; Stage III, miniaturized HF with complete loss of the DP; Stage IV, miniaturized HF retaining sebaceous glands (SG) with loss of HF bulge (Bg) and hair shaft; Stage V, complete disappearance of HF, occasionally with mild fibrosis (FB). (G) Number of each HF stage per mm; >100 HF from multiple samples were examined for each group. (H to K) Reduction of HFSC markers with chronological aging in mice. (H) Immunofluorescence (IF) images with the HFSC marker CD34 at 8 weeks and at 24 months of HL and H areas. (I) IF images of Stage I HF at 8 weeks, 16 months, and 24 to 26 months for COL17A1, LHX2, and SOX9. (J) Quantitative analysis of fluorescence intensity of COL17A1, K15, and S100A6 in bulge areas of 8-week-old, 16- to 18-month-old, and 24- to 25-month-old mice; several HF (>5) at Stage I and II from each group were examined. *N* = 3 mice for each group. (K) Quantitative analysis of the number of LHX2⁺ and SOX9⁺ nuclei in bulge cells of 8-week-old, 16-month-old, and 24-month-old mice. (L) FACS analyses of the CD34^{high}ITGA6^{high}SCA-1⁻ fraction to detect HFSCs in young (8 weeks) and in aged (28 months) mouse skin. Although 28-month-old hairy skin maintains the HFSC fraction similarly to 8-week-old mouse skin, 28-month-old HL areas show a significant reduction of the CD34^{high}ITGA6^{high}SCA-1⁻ fraction. Error bars, mean ± SEM; **P* < 0.05; ***P* < 0.01; ****P* < 0.001 (Student's *t* test).

cells, including dermal papilla cells (fig. S2, B to F). Furthermore, fluorescence-activated cell sorting (FACS) analysis of the HFSC fraction ($CD34^{high}ITGA6^{high}$) (40) showed that the cellular ratio is apparently diminished in HL areas but not in H areas, where reduction of CD34-expressing cells was already detectable in tissue sections (Fig. 1L and fig. S2A, H, and I). Taken together, these data demonstrate that aging-associated hair loss and the underlying HF miniaturization and loss are preceded by the dysregulation in HFSCs characterized by their loss of HFSC signatures during physiological aging.

Epidermal differentiation of HFSCs drives HF miniaturization

To characterize the mechanism(s) of the aging-associated HFSC dysregulation and depletion, we examined the expression of different cell fate markers, including those for cell death and cellular senescence, in aging tissues. However, we did not detect any significant increase in markers for apoptosis or cellular senescence (fig. S3), indicating that cell death and cellular senescence are not likely to be the major fate of HFSCs during HF aging. Next, to investigate the possibility that aged HFSCs may leave the niche and change their fate, we traced the fate of HFSCs during physiological aging using *K15-CrePR;CAG-CAT-EGFP* mice (Fig. 2). We treated those mice with RU486 at 7 weeks of age to genetically tag HFSC-derived cells with green fluorescent protein (GFP) and then analyzed the fate of HFSC-derived cells during the process of hair cycle progression (Fig. 2A). In young mice, GFP⁺ cells, which are originally localized in the bulge area of resting HFs, formed the lower permanent portion to grow each hair during hair cycle progression. In contrast, in presenile mice as early as 16 months, they became distributed in the junctional zone (JZ) located above the bulge area, then in the suprabasal epidermis, and eventually on the skin surface (Fig. 2B). This indicates that aged HFSC-derived progeny migrate up toward the skin surface through the JZ and the epidermis without renewing themselves in the niche upon induction of a hair cycle. Interestingly, those HFSC-derived GFP⁺ cells ectopically express the epidermal differentiation markers keratin 1 (Krt1/K1) and its partner keratin 10 (Krt10/K10), both of which are normally expressed by suprabasal cells in the interfollicular epidermis (IFE), even in the niche (Fig. 2, B and C, and fig. S4, A and B). They also expressed other epidermal differentiation markers, including involucrin, ectopically in the JZ, where they coexpressed the JZ keratinocyte marker LRIG1 (Fig. 2, D and E). Those cells are often connected to each other showing a string-like distribution mostly within the suprabasal layer of the JZ and in the epidermis. This indicates that aged HFSCs that committed to epidermal terminal differentiation concomitantly leave the niche to collectively migrate to the suprabasal layer of the epidermis upon their activation at anagen. A similar elimination of LacZ-tagged HFSCs from the niche was observed using *K15-CrePR; Rosa26R* mice at 16 months but not in young mice

(12 weeks) (Fig. 2F). HF differentiation markers, such as AE15, were not found in keratinocytes in the bulge area of aged HFs (fig. S4C). These data demonstrate that aged HFSCs have committed to epidermal terminal differentiation and keratinization to be eliminated from the stem cell pool and the skin (Fig. 2G).

To understand the mechanism of epidermal differentiation of HFSCs, we performed microarray gene expression profiling of the HFSC fraction ($CD34^{high}ITGA6^{high}$) of mouse dorsal skin containing either resting (telogen) or activated (anagen) HFs (tHFSCs or aHFSCs, respectively) from young (8 weeks) and from aged (24 to 25 months) mice (fig. S5). As shown in fig. S6, A and B, gene set enrichment analysis (GSEA) of the transcriptomes of young and aged HFSCs showed that the general stemness gene expression signature, which is maintained in young mice, is significantly abrogated in both tHFSCs and aHFSCs in aged mice. Analysis of mRNA expression of individual HFSC signature genes also showed some reduction in the tHFSC fraction (fig. S6C). Then we compared the transcriptome data of young and aged HFSCs in activated HFs with those from the IFE by hierarchical clustering. The heat map shows that aHFSCs from aged mice show significant similarity to the IFE (fig. S6D). Gene Ontology (GO) analysis of the transcriptome also revealed that aged aHFSCs show significant induction of genes related to epidermal keratinocyte differentiation (Fig. 2, H and I). Microarray, quantitative reverse transcription polymerase chain reaction (QPCR), and immunohistochemical analysis all showed that NOTCH1 (41, 42) and c-MYC, key factors for epidermal differentiation (43), are induced in aged HFSCs at anagen phase (Fig. 2J and figs. S6E and S7). Moreover, down-regulation of *Fbxw7*, which encodes a ubiquitin ligase for c-MYC and NOTCH1 (44, 45), was also found in aged HFSCs (Fig. 2J and fig. S6E). As overexpression of c-MYC or NOTCH1 intracellular domain (NICD) in basal keratinocytes of mice induces the epidermal differentiation of stem cells and their eventual depletion (41, 42) and *Fbxw7* deficiency in mice induces keratinocyte differentiation (45), the excessive induction of c-MYC and NOTCH1 in aged HFSCs is most likely to cause the epidermal differentiation of aged HFSCs upon their activation.

Sustained DDR in HFSCs by aging

To understand the underlying mechanism(s) for the commitment of aged HFSCs to epidermal differentiation, we performed GO analysis and GSEA for quiescent HFSCs in resting tHFSCs from young versus aged mice. This analysis revealed that genes involved in cellular stress responses, including DNA damage response (DDR), are enriched in aged HFSCs, whereas genes involved in DNA repair execution are conversely enriched in young HFSCs (Fig. 3, A to C). These data suggest that aged quiescent HFSCs are responding to accumulating DNA damage that has not been repaired. Indeed, comet assays, a method to evaluate DNA damages, of the sorted aged HFSCs in resting HFs show a significant comet tail moment indicative of DNA strand breaks (Fig. 3, D and E), demon-

strating that DNA damage accumulates in HFSCs during aging.

Because premature hair loss can be induced by exogenous genomic stress such as exposure to IR, as well as by endogenous genomic instability in progeroid syndromes (12, 15, 46–48), we first investigated whether HFSCs are responding to accumulating DNA damage in HFSCs and then whether the DDR mediates their epidermal commitment. We found that the formation of γ -H2AX foci (a marker of DDR representing sites of DNA strand breaks) was significantly increased in bulge/sub-bulge keratinocytes in resting HFs (telogen) from aged mice (Fig. 3, F and G, and fig. S8A) and was even greater in more advanced HL areas (fig. S8B). Because DDR is usually induced only transiently just after the induction of DNA damage, the sustained DDR in quiescent HFSCs is a notable event. Notably, the increased number of foci was found not only in K15⁺ cells but also in adjacent K15⁻ cells in the bulge and sub-bulge area (Fig. 3F), suggesting that quiescent HFSCs lose their stem cell signature after sustained DDR. Thus, the sustained DDR in HFSCs is likely to be an early sign of HFSC aging, which precedes the loss of the stem cell signature. Furthermore, we found that hair cycling induction itself is sufficient to induce abundant DNA damage foci formation in renewing HFSCs (fig. S8C), indicating that physiological hair cycling itself generates DNA damage in HFSCs. More DNA damage foci were found in remaining bulge keratinocytes in hair loss areas on the dorsal-most area compared with surrounding less-affected areas (fig. S8B), often with reduction of HFSC marker expression in those cells. These data suggest that the accumulation of unrepaired DNA damage in tHFSCs over anagen phase causes the HFSC-aging state that is characterized by their loss of the HFSC signature with sustained DDR and their epidermal commitment.

Wnt signaling drives hair cycle induction and maintenance (49), and the persistent activation causes DDR in HFSCs (50), whereas inactivation of Wnt signaling has been implicated in male-pattern baldness [androgenic alopecia (AGA)] (51). To investigate the possible involvement of Wnt signaling in HFSC aging, we performed GSEA for tHFSCs from young versus aged mice and found that Wnt signaling is less activated in aged tHFSCs than in young tHFSCs (fig. S9A), but it was not significant with aHFSCs as well as with immunostaining (fig. S9, B to D). Therefore, we concluded that HF aging is not simply explained by altered Wnt signaling, yet Wnt signaling is likely to indirectly mediate the accumulation of DNA damage via replicative stress in HFSCs.

Genomic instability accelerates HFSC aging

Because sustained DDR is found in quiescent HFSCs during aging, extrinsic genomic instability, such as that caused by IR, or by intrinsic instability by DNA-repair-deficient, progeroid mutations may cause similar changes in HFSCs. Indeed, the loss and reduction of HFSC signatures was induced

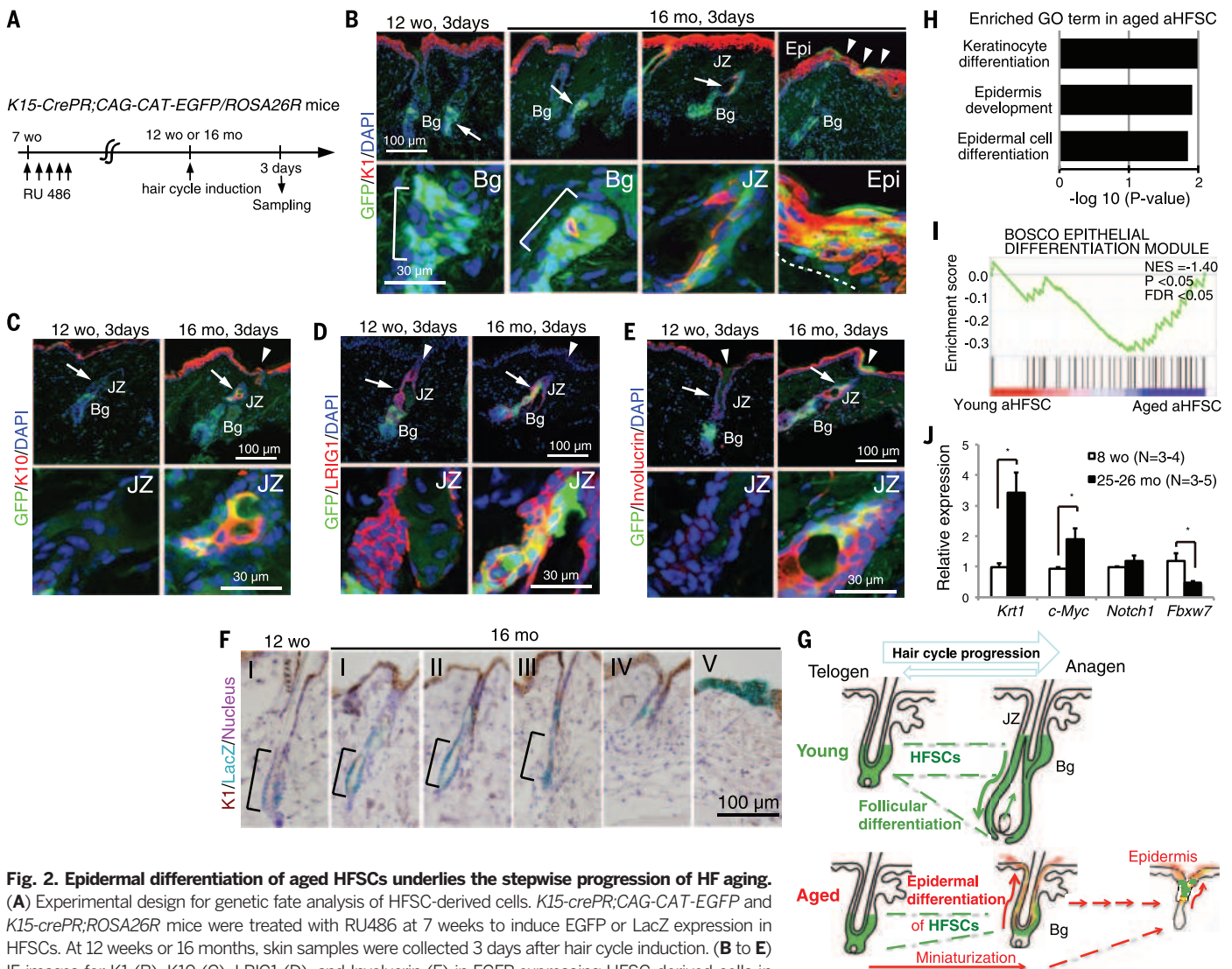


Fig. 2. Epidermal differentiation of aged HFSCs underlies the stepwise progression of HF aging. (A) Experimental design for genetic fate analysis of HFSC-derived cells. *K15-crePR;CAG-CAT-EGFP* and *K15-crePR;ROSA26R* mice were treated with RU486 at 7 weeks to induce EGFP or LacZ expression in HFSCs. At 12 weeks or 16 months, skin samples were collected 3 days after hair cycle induction. (B to E) IF images for K1 (B), K10 (C), LRIG1 (D), and Involucrin (E) in EGFP-expressing HFSC-derived cells in *K15-crePR;CAG-CAT-EGFP* after hair cycle induction. K1⁺/K10⁺/LRIG1⁺/Involucrin⁺ cells were induced at 16 months in the bulge or JZ of early anagen HFs (shown by arrows). In addition, some of these K1⁺ cells appeared in the epidermis (B). (F) Similar experiments were performed using *K15-crePR;ROSA26R* mice. IF images for K1 combined with LacZ staining revealed that HFSC-derived LacZ-tagged cells are distributed to the bulge (I to III), the JZ (IV to VI), and the epidermis (V) in the indicated HF stages, with the coexpression of K1. (G) Schematic for the fate of HFSC-derived cells. Young HFSCs contribute to follicular differentiation, whereas aged HFSCs contribute to epidermal differentiation, thereby causing HF miniaturization. (H) GO analysis between aged and young aHFSCs in ≥2-fold up-regulated genes. The GO terms for epidermal keratinocyte differentiation were significantly enriched in aged aHFSCs. (I) GSEA enrichment score curve of young versus aged aHFSCs with gene sets for epithelial differentiation. NES, normalized enrichment score. (J) Quantitative RT-PCR analysis of *K1*, *c-Myc*, *Notch1*, and *Fbxw7* mRNA expression in aHFSCs (CD34^{high}ITGA6^{high}SCA-1⁺ fraction) in aged (25- to 26-month-old) mice and in 8-week-old control mice; N = 3 to 5 mice for each group. Error bars, mean ± SEM; *P < 0.05 (Student's *t* test).

after exposure of the skin to 10-Gy (gray) irradiation (IR), which induces sustained DNA-damage foci formation in HFSCs, even in young mice (fig. S10). Genetic fate-tracing studies of HFSCs in irradiated mice (fig. S11A) showed that the expression of K1 was induced in HFSC-derived LacZ⁺/GFP⁺ keratinocytes in the permanent portion of HFs, including the bulge, isthmus JZ, and infundibulum within 1 week after hair cycle induction by 10-Gy IR (fig. S11, B and C). These data indicate that genomic stress is sufficient to induce the epidermal commitment of quiescent HFSCs. Furthermore, those K1⁺LacZ⁺ cells often showed a string-like distribution from the upper portion

of HFs to the overlying epidermis, including from the suprabasal to the uppermost layer, which is desquamated at 1 week or later (fig. S11, B and C). Furthermore, excessive expression of c-MYC and NOTCH1, key drivers of epidermal differentiation, were also induced in K15⁺ bulge keratinocytes in irradiated mice at 3 days after hair cycle induction (fig. S12). Coupled with the epidermal differentiation of HFSCs and their migration toward the epidermis, HF miniaturization was triggered (fig. S13, A to C). These data indicate that genomic stress causes HFSC dysregulation which closely mimics physiological the “HFSC aging state” characterized by sustained DDR in HFSCs,

loss of HFSC signatures, and their epidermal commitment.

We found a similar phenomenon with *XPD*^{TTD/TTD} mutant mice, a progeroid mouse model for human DNA repair syndrome trichothiodystrophy (TTD) (52, 53). Those mice also show a diffuse patterned hair loss that starts from the dorsal neck area (fig. S13D) and a reduction of HFs by HF miniaturization, thinning of the skin, and cyst formation in hair loss areas (fig. S13E), as was seen in aged mouse HFs. *XPD*^{TTD/TTD} mutant mice also show similar sustained formation of γ-H2AX foci and loss or reduction of HFSC signature expression (fig. S13F). These data demonstrate that HFSCs

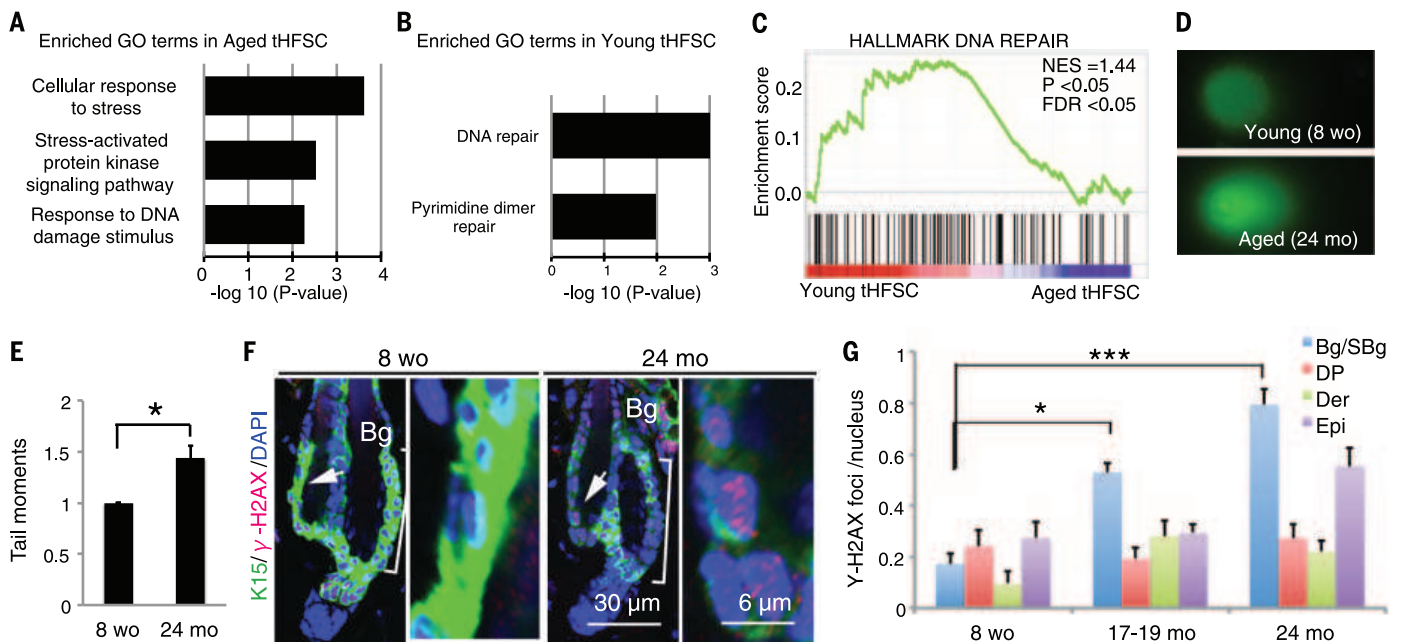


Fig. 3. Accumulation of DNA damage and sustained DDR in aged HFSCs.

(A and B) Enriched GO terms related to DNA damage in the ranked lists of genes significantly up-regulated or down-regulated (≥ 2 -fold) between aged and young tHFSCs. (C) GSEA enrichment score curve of DNA repair-related gene sets for young versus aged tHFSC illustrates efficient DNA repair in young tHFSCs. (D and E) Comet analysis of the HFSC ($CD34^{\text{high}}ITGA6^{\text{high}}SCA-1^{-}$) fraction from aged (24 months) and young (8 weeks) mice. (D) Representative tail moments stained with cyber green. (E) Frequency of tail moments in aged and young

HFSCs. (F) Representative IF images for γ -H2AX foci (red dots) in $K15^{+}$ HFSCs (green) located in the bulge/sub-bulge (Bg/SBg) area of telogen HF from young (8 weeks) and aged (24 months) wild-type mice. (G) The number of γ -H2AX foci per cell nucleus in 10- μm sections; $N = 2$ to 4 mice for each group. Error bars, mean \pm SEM. γ -H2AX foci were not significantly found in any cell population [dermal cells (Der), epidermal cells (Epi), or DP cells] in young (8-week-old) HFSCs but were found more frequently in $K15^{+}$ bulge/sub-bulge cells (Bg/SBg) of aged mouse skin. Error bars, mean \pm SEM; * $P < 0.05$; *** $P < 0.001$ (Student's t test).

with intrinsic or extrinsic genomic instability attain the HFSC aging state after sustained DDR. Importantly, the corresponding histological changes represented by HF miniaturization/loss and skin thinning by the $XPD^{\text{TTD}/\text{TTD}}$ mutation show similarities to those of physiological HF aging and associated skin changes as seen in aged wild-type mice (fig. S13, G and H), which indicates the existence of a common skin aging process or program.

COL17A1 proteolysis in HFSCs triggers HFSC aging

To understand the key mechanism for HFSC aging, we compared the gene expression profiles of quiescent HFSCs from aged mice with young mice. Genes that encode hemidesmosomal components, including *Col17a1*, were specifically reduced in aged tHFSCs, whereas genes that encode junctional components of desmosomes and adherens junctions were not affected (fig. S14, A and B). Because hemidesmosomal collagen COL17A1 (BP180/BPAG2), which we previously reported to be critical for HFSC maintenance (39), is anchored to Laminin332 (Laminin5) with their direct association with $\beta 4$ integrin (54) to stabilize the complex, we focused on the role of COL17A1 and its dysfunction in HFSCs. COL17A1 distribution was abundantly found on the whole-cell surface and the cytoplasm of young bulge keratinocytes, but there was a profound reduction of COL17A1, often with a fine linear distribution on the basement membrane zone, in a number of HFSCs by aging (Fig. 1I). A

similar pattern of COL17A1 distribution and accelerated loss was found in bulge keratinocytes of TTD progeroid mice as well (fig. S13I). These findings suggested the possibility that the nonhemidesmosomal COL17A1 in HFSCs is preferentially degraded by proteolysis during aging and is accelerated by genomic stress.

Because COL17A1 is known to be degraded or shed by induction of several different proteases, such as ADAM9, ADAM10, ADAM17 (55, 56), MMP9 (57), and ELANE/ELA2 (58), we searched for potentially responsible proteases that are induced in aged HFSCs as identified by the microarray data (fig. S14C). That analysis showed that *Elane*, which encodes neutrophil elastase/elastase 2 (59), known as a cellular toxic protease when aberrantly secreted, is ectopically induced within aged HFSCs but is undetectable in young HFSCs (Fig. 4A). Immunohistochemical analysis showed that ELANE, which is normally expressed in the nonbasal layer of the mouse epidermis but not in HFSCs, is conspicuously and aberrantly induced in the bulge area by aging (Fig. 4, A and B, and fig. S14D) in approximately 40% of HFSCs at 16 months and in 60% of HFSCs at 25 to 27 months. The aberrant induction of ELANE in HFSCs was also detectable in vivo 12 hours after genomic stress such as 10-Gy IR (Fig. 4C). It is notable that the exogenous genomic stress, which was sufficient to induce sustained DDR in HFSCs (fig. S10), also induces COL17A1 depletion, often with linear remnant distribution at the basement membrane zone in HFSCs, even in young mice (Fig. 4C). Reduced levels of COL17A1

and sustained expression of ELANE often show a reciprocal distribution in bulge keratinocytes, which suggests that ELANE directly degrades COL17A1 in vivo. Indeed, primary keratinocytes treated with ELANE showed that both the 180-kD COL17A1 and its shed form of the 120 kD ectodomain are quickly degraded by ELANE in vitro (Fig. 4D). That degradation is completely inhibited by the protease inhibitor $\alpha 1$ -antitrypsin (A1AT), suggesting that COL17A1 is efficiently proteolytically degraded by ELANE, which is induced within HFSCs in response to DNA damage. Some HFSCs restored the original distribution pattern and expression level of COL17A1 within a week after IR, whereas other refractory HFSCs with reduced COL17A1 expression in the bulge often showed a down-regulation of other key HFSC molecules (fig. S10E). This indicates that depletion of COL17A1 becomes stabilized in some HFSCs after the DDR-induced proteolysis of COL17A1 in HFSCs. Consistently, we found a statistically significant reduction or loss of COL17A1 in bulge keratinocytes with sustained foci formation of 53BP1 and γ -H2AX in aged mice (Fig. 4, E and F). Therefore, unrepaired DNA damage in HFSCs is most likely to cause the "HFSC aging state" characterized by their COL17A1 depletion with sustained DDR, their loss of stem cell signature, and their epidermal commitment upon their activation.

Our previous study showed that HFSCs in *Col17a1*-deficient mice show complete HFSC depletion after the loss of the HFSC signature in bulge cells as early as 7 to 8 weeks and show progressive hair thinning and graying (39). To

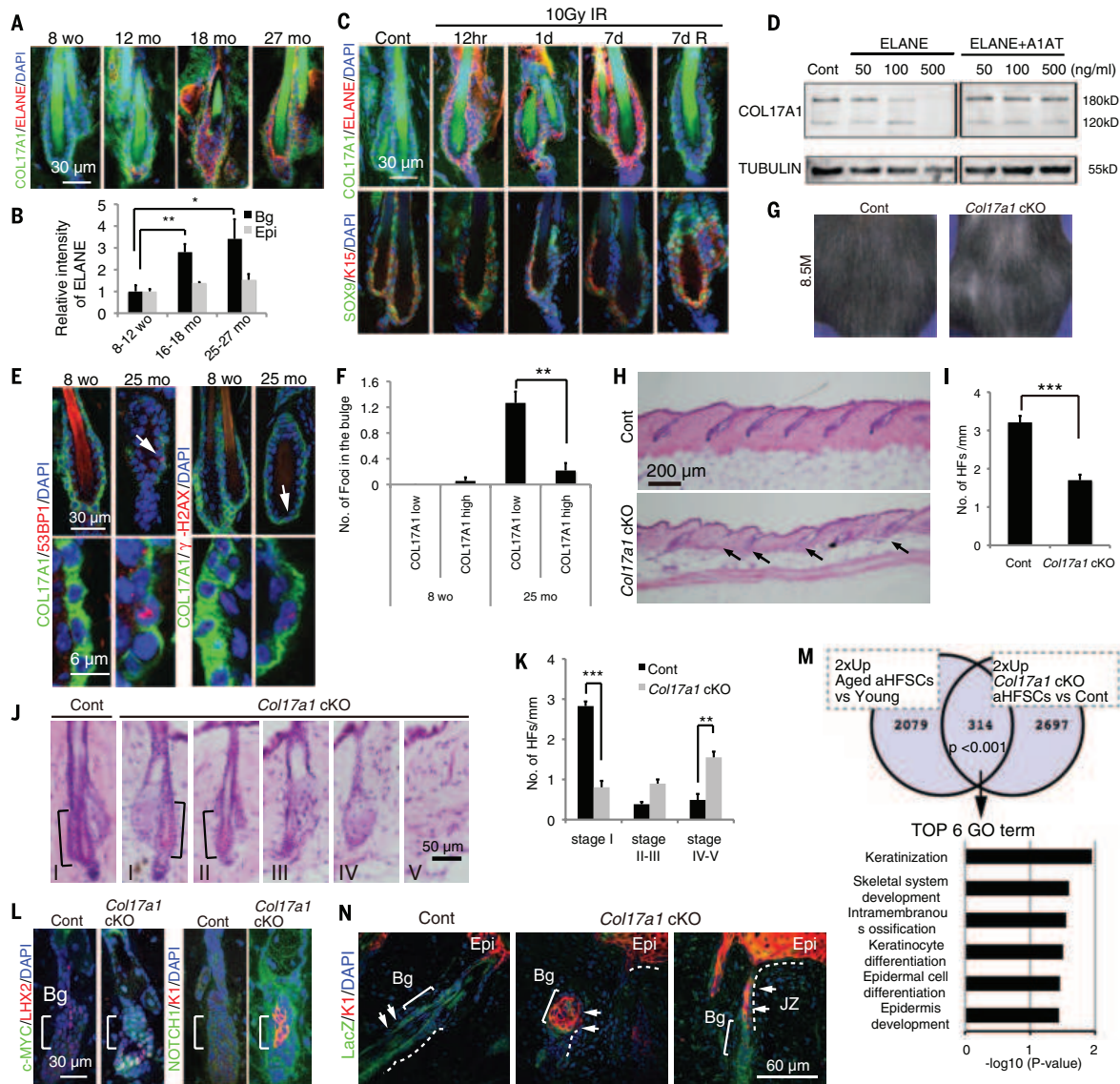


Fig. 4. DDR-induced proteolysis of COL17A1 in HFSCs induces dynamic HF miniaturization through their epidermal differentiation. (A to C) Aging- or DDR-induced COL17A1 proteolysis by ELANE. (A) IF images for COL17A1 and ELANE in the HF bulge of young (8-week-old), presenile (12 to 16-month-old), and aged (27-month-old) mice. (B) Quantitative analysis of fluorescence intensity of ELANE in the bulge (Bg) and in the basal epidermis (Epi) of 8- to 12-week-old, 16- to 18-month-old, and 25- to 27-month-old mice; several HF_s (>5) at stage I and II from each group were examined. *N* = 3 mice for each group. (C) IF images for COL17A1 and ELANE or SOX9 and keratin 15 (K15) in the HF bulge (8 weeks) at 12 hours, 1 day, and 7 days after 10-Gy irradiation. 7d indicates typical HF_s that have lost COL17A1 expression and other HFSC markers with ELANE induction, whereas 7d R indicates typical HF_s that have restored or maintained normal HFSC marker expression at 7 days after 10-Gy irradiation. (D) Dose-dependent proteolysis of COL17A1 by ELANE and its inhibition by A1AT in primary keratinocytes at 2 hours of treatment. (E) IF images of 53BP1 and γ -H2AX foci (red) in COL17A1⁺ bulge cells (green) from young (8-week-old) and from aged (25-month-old) wild-type mice. The foci were found in the COL17A1^{low} area as shown with arrows. (F) Number of 53BP1 foci in the COL17A1^{low} area and COL17A1^{high} area at 8 weeks or 25 months. 53BP1 foci were significantly found in the COL17A1^{low} area at 25 months. (G to M) Analysis of HFSC-specific *Col17a1*-deficient (*Col17a1* cKO) mice and control (Cont) mice after repeated depilation. (G) Hair coats on the backs of control (Cont) and *Col17a1* cKO mice at 8.5 months. Hair loss and graying was induced

in *Col17a1* cKO but not in control mice after depilation. (H) Histological images of Cont and *Col17a1* cKO mouse skin; miniaturization of HF_s found in a *Col17a1* cKO mouse (arrows). (I) HF number per mm of Cont (*N* = 3) and *Col17a1* cKO (*N* = 6) mice. (J) Stepwise HF miniaturization by *Col17a1* deficiency is morphologically similar to physiological HF aging; representative histological images are shown. (K) Number of HF_s at each HF stage per mm in Cont (*N* = 3) and in *Col17a1* cKO (*N* = 6) mice. *Col17a1* cKO mice show the premature increase of HF miniaturization. (L and M) Induction of epidermal differentiation concomitant with the up-regulation of c-MYC and NOTCH1 expression by *Col17a1* deficiency. (L) Immunostaining images for c-MYC and LHX2 or NOTCH1 and K1 in Cont and in *Col17a1* cKO mice at 12 weeks old after hair cycle induction. c-MYC expression was ectopically induced in the LHX2⁺ bulge area of *Col17a1* cKO mice. NOTCH1⁺K1⁺ cells were found in the upper bulge area of *Col17a1* cKO mice. (M) Venn diagram showing overlap between ≥ 2 -fold increased genes in aged versus young aHFSCs and ≥ 2 -fold increased genes in *Col17a1* cKO versus Cont aHFSCs. GO analysis for genes commonly up-regulated in aged aHFSCs and *Col17a1* cKO aHFSCs. The top GO terms enriched in the overlap are related to epidermal differentiation and to keratinization. (N) Genetic fate analysis of HFSC-derived cells in *Col17a1*-deficient mice with *K15-crePR* and *ROSA26R* alleles. Ectopic appearance of K1⁺LacZ⁺ HFSC-derived cells in the bulge at 7 days in the JZ and in the epidermis after hair cycle induction in *Col17a1* cKO mice (shown by arrows). Error bars, mean \pm SEM; **P* < 0.05; ***P* < 0.01; ****P* < 0.001 (Student's *t* test).

investigate whether the COL17A1 deficiency in HFSCs recapitulates the “HFSC aging state” and to determine the tissue outcome, we generated HFSC-specific *Col17a1*-deficient mice (*Col17a1* cKO) (fig. S15). We found that those mice also show thinning hair and graying hair (Fig. 4G). GSEA of tHFSCs revealed that the general stemness gene expression signature is abrogated upon *Col17a1* deficiency (fig. S16, A and B). The heat map for the global transcriptome of activated HFSC fractions (aHFSCs) revealed a significantly close relationship between *Col17a1* cKO HFSCs and aged HFSCs (fig. S16C). The aberrant induction of c-MYC and NOTCH1, as well as epidermal differentiation markers, was found in HFSCs upon their activation during hair cycle progression and eventual HF miniaturization and skin thinning (Fig. 4, H to L). Indeed, the most highly enriched GO terms in the overlap of up-regulated genes between *Col17a1*-deficient HFSCs versus control and aged HFSCs versus young HFSCs were epidermal differentiation and keratinization (Fig. 4M). Furthermore, the fate analysis of *Col17a1*-deficient HFSCs also showed that HFSC-derived cells coexpress KI in the bulge area and also in the upper JZ and the epidermis during hair cycle progression (Fig. 4N), similar to that seen during physiological aging and IR (Fig. 2, A to E, and fig. S11). It is also notable that HFSC aging directly or indirectly involves various surrounding cells to drive the stepwise HF miniaturization and skin thinning. These data collectively demonstrate that the COL17A1 deficiency in HFSCs recapitulates the “HFSC aging” state and drives the HF aging process.

COL17A1 rescues HFSC aging and HF miniaturization

To address whether age-associated depletion of COL17A1 is a key for induction of the “HFSC aging state” and associated HF aging processes, we analyzed COL17A1-overexpressing mice [*K14-hCOL17A1* transgenic (tg)] (60) and examined whether the forced maintenance of COL17A1 in HFSCs can rescue HFSC depletion and age-associated HF miniaturization or loss. Most of those mice showed significantly fewer miniaturized HF and an apparent retardation of hair loss even in mice surviving for 24 months ($N = 3$ mice) and 32 months ($N = 2$ mice) (Fig. 5, A to D). In contrast, all aged wild-type littermates showed HF miniaturization or loss, skin thinning, and age-associated hair loss. Consistently, the forced maintenance of COL17A1 significantly rescued the age-associated down-regulation of the HFSC signature (Fig. 5, E and F). These results demonstrate that the maintenance of COL17A1 is not only indispensable for HFSC maintenance but also effective for the protection of HFSCs against “HFSC aging” and resultant “HF aging” characterized by HF miniaturization, hair loss, and skin thinning.

Human HF miniaturization with COL17A1 depletion

To examine whether human HF also have a similar aging program that leads to senile alopecia, we analyzed the histology of healthy human scalp skin from the temporal areas of women at ages

ranging from 22 to 70 years old. We found that human female scalps from the aged group (55 to 70 years old) contain significantly more miniaturized HF (defined as HF measuring $<30 \mu\text{m}$ in diameter) compared with the younger group (35 to 45 years old) (Fig. 6, A and B, and fig. S17). To examine the changes of human HFSC signatures with aging, we performed a quantification analysis of the immunofluorescent intensities for human HFSC markers (61). We found that COL17A1, KI5, and CD200 expression is significantly decreased only in miniaturized HF but not in nonminiaturized HF, even in aged scalp skin (Fig. 6, C and D, and fig. S18). Furthermore, the size of the KI5⁺ bulge region is significantly decreased in miniaturized HF (Fig. 6E), and the number of DNA damage foci is significantly greater in bulge keratinocytes from middle-aged or aged female scalp skin compared with younger scalp skin (Fig. 6, F and G). Furthermore, KI5⁺ bulge cells that coexpress KI were also occasionally found in aged HF (Fig. 6H), indicating the defective renewal of HFSCs. Taken together, these data demonstrate the existence of human HFSC aging that is triggered by sustained DDR and the associated COL17A1 depletion and resultant progression of the HF aging process.

Mechanisms of mammalian HF aging

Tissues and organs generally become smaller and atrophic with aging (1). Our findings now provide evidence that an epithelial tissue aging program driven by “HFSC aging” exists and that this program is triggered by the proteolysis of COL17A1 in HFSCs and progressively advances in a stepwise manner with dynamic tissue architectural changes (Fig. 7). The stepwise dynamics have not been explained by previous stem cell aging theories (18, 62). It is notable that the “HFSC aging state” triggered by the DDR-induced deficiency of COL17A1 causes a cyclic progression of aging-associated HF changes (HF aging) characterized by HF miniaturization with profound involvement of many other types of surrounding cells in the skin and resultant hair loss. It is also notable that the aged mini-organ eventually disappears from the skin with retention of many other surrounding intact HF. The HF aging process was delayed or rescued by repressing HFSC aging with the forced maintenance of COL17A1 in HFSCs. These results demonstrate that stem cell aging is the keystone for induction of the tissue aging program that brings about thinning hair and underline that the stabilization of COL17A1 in HFSCs is critical and also effective to prevent HFSC aging and associated skin tissue changes.

Previous studies reported that the cellular ratio of the HFSC fraction (CD34^{high}ITGA6^{high}) is often paradoxically increased in aged mouse skin compared with young skin (27–29). This is probably because the aging skin contains HF at different HF stages and with a single bulge or multiple bulges (Figs. 1G and 7A). In any case, the complete depletion of HFSCs was apparent in more advanced skin areas of aged mice. Because the genetic background (31), gender, circadian rhythms (63), and even the housing environment

affect the onset of aging-associated baldness in wild-type mice, the combination of those factors (63) may determine the onset of HFSC aging.

Miniaturization of HF has long been believed to be a specific key phenomenon for male-pattern baldness [androgenic alopecia (AGA)] but not for HF aging (64). Our study revealed that mammalian HF do miniaturize during aging regardless of sex. Because HFSCs are maintained at least at the onset of AGA (65), AGA-associated HF miniaturization seen in the advanced stage of AGA may represent HF aging that progresses inevitably during repeated hair follicle cycles.

Finally, what is the physiological role of the aging program? Our previous study with melanocyte stem cells (18, 66) and other studies with hematopoietic stem cells (67) reported the existence of the “stemness checkpoint” that determines whether stem cells stay in an immature state or commit to differentiation to eliminate the damaged and stressed cells from the stem cell pool. Furthermore, the role of the checkpoint as a cancer barrier also has been proposed with leukemic stem cells (68). Similarly, the elimination of stressed and damaged HFSCs from the skin surface as shed corneocytes through their terminal epidermal differentiation may also be useful to maintain the high quality of HFSCs. Therefore, the active restoration of stem cell pools by use of residual intact stem cells before the irreversible advancement of tissue architectural changes may be essential for successful tissue regeneration and anti-aging in solid tissues such as the skin.

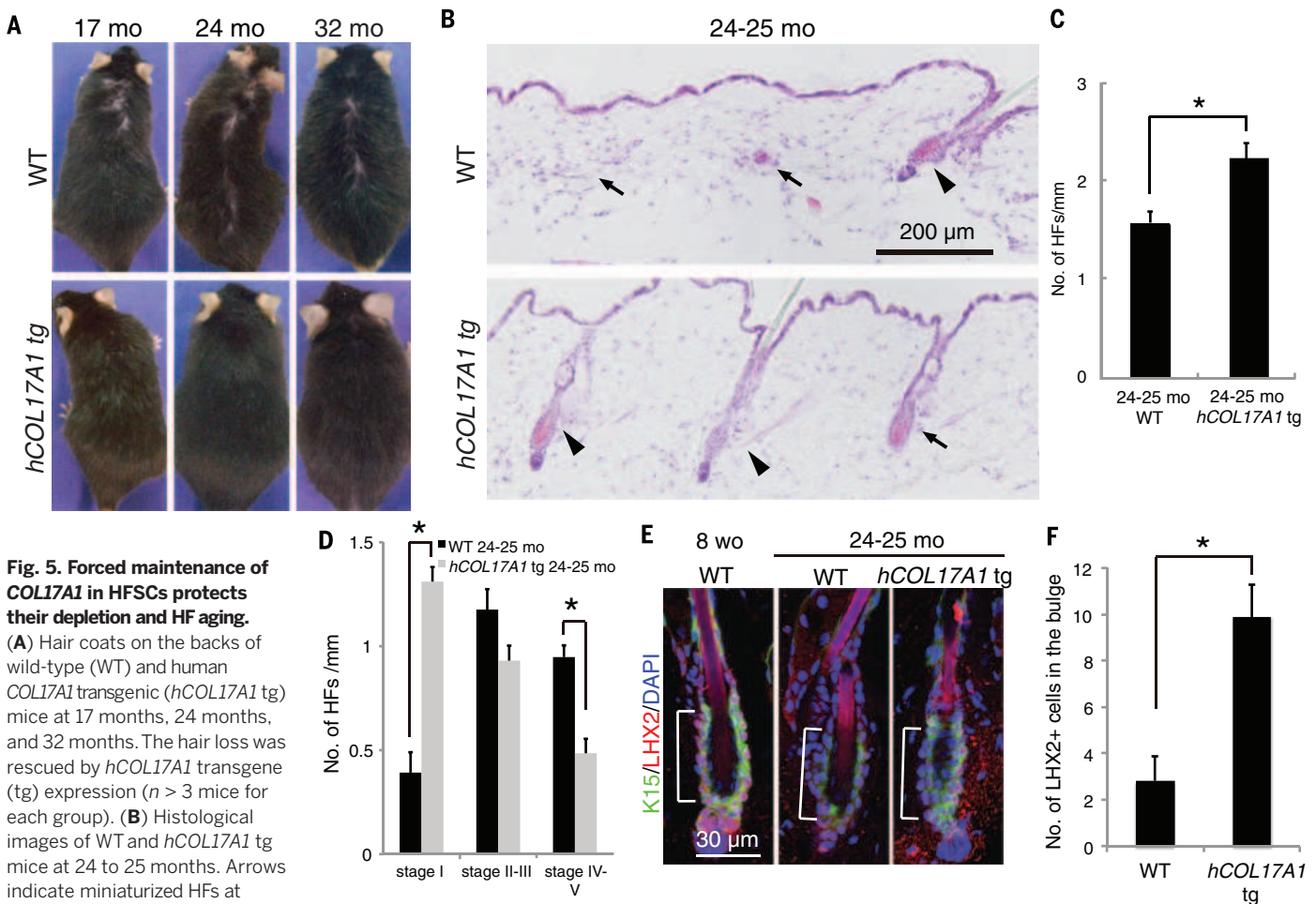
Materials and methods

Animals

C57BL/6N mice were purchased from Sankyo Lab Service (Tokyo, Japan) and from CLEA Japan (Tokyo, Japan). *XPD* mutant mice (52), *K15-CrePRL1* (69), *Rosa26R* mice (70, 71), *K14-CreERT2*, *CAG-CAT-EGFP*, and *Keratin14-human COL17A1* transgenic mice (72) have been described previously. For conditional knockout of the *Col17a1* gene in mice, *Col17a1* floxed mice whose exon2 is flanked by 2 loxP sequences were generated. All transgenic and mutant mice were backcrossed to *C57BL/6J* mice from Sankyo Lab Service. Mice with asymmetrical hair loss patches or whisker trimming were not used to exclude mice with excessive grooming. Animal care was in accordance with the guidance of Kanazawa University and the Tokyo Medical and Dental University for animal and recombinant DNA experiments. All animal experiments were performed following the Guidelines for the Care and Use of Laboratory Animals and were approved by the Institutional Committee of Laboratory Animals. Offspring were genotyped by PCR-based assays of mouse tail DNA.

Hair cycle induction by depilation or SAG (smoothed agonist) administration

For hair cycle induction, hair on the dorsal skin of 7- to 8-week old mice was manually depilated to induce a new hair cycle only after confirmation that the skin had a light pink color, which indicates that HF are synchronized at the telogen phase. For SAG treatment, the neck regions of



12-week-old and 19-month-old mice were shaved using an automatic hair shaver. Then, 100 μ l SAG (100 μ M) (Santa Cruz Biotechnology, Santa Cruz, CA, USA) was topically applied to the shaved area once a day for 5 days.

Ionizing irradiation and hair cycle induction

Mouse skin was irradiated with x-rays at 7 to 8 weeks of age only after confirmation that the skin had a light pink color, which indicates that HF are synchronized at the telogen phase. Irradiation was carried out by placing each mouse in a thin-walled plastic box. Low-pressure irradiation of mouse skin was performed using a Hitachi MBR-1520 (Hitachi Medical, Tokyo, Japan) operating at 50 kVp, 20 mA with a 2.0-mm Al filter (dose rate \approx 0.4 Gy/min) or a RX-650 machine (Faxitron X ray) operating at 100 kVp with a 2.0-mm Al filter (dose rate \approx 0.3 Gy/min).

ELANE (neutrophil elastase) and A1AT (alpha 1-antitrypsin) treatment in vitro

To test the proteolytic activity of ELANE against COL17A in primary keratinocytes (Kurabo, Osaka, Japan), primary keratinocytes were cultured for

24 hours in DermLife K Medium Complete Kit (Kurabo) containing human neutrophil elastase (ELANE) (50 to 500 ng/ml) (Millipore, Watford, UK) with or without A1AT (3.48 μ g/ml) (Athens Research and Technology, GA, USA).

Western blotting

Primary keratinocytes (Kurabo) and HaCaT cells were harvested, homogenized, and sonicated with TNE buffer (10 mM Tris-HCl, pH 7.5, 150 mM NaCl, and 1 mM EDTA) containing 1X Protease inhibitor tablet (Roche, Mannheim, Germany), 1X Phosphatase inhibitor tablet (Roche), and 1% NP-40. Protein concentrations were measured using a BCA Protein Assay Kit (Pierce, Rockford, IL). The whole-cell lysates were subjected to mini-protean-tgx-precast gel (Bio-Rad, Hercules, CA, USA) electrophoresis (0.02 mA/mini-gel) for 1 hour. Using semidry transfer, the proteins were transferred to polyvinylidene fluoride (PVDF) membranes for 1 hour at 0.25 mA/mini-gel using a Transblot SD (Bio-Rad). The membranes were then immersed in Blocking One (Nacalai) for 30 min and were then incubated overnight with each primary antibody diluted in Blocking One. Primary

antibodies used were mouse polyclonal antibody to human COL17A1 (Clone NC16A3, 1:100) and polyclonal antibody to α -tubulin (1:500) (all from Abcam, Cambridge, MA, USA). After washing three times for 5 min each with 1xTBST, the membranes were incubated for 2 hours with horseradish peroxidase (HRP) conjugated secondary antibodies diluted in Blocking One and washed three times for 5 min each with 1xTBST. After incubation with a Luminata Forte Western HRP Substrate detection system (Millipore) for a few minutes, immunoblot images were acquired using an LAS-3000 luminescence image analyzer (Fuji Photo film, Tokyo, Japan).

Preparation of paraffin and frozen sections

For paraffin sections, mouse skin or human scalp skin was fixed in 10% formalin solution at 4°C overnight and was then embedded in paraffin. Paraffin-embedded skin specimens were cut in 5- μ m-thick sections (Rotary Microtome HM325, MICROM International GmbH, Walldorf, Germany). For frozen sections, mouse skin or human scalp skin was immersed in ice-cold 4% paraformaldehyde (4% PFA) in phosphate-buffered saline (PBS) (pH 7.4) and then was irradiated in a 500-W microwave

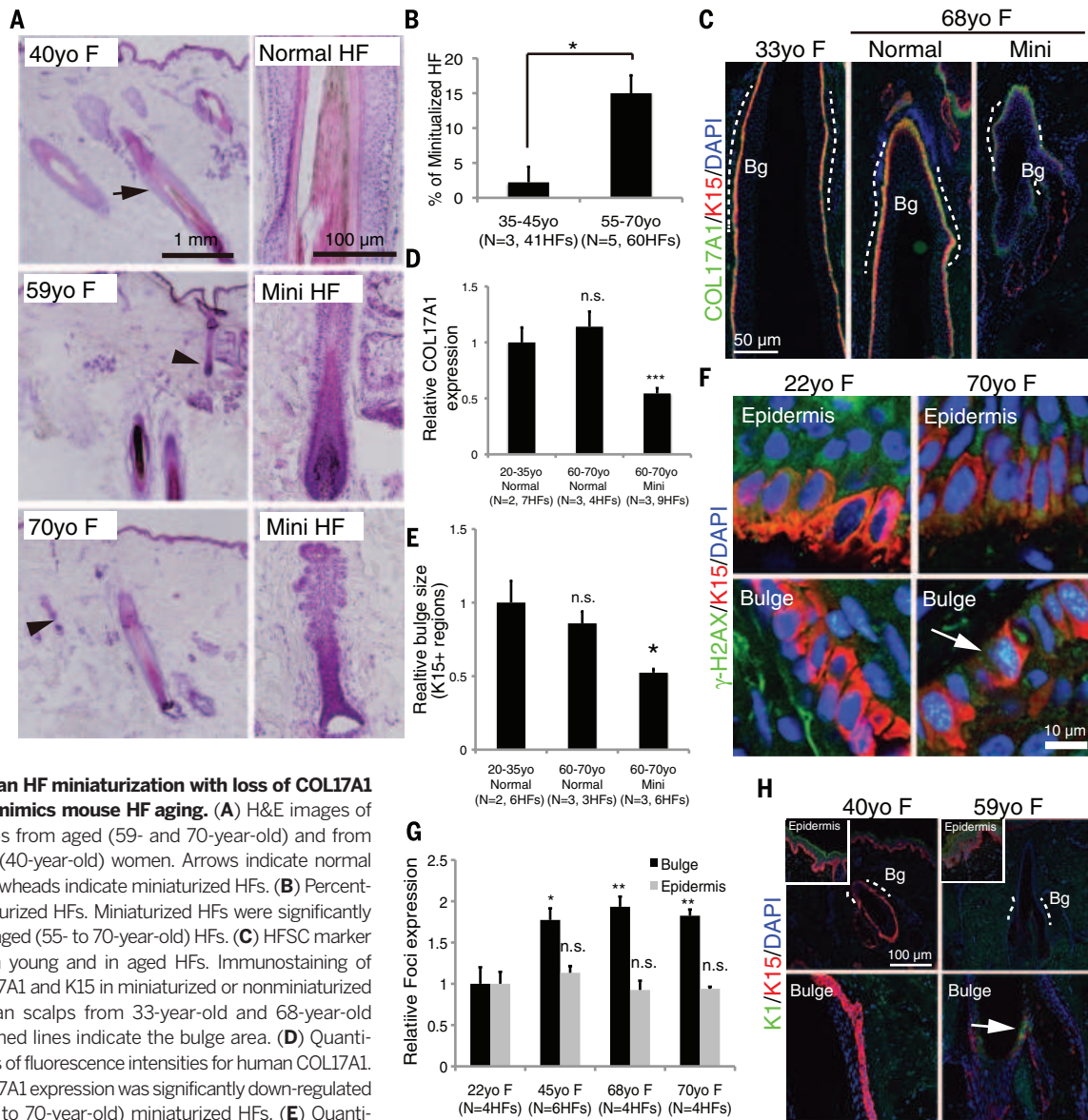


Fig. 6. Human HF miniaturization with loss of COL17A1 expression mimics mouse HF aging. (A) H&E images of human scalps from aged (59- and 70-year-old) and from middle-aged (40-year-old) women. Arrows indicate normal HFs, and arrowheads indicate miniaturized HFs. (B) Percentage of miniaturized HFs. Miniaturized HFs were significantly increased in aged (55- to 70-year-old) HFs. (C) HFSC marker expression in young and in aged HFs. Immunostaining of human COL17A1 and K15 in miniaturized or non-miniaturized HFs in human scalps from 33-year-old and 68-year-old women. Dashed lines indicate the bulge area. (D) Quantitative analysis of fluorescence intensities for human COL17A1. Human COL17A1 expression was significantly down-regulated in aged (60- to 70-year-old) miniaturized HFs. (E) Quantitative size analysis of K15⁺ bulge area. The bulge size is significantly diminished in aged (60- to 70-year-old) miniaturized HFs. (F) γ -H2AX foci formation in K15⁺ bulge keratinocytes and in K15⁺ IFE of human scalps at different ages. Immunostaining for γ -H2AX and Keratin 15 is shown. Arrow indicates γ -H2AX foci. (G) Quantitative analysis of γ -H2AX foci fluorescence intensity. The fluorescence level was significantly increased in aged (45- to 70-year-old) bulge areas but not in aged interfollicular epidermal basal cells. (H) Ectopic epidermal differentiation in the human bulge (Bg) area. Representative immunostaining for K1 (green) and K15 (red) are shown. K1 expression was induced in the 59-year-old scalp. All scalps were derived from temporal regions. Error bars, mean \pm SEM. n.s., no significant difference; * P < 0.05; ** P < 0.01; *** P < 0.001 (Student's t test). yo, years old.

oven for three 30-s cycles with intervals and then kept on ice for 20 min. The fixed skin samples were embedded in optimal cutting temperature (OCT) compound (Sakura Finetechnical Co. Ltd., Tokyo, Japan), snap-frozen in liquid nitrogen, and stored at -80°C . Frozen samples were cut in 10- μm -thick sections (Cryomicrotome CM 1850, Leica Microsystems Nussloch GmbH, Nussloch, Germany).

Hematoxylin and eosin (HE) staining

Paraffin sections were deparaffinized and then rehydrated. Frozen sections were removed from the OCT compound and then were stained with hematoxylin-eosin (Sakura Finetechnical Co. Ltd.)

for analysis of tissue histology using an optical microscope.

Assessment of HF changes by aging, genomic stress, XPD^{TTD/TTD} mutation, Col17a1 deficiency, and human COL17A1 overexpression

Five- μm -thick sections of murine skin were stained with HE. To properly assess skin sections that contain upright HFs, we chose sections that met the following criteria for further analysis. First, the section must include full-length cross sections of hair shafts in multiple HFs. Second, the section should not contain any exceptional pathological

changes, including skin wounding. More than three different skin areas from the indicated number of mice were analyzed.

Staging of chronological HF aging

We categorized telogen HFs of *C57BL/6N* mice at different ages into five different stages by following the HF structural changes during chronological aging, as described in the legend for Fig. 1. Briefly, at Stage I, HFs show a normal structure and size. At Stage II, HFs show a slight shortening with proportional size and structure. At Stage III, HFs are miniaturized with complete loss of the dermal papillae, with retention of the

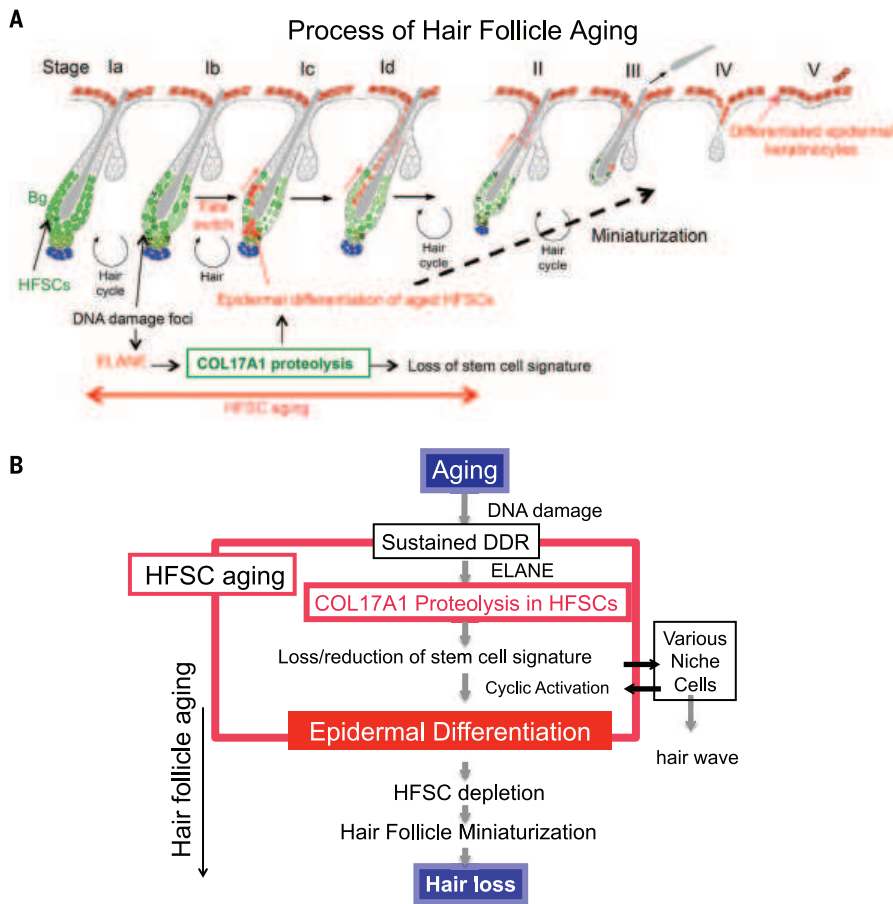


Fig. 7. Mechanisms for HFSC aging and execution of the HF-aging program. (A and B) Schematic for the mechanism of HF aging. The HFSC pool is maintained in a long quiescent state in the HF bulges (Bg) during aging (Stage Ia). HFSCs with sustained DDR undergo COL17A1 proteolysis through induction of ELANE protease (Stage Ib). Those COL17A1^{low/-} HFSCs lose their stem cell signature and commit to epidermal keratinocytes (Epi KC) in the niche. Those “aged” HFSCs migrate up toward the epidermis upon their cyclic activation through the JZ. They terminally differentiate into cornified keratinocytes to be eliminated from the skin surface, thereby causing the stepwise miniaturization of HFs and hair thinning and loss.

hair shaft. At Stage IV, HFs are miniaturized with retention of sebaceous glands and the infundibulum. At Stage V, HFs have completely disappeared with or without retention of different degrees of fibrosis in the dermis. This staging method tends to underestimate the structural changes of large HF types, including tylotrich follicles that grow guard hairs. Those follicles also miniaturize and become indistinguishable from other smaller HF types, including those growing short zigzag hairs (underfur) during aging. We thus categorized all HFs that are the same or larger than young (7- to 8-week-old) zigzag HFs with proportional HF structure and size as Stage I, although this underestimates the size changes of the large types of HFs that grow over hair.

Assessment of human HF miniaturization

HE images of 10- μ m skin sections of at least four randomized different areas in each sample were acquired using an upright BX51 microscope (Olympus, NY, USA). The percentage of miniaturized HFs

(defined as HFs measuring <30 μ m in diameter) in total HFs were counted (73).

Immunofluorescence staining

Frozen sections were used for immunofluorescence analysis. For c-Myc immunostaining, antigen retrieval was performed by boiling the slides for 20 min in Dako target retrieval solution (Dako, Carpinteria, CA, USA). Nonspecific staining was blocked by incubation with PBS containing 3% skim milk (Difco, Detroit, USA) for 30 min. Tissue sections were incubated with the primary antibody at 4°C overnight and were subsequently incubated with secondary antibodies conjugated with Alexa Fluor 488, 594, or 680 (Invitrogen, Hercules, CA, USA). After washing in PBS, 4',6-diamidino-2'-phenylindole dihydrochloride (DAPI) (Invitrogen-Molecular Probes, Eugene, OR, USA) was added for nuclear counterstaining. Coverslips were mounted onto glass slides with fluorescent mounting medium (Thermo Electron Corp., Waltham, MA, USA). All images were obtained using

an upright BX51 microscope (Olympus) or an FV1000 confocal microscope system (Olympus).

Antibodies

Primary antibodies used: Rabbit antibody to phospho histone H2AX (Cell Signaling, Danvers, MA, USA); chicken antibody to human keratin 15 (Covance, Berkeley, CA, USA); rabbit antibody to S100A6 (Lab Vision, Fremont, CA, US); goat antibody to mouse LHX2 (Santa Cruz Biotechnology); rabbit antibody to mouse SOX9 (Santa Cruz Biotechnology); rat antibody to mouse COL17A1 (Nishimura's laboratory); rabbit antibody to mouse keratin 1 (Covance); rabbit antibody to mouse keratin 10 (Covance); rabbit antibody to mouse filaggrin (Covance); rabbit antibody to mouse involucrin (Covance); mouse antibody to Trichohyalin (AE15) (Abcam); rabbit antibody to human TP53BP1 (Life-span BioScience, WA, USA); rabbit antibody to mouse AXIN2 (abcam); rabbit antibody β -catenin (sigma); rabbit antibody to cleaved caspase-3 (Cell Signaling); FITC-conjugated antibody to mouse CD34 (eBioscience, San Diego, CA, USA); goat antibody to mouse NOTCH1 (Santa Cruz Biotechnology); chicken antibody to β galactosidase (Abcam); rabbit antibody mouse P16 (Santa Cruz Biotechnology); rabbit antibody to c-MYC (Abcam); goat antibody to mouse LRIG1 (R&D Systems, Abingdon, Oxfordshire, UK); rat antibody to mouse PDGFR α (eBioscience); rabbit antibody to mouse keratin 6 (Covance); mouse antibody to human COL17A1 (Clone D20, Nishimura laboratory); rabbit antibody to human COL17A1 (Clone NC16A3, Abcam); rabbit antibody to human ELANE (Abcam); Alexa 647 rat antibody to human CD200 (Serotec, Oxfordshire, UK); and mouse antibody to human keratin 1 (Leica microsystems).

Secondary antibodies used: Alexa Fluor 488 goat antibody to rat immunoglobulin (IgG) (Molecular Probes); Alexa Fluor 488 goat antibody to chicken IgY (Molecular Probes); Alexa Fluor 594 goat antibody to rabbit IgG (Molecular Probes); Alexa Fluor 594 goat antibody to rat IgG (Molecular Probes); Alexa Fluor 488 goat antibody to Fluorescein (Molecular Probes); Alexa Fluor 680 donkey antibody to rabbit IgG (Molecular Probes); Alexa Fluor 594 donkey antibody to goat IgG (Molecular Probes); and FITC donkey antibody to chicken IgY (Abcam).

Senescence-Associated β -Galactosidase (SA- β -Gal) staining

A Senescence Cells Histochemical Staining kit was used (Sigma-Aldrich, St Louis, MO, USA) according to the manufacturer's instructions.

FACS analysis and isolation of HFSCs

Subcutaneous fat was removed with a scalpel, and the whole skin was placed dermis down in 0.25% trypsin (GIBCO) for 10 to 13 hours at 4°C, then was moved to 37°C for 20 min. Single-cell suspensions were obtained by scraping the skin gently. The cells were then filtered with strainers (40 μ m) (BD Falcon, San Jose, CA, USA). Cell suspensions were incubated with the appropriate antibodies for 1 hour at 4°C. The following antibodies

were used: CD34-FITC (eBioscience), Integrin $\alpha 6$ -PE (BD Bioscience, San Jose, CA, USA), and Scal-APC (MACS; Miltenyi Biotec, Bergisch Gladbach, Germany). 7-AAD (BD Bioscience) was used to exclude dead cells. Cell isolations were performed using a FACS AriaII equipped with Diva software (BD Bioscience). For RNA extraction of HFSCs, CD34^{high}ITGA6^{high}SCA-1⁺ cells were sorted directly into Buffer RLT (Qiagen, Valencia, CA, USA).

Alkaline comet assay

Alkaline comet assays were performed with FACS-sorted HFSCs (CD34^{high}ITGA6^{high}SCA-1⁺) according to the manufacturer's instructions (Trevigen, Gaithersburg, MD, USA). Briefly, 2×10^3 cells diluted in 10 μ l PBS were added to 100 μ l 1% Low Melting Agarose and placed onto slides. Cells were lysed in lysis solution (2.5 M NaCl, 100 mM EDTA, pH 10.0, 10 mM TrisHCl, 1% sodium lauryl sacosinate) for 60 min on ice and then were placed in alkaline lysis solution (200 mM NaOH, 1 mM EDTA, pH>13) for 60 min at room temperature. Slides were then run for 30 min at 21 V. Nuclei were stained with Cyber Green. As a positive control, DNA damage was induced by soaking in a 100 μ M H₂O₂ solution for 10 min. Images of DNA damage comets were acquired using an upright BX51 microscope (Olympus). A percentage of Tail DNA [Tail intensity/(Tail intensity + Head intensity) \times 100] and the tail moment (Tail length \times a percentage of Tail DNA/100) were measured using Image J software. The tail moments were measured on 40 to 100 cells per slide.

Microarray analysis

To analyze global gene expression changes by aging both in activated and in quiescent HFSCs and IFE keratinocytes, HFSCs (CD34^{high}ITGA6^{high}SCA-1⁺), IFE (ITGA6^{high}SCA-1^{high}), and total epidermal cells were harvested from young and from aged mice. To analyze global gene expression changes by *Col17A1* gene deficiency in HFSCs, HFSCs were harvested from control wild-type mice and *K14-creERT2;Col17a1 flox/flox* mice at 12 weeks old after intraperitoneal (i.p.) administration of Tamoxifen (TAM) (4 mg/mouse for 5 days from 7 to 8 weeks old). Dissociated cells were FACS-sorted and reserved into Buffer RLT (Qiagen) by FACS aria II. Total RNAs were isolated using a RNA easy micro Kit (Qiagen) according to the manufacturer's instructions. cDNA samples were prepared from purified ng RNA using the Ovation Pico WTA System V2 (NuGen, San Carlos, CA, USA) according to the manufacturer's instructions. Amplified cDNAs were labeled with Cyanine 3 (Cy3) using a SureTag DNA Labeling Kit (Agilent Technologies, Santa Clara, CA, USA) following the manufacturer's instructions. RNA and cDNA quality and cyanine incorporation were analyzed using an Agilent Bioanalyzer 2100 (Agilent) and a Nanodrop ND-1000 Spectrophotometer (Thermo Fisher Scientific, Waltham, MA, USA). For each hybridization, 1.3 μ g Cy3-labeled cDNA were fragmented, and hybridized at 65°C for 17 hours to an Agilent SurePrint G3 Mouse GE v2 8x60K Microarray (Design ID: 028005). After washing, microarrays were scanned using an Agilent DNA microarray scanner. For normalization of microarray data, intensity values of each scanned feature were

quantified using Agilent feature extraction software version 10.7.3.1, which performs background subtractions. We only used features that were flagged as no errors (Detected flags) and excluded features that were not positive, not significant, not uniform, not above background, saturated, or population outliers (Compromised and Not Detected flags). Normalization was performed using Agilent GeneSpring version 13.0 (per chip: normalization to 75 percentile shift; per gene: normalization to median of all samples). There are a total of 55,681 probes on the Agilent SurePrint G3 Mouse GE 8x60K Microarray (Design ID: 028005) without control probes. The altered transcripts were quantified using the comparative method. We applied more than a 2.0-fold change in signal intensity to identify significant differences of gene expression in this study.

Hierarchical clustering and Gene Ontology analysis by GeneSpring, MeV and DAVID software

Hierarchical clustering using the Pearson correlation was performed using Agilent GeneSpring version 13.0 or TIGR MeV software (version 4.8.1, www.tm4.org/mev.html). To generate the Venn diagram, TIGR MeV software was used. To analyze the GO terms of ≥ 2.0 -fold increased or decreased gene cluster and also the common gene cluster in the Venn diagram, the web-based Database for Annotation, Visualization and Integrated Discovery (DAVID) 6.7 was used (74). To extract reliable GO terms belonging to biological process, Fisher's exact test and multiple test correction ($P < 0.05$) were used.

Gene set enrichment analysis

GSEA software is provided by the Broad Institute of MIT and Harvard University. To define the lists of genes involved in "DNA repair," "Epidermal differentiation," and "Stemness," the Molecular signature (MSig) list was searched on MSig (Database) DB of the Broad Institute web site (<http://software.broadinstitute.org/gsea/msigdb>). We selected and applied "HALLMARK OF DNA REPAIR" as "DNA repair" MSig, "BOSCO EPITHELIAL DIFFERENTIATION" as "epidermal differentiation" MSig, "RAMALHO STEMNESS UP" as "stemness" MSig, and "RAMALHO STEMNESS DOWN" as "dominant negative stemness" MSig. To apply the Normalized chip expression data into GSEA software, the Mouse chip annotation file was changed to the Human chip annotation file. For GSEA, the following parameter settings were used: number of permutations = 1000; collapsed data set to gene = true; permutation type = gene set; enrichment statistics = weighted; metric for ranking genes = signal to noise. To decide significant MSig change of GSEA results, the nominal P values (< 0.05) and false discovery rate (FDR) q values (< 0.05) were used.

Accession number

Microarray data were deposited in the Gene Expression Omnibus (www.ncbi.nlm.nih.gov/geo/) under series identifier GSE72863.

Quantitative RT-PCR

Total RNAs were purified from FACS-sorted cells by directly sorting into Buffer RLT (Qiagen) using

a RNA easy micro Kit (Qiagen). cDNAs were then synthesized from equal amounts of RNA in 20- μ l reaction mixtures using a High Capacity cDNA Reverse Transcription kit (Applied Biosystems, Foster City, CA, USA) according to standard procedures. For quantitative PCR, cDNA was added to 20 μ l of the reaction mixture containing 10 μ l SYBR Green qPCR Kit (Agilent Technology) and 0.5 μ l 12.5 μ M primers (forward and reverse). Relative levels of expression were determined by normalization to acidic ribosomal phosphoprotein PO (*arbp*) or hypoxanthine-guanine phosphoribosyltransferase (*Hprt*), using the $\Delta\Delta C_t$ method (Biological replicate, pool of 6 to 10 mice). The reactions were run in Mx3000P Real-Time QPCR System (Agilent Technology). The primer sequences used were as follows: *Arbp*: 5'-ATAACCCCTGAAGTGC-TCCGACAT-3', 5'-GGGAAGGTGTAAGTCTCCA-3'. *Hprt*: 5'-CAACGGGGACATAAAAGTTATTGGTGG-3', 5'-TGCAACCTTAACCATTTTGGGGCTGT-3'. *Notch1*: 5'-ACAACAACGAGTGTGAGTCC-3', 5'-ACACGTG-GCTCTGTATATG-3'. *c-myc*: 5'-GCCCTAGTGTG-CATGAG-3', 5'-CCACAGACACCACATCAATTTCTT-3'. *Keratin1*: 5'-AGGATCTTGCCAGATTGCTG-3', 5'-CTA-CTGCTTCGCTCATGCT-3'. *P16*: 5'-GGGTTTCGCCAA-CGCCCCGA-3', 5'-TGCAAGCACCACCGGTGTC-3'. *Fbxw7*: 5'-TCTTGTCTCTGGAAATGCAG-3', 5'-CCGTG-TCTGAGCTGGTAAT-3'.

HFSC fate analysis with K15-CrePR; Rosa26R/CAG-CAT-EGFP mice

For induction of β -galactosidase or enhanced green fluorescent protein (EGFP) expression in K15-expressing cells, *K15-CrePR;CAG-CAT-EGFP* mice and *K15-CrePR;Rosa26R* mice were treated with RU486 (2.5 mg/day, diluted in 80% ethanol; Sigma) topically on their dorsal skin during telogen (7 weeks old) for 5 days. For hair cycle induction, telogen hairs at 7 to 8 weeks old, 16 months old, or just after 10-Gy irradiation were manually depilated under anesthesia.

Quantification of γ -H2AX foci

The images of immunostaining for γ -H2AX were acquired by FV1000 confocal microscopy (Olympus). Visible foci were counted in > 100 nuclei for each cell type (bulge/sub-bulge; dermal papilla; epidermis and dermis). The number of foci per nucleus was calculated as mean \pm SEM.

Measurement of fluorescence intensity and the number of positive signals in bulge nuclei

Images of immunostaining for K15, S100A6, and mouse COL17A1 in mouse bulge areas or images of immunostaining for K15, CD200, human COL17A1, and γ -H2AX in human bulge areas were acquired by confocal microscopy (Olympus). The images were then quantified using Olympus fluoview software (version 1.7) or ImageJ software (NIH image). The fluorescent intensity of the background was removed and then normalized against DAPI intensity. For counting the number of cells with positive signals (SOX9, LHX2) in K15+ bulge nuclei, the images of immunostaining for SOX9 and LHX2 were acquired by confocal microscopy (Olympus), and

67. J. Wang *et al.*, A differentiation checkpoint limits hematopoietic stem cell self-renewal in response to DNA damage. *Cell* **148**, 1001–1014 (2012). doi: [10.1016/j.cell.2012.01.040](https://doi.org/10.1016/j.cell.2012.01.040); pmid: [22385964](https://pubmed.ncbi.nlm.nih.gov/22385964/)
68. M. A. Santos *et al.*, DNA-damage-induced differentiation of leukaemic cells as an anti-cancer barrier. *Nature* **514**, 107–111 (2014). doi: [10.1038/nature13483](https://doi.org/10.1038/nature13483); pmid: [25079327](https://pubmed.ncbi.nlm.nih.gov/25079327/)
69. M. Ito *et al.*, Stem cells in the hair follicle bulge contribute to wound repair but not to homeostasis of the epidermis. *Nat. Med.* **11**, 1351–1354 (2005). doi: [10.1038/nm1328](https://doi.org/10.1038/nm1328); pmid: [16288281](https://pubmed.ncbi.nlm.nih.gov/16288281/)
70. R. J. Morris *et al.*, Capturing and profiling adult hair follicle stem cells. *Nat. Biotechnol.* **22**, 411–417 (2004). doi: [10.1038/nbt950](https://doi.org/10.1038/nbt950); pmid: [15024388](https://pubmed.ncbi.nlm.nih.gov/15024388/)
71. P. Soriano, Generalized lacZ expression with the ROSA26 Cre reporter strain. *Nat. Genet.* **21**, 70–71 (1999). doi: [10.1038/5007](https://doi.org/10.1038/5007); pmid: [9916792](https://pubmed.ncbi.nlm.nih.gov/9916792/)
72. E. B. Olasz *et al.*, Human bullous pemphigoid antigen 2 transgenic skin elicits specific IgG in wild-type mice. *J. Invest. Dermatol.* **127**, 2807–2817 (2007). doi: [10.1038/sj.jid.5700970](https://doi.org/10.1038/sj.jid.5700970); pmid: [17657247](https://pubmed.ncbi.nlm.nih.gov/17657247/)
73. O. de Lacharrière *et al.*, Hair diameter diversity: A clinical sign reflecting the follicle miniaturization. *Arch. Dermatol.* **137**, 641–646 (2001). pmid: [11346342](https://pubmed.ncbi.nlm.nih.gov/11346342/)
74. W. Huang, B. T. Sherman, R. A. Lempicki, Systematic and integrative analysis of large gene lists using DAVID bioinformatics resources. *Nat. Protoc.* **4**, 44–57 (2009). doi: [10.1038/nprot.2008.211](https://doi.org/10.1038/nprot.2008.211); pmid: [19131956](https://pubmed.ncbi.nlm.nih.gov/19131956/)

ACKNOWLEDGMENTS

We thank Y. Nishimori, K. Inomata, Y. Tadokoro, R. Yajima, D. Nanba, H. Shimizu, K. Yancey, I. Morita, F. Ishino, M. Kanai, M. Ohyama, S. Inui, S. Itami, and M. Amagai for their helpful support and DASS Manuscript for editing. E.K.N. has been supported by a

Grant-in-Aid for Scientific Research S (26221303), a Grant-in-Aid for Scientific Research on Innovative Areas “Stem Cell Aging and Disease” (26115003), Funding Program for Next Generation World-Leading Researchers (NEXT Program) (LS042), Grant-in-Aid for Young Scientists from the Ministry of Education, Culture, Sports, Science and Technology of Japan, and also by the Takeda Science Foundation. E.N. and H.M. are authors on a patent applied for by Tokyo Medical and Dental University that relates to drugs that modulate COL17A1 or ELANE expression or function for alopecia.

SUPPLEMENTARY MATERIALS

www.sciencemag.org/content/351/6273/aad4395/suppl/DC1

Figs. S1 to S18
Reference (75)

15 September 2015; accepted 17 December 2015
[10.1126/science.aad4395](https://doi.org/10.1126/science.aad4395)

This copy is for your personal, non-commercial use only.

If you wish to distribute this article to others, you can order high-quality copies for your colleagues, clients, or customers by [clicking here](#).

Permission to republish or repurpose articles or portions of articles can be obtained by following the guidelines [here](#).

The following resources related to this article are available online at www.sciencemag.org (this information is current as of February 4, 2016):

Updated information and services, including high-resolution figures, can be found in the online version of this article at:

</content/351/6273/aad4395.full.html>

Supporting Online Material can be found at:

</content/suppl/2016/02/03/351.6273.aad4395.DC1.html>

A list of selected additional articles on the Science Web sites **related to this article** can be found at:

</content/351/6273/aad4395.full.html#related>

This article **cites 72 articles**, 18 of which can be accessed free:

</content/351/6273/aad4395.full.html#ref-list-1>

This article has been **cited by** 1 articles hosted by HighWire Press; see:

</content/351/6273/aad4395.full.html#related-urls>

This article appears in the following **subject collections**:

Development

</cgi/collection/development>

REPORTS

SUPERCONDUCTIVITY

Nematicity in stripe-ordered cuprates probed via resonant x-ray scattering

A. J. Achkar,¹ M. Zwiebler,² Christopher McMahon,¹ F. He,³ R. Sutarto,³ Isaiah Djianto,¹ Zhihao Hao,¹ Michel J. P. Gingras,^{1,4,5} M. Hücker,⁶ G. D. Gu,⁶ A. Revcolevschi,⁷ H. Zhang,⁸ Y.-J. Kim,⁸ J. Geck,^{2,9} D. G. Hawthorn^{1,4*}

In underdoped cuprate superconductors, a rich competition occurs between superconductivity and charge density wave (CDW) order. Whether rotational symmetry-breaking (nematicity) occurs intrinsically and generically or as a consequence of other orders is under debate. Here, we employ resonant x-ray scattering in stripe-ordered superconductors (La,M)₂CuO₄ to probe the relationship between electronic nematicity of the Cu 3d orbitals, structure of the (La,M)₂O₂ layers, and CDW order. We find distinct temperature dependences for the structure of the (La,M)₂O₂ layers and the electronic nematicity of the CuO₂ planes, with only the latter being enhanced by the onset of CDW order. These results identify electronic nematicity as an order parameter that is distinct from a purely structural order parameter in underdoped striped cuprates.

Key challenges in resolving the cuprate phase diagram are to identify the broken symmetries that generically occur and understand how they are interrelated. Recently, a series of measurements have shown translational symmetry-breaking in the form of charge density wave (CDW) order to be generic to underdoped cuprates (1–9). It has also been proposed that electronic nematicity (intra-unit cell C₄ rotational symmetry-breaking) occurs in the cuprates (10), with experimental evidence for electronic nematicity coming from bulk transport (11–13) and scanning tunneling microscopy (STM) measurements (2, 14). Despite these developments, the role of electronic nematicity, such as whether it is common to the cuprates and how it relates to CDW order or the crystal structure of different cuprate families, has not yet been established.

Relevant in this context are the stripe-ordered La_{2–x}M_xCuO₄ (M is Sr, Ba, Eu, or Nd) cuprates, where it is known that the low-temperature orthorhombic (LTO) phase to low-temperature tetragonal (LTT) structural phase transition (15–18) plays an important role in stabilizing spin and

charge stripe order (1, 18). The LTT phase is understood in terms of rotations of the CuO₆ octahedra about axes parallel to the Cu–O bonds, with the rotation axis of the octahedra alternating between the *a* and *b* axes (19) of neighboring planes (Fig. 1) (15–18). This induces C₄ symmetry-breaking of the average (or intra-unit cell) electronic structure within an individual CuO₂ plane (referred to here as electronic nematicity) and stabilizes stripes whose orientation rotates by 90° between neighboring planes (1). The LTT distortions are understood to be a structural phenomenon, occurring in order to alleviate a lattice mismatch between the preferred Cu–O bond length of the CuO₂ planes and the (La,M)–O bond length in the (La,M)₂O₂ layer (16). It is unclear, however, whether there are additional contributions to the electronic nematicity of the CuO₂ planes distinct from that engendered by a purely structural distortion and possibly generic to underdoped cuprates.

To address this question, we use resonant soft x-ray scattering (RSXS) at different photon energies to probe the relationship between electronic nematicity of the CuO₂ planes, structural distortions, and CDW order. As shown in (20), with the x-ray photon energy tuned to the O *K*-edge (at an energy that is sensitive to apical oxygen), the (001) Bragg peak can be used to probe the LTO to LTT phase transition. The (001) peak is forbidden in conventional diffraction but is allowed when the photon energy is tuned to an x-ray resonance (21, 22). This occurs because on resonance the scattering cross section develops sensitivity to the orbital symmetry of atoms (21, 22), which differs for atoms in neighboring planes in the LTT phase.

Here, we exploit this orbital and element-selective sensitivity and measure the (001) Bragg peak at photon energies corresponding to dif-

ferent elements/orbitals (at the Cu *L*-, La *M*-, Eu *M*-, and O *K*-edges). This enables one to differentiate the CuO₂ planes from the (La,M)₂O₂ layer and isolate the orbital symmetry of the Cu 3d states that are most relevant to the low-energy physics of the cuprates. We show that at the Cu *L*-edge, the (001) peak intensity corresponds to C₄ symmetry-breaking of the Cu 3d states, which we identify as a measure of the degree of electronic nematicity of the CuO₂ planes.

In Fig. 2 we show the (001) peak intensity, *I*₀₀₁, as a function of temperature at absorption edges corresponding to different elements/orbitals: La *M*, Cu *L*, Eu *M*, and O *K*. At the O *K*-edge, the in-plane and apical oxygen sites are further distinguished by photon energy, with 528 eV corresponding to in-plane oxygen, O(1), and ~532 eV corresponding to apical oxygen, O(2) (20, 23) (see Fig. 1). We investigated three samples—La_{1.475}Nd_{0.4}Sr_{0.125}CuO₄ (LNSCO), La_{1.875}Ba_{0.125}CuO₄ (LBCO), and La_{1.65}Eu_{0.2}Sr_{0.15}CuO₄ (LESCO)—having different LTT and CDW transition temperatures, *T*_{LTT} and *T*_{CDW}, respectively. Our principal observation is that measurements of *I*₀₀₁ for atoms in the CuO₂ planes [Cu and O(1)] have a distinct temperature dependence from atoms in the (La,M)₂O₂ layer [La, Eu, and O(2)]. Specifically, the former displays a more gradual temperature dependence than the latter, which exhibits a more pronounced first-order-like phase transition. We ascribe this difference to an additional electronic nematicity in the CuO₂ planes beyond the structural distortions affecting the (La,M)₂O₂ layer.

The intensity of the (001) peak at the Cu *L*-edge directly measures the nematicity of the Cu 3d states (24). Specifically, *I*_{Cu,001} ∝ |η|², where η = *f*_{aa}(0) – *f*_{aa}(0.5) [or = *f*_{bb}(0.5) – *f*_{bb}(0) by symmetry] and *f*_{aa}(*z*) and *f*_{bb}(*z*) are diagonal components of the atomic scattering form factor tensor (25) averaged over all Cu sites in neighboring CuO₂ planes at *z* = 0 or *z* = 0.5 (Fig. 1). At the Cu *L*-edge, which probes the Cu 2*p* to 3*d* transition, *f*_{aa} and *f*_{bb} are directly related to the orbital occupation of the Cu 3*d* states projected onto the *a* or *b* axes, respectively. As such, η corresponds to a difference in the symmetry of the Cu 3*d* states between planes. However, because *f*_{aa}(0.5) = *f*_{bb}(0) by symmetry, one can express η as η = *f*_{aa}(0) – *f*_{bb}(0), and it thus follows that the (001) peak at the Cu *L*-edge measures the electronic nematicity of the Cu 3*d* states within a single CuO₂ plane.

The (001) peak intensity at other absorption edges has similar sensitivity to orbital asymmetry. For the (La,M)₂O₂ layer, this orbital asymmetry tracks the ionic displacements. The (001) peak intensity measured at a photon energy primarily sensitive to apical O exhibits the same temperature dependence as the (1 0 12) Bragg peak from conventional x-ray scattering, which is sensitive to ionic positions (26). Our measurements of *I*₀₀₁ at energies corresponding to La or apical O also show good agreement with conventional x-ray (26–28) or neutron scattering (1), reinforcing our view of a linear relationship between

¹Department of Physics and Astronomy, University of Waterloo, Waterloo, Ontario N2L 3G1, Canada. ²Leibniz Institute for Solid State and Materials Research IFW Dresden, Helmholtzstrasse 20, 01069 Dresden, Germany. ³Canadian Light Source, Saskatoon, Saskatchewan, S7N 2V3, Canada. ⁴Canadian Institute for Advanced Research, Toronto, Ontario M5G 1Z8, Canada. ⁵Perimeter Institute for Theoretical Physics, 31 Caroline Street North, Waterloo, Ontario N2L 2Y5, Canada. ⁶Condensed Matter Physics and Materials Science Department, Brookhaven National Laboratory, Upton, NY 11973, USA. ⁷Synthèse Propriétés et Modélisation des Matériaux (SP2M), UMR 8182, Université Paris-Sud, 91405 Orsay Cedex, France. ⁸Department of Physics, University of Toronto, Toronto, Ontario M5S 1A7, Canada. ⁹Paris Lodron University Salzburg, Chemistry and Physics of Materials, Hellbrunner Strasse 34, 5020 Salzburg, Austria. *To whom correspondence should be addressed. E-mail: dhawthor@uwaterloo.ca

structural distortions and the $(\text{La,M})_2\text{O}_2$ layer (001) peaks measured at these photon energies.

Coupling of the symmetry of the electronic structure to ionic positions (e.g., displacements of in-plane oxygen along the c axis in the LTT phase) is also expected for the CuO_2 planes (29). However, the difference in the temperature dependence of the (001) peak between the CuO_2 planes and the $(\text{La,M})_2\text{O}_2$ layer shows that electronic nematicity of the CuO_2 planes is not simply a trivial consequence of distortions of the $(\text{La,M})_2\text{O}_2$ layer and that there is an additional, possibly intrinsic, susceptibility to nematic order in the CuO_2 planes.

We next explore the relationship between intracell ($Q_x = Q_y = 0$) C_4 symmetry-breaking probed by the (001) peak and inter-unit cell C_4 symmetry-breaking arising from unidirectional CDW order. In Fig. 3, we compare measurements of the temperature dependence of the (001) and CDW maximum peak intensities at the Cu L -edge. An important case is LESCO, where CDW order onsets at temperatures well below T_{LTT} (Fig. 3B). Here, the key observation is that the Cu (001) peak is enhanced below ~ 65 K, coincidentally with the onset of CDW order. This suggests that nematicity of the CuO_2 planes and translational

symmetry-breaking of the CDW order are intertwined, having a cooperative relationship where CDW order enhances nematicity and vice versa. In contrast, the structural distortion of the $(\text{La,M})_2\text{O}_2$ layer, measured by the (001) peak at the Eu M , La M or O K (apical) energies, exhibits no such enhancement at T_{CDW} (Fig. 2B). Whereas the LTT structural distortion of the $(\text{La,M})_2\text{O}_2$ layer plays an important role in stabilizing CDW order and nematicity in the CuO_2 planes, it does not appear to be coupled as strongly with the CDW order as the nematicity of the CuO_2 planes is.

In LBCO at a doping of $x = 1/8$, I_{CDW} behaves roughly as the fourth power of $I_{\text{Cu},001}$ ($I_{\text{CDW}} \propto I_{\text{Cu},001}^4$) (Fig. 3A). However, this power-law relationship is not generic, being seemingly not applicable to LESCO and LNSCO, and may be coincidental. As discussed below, it may also be that 1/8-doped LBCO represents a special case where the order parameters (and/or the coupling parameters) for CDW order, CuO_2 plane nematicity, and structural distortion of the $(\text{La,M})_2\text{O}_2$ layer are tuned to a common critical point.

In a minimal Landau theory that captures the essential aspects of the relationship between CDW,

nematic, and structural orders, we consider two types of order parameters, the electronic nematic order parameter η and the CDW order parameter Ψ_α ($\alpha = x, y$). η breaks the point-group symmetry C_4 down to C_2 . Ψ_α , the complex amplitude of the CDW, also generally breaks translational symmetry. Given this, a suitable Landau free energy, F , is

$$F = a\eta^2 - w\eta\Phi + r(|\Psi_x|^2 + |\Psi_y|^2) + g(\eta + \varepsilon\Phi)(|\Psi_x|^2 - |\Psi_y|^2) + u(|\Psi_x|^2 + |\Psi_y|^2)^2 + v(|\Psi_x|^4 + |\Psi_y|^4) \quad (1)$$

Here, Φ is the structural C_4 symmetry-breaking associated with distortions of the $(\text{La,M})_2\text{O}_2$ layer, representing the three-dimensional (3D) structural phase transition with the octahedral tilting axis rotated by 90° between neighboring planes in the LTT phase. η and Ψ_α are associated with a single CuO_2 plane within the 3D unit cell. The parameters $a, w, g, \varepsilon, r, u$, and v are functions of temperature. From experimental observation, Φ acquires a nonzero value through a first-order phase transition at T_{LTT} , as described by a supplementary part of the Landau theory (16). We assume that $\varepsilon\Phi \ll 1$ because the “direct”

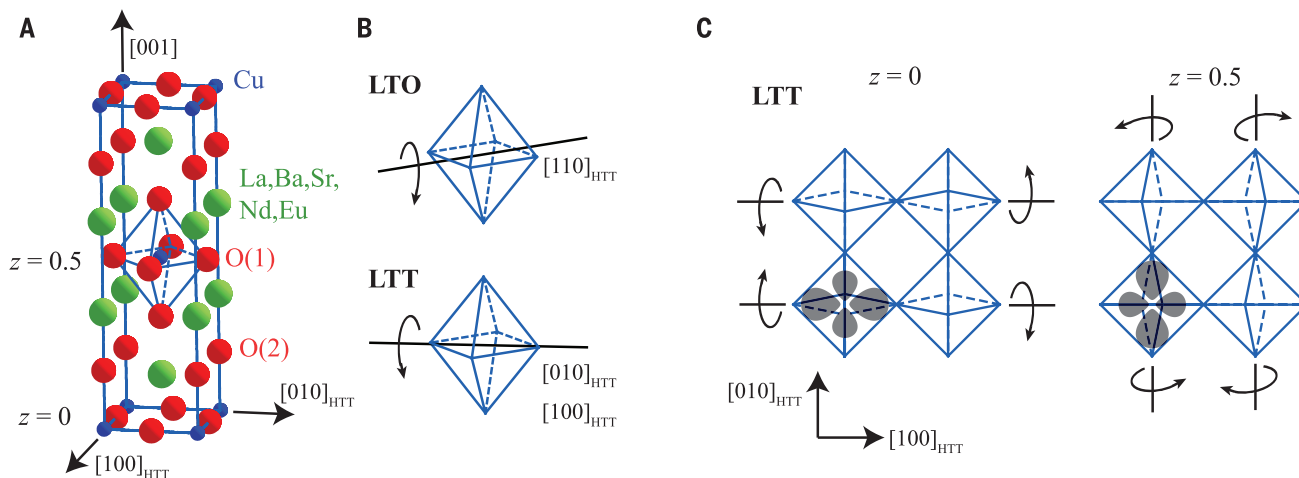


Fig. 1. Structure of La-based cuprates. (A) Unit cell of $(\text{La,M})_2\text{CuO}_4$ in the high-temperature tetragonal phase (HTT). O(1) and O(2) are in-plane and apical oxygen sites, respectively. (B) Octahedral distortions in the LTO and LTT phases. (C) CuO_2 planes showing the octahedral tilt pattern in neighboring layers ($z = 0$ and 0.5) in the LTT phase. The structural C_4 symmetry-breaking and electronic nematicity alternates between neighboring planes, $z = 0$ and $z = 0.5$.

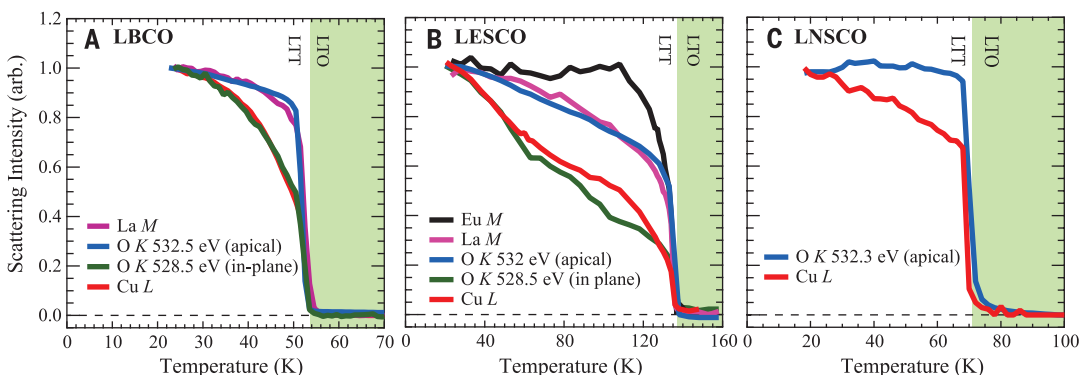
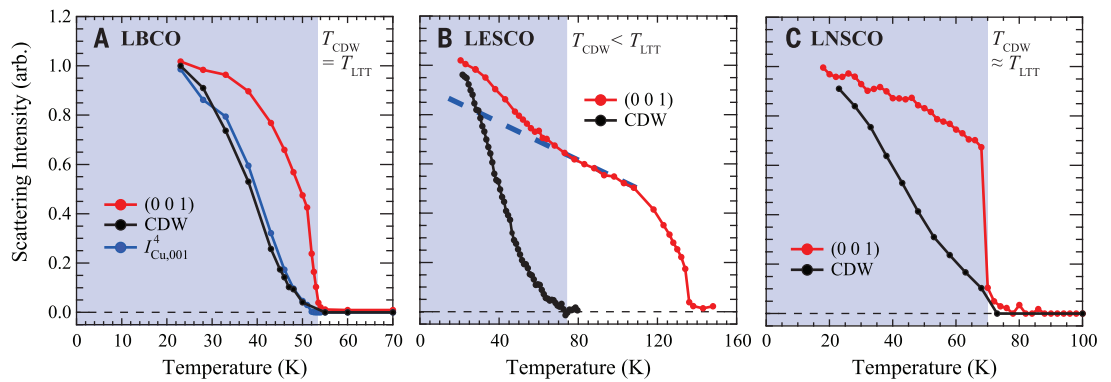


Fig. 2. Temperature dependence of the (001) Bragg peak intensity. The intensities are normalized by the corresponding low-temperature values, $I_{001}(T)/I_{001}(\sim 20\text{K})$, with photon energy tuned to the La M -, Eu M -, O K -, and Cu L -edges for (A) LBCO, (B) LESCO, and (C) LNSCO. In all cases, the (001) peak has a more gradual temperature dependence for Cu and O in the CuO_2 planes than for atoms in the $(\text{La,M})_2\text{O}_2$ layer.

Fig. 3. Comparison between nematicity and CDW order.

Shown is the temperature dependence of the (001) and CDW Bragg peak maximum intensities (normalized by the low-temperature value) at the Cu *L*-edge in (A) LBCO, (B) LESCO, and (C) LNSCO. In LESCO, the (001) intensity is enhanced below T_{CDW} , indicating a cooperative coupling between nematic and CDW orders. In LBCO, the CDW peak intensity is in good agreement with $I_{Cu,001}^4$. CDW peaks were measured at $Q = (\delta_H 0 1.5)$, where $\delta_H = -0.238, 0.264,$ and 0.236 for LBCO, LESCO, and LNSCO respectively.



coupling of the electronic η order parameter to $(|\Psi_x|^2 - |\Psi_y|^2)$ can be expected to be much stronger than the atomic/structural coupling between Φ and the latter CDW terms. As such, we neglect the $\epsilon\Phi$ term. Also neglected is interlayer coupling of the electronic nematicity beyond that imposed by Φ . Our measurements support this omission, being consistent with the LTT distortion inducing long-range nematic ordering along the *c* axis. Although limited by the *c*-axis penetration depth of the x-rays, measurements provide no evidence for a temperature dependent *c*-axis correlation length to the (001) peak, which would indicate an important role of additional interlayer coupling (24).

Within the context of this model, the observed differences among LBCO, LESCO, and LNSCO involve a material and doping dependence of Φ and also possibly of w , the coupling strength between the LTT structural distortion and electronic nematicity. In contrast, we may conjecture that r and a (the CDW and electronic nematic order inverse susceptibilities) are similar for different cuprate materials at the same hole doping. We identify three distinct cases in the theory and their possible correspondence to materials: Case 1: $\left(r - \frac{gw\Phi}{2a}\right) < 0$ at $T = T_{LTT}$. Here, the first-order jump in Φ at T_{LTT} is sufficient to induce first-order jumps in η and Ψ_x . This case may correspond to LBCO, with lower of $x = 0.095$ or 0.110 (27), and possibly LNSCO presented here (Fig. 3C). Case 2: $\left(r - \frac{gw\Phi}{2a}\right) = 0$ at $T = T_{LTT}$. For $T < T_{LTT}$, this coefficient ultimately becomes negative. Here, the first-order jump in F moves the system to the critical point of the CDW order. This special case requires fine-tuning of parameters but may in fact correspond to LBCO at $\sim 1/8$ doping (Fig. 3A). Whether such tuning plays a role in the enhancement of CDW order in $1/8$ -doped LBCO, where the longest-range CDW order of any cuprate is observed, or in the apparent $I_{CDW}(T) \propto I_{Cu,001}^4(T)$ relationship is presently unclear. Case 3: $\left(r - \frac{gw\Phi}{2a}\right) > 0$ at $T = T_{LTT}$. For $T = T_{CDW} < T_{LTT}$, this coefficient becomes negative. Here, the CDW ordering temperature is well separated from the LTT phase transition,

as in LESCO (Fig. 3B) or LBCO, with $x = 0.15$ (27). Additional work is required to further explore this Landau theory and the relationship of its parameters to material properties (structure, doping, and disorder) and other cuprates.

Further context is obtained by contrasting these results to previous reports of nematicity in $YBa_2Cu_3O_{6-x}$ (YBCO), $Bi_2Sr_2CaCu_2O_{8+\delta}$ (Bi-2212), and $Na_xCa_{2-x}CuO_2Cl_2$ (NCCOC). Transport measurements of YBCO have shown in-plane anisotropy that is not solely due to crystalline anisotropy (*I₁₁-I₃₃*), and x-ray diffraction measurements have shown CDW order to have unidirectional character (30–33). However, the relationship between the orthorhombic structure of YBCO, unidirectional CDW order, and intra-unit cell electronic nematicity is not fully resolved. STM measurements on Bi-2212 and NCCOC arguably show more direct evidence for intra-unit cell electronic nematicity distinct from structure (2, 14, 34). Due to C_4 structural symmetry in these materials, nematicity occurs in Ising-like nanoscale domains. The intra-unit cell electronic nematicity identified here in stripe-ordered La-based cuprates likely represents a long-range ordered analog. This suggests that, like CDW order (*I-9*), intra-unit cell electronic nematicity may be a generic feature of underdoped cuprates.

REFERENCES AND NOTES

- J. M. Tranquada, B. J. Sternlieb, J. D. Axe, Y. Nakamura, S. Uchida, *Nature* **375**, 561–563 (1995).
- K. Fujita *et al.*, *J. Phys. Soc. Jpn.* **81**, 011005 (2011).
- T. Wu *et al.*, *Nature* **477**, 191–194 (2011).
- G. Ghiringhelli *et al.*, *Science* **337**, 821–825 (2012).
- J. Chang *et al.*, *Nat. Phys.* **8**, 871–876 (2012).
- A. J. Achkar *et al.*, *Phys. Rev. Lett.* **109**, 167001 (2012).
- E. H. da Silva Neto *et al.*, *Science* **343**, 393–396 (2014).
- R. Comin *et al.*, *Science* **343**, 390–392 (2014).
- W. Tabis *et al.*, *Nat. Commun.* **5**, 5875 (2014).
- S. A. Kivelson, E. Fradkin, V. J. Emery, *Nature* **393**, 550–553 (1998).
- Y. Ando, K. Segawa, S. Komiya, A. N. Lavrov, *Phys. Rev. Lett.* **88**, 137005 (2002).
- R. Daou *et al.*, *Nature* **463**, 519–522 (2010).
- O. Cyr-Choinière *et al.*, *Phys. Rev. B* **92**, 224502 (2015).
- M. J. Lawler *et al.*, *Nature* **466**, 347–351 (2010).
- T. Suzuki, T. Fujita, *J. Phys. Soc. Jpn.* **58**, 1883–1886 (1989).
- J. D. Axe *et al.*, *Phys. Rev. Lett.* **62**, 2751–2754 (1989).
- M. Hücker, *Physica C* **481**, 3–14 (2012).
- M. Hücker *et al.*, *Phys. Rev. Lett.* **104**, 057004 (2010).
- a* and *b* are referenced to the high-temperature tetragonal phase and denote directions parallel to the CuO bonds.

- J. Fink *et al.*, *Phys. Rev. B* **83**, 092503 (2011).
- V. E. Dmitrienko, *Acta Crystallogr. A* **39**, 29–35 (1983).
- D. H. Templeton, L. K. Templeton, *Acta Crystallogr. A* **36**, 237–241 (1980).
- M. Haruta *et al.*, *J. Appl. Phys.* **114**, 083712 (2013).
- See supplementary materials on Science Online.
- M. Haverkort, N. Hollmann, I. Krug, A. Tanaka, *Phys. Rev. B* **82**, 094403 (2010).
- S. B. Wilkins *et al.*, *Phys. Rev. B* **84**, 195101 (2011).
- M. Hücker *et al.*, *Phys. Rev. B* **83**, 104506 (2011).
- Y.-J. Kim, G. D. Gu, T. Gog, D. Casa, *Phys. Rev. B* **77**, 064520 (2008).
- Note that the structure factor of the (100) or related Bragg peaks measured by conventional diffraction can be shown to only have contributions from atoms in the (La,M)₂O₂ layer and not the CuO₂ planes.
- E. Blackburn *et al.*, *Phys. Rev. Lett.* **110**, 137004 (2013).
- S. Blanco-Canosa *et al.*, *Phys. Rev. Lett.* **110**, 187001 (2013).
- A. J. Achkar, F. He, R. Sutarto, C. McMahon, M. Zwiebler, M. Hücker, G. D. Gu, R. Liang, D. A. Bonn, W. N. Hardy, J. Guck, D. G. Hawthorn, Orbital symmetry of charge density wave order in La_{1.875}Ba_{0.125}CuO₄ and YBa₂Cu₃O_{6.67} (2014); ArXiv:1409.6787.
- R. Comin *et al.*, *Science* **347**, 1335–1339 (2015).
- A. Mesaros *et al.*, *Science* **333**, 426–430 (2011).

ACKNOWLEDGMENTS

The authors acknowledge insightful discussions with J. Tranquada, S. A. Kivelson, L. Taillefer, I. Fischer, K. M. Shen, and G. A. Sawatzky. This work was supported by the Canada Foundation for Innovation (CFI), the Canadian Institute for Advanced Research (CIFAR), the Natural Sciences and Engineering Research Council of Canada (NSERC), and the Canada Research Chair Program (M.J.P.G.). Research described in this paper was performed at the Canadian Light Source, which is funded by the CFI, the NSERC, the National Research Council Canada, the Canadian Institutes of Health Research, the Government of Saskatchewan, Western Economic Diversification Canada, and the University of Saskatchewan. The work at Brookhaven National Laboratory was supported by the Office of Basic Energy Sciences, Division of Materials Science and Engineering, U.S. Department of Energy, under contract DE-AC02-98CH10886. M.J.P.G. acknowledges support from the Canada Council for the Arts and the Perimeter Institute (PI) for Theoretical Physics. Research at PI is supported by the Government of Canada through Industry Canada and by the Province of Ontario through the Ministry of Economic Development and Innovation. J.G. and M.Z. were supported by the German Science Foundation (DFG) through the Emmy-Noether (GE1647/2-1) and the D-A-CH program (GE 1647/3-1). A.R. was supported by the French Ministry of Education.

SUPPLEMENTARY MATERIALS

www.sciencemag.org/content/351/6273/576/suppl/DC1
Materials and Methods
Supplementary Text
Figs. S1 to S4
References (35–39)

5 August 2015; accepted 8 January 2016
10.1126/science.aad1824

MATERIALS SCIENCE

Transmutable nanoparticles with reconfigurable surface ligands

Youngeun Kim,^{1,2} Robert J. Macfarlane,^{2,3,*†} Matthew R. Jones,^{1,2,*‡} Chad A. Mirkin^{1,2,3,§}

Unlike conventional inorganic materials, biological systems are exquisitely adapted to respond to their surroundings. Proteins and other biological molecules can process a complex set of chemical binding events as informational inputs and respond accordingly via a change in structure and function. We applied this principle to the design and synthesis of inorganic materials by preparing nanoparticles with reconfigurable surface ligands, where interparticle bonding can be programmed in response to specific chemical cues in a dynamic manner. As a result, a nascent set of “transmutable nanoparticles” can be driven to crystallize along multiple thermodynamic trajectories, resulting in rational control over the phase and time evolution of nanoparticle-based matter.

The configurations of valence electrons that largely dictate the structural arrangement of atoms in crystals are more or less immutable. In contrast, the surface ligands that dictate analogous “bonds” in nanoparticle-based crystals are molecular in nature (1–8) and are therefore sensitive to the presence of various chemical signals. As a result, nanoparticle building blocks offer the possibility for dynamic and rational reconfiguration of the surface ligands in response to external stimuli (9, 10). Consequently, the preference for different nanoparticle components to bond to one another can be switched reversibly, allowing for a set of nascent particles to be driven down specific thermodynamic pathways via chemical binding events. To realize this goal, surface ligands must be capable of processing molecular binding events as inputs while producing changes in the nanoparticle bonding mode as outputs, all in a deterministic and reproducible manner. We show that DNA-based hairpin ligands, which undergo well-defined conformational changes upon binding of effector oligonucleotides, can be used to alter the bonding properties of the nanoparticles to which they are anchored. Inspired by pluripotent stem cells, which are capable of differentiating into multiple biological tissues, we introduce the concept of a transmutable nanoparticle—a building block with different possible binding characteristics that can be selectively activated and deactivated (with the appropriate chemical cues) and then used to generate discrete forms of complex crystalline matter.

Transmutable nanoparticle constructs were created by functionalizing citrate-stabilized gold

nanoparticles with a dense monolayer of DNA (1, 11–13). Free DNA “linkers” containing a sequence complementary to the nanoparticle-bound strands were then hybridized to these constructs, transforming them into nanoscale programmable atom equivalents (PAEs) (14). Bonding interactions between PAEs have been examined for nanoparticle constructs of various sizes (11, 15), shapes (16, 17), and compositions (18–20) and can be determined a priori using a set of well-established design rules (11). Individual bonds between particles are formed via the hybridization of short complementary “sticky ends” that are located at the terminus of each DNA linker (6, 11, 12). Therefore, the bonding identity of a particle is dictated by its sticky ends—the base sequence, the number of strands attached to a particle, and the location of the sticky ends relative to the particle surface.

We studied four factors that are important in dictating the bonding interactions between PAEs: (i) the type of recognition sequence that defines the type of bonding, (ii) the effective stoichiometry of PAEs, (iii) the density of bonding elements on individual PAEs, and (iv) the hydrodynamic size of PAEs. Oligonucleotide-based ligands represent an ideal means to control these bonding properties, as a variety of DNA motifs have been designed that enable structural reconfigurability

in both nanoparticle-based and DNA origami-based materials (6, 21–31). In this work, dynamic control of particle bonding is enabled by the introduction of multiple “protecting groups” placed adjacent to the sticky ends in the linker sequences; these protecting groups consist of sequences that form hairpin structures (Fig. 1) (28–30). When these hairpins are in a “protected” state (where opposite ends of the hairpin sequence hybridize to one another), the sticky ends are buried within the dense DNA monolayer, sterically inhibiting the interparticle hybridization events necessary to mediate particle association. This hairpin structure can undergo a transition to an activated state via the introduction of a short “effector” oligonucleotide that is complementary to the full hairpin sequence. The resulting conformational change pushes the sticky ends to the periphery of the particles, allowing constructs with complementary sticky ends to bind to one another. These effector strands contain a short overhang sequence that does not hybridize to the hairpin (32, 33); this allows the hairpin structures to be reprotected by adding a second oligonucleotide that is fully complementary to the effector strand, resulting in refolding of the hairpin and steric inhibition of the sticky end (fig. S1).

The transmutable nature of these particles is most simply demonstrated by controlling the type of bonding elements (i.e., the sequence of the sticky ends) to be either self-complementary or non-self-complementary. Unary systems with self-complementary sticky ends typically form face-centered cubic (fcc) lattices, whereas binary systems with particles of equal size but complementary sticky ends typically form body-centered cubic (bcc) lattices (11–13). Therefore, in principle, the bonding specificity of a particle could be switched between the self-complementary and non-self-complementary [i.e., fcc-favoring or bcc-favoring] states by functionalizing a particle with both types of sticky ends, each with separately addressable protecting groups (Fig. 2A and tables S1 to S9).

When both types of sticky ends were protected and hidden, the transmutable nanoparticles remained in their nascent state; small-angle x-ray scattering (SAXS) data confirmed that there were no interparticle hybridization events occurring

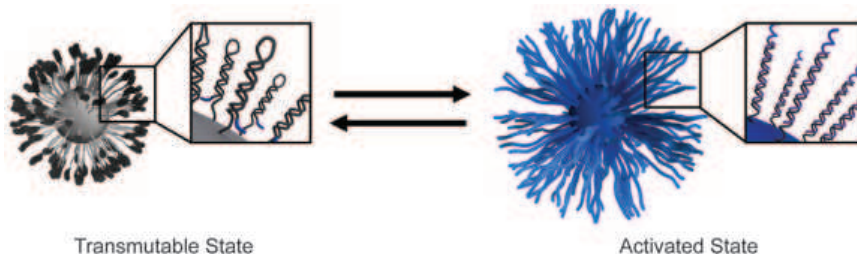


Fig. 1. Scheme of transmutable nanoparticles and their activation pathways. DNA hairpin-based “protecting groups” disguise terminal sticky end sequences (blue DNA segments) that mediate particle bonding, allowing PAEs to be selectively and reversibly transformed from an unactivated, “transmutable” state (left) to an “activated” state (right) through the binding of sequence-specific effector oligonucleotides (purple strands, right image).

¹Department of Materials Science and Engineering, Northwestern University, Evanston, IL 60208, USA.

²International Institute of Nanotechnology, Northwestern University, Evanston, IL 60208, USA. ³Department of Chemistry, Northwestern University, Evanston, IL 60208, USA.

*These authors contributed equally to this work. †Present address: Department of Materials Science and Engineering, Massachusetts Institute of Technology, Cambridge, MA 02139, USA. ‡Present address: Department of Chemistry, University of California, Berkeley, CA 94720, USA. §Corresponding author. E-mail: chadnano@northwestern.edu

and that all particles remained dispersed (Fig. 2A, center). When the particles were exposed to DNA strands that opened the hairpin protecting groups and activated the self-complementary sticky ends, the particles immediately assembled and subsequently formed an fcc lattice upon brief annealing (Fig. 2A, bottom, and table S10). Conversely, when the protecting groups adjacent to the non-self-complementary sticky ends were activated, the particles formed a bcc lattice (Fig. 2A, top). No evidence of a bcc lattice was found when the self-complementary sticky ends were deprotected, and vice versa, indicating that the separate hairpin structures were opened in a completely orthogonal manner. In both the fcc- and bcc-forming systems, the introduction of a short oligonucleotide that caused the hairpins to reform resulted in a complete loss of structure, with the particles returning to their nascent state. The particles were able to undergo at least three rounds of deprotection/reprotection to transition to either an fcc or bcc lattice, independent of their previously assembled states; beyond three cycles, extended x-ray beam exposure caused sample degradation. The bonding modes of the particles could even be directly switched in a one-step process, without having to drive the particles to their nascent state, by adding two different oligonucleotides simultaneously—one that deprotected the sticky ends not engaged in interparticle bonding, and one that reprotected the sticky ends already engaged in particle bonding. These transitions were exacted through three cycles, where addition of the oligonucleotides caused near-instantaneous transitions of the bonding specificity of the particles, thereby allowing particles to reversibly switch between bonding modes in a rapid and robust manner (Fig. 2B).

Another mechanism for controlling nanoparticle bond identity is to toggle the number of bonds that can be formed between particles (Fig. 3) (11, 34). This can be done either by changing the number of particles available to engage in bonding (Fig. 3A) or by changing the density of bonding elements on the individual particle constructs (Fig. 3B). Both methods can be achieved by using two different protecting groups simultaneously, which enables control over the number of bonds that are activated by the introduction of effector strands. In the first method, transmutable particles are functionalized with a single type of protecting group and are turned “on” or “off” in order to control the relative stoichiometry of particle types in solution. In the second method, transmutable particles possess both types of protecting groups, allowing for the formation of low and high valence states through the activation of one or both sets of protecting groups, respectively.

The first method was examined by designing a system where bcc and AlB_2 lattices would be predicted to exhibit similar stabilities. In such a system, it has been shown that the molar ratio of particles influences the structure that is obtained; a 1:1 molar ratio of particles results in the formation of a bcc lattice, whereas a 5:1 molar ratio results in the formation of an AlB_2 lattice (11). To

test this capability, we synthesized two types of transmutable particles, each with a unique protecting group sequence but the same sticky end type; 20% contained one protecting group and 80% contained a second protecting group. This batch of particles was then combined in a 5:1 ratio with nontransmutable particles containing a complementary sticky end. When the first protecting group type was activated, complementary particles existed in a 1:1 ratio and a bcc lattice was synthesized; the particles that were not deprotected remained unbound in solution (Fig. 3A, left). Upon unfolding of the second protecting group, the activated and nontransmutable particles existed in a 5:1 ratio, which drove the lattice toward the formation of an AlB_2 -type structure (Fig. 3A, right). This system could also be driven between the two lattice types in a reversible manner by selectively protecting/deprotecting one or both sets of particles (fig. S2 and table S11).

The second method was examined by designing a system where changing the relative number of sticky ends on complementary particles would favor different phases. Because each transmutable particle in this system included two different protecting groups that could be addressed ortho-

gonally, the particles could access “low-density” and “high-density” states. In the low-density state, the transmutable particles possessed fewer accessible sticky ends than their complements; in the high-density state, the transmutable particles possessed more accessible sticky ends than their complements (Fig. 3B). The former favored a bcc lattice, whereas the latter favored an AlB_2 lattice. Note that these crystal structures matched those that would be predicted from a previously established phase diagram for conventional PAEs (11). This indicates that despite the large number of inactive linkers on the particle surface in the low valence state, these protected binding elements did not interfere with the hybridization of the activated sticky ends. As in each of the previous cases, the transitions between different bonding modes were fully reversible (fig. S3).

The final factor investigated in this work was the hydrodynamic size of the PAEs, because a particle's coordination number is dictated by the relative sizes of the particles bonded to one another (2, 11). Hairpin structures can be used to modify the length of a DNA bond, as the folded state of a hairpin is significantly shorter (3 to 9 nm difference) than the unfolded state (25, 26). In this

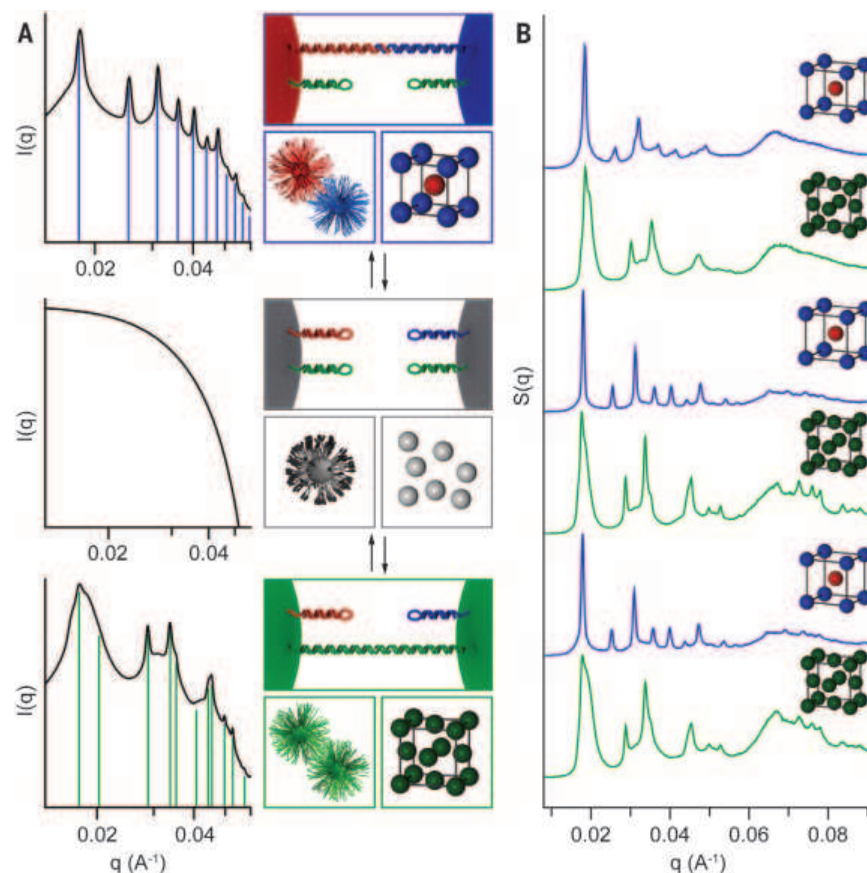


Fig. 2. Programming the type of bonding of transmutable nanoparticles. (A) Transmutable particles can be driven from an unactivated state (center) to crystallize down distinct thermodynamic pathways by selectively deprotecting self-complementary (green) or non-self-complementary (blue and red) sticky ends, which favor fcc (bottom) or bcc (top) lattice symmetries, respectively. (B) SAXS data for transmutable particles cycled between fcc and bcc phases with no observable structural hysteresis.

particular design, the sticky ends were able to form a bond when the hairpins were both folded and unfolded (Fig. 4A). This is because a short duplex region was used to increase the distance between the sticky ends and the hairpins; hence, the sticky ends were not sterically inhibited from bonding when the hairpin was in the folded state (25). As a result, the bonds between particles were not being formed and broken with the introduction of effector strands, but rather the length of the bonds and size of the PAE were being dy-

namically changed. In these transmutable particles, two hairpins were included within each linker strand to maximize the difference in length between the folded (PAE radius 35 nm) and unfolded (PAE radius 41 nm) states.

When these size-adjustable transmutable particles were combined with complementary particles that had a fixed radius of 14 nm, the particles' coordination numbers were different for the folded and unfolded states: An AlB_2 lattice was favored for the folded state, whereas a Cs_6C_{60} lattice was

favored for the unfolded state. This is because the coordination number of the larger particles is determined by how many smaller particles can physically fit around them (11). Therefore, when the radius of the transmutable particles was extended, the particles were able to achieve a larger coordination number.

This change could be monitored via in situ SAXS measurements, giving insight into how these transmutable particles transitioned between two different states (Fig. 4, B and C). Starting at

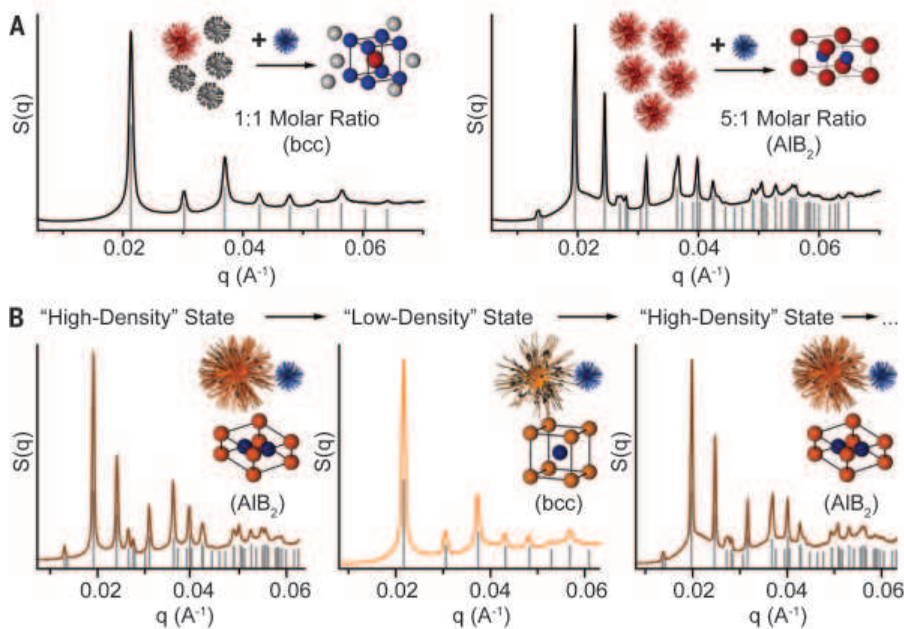


Fig. 3. Changing particle stoichiometry and linker density of transmutable nanoparticles.

Transmutable particles functionalized with two types of oligonucleotides that contain the same sticky end but different protecting groups can be used to control (A) effective PAE stoichiometry and (B) linker density per particle. (A) At a 1:1 ratio of activated transmutable particles (red) and nontransmutable (blue) particles, a bcc lattice was formed and unactivated particles (gray) remained in the supernatant. At a 5:1 ratio, an AlB_2 lattice was formed. (B) Upon the introduction of complementary nontransmutable particles (blue), the low-linker density state favored a bcc lattice, whereas the high-linker density state favored an AlB_2 lattice. In both cases, transmutable particles could be repeatedly cycled between the different states.

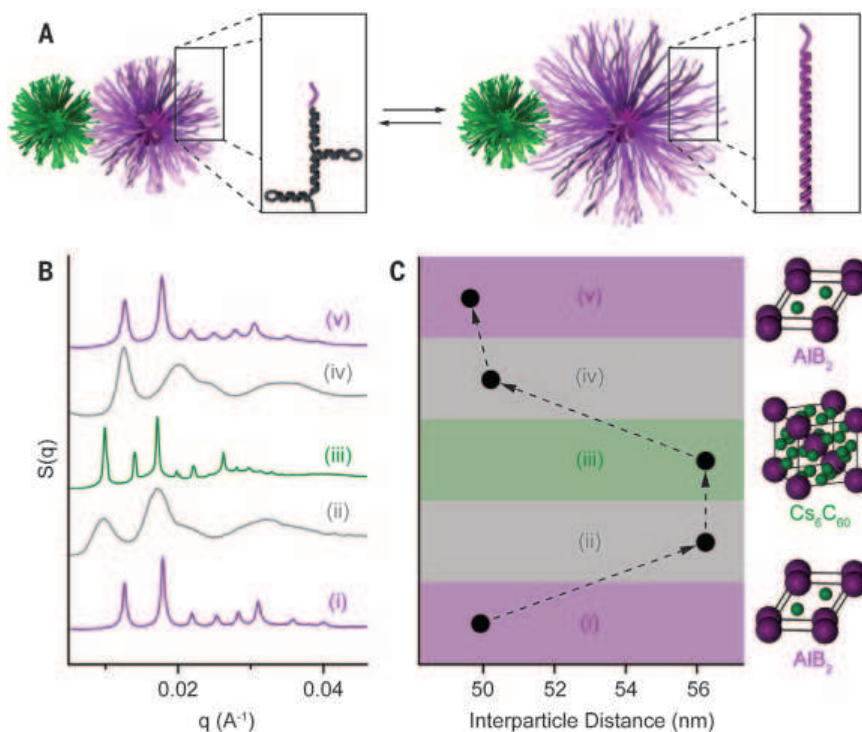


Fig. 4. Programming the hydrodynamic size of transmutable particles.

(A) The selective folding or unfolding of hairpin segments in DNA linkers can be used to shorten or lengthen DNA bonding elements, and therefore the effective size of the PAEs. (B) SAXS data confirm that short DNA bonding elements (folded hairpins) favored the formation of AlB_2 lattices (state i). Unfolding these hairpins resulted in an increase in interparticle distance and a loss of long-range order (state ii), but annealing caused the particles to reorganize into a Cs_6C_{60} lattice (state iii). Upon refolding the hairpins, the particles followed the reverse trajectory with a decrease in interparticle distance and a loss of long-range order (state iv), but annealing the lattice restored the original AlB_2 structure (state v). (C) Interparticle distances measured at each of the states shown in (B) indicated a rapid change in bond length relative to the time scale of crystal formation.

the folded state (AlB₂ lattice), when the hairpin structures were unfolded, the lattice retained the same basic structure, but with expanded lattice parameters and a substantial loss of long-range order (indicated by a shift to a smaller *q* values and broadening in the scattering peaks). After a brief annealing period, the lattices transformed into a Cs₆C₆₀ structure with long-range order. The reverse transition occurred in a similar manner, where the readjustment of the lattice parameters occurred first (with a corresponding loss of long-range order), followed by reorganization and change in particle coordination number (fig. S4). From this observation, it can be concluded that changes to the bonding nature of the particles occur on a faster time scale than the lattice formation and reorganization processes. Indeed, the bonding mode appears to change nearly instantaneously upon introduction of the appropriate chemical stimuli, whereas the crystallization process for these transmutable particles occurs on a similar time scale and manner as previous PAE constructs (35). Taken together, these data indicate that activated transmutable PAEs are nearly indistinguishable from nontransmutable PAEs, enhancing their utility in materials synthesis schemes.

We have used the programmable nature of DNA hairpins and the concept of nanoparticle-based PAEs to develop constructs with bonding behaviors that can be dynamically modulated in response to specific chemical stimuli. The resulting structural plasticity manifested in transmutable particles delineates the power and potential to control PAE architectures, and lays an important foundation for more complex and exotic forms of adaptive matter.

REFERENCES AND NOTES

- C. A. Mirkin, R. L. Letsinger, R. C. Mucic, J. J. Storhoff, *Nature* **382**, 607–609 (1996).
- E. V. Shevchenko, D. V. Talapin, N. A. Kotov, S. O'Brien, C. B. Murray, *Nature* **439**, 55–59 (2006).
- D. V. Talapin, J.-S. Lee, M. V. Kovalenko, E. V. Shevchenko, *Chem. Rev.* **110**, 389–458 (2010).
- C. Knorowski, S. Burleigh, A. Travesset, *Phys. Rev. Lett.* **106**, 215501 (2011).
- Z. Tang, Z. Zhang, Y. Wang, S. C. Glotzer, N. A. Kotov, *Science* **314**, 274–278 (2006).
- M. R. Jones, N. C. Seeman, C. A. Mirkin, *Science* **347**, 1260901 (2015).
- Y. Wang *et al.*, *Nature* **491**, 51–55 (2012).
- B. A. Grzybowski, A. Winkleman, J. A. Wiles, Y. Brumer, G. M. Whitesides, *Nat. Mater.* **2**, 241–245 (2003).
- K. Zhang, X. Zhu, F. Jia, E. Auyeung, C. A. Mirkin, *J. Am. Chem. Soc.* **135**, (2013).
- P. K. Kundu *et al.*, *Nat. Chem.* **7**, 646–652 (2015).
- R. J. Macfarlane *et al.*, *Science* **334**, 204–208 (2011).
- S. Y. Park *et al.*, *Nature* **451**, 553–556 (2008).
- D. Nykypanchuk, M. M. Maye, D. van der Lelie, O. Gang, *Nature* **451**, 549–552 (2008).
- R. J. Macfarlane, M. N. O'Brien, S. H. Petrosko, C. A. Mirkin, *Angew. Chem. Int. Ed.* **52**, 5688–5698 (2013).
- R. J. Macfarlane *et al.*, *Angew. Chem. Int. Ed.* **49**, 4589–4592 (2010).
- M. R. Jones *et al.*, *Nat. Mater.* **9**, 913–917 (2010).
- M. N. O'Brien, M. R. Jones, B. Lee, C. A. Mirkin, *Nat. Mater.* **14**, 833–839 (2015).
- C. Zhang *et al.*, *Nat. Mater.* **12**, 741–746 (2013).
- Y. Zhang, F. Lu, K. G. Yager, D. van der Lelie, O. Gang, *Nat. Nanotechnol.* **8**, 865–872 (2013).
- J. D. Brodin, E. Auyeung, C. A. Mirkin, *Proc. Natl. Acad. Sci. U.S.A.* **112**, 4564–4569 (2015).
- J. Bath, A. J. Turberfield, *Nat. Nanotechnol.* **2**, 275–284 (2007).
- S. Angioletti-Uberti, B. M. Mognetti, D. Frenkel, *Nat. Mater.* **11**, 518–522 (2012).
- W. B. Rogers, V. N. Manoharan, *Science* **347**, 639–642 (2015).
- R. J. Macfarlane, M. R. Jones, B. Lee, E. Auyeung, C. A. Mirkin, *Science* **341**, 1222–1225 (2013).
- Y. Kim, R. J. Macfarlane, C. A. Mirkin, *J. Am. Chem. Soc.* **135**, 10342–10345 (2013).
- M. M. Maye, M. T. Kumara, D. Nykypanchuk, W. B. Sherman, O. Gang, *Nat. Nanotechnol.* **5**, 116–120 (2010).
- N. C. Seeman, *Nature* **421**, 427–431 (2003).
- B. Yurke, A. J. Turberfield, A. P. Mills Jr., F. C. Simmel, J. L. Neumann, *Nature* **406**, 605–608 (2000).
- K. Lund *et al.*, *Nature* **465**, 206–210 (2010).
- P. Yin, H. M. T. Choi, C. R. Calvert, N. A. Pierce, *Nature* **451**, 318–322 (2008).
- Y. Zhang *et al.*, *Nat. Mater.* **14**, 840–847 (2015).
- D. Y. Zhang, G. Seelig, *Nat. Chem.* **3**, 103–113 (2011).
- D. Y. Zhang, E. Winfree, *J. Am. Chem. Soc.* **131**, 17303–17314 (2009).
- E. Auyeung *et al.*, *Nature* **505**, 73–77 (2014).
- R. J. Macfarlane *et al.*, *Proc. Natl. Acad. Sci. U.S.A.* **106**, 10493–10498 (2009).

ACKNOWLEDGMENTS

This material is based on work supported by Air Force Office of Scientific Research award FA9550-11-1-0275 (C.A.M., Y.K., R.J.M., M.R.J.) and by the Center for Bio-Inspired Energy Science (CBES), an Energy Frontier Research Center funded by the U.S. Department of Energy, Office of Science, Basic Energy Sciences under award DE-SC000989-0002 (C.A.M., Y.K.), Y.K., R.J.M., and M.R.J. acknowledge the Ryan Fellowship at Northwestern University. M.R.J. acknowledges the NSF for a graduate research fellowship. Portions of this work were carried out at the DuPont-Northwestern-Dow Collaborative Access Team (DND-CAT) beamline located at Sector 5 of the Advanced Photon Source. DND-CAT is supported by E. I. DuPont de Nemours & Co., Dow Chemical Company, and the state of Illinois.

SUPPLEMENTARY MATERIALS

www.sciencemag.org/content/351/6273/579/suppl/DC1
Materials and Methods
Supplementary Text
Figs. S1 to S4
Tables S1 to S11

10 August 2015; accepted 26 November 2015
10.1126/science.aad2212

MATERIALS SCIENCE

Diamond family of nanoparticle superlattices

Wenyan Liu,¹ Miho Tagawa,² Huolin L. Xin,¹ Tong Wang,³ Hamed Emamy,⁴ Huilin Li,^{3,5} Kevin G. Yager,¹ Francis W. Starr,⁴ Alexei V. Tkachenko,¹ Oleg Gang^{1*}

Diamond lattices formed by atomic or colloidal elements exhibit remarkable functional properties. However, building such structures via self-assembly has proven to be challenging because of the low packing fraction, sensitivity to bond orientation, and local heterogeneity. We report a strategy for creating a diamond superlattice of nano-objects via self-assembly and demonstrate its experimental realization by assembling two variant diamond lattices, one with and one without atomic analogs. Our approach relies on the association between anisotropic particles with well-defined tetravalent binding topology and isotropic particles. The constrained packing of triangular binding footprints of truncated tetrahedra on a sphere defines a unique three-dimensional lattice. Hence, the diamond self-assembly problem is solved via its mapping onto two-dimensional triangular packing on the surface of isotropic spherical particles.

The diamond lattice holds a special place among known crystal structures because it is simultaneously simple, yet nontrivial. Tetravalent atoms, such as carbon or silicon, and molecular systems such as water form this lattice under appropriate conditions. However, because of the openness of the lattice, whose volume fraction is only 34% of the hard-sphere limit, higher-density packings frequently prevail. The structure of atomic diamond gives rise to its distinct properties, such as extreme mechanical hardness and a combination of high

thermal conductivity and electrical insulation (1). The immense historical interest in colloidal diamond lattices is due to the predicted optical response—in particular, its potential application as a full three-dimensional (3D) photonic band gap material (2). Yet, building 3D diamond lattices from nano- and microscale particles by means of self-assembly has proven to be remarkably difficult.

Computationally, it was predicted that a delicate balance of isotropic interactions and packing effects might permit the formation of diamond-ordered lattices (3–6). Indeed, diamond-like structures of isotropically interacting systems were observed in polymers (7, 8) and in a binary system of charged nanoparticles (NPs) (9). However, the interactions are typically highly system-specific; thus, it is difficult to generalize such a strategy for the rational assembly of a diamond lattice. Alternatively, engineered anisotropic interactions have been considered. For example,

¹Center for Functional Nanomaterials, Brookhaven National Laboratory, Upton, NY 11973, USA. ²Department of Materials Science and Engineering, Nagoya University, Furo-cho, Chikusa-ku, Nagoya 464-8603, Japan. ³Biology Department, Brookhaven National Laboratory, Upton, NY 11973, USA. ⁴Department of Physics, Wesleyan University, Middletown, CT 06459, USA. ⁵Department of Biochemistry and Cell Biology, Stony Brook University, Stony Brook, NY 11794, USA.

*Corresponding author. E-mail: ogang@bnl.gov

precisely truncated tetrahedra were computationally predicted to show a diamond lattice (10). Micrometer-scale colloids with tetrahedrally arranged binding sites (11), known as “patchy” particles, were developed experimentally (12–14). Similar to the tetrahedral symmetry of covalent bonds in atomic systems, such as carbon or silicon, such patchy particles should naturally form diamond lattices. However, recent computational studies proved that at equilibrium, cubic diamond (CD) is degenerate with its hexagonal counterpart when there are only short-range interactions (12). Moreover, both these structures compete with an amorphous tetrahedral “liquid,” which is thermodynamically favored unless the bonding is highly directional (15–17). Free rotation about bonds easily introduces defects, including a mixture of both cubic and hexagonal local structures and leading to a kinetically arrested, disordered state. Thus, tetrahedral motifs on their own are not sufficient for the robust assembly of a diamond crystal. Furthermore, the high sensitivity of the lattices to the position

of binding spots imposes exceptionally stringent requirements on the fidelity of particle fabrication. Combined, these complications have hindered the rational assembly of diamond from either micro- or nanoscale particles.

Here, we demonstrate self-assembly of nanoscale cubic diamond superlattices. In our approach, the 3D assembly problem is transformed into a 2D packing problem, bypassing the enumerated challenges. Specifically, our central hypothesis is that the assembly of a diamond structure might be realized without imposing strict requirements on the position, orientation, and shape of binding spots but rather by relying on the self-organization of the binding “footprints” of shaped particles on the surface of isotropic spherical particles (Fig. 1). Although this assembly scenario might seem hopelessly unconstrained, we demonstrate experimentally that our approach leads to the desired diamond structure, drastically streamlining the assembly process. In essence, the engineered topology of interparticle connections encodes a 3D lattice owing to the par-

ticular way the footprints of these particles can organize on the surface of the isotropic particles. We show the fabrication of a family of lattices based on the diamond motif using NPs of different types.

Given its distinct selectivity of interactions and structural plasticity, DNA provides a versatile tool for the programmable assembly of finite-sized and extended nanoparticle structures (18–22) and close-packed lattices (23–26). Our strategy allows for assembly of the diamond family of lattices by using tetrahedral cages, constructed using DNA origami technology (27, 28), as topological linkers between isotropic NPs. Because the size of the origami structure is comparable with a nanoparticle diameter, the tetrahedral linker can be viewed practically as a vertex-truncated tetrahedron (Fig. 1, zoom-in view) with a triangular footprint, which can bind to the isotropic DNA-coated gold NPs via hybridization (Fig. 1).

Isotropic particles and tetrahedral origami self-assemble into an open face-centered cubic (FCC) lattice (Fig. 1, route A). By caging an additional

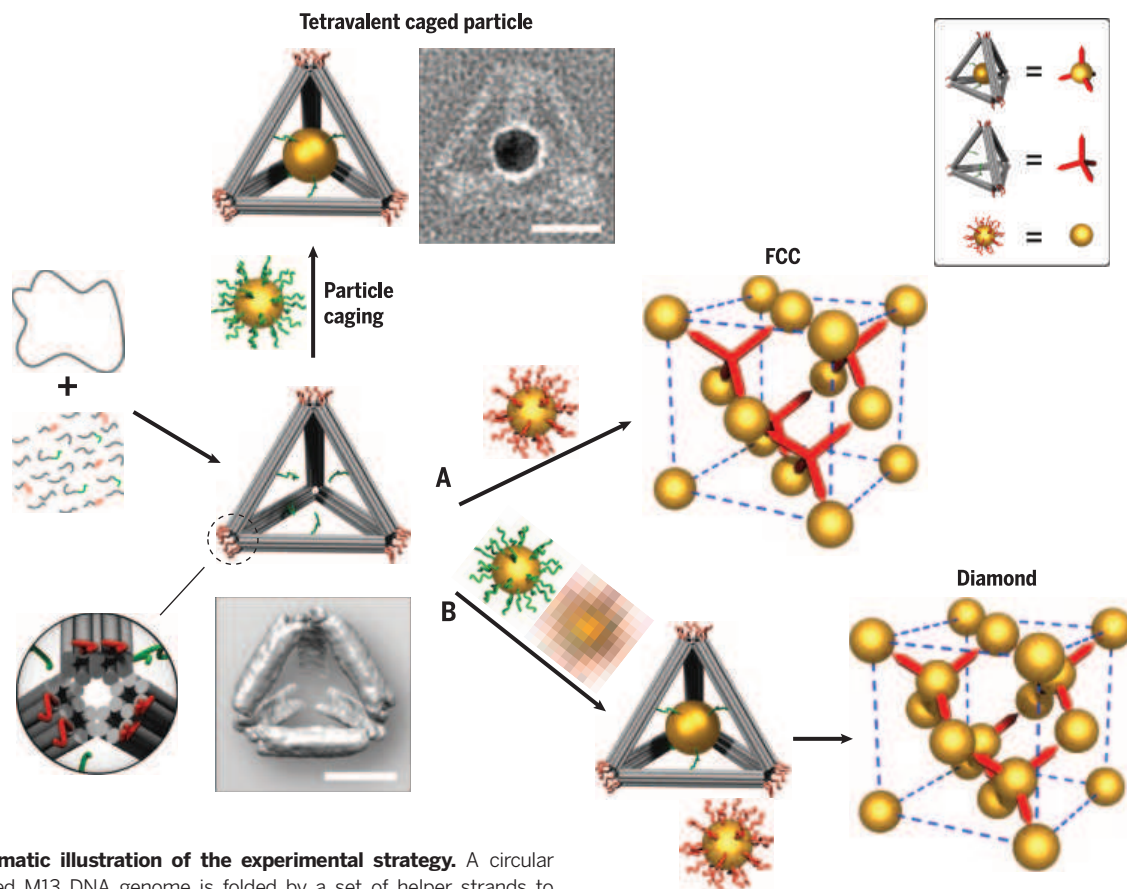


Fig. 1. Schematic illustration of the experimental strategy. A circular single-stranded M13 DNA genome is folded by a set of helper strands to generate a rigid tetrahedral DNA origami cage containing two sets of sticky-ended DNA strands. One set (green) is projected from the inner faces of the edges, functioning as an anchor to encapsulate and hold the guest particle (uniformly coated with green strands) inside the cage; another set (red) is installed at each vertex of the tetrahedral cage, acting as a sticky patch to provide binding to the basis particles (uniformly coated with red strands). (Zoom in) A detailed view of the vertex (truncated) of the tetrahedron cage. The image below the tetrahedron model is a reconstructed cryo-EM density map of the tetra-

hedron. The guest and the basis particles coated with corresponding complementary DNA can either individually interact with the tetrahedral cages to form tetrahedral caged particles and FCC superlattices (route A, empty cages), respectively, or together hybridize with the tetrahedral cages to create diamond crystals (route B, with caged particle). A representative of a constructed tetrahedral caged particle is shown in a negative-staining TEM image beside the model. (Top right) A visual definition of the system components for simplified illustration of shown FCC and diamond superlattices. Scale bars, 20 nm.

NP inside each tetrahedron, coassembly with uncaged, isotropic NPs (Fig. 1, route B) instead gives rise to a diamond lattice.

The DNA origami tetrahedron cage is constructed with each of its six edges containing a rigid 10-helix bundle with a length of ≈ 36 nm and a cross section of ≈ 9 by 6 nm (Fig. 1). This design creates roughly triangular footprints at the vertices, which contain six dangling single-stranded DNA (ssDNA) (Fig. 1, red strands) for binding of isotropically DNA-coated “basis particles” (melting temperature for DNA links, $T_m \approx 42.3^\circ\text{C}$). Selected tetrahedral edges are encoded with a different ssDNA sequence that projects toward the interior (Fig. 1, green strands). These internal strands contain ssDNA overhangs ($T_m \approx 48^\circ\text{C}$) that anchor the “guest particles” (up to ≈ 26 nm in diameter) inside the tetrahedra, forming tetravalent caged particles (details are provided in the supplementary materials). To achieve single-particle encapsulation, we used gold NPs with a core diameter of 14.5 nm (excluding DNA shell).

We examined the assembled constructs using transmission electron microscopy (TEM). The structure of the DNA origami tetrahedron was resolved by use of cryogenic EM (cryo-EM) and

single-particle 3D reconstruction techniques and showed excellent agreement between reconstruction and design (Fig. 1 and fig. S3A). Negative-stain TEM images reveal the high-fidelity positioning of the central guest particle within the tetrahedron, as well as the undistorted cage-particle construct (Fig. 1 and fig. S3B).

We asked whether these nanocomponents—basis isotropic particles, tetrahedra, and tetravalent caged NPs—could be assembled into superlattices. We first tested the assembly of the basis particles (core diameter, 14.5 nm) with the tetrahedral cages, whose vertices host complementary ssDNA (Fig. 1, route A). We mixed and annealed the two components and probed the assembled structure by means of in situ small-angle x-ray scattering (SAXS). The 2D scattering pattern and the associated structure factor $S(q)$ revealed a series of sharp scattering peaks. The ratio of the positions of the peaks (q^1/q^2) matches 1: $\sqrt{4/3}$: $\sqrt{8/3}$: $\sqrt{11/3}$: 2: $\sqrt{16/3}$..., indicating the formation of a well-defined FCC lattice (Fig. 2, A and C). Our modeling of $S(q)$ —which accounts for particle size, origami dimensions, and lattice correlation length (a description of the SAXS modeling is available in the supplementary materials)—is in excellent agreement with the

experimental curve (29) (Fig. 2C, top channel, and fig. S10). How the basis particles are linked by DNA tetrahedra in the FCC lattice is illustrated in Fig. 2D. The interparticle distance d is 71.9 nm, which is consistent with the spacing calculated from the sizes of our components (a detailed calculation is provided in the supplementary materials). Formation of the FCC lattice per se is noteworthy, given the rotational freedom of the tetrahedra when they interact with isotropic particles in the lattice.

The FCC structure provides a platform for the assembly of a CD lattice because the unit cell of diamond can be viewed as a FCC cell with four additional objects located at $(1/4, 1/4, 1/4)$, $(3/4, 3/4, 1/4)$, $(1/4, 3/4, 3/4)$, and $(3/4, 1/4, 3/4)$, the exact centers of the tetrahedra (Fig. 1). Thus, to assemble a CD lattice, we used isotropic gold NPs of 14.5-nm core diameter both as the basis particles and the guest particles. Using a one-pot slow annealing process, we mixed an equal molar ratio of two types of NPs coated with different DNA (sequence designs are provided in the supplementary materials) (table S1). Because of the separation of melting temperatures of anchoring strands inside tetrahedra and at the vertices, the lattice assembly occurs in two distinct steps

Fig. 2. SAXS characterization of the diamond family of nanoparticle superlattices. (A) 2D SAXS pattern of the FCC superlattices constructed with basis particles (core diameter, 14.5 nm) and tetrahedral DNA origami cages. (B) 2D SAXS pattern of the diamond superlattices formed from basis particles (core diameter, 14.5 nm) and tetravalent caged particles (core diameter, 14.5 nm). (C) Integrated 1D patterns. The top channel shows experimental (red) and calculated (black) 1D SAXS patterns for the FCC crystals. The bottom channel shows experimental (green) and calculated (black) 1D SAXS patterns for the diamond crystals. (Insets) Standard FCC (top) and diamond unit cells (bottom). (D) Unit cell model of the assembled FCC superlattice. (E) Unit cell model of the constructed diamond crystal. (F) 2D SAXS pattern of the zinc blende lattices constructed with basis particles (core diameter, 8.7 nm) and tetravalent caged particles (core diameter, 14.5 nm). (G) 2D SAXS pattern of the wandering zinc blende lattices formed from basis particles (core diameter, 8.7 nm) and guest particle pairs (core diameter, 8.7 nm) caged inside the tetrahedra. (H) Integrated 1D patterns. The top channel shows experimental (red) and modeled (black) structure factors, $S(q)$, for the zinc blende crystals (inset, standard zinc blende unit cell). The bottom channel shows experimental (green) and modeled (black) structure factors for the wandering zinc blende lattices. (I) Unit cell model of the assembled zinc blende superlattice. (J) Unit cell model of the wandering zinc blende lattice, where caged particle pairs have no specific orientation in the tetrahedra.

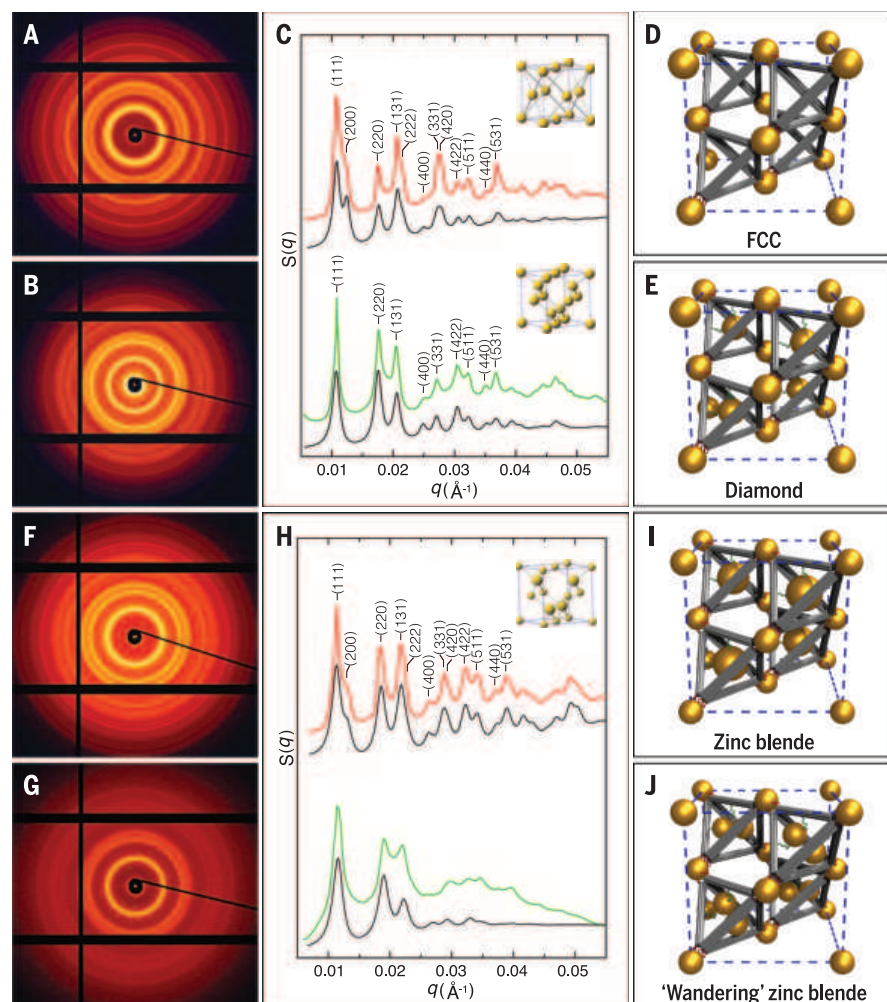


(Fig. 1): The guest particles with DNA shells complementary to inner (green) strands were first trapped inside the cages, forming the tetra-valent caged particles; these caged particles subsequently hybridized with the basis particles to form lattices. The SAXS reveals a crystalline organization with a substantial degree of long-range order, as evident from >15 sharp diffraction peaks (Fig. 2, B and C). The peak positions correspond to $q^n/q^1 \approx 1: \sqrt{8}/3: \sqrt{11}/3: \sqrt{16}/3: \sqrt{19}/3: \sqrt{8}: 3\dots$, which is in precise agreement with a cubic diamond lattice. The measured lattice constant is 100.7 nm ($2\pi\sqrt{3}/q^1$), which is consistent with the 43.7-nm center-to-center distance between the basis and caged particles ($a\sqrt{3}/4$) and the 71.2-nm distance between the two basis particles ($a/\sqrt{2}$). The agreement between the calculated and experimental $S(q)$ profiles further confirms the formation of a well-ordered diamond lattice (Fig. 2C, bottom channel, and fig. S11), whose unit cell model is shown in Fig. 2E.

On the basis of the same strategy, we built two variant lattices in the CD family: a zinc blende lattice and another lattice for which there is no known atomic analog. The zinc blende lattice was obtained by replacement of the 14.5-nm basis particles in the CD with smaller 8.7-nm particles. Our assembled zinc blende structures exhibited excellent long-range crystalline order (Fig. 2, F and H, and fig. S4). Again, we observed a precise correspondence between experimental and modeled scattering curves (Fig. 2H, top channel, and fig. S12), confirming the formation of the designed zinc blende lattice shown in Fig. 2I.

To assemble the second variety of the CD family lattice, we used a pair of 8.7-nm core diameter guest NPs for caging inside the tetrahedra and NPs, with a core diameter of 8.7 nm as the basis particles. The tetrahedron interiors were decorated with two additional anchoring strands, for a total of 6 ssDNA. The reduced NP size and the increased anchor points allow for the caging of two particles within one DNA origami tetra-

hedron (fig. S8). We call the assembled structure a “wandering” zinc blende lattice because the guest particles have greater positional freedom. Its x-ray diffraction pattern is similar to that of the canonical zinc blende structure, but of a lower quality (Fig. 2, G and H). The absence of higher-order diffraction peaks is likely due to the random occupancy of the two distinct but equally sized particles within the tetrahedra. Our SAXS modeling in this case assumed that the two caged particles were randomly and isotropically oriented. The modeled profile approximately matches the experimental curve (Fig. 2H, bottom channel, and fig. S13), supporting our predicted structural organization (Fig. 2J). This binary organization is notable because one nanocomponent (the basis particle) is well positioned, whereas another component (the guest particle pair) has considerable local freedom.

We also applied cryo-scanning transmission electron microscopy (cryo-STEM) to directly visualize the assembled lattices. The cryo-STEM images of the assembled diamond-family superlattices are shown in Fig. 3, plunge-frozen from their native liquid environment (figs. S5 to S7). In this experiment, the image formation is dominated by Rutherford scattering from the atomic nuclei in the sample. Thus, the image reflects the projected atomic mass contrast, in which areas with gold would have intensities higher than those of ice. As can be seen in Fig. 3, A, E, and I, respectively, all three assemblies—FCC, diamond, and zinc blende—exhibit well-ordered lattices of NPs. The enlarged images of each self-assembled superlattice shown in Fig. 3, B, F, and J, respectively, match the [110] projections of their corresponding models (Fig. 3, C, G, and K). To draw an analogy between our self-assembled superlattices and naturally occurring atomic crystals, the atomic-resolution images of platinum (FCC), silicon (CD), and zinc telluride (zinc blende) along the [110] zone axis are shown in Fig. 3, D, H, and L, respectively. The self-assembled nanoparticle superlattices (Fig. 3, B, F, and J) closely match their atomic analogs.

The mechanism of formation for these diamond-family lattices is quite intricate. Over short ranges, the energy of the FCC lattice is identical to that of the hexagonally closed packed (HCP) lattice, as well as their derivatives such as CD, zinc blende, and hexagonal diamond (HD). The CD and HD lattices are indistinguishable from the point of view of the nearest-neighbor coordination because in both scenarios, tetrahedra can connect to four particles. Furthermore, whereas the DNA tetrahedron binds anisotropically, the basis particles interact isotropically. In other words, there is seemingly substantial freedom in the way in which the tetrahedra can attach to a particle surface.

Below, we present a simple model that explains the formation of the observed superlattices. This model attributes their robust self-assembly to the specific truncated architecture of the DNA cages (Fig. 4A), not merely to their overall tetrahedral symmetry. In this model, steric and electrostatic repulsion between the cages is represented

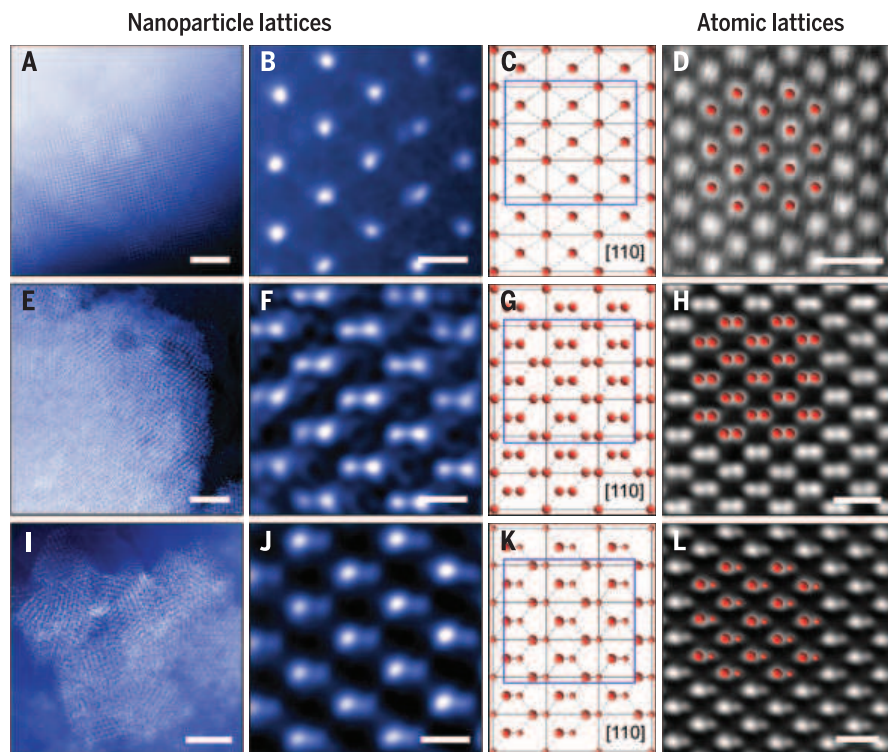


Fig. 3. Cryo-STEM images of the diamond family of nanoparticle superlattices. (A and B) FCC superlattices constructed with basis particles (core diameter, 14.5 nm) and tetrahedral DNA origami cages. (A) Low-magnification image. (B) High-magnification image taken along the [110] zone axis. (C) Schematic projection of a FCC lattice along [110] zone axis. (D) High-angle annular dark-field scanning-STEM (HAADF-STEM) image of platinum viewed in the [110] direction. (E and F) Diamond superlattices formed from basis particles (core diameter, 14.5 nm) and tetra-valent caged particles (core diameter, 14.5 nm). (E) Low-magnification image. (F) High-magnification image taken along the [110] zone axis. (G) Schematic projection of a diamond lattice along [110] zone axis. (H) HAADF-STEM image of silicon viewed along the [110] direction. (I and J) Zinc blende lattices constructed with basis particles (core diameter, 8.7 nm) and tetra-valent caged particles (core diameter, 14.5 nm). (I) Low-magnification image. (J) High-magnification image taken along the [110] zone axis. (K) Schematic projection of a zinc blende lattice along [110] zone axis. (L) HAADF-STEM image of zinc telluride viewed along the [110] direction. The match between the nanoparticle lattices and the atomic analogs confirms the successful assembly of the diamond family of nanoparticle superlattices. Scale bars, (A), (E), and (I), 500 nm; (B), (F), and (J), 50 nm; (D), (H), and (L), 0.5 nm.

by the rigid-body interaction between the truncated tetrahedra.

Each tetrahedron binds to a spherical particle, through a large “footprint” on its surface, as shown in Fig. 4A (red triangle), owing to its truncation. This footprint is approximately an equilateral triangle, with side length $b \approx 10\sigma \approx 20$ nm (where $\sigma \approx 2$ nm is the diameter of a DNA duplex). For the combination of sizes used in our experiments, the hard-core constraint between truncated tetrahedra is equivalent to the requirement of no overlap between their respective footprints on the spherical particle surface. In this way, we map the 3D assembly of NPs and cages onto the 2D arrangement of triangles on a spherical surface. In this mapping, the sphere corresponds to a NP with its DNA shell, including the double-stranded DNA (dsDNA) segments formed upon hybridization with the cages. The diameter D of this sphere in our experiments is $D \approx 35$ nm, out of which 14.5 nm is the gold core and 10 nm is an approximate thickness of the ssDNA/dsDNA shell.

Shown in Fig. 4B are three examples of the triangle-on-a-sphere arrangements that correspond to three plausible superlattices: FCC (with 1:1 NP to DNA cage ratio, as shown in Fig. 4C), HCP, and FCC (with 1:2 ratio). FCC (1:1) clearly corresponds to the most compact footprint arrangement. Whereas FCC (1:2) can be discarded

as geometrically impossible for our size ratio ($b/D \approx 0.6$), in the case of HCP, the noncompact footprint arrangement translates into a significant entropic cost compared with that of FCC (1:1). As we show, this entropy is associated primarily with rotational degrees of freedom of DNA cages (supplementary materials), and the corresponding correction to the free energy per cage is

$$\Delta F \approx 2kT \ln \left(\frac{b^* - b}{b^*/2 - b} \right)$$

Here, $b^* = \sqrt{6D^2 - 8b^2}$. In our case ($b/D \approx 0.6$), a substantial thermodynamic advantage to FCC is given by $\Delta F \approx 2.8kT$. In addition, electrostatics and steric repulsions between cages would also favor FCC over HCP.

To further validate this conclusion, we performed numerical simulations of ground-state structures of the DNA-origami-linked nanoparticle structures using a coarse-grained representation, previously validated experimentally (30). We examined configurations of basis particles linked by tetrahedra in either FCC or HCP arrangements. In the FCC (or CD) configuration, the faces of tetrahedra are aligned (Fig. 4D), whereas in the HCP (or HD), only alternating planes align (Fig. 4E). Consequently, the longer-ranged repulsion between edges results in an energy gap that favors FCC (Fig. 4F). The size of

this gap is related to the screening length of the potential. Thus, the medium-ranged repulsion of the truncated tetrahedral linkers provides another thermodynamic driving force to stabilize FCC (or CD) over otherwise similar structures.

Thus, we have demonstrated how packing of linker footprints on the surface of isotropic nanoparticles can enforce the formation of a desired lattice, including the experimental realization of the elusive diamond superlattice and its derivatives.

REFERENCES AND NOTES

- J. E. Field, *Rep. Prog. Phys.* **75**, 126505 (2012).
- E. Yablonovitch, *J. Opt. Soc. Am. B* **10**, 283–295 (1993).
- A. V. Tkachenko, *Phys. Rev. Lett.* **89**, 148303 (2002).
- É. Marcotte, F. H. Stillinger, S. Torquato, *J. Chem. Phys.* **138**, 061101 (2013).
- A. Jain, J. R. Errington, T. M. Truskett, *Phys. Rev. X* **4**, 031049 (2014).
- A. P. Hynninen, J. H. J. Thijssen, E. C. M. Vermolen, M. Dijkstra, A. van Blaaderen, *Nat. Mater.* **6**, 202–205 (2007).
- B. Capone, I. Coluzza, F. LoVerso, C. N. Likos, R. Blaak, *Phys. Rev. Lett.* **109**, 238301 (2012).
- E. L. Thomas *et al.*, *Macromolecules* **19**, 2197–2202 (1986).
- A. M. Kalsin *et al.*, *Science* **312**, 420–424 (2006).
- P. F. Damasceno, M. Engel, S. C. Glotzer, *ACS Nano* **6**, 609–614 (2012).
- Y. Wang *et al.*, *Nature* **491**, 51–55 (2012).
- F. Romano, E. Sanz, F. Sciortino, *J. Chem. Phys.* **132**, 184501 (2010).
- Z. Zhang, A. S. Keys, T. Chen, S. C. Glotzer, *Langmuir* **21**, 11547–11551 (2005).
- N. Kern, D. Frenkel, *J. Chem. Phys.* **118**, 9882–9889 (2003).
- F. Smallegang, L. Filion, F. Sciortino, *Nat. Phys.* **10**, 653–657 (2014).
- F. W. Starr, F. Sciortino, *Soft Matter* **10**, 9413–9422 (2014).
- W. Dai, C. W. Hsu, F. Sciortino, F. W. Starr, *Langmuir* **26**, 3601–3608 (2010).
- C. Zhang *et al.*, *ACS Nano* **8**, 1130–1135 (2014).
- J. Zheng *et al.*, *Nano Lett.* **6**, 1502–1504 (2006).
- D. Nykypanchuk, M. M. Maye, D. van der Lelie, O. Gang, *Langmuir* **23**, 6305–6314 (2007).
- S. Y. Park *et al.*, *Nature* **451**, 553–556 (2008).
- A. Kuzyk *et al.*, *Nature* **483**, 311–314 (2012).
- R. J. Macfarlane *et al.*, *Science* **334**, 204–208 (2011).
- T. Vo *et al.*, *Proc. Natl. Acad. Sci. U.S.A.* **112**, 4982–4987 (2015).
- M. T. Casey *et al.*, *Nat. Commun.* **3**, 1209 (2012).
- F. Lu, K. G. Yager, Y. Zhang, H. Xin, O. Gang, *Nat. Commun.* **6**, 6912 (2015).
- P. W. K. Rothmund, *Nature* **440**, 297–302 (2006).
- S. M. Douglas *et al.*, *Nature* **459**, 414–418 (2009).
- K. G. Yager, Y. G. Zhang, F. Lu, O. Gang, *J. Appl. Cryst.* **47**, 118–129 (2014).
- C. Chi, F. Vargas-Lara, A. V. Tkachenko, F. W. Starr, O. Gang, *ACS Nano* **6**, 6793–6802 (2012).

ACKNOWLEDGMENTS

Research carried out at the Center for Functional Nanomaterials, Brookhaven National Laboratory, was supported by the U.S. Department of Energy, Office of Basic Energy Sciences (contract DE-SC0012704). H.L. was supported by a National Institutes of Health R01 grant (AG029979). F.W.S. was supported by National Institute of Standards and Technology award 70NANB13H202. We thank K. Kisslinger for help with sample preparation for TEM and J. Neitzel for the contribution to the simulation work.

SUPPLEMENTARY MATERIALS

www.sciencemag.org/content/351/6273/582/suppl/DC1
Materials and Methods
Supplementary Text
Figs. S1 to S15
Tables S1
References (31–42)
Movie S1

7 August 2015; accepted 18 December 2015
10.1126/science.aad2080

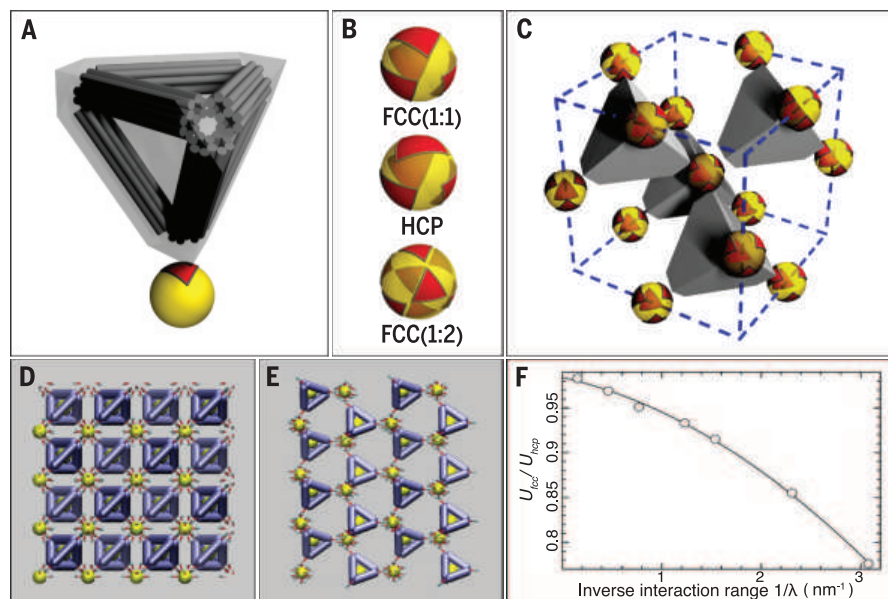


Fig. 4. Mechanism of the formation of the FCC and diamond superlattices. (A) Model of the binding interaction between the DNA tetrahedral cage and the nanoparticle. The DNA tetrahedral cage was modeled as a truncated tetrahedron completely encompassing the cage. The binding of the tetrahedral cage to the nanoparticle leaves an equilateral triangular footprint on the particle surface. (B) Triangle-on-a-sphere arrangement. (Top) For the FCC superlattice (with 1:1 NP to DNA cage ratio). (Middle) For the HCP superlattice. (Bottom) The FCC superlattice (with 1: 2 NP to DNA cage ratio). (C) Illustration of the FCC lattice of isotropic particles formed because of their connection by truncated tetrahedra in the regime shown in (B) [top, FCC (1:1)]. (D) Snapshot of the simulation for FCC (or cubic diamond) configuration. (E) Snapshot of the simulation for HCP (or hexagonal diamond) configuration. (F) Ratio of electrostatic energy for FCC (or CD) and HCP (or HD) organizations, based on screened Coulombic interactions between the negatively charged DNA bundles that comprise the tetrahedral cages. The lower energy of FCC organizations is favored.

SPINTRONICS

Electrical switching of an antiferromagnet

P. Wadley,^{1,*†} B. Howells,^{1,*} J. Železný,^{2,3} C. Andrews,¹ V. Hills,¹ R. P. Campion,¹ V. Novák,² K. Olejník,² F. Maccherozzi,⁴ S. S. Dhesi,⁴ S. Y. Martin,⁵ T. Wagner,^{5,6} J. Wunderlich,^{2,5} F. Freimuth,⁷ Y. Mokrousov,⁷ J. Kuneš,⁸ J. S. Chauhan,¹ M. J. Grzybowski,^{1,9} A. W. Rushforth,¹ K. W. Edmonds,¹ B. L. Gallagher,¹ T. Jungwirth^{2,1}

Antiferromagnets are hard to control by external magnetic fields because of the alternating directions of magnetic moments on individual atoms and the resulting zero net magnetization. However, relativistic quantum mechanics allows for generating current-induced internal fields whose sign alternates with the periodicity of the antiferromagnetic lattice. Using these fields, which couple strongly to the antiferromagnetic order, we demonstrate room-temperature electrical switching between stable configurations in antiferromagnetic CuMnAs thin-film devices by applied current with magnitudes of order 10^6 ampere per square centimeter. Electrical writing is combined in our solid-state memory with electrical readout and the stored magnetic state is insensitive to and produces no external magnetic field perturbations, which illustrates the unique merits of antiferromagnets for spintronics.

In charge-based information devices, perturbations such as ionizing radiation can lead to data loss. In contrast, spin-based devices, in which different magnetic moment orientations in a ferromagnet (FM) represent the zeros and ones (1), are robust against charge perturbations. However, the FM moments can be unintentionally reoriented and the data erased by perturbing magnetic fields generated externally or internally within the memory circuitry. If magnetic memories were based on antiferromagnets (AFMs) instead, they would be robust against charge and magnetic field perturbations. Additional advantages of AFMs compared to FMs include the invisibility of data stored in AFMs to external magnetic probes, ultrafast spin dynam-

ics in AFMs, and the broad range of metal, semiconductor, or insulator materials with room-temperature AFM order (2–7).

The energy barrier separating stable orientations of ordered spins is due to the magnetic anisotropy energy. It is an even function of the magnetic moment, which implies that the magnetic anisotropy and the corresponding memory functionality are readily present in both FMs and AFMs (8, 9). The magneto-transport counterpart of the magnetic anisotropy energy is the anisotropic magnetoresistance (AMR). In the early 1990s, the first generation of FM magnetic random access memory (MRAM) microdevices used AMR for the electrical readout of the memory state (10). AMR is an even function of the mag-

netic moment, which again implies its presence in AFMs (11). Although AMR in AFMs was experimentally confirmed in several recent studies (12–17), efficient means for manipulating AFM moments have remained elusive.

It has been proposed that current-induced spin transfer torques of the form $dM/dt \sim M \times (M \times p)$, which are used for electrical writing in the most advanced FM MRAMs (1), could also produce large-angle reorientation of the AFM moments (18). In these antidamping-like torques, M is the magnetic moment vector and p is the electrically injected carrier spin polarization. Translated to AFMs, the effective field proportional to $(M_{A,B} \times p)$ that drives the antidamping-like torque $dM_{A,B}/dt \sim M_{A,B} \times (M_{A,B} \times p)$ on individual spin sublattices A and B has the favorable staggered property, i.e., alternates in sign between the opposite spin sublattices.

In FM spin-transfer-torque MRAMs, spin-polarized carriers are injected into the free FM layer from a fixed FM polarizer by an out-of-plane electrical current driven through the FM-FM stack. In analogy, (18) assumes injection of the spin-polarized carriers into the AFM

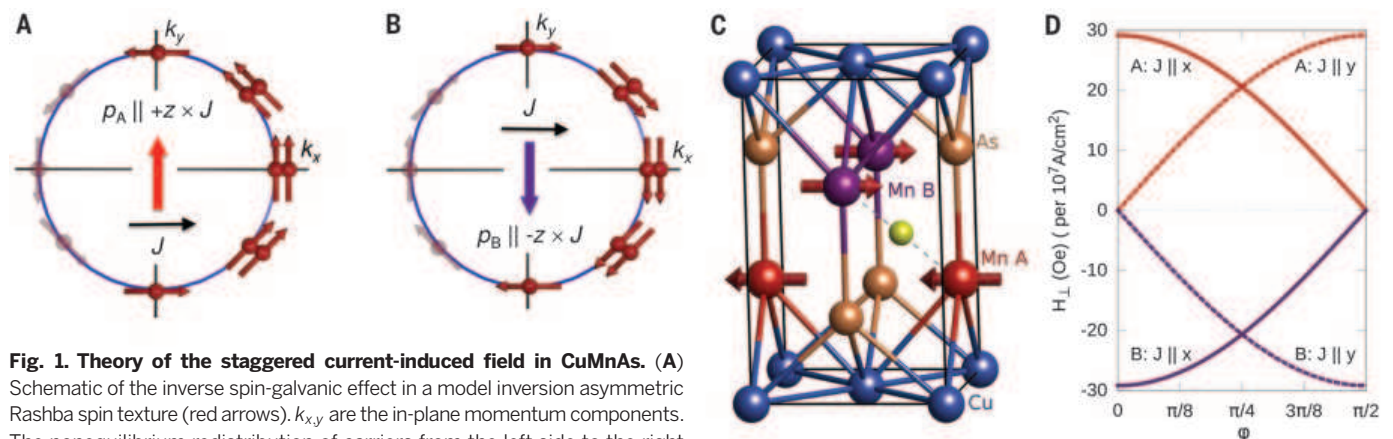


Fig. 1. Theory of the staggered current-induced field in CuMnAs. (A) Schematic of the inverse spin-galvanic effect in a model inversion asymmetric Rashba spin texture (red arrows). $k_{x,y}$ are the in-plane momentum components. The nonequilibrium redistribution of carriers from the left side to the right side of the Fermi surface results in a net in-plane spin polarization (thick red arrow) along $+z \times J$ direction, where J is the applied current (black arrow). (B) Same as (A) for opposite sense of the inversion asymmetry, resulting in a net in-plane spin polarization (thick purple arrow) along $-z \times J$ direction. (C) CuMnAs crystal structure and AFM ordering. The two Mn spin-sublattices A and B (red and purple) are inversion partners. This and panels A and B imply opposite sign of the respective local current-induced spin polarizations,

$p_A = -p_B$, at spin sublattices A and B. The full CuMnAs crystal is centrosymmetric around the interstitial position highlighted by the green ball. (D) Microscopic calculations of the components of the spin-orbit field transverse to the magnetic moments per current density 10^7 A cm^{-2} at spin sublattices A and B as a function of the magnetic moment angle ϕ measured from the x axis ([100] crystal direction). The electrical current is applied along the x and y axes.

¹School of Physics and Astronomy, University of Nottingham, Nottingham NG7 2RD, UK. ²Institute of Physics, Academy of Sciences of the Czech Republic, Cukrovarnická 10, 162 00 Praha 6, Czech Republic. ³Faculty of Mathematics and Physics, Charles University, Ke Karlovu 3, 121 16 Prague 2, Czech Republic. ⁴Diamond Light Source, Chilton, Didcot, Oxfordshire, OX11 0DE, UK. ⁵Hitachi Cambridge Laboratory, J. J. Thomson Avenue, Cambridge CB3 0HE, UK. ⁶Department of Materials Science and Metallurgy, University of Cambridge, Cambridge CB3 0HE, UK. ⁷Peter Grünberg Institut and Institute for Advanced Simulation, Forschungszentrum Jülich and JARA, 52425 Jülich, Germany. ⁸Institute of Physics, Academy of Sciences of the Czech Republic, Na Slovance 2, 182 21 Praha 8, Czech Republic. ⁹Institute of Physics, Polish Academy of Sciences, al. Lotnikow 32/46, PL-02-668 Warsaw, Poland.

*These authors contributed equally to this work. †Corresponding author. E-mail: peter.wadley@nottingham.ac.uk

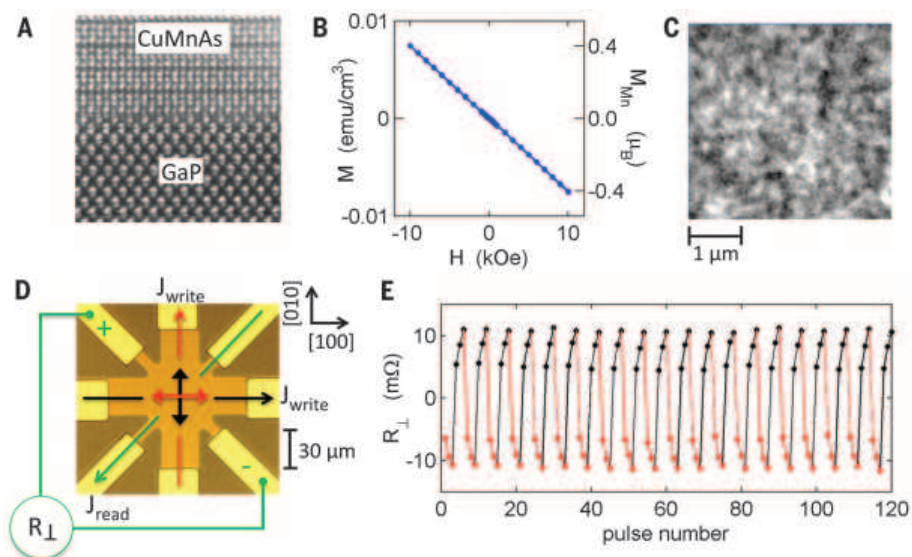


Fig. 2. Electrical switching of the AFM CuMnAs. (A) Scanning transmission electron microscopy image of CuMnAs/GaP in the [100]–[001] plane. (B) Magnetization versus applied field of an unpatterned piece of the CuMnAs/GaP wafer measured by SQUID magnetometer. (C) XMLD-PEEM image of the CuMnAs film with x-rays at the Mn L_3 absorption edge incident at 16° from the surface along the [100] axis. (D) Optical microscopy image of the device and schematic of the measurement geometry. (E) Change in the transverse resistance after applying three successive 50-ms writing pulses of amplitude $J_{\text{write}} = 4 \times 10^6 \text{ A cm}^{-2}$ alternately along the [100] crystal direction of CuMnAs (black arrow in panel D and black points in panel E) and along the [010] axis (red arrow in panel D and red points in panel E). The reading current J_{read} is applied along the $[\bar{1}10]$ axis, and transverse resistance signals R_{\perp} are recorded 10 s after each writing pulse. A constant offset is subtracted from R_{\perp} . Measurements were done at a sample temperature of 273 K.

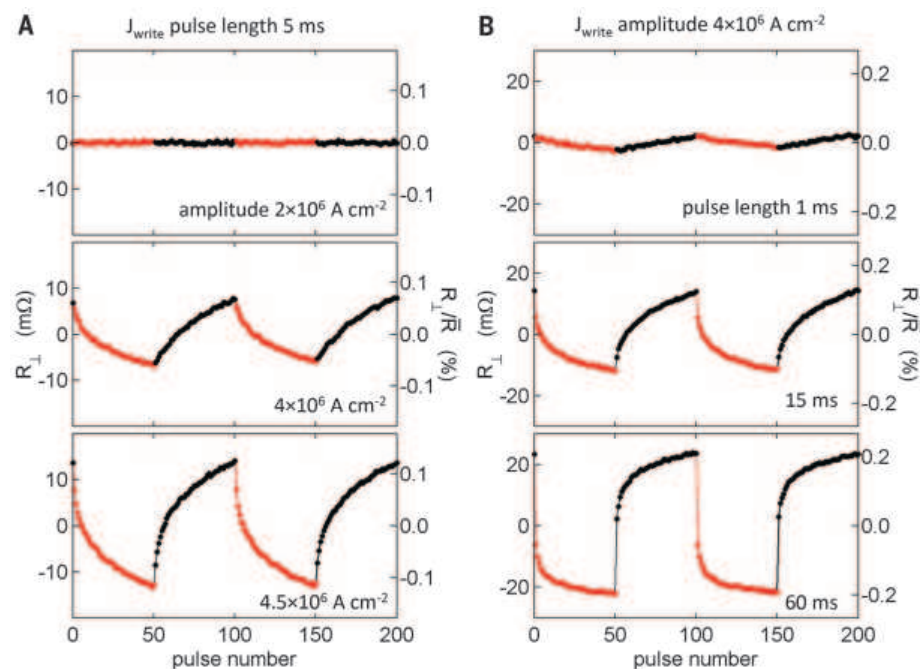


Fig. 3. Dependence of the switching on the writing pulse length and amplitude. Transverse resistance after successive writing pulses along the [100] axis (black points) and [010] axis (red points) for different current amplitudes (A) or pulse lengths (B). R_{\perp} is recorded 10 s after each writing pulse. \bar{R} is the average of the longitudinal resistance R . Measurements were done at sample temperature of 273 K. A constant offset is subtracted from R_{\perp} .

from a fixed FM polarizer by out-of-plane electrical current driven in a FM-AFM stack. However, relativistic spin-orbit coupling may offer staggered current-induced fields, which do not require external polarizers and which act in bare AFM crystals (19). The effect occurs in AFMs with specific crystal and magnetic structures for which the spin sublattices form space-inversion partners. Among these materials is a high-Néel temperature AFM, tetragonal-phase CuMnAs, which was recently synthesized in the form of single-crystal epilayers on III-V semiconductor substrates (20).

Relativistic current-induced fields observed previously in broken inversion-symmetry FM crystals (21–29) can originate from the inverse spin-galvanic effect (30–34) (Fig. 1, A and B). The full lattice of the CuMnAs crystal (Fig. 1C) has an inversion symmetry with the center of inversion at an interstitial position (green ball in the figure). This implies that the mechanism described in Fig. 1, A and B, will not generate a net current-induced spin density when integrated over the entire crystal. However, Mn atoms form two sublattices (depicted in Fig. 1C in red and purple) whose local environment has broken inversion symmetry, and the two Mn sublattices form inversion partners. The inverse spin-galvanic mechanisms of Fig. 1, A and B, will generate locally nonequilibrium spin polarizations of opposite signs on the inversion-partner Mn sublattices. For these staggered fields to couple strongly to the AFM order, it is essential that the inversion-partner Mn sublattices coincide with the two spin sublattices A and B of the AFM ground state (19). The resulting spin-orbit torques have the form $dM_{A,B}/dt \sim M_{A,B} \times p_{A,B}$, where the effective field proportional to $p_A = -p_B$ acting on the spin-sublattice magnetizations $M_{A,B}$ alternates in sign between the two sublattices. The CuMnAs crystal and magnetic structures (Fig. 1C) fulfill these symmetry requirements (20).

To quantitatively estimate the strength of the staggered current-induced field, we performed microscopic calculations based on the Kubo linear response formalism (35) (see supplementary text for details). The calculations (Fig. 1D) confirm the desired opposite sign of the current-induced field on the two spin sublattices and highlight the expected dependence on the magnetic moment angle, which implies that the AFM moments will tend to align perpendicular to the applied current. For reversible electrical switching between two stable states and the subsequent electrical detection by the AMR, the setting current pulses can therefore be applied along two orthogonal in-plane cubic axes of CuMnAs. The magnitude of the effect seen in Fig. 1D is comparable to that of typical current-induced fields applied in FMs, suggesting that CuMnAs is a favorable material for observing current-induced switching in an AFM.

Our experiments were conducted on epitaxial films of the tetragonal phase of CuMnAs, which is a member of a broad family of high-temperature I-Mn-V AFM compounds (6, 7, 20). We have observed the electrical switching and readout

effects described below in more than 20 devices fabricated from five different CuMnAs films, with thicknesses ranging from 40 to 80 nm, grown on either GaP or GaAs substrates. The electrical data shown in Figs. 2 to 4 were obtained on a 46-nm epilayer on lattice-matched GaP(001), whose transmission electron microscopy image (Fig. 2A) demonstrates excellent structural and chemical order (20). Consistent with the AFM order of the CuMnAs film, superconducting quantum interference device (SQUID) magnetometry measurements (Fig. 2B) show only the diamagnetic background of the sample substrate. X-ray magnetic linear dichroism–photoelectron emission microscopy (XMLD-PEEM) measurements at the Mn *L*3 absorption edge show that the AFM moments are oriented in the plane of the film, with a submicrometer-scale domain structure (Fig. 2C). Neutron diffraction confirmed collinear AFM order with a Néel temperature $T_N = 480$ K (20, 36). The CuMnAs film is metallic with a room-temperature sheet resistivity of 160 microhm cm.

In Fig. 2E, we demonstrate the electrical writing in a CuMnAs device (Fig. 2D). The sample was held at a stable temperature of 273 K inferred from the temperature calibration of the resistivity of the CuMnAs film. Three successive 50-ms writing pulses of amplitude $J_{\text{write}} = 4 \times 10^6$ Acm⁻² were applied alternately along the

[100] crystal axis of CuMnAs (black arrow in Fig. 2D and black points in Fig. 2E) and along the [010] axis (red arrow in Fig. 2D and red points in Fig. 2E). Note that $J_{\text{write}} = 4 \times 10^6$ Acm⁻² is the current density in the central region of the device obtained from finite element modeling for the applied current of 90 mA driven through the 28- μ m-wide writing arms of the device. The reading current J_{read} was applied along the $[\bar{1}10]$ in-plane diagonal and resistance signals, R_{\perp} , transverse to J_{read} are recorded 10 s after each J_{write} pulse. A constant offset is subtracted from R_{\perp} .

The [100]-directed writing pulses are expected to set a preference for domains with AFM spin axis along the [010] direction (black double-arrow in Fig. 2D) and the [010]-directed pulses for domains with AFM spin axis along the [100] direction (red double-arrow in Fig. 2D). Consistent with this picture, successive J_{write} pulses in one direction increase the amplitude of the readout R_{\perp} signal of one sign and pulsing in the orthogonal direction increases the amplitude of R_{\perp} of the opposite sign. As seen in Fig. 2E, all the AFM memory states can be written reproducibly. The signals are independent of the polarity of the writing current, which is expected for the current-induced switching in AFMs. The amplitude of the switching current applied in our AFM memory is comparable to that of FM

spin transfer torque MRAMs and is much lower than in the early observations of spin-orbit torque switching in FM metals, where 100 MA cm⁻² pulses were used to reverse magnetization in a Pt/Co bilayer (29).

In Fig. 3, A and B, we explore in more detail the domain reconfiguration by applying a series of 50 J_{write} pulses of varying length and amplitude along the [010] direction (red points) and [100] direction (black points) at 273 K. The data, which again show highly reproducible switching patterns, illustrate that the imbalance in the domain populations increases with the length and amplitude of the writing pulses and tends to saturate with the increasing number of pulses. Because in these measurements, heating of the central region of the device can reach tens of degrees during the writing pulses, we did not explore the switching behavior further beyond the pulse lengths and amplitudes shown in Fig. 3, A and B. More intense pulses in our device design can lead to irreproducible characteristics or device failure due to structural changes. Apart from the absolute R_{\perp} values, we also indicate in Fig. 3, A and B, relative values R_{\perp}/\bar{R} of the signal, where \bar{R} is the longitudinal resistance R averaged over the different states set by the writing pulses along the [100]/[010] directions. Below we will associate R_{\perp}/\bar{R} , reaching 0.2%, with the transverse AFM AMR. Further confirmation of the picture of the current-induced domain reconfiguration by the applied writing pulses is given by XMLD-PEEM measurements and XMLD spectroscopy (see figs. S1 and S2 and supplementary text.)

We now analyze the symmetry of the measured resistances for different probe current directions. Figure 4 shows switching data for both the transverse resistance signal and the longitudinal signal, $\Delta R/\bar{R}$, where $\Delta R = R - \bar{R}$, obtained at the sample temperature of 150 K. In these lower-temperature experiments, we applied five successive 275-ms pulses of amplitude $J_{\text{write}} = 4.5 \times 10^6$ Acm⁻² along the [100] or [010] axis to obtain signals comparable to the higher-temperature measurements. Each row in Fig. 4 corresponds to a different axis along which we apply the probe current J_{read} . From top to bottom, the reading current is applied along the crystal axis $[\bar{1}10]$, [110], [100], and [010].

Consistent with the AMR symmetry, the transverse signals (also known as the planar Hall effect) are detected for the AFM spin-axes angle set toward $\pm 45^\circ$ from the probe current, and the transverse signal flips sign when the probe current is rotated by 90° . The corresponding longitudinal signals vanish in this geometry. For AFM spin axes set toward $\pm 90^\circ$ from the probe current, the transverse signal vanishes and the longitudinal signal is detected, which is again consistent with the AMR symmetries. The AMR nature of the electrical signals is further confirmed by the comparable amplitudes of the transverse and longitudinal signals. We note that apart from the stable AMR signals, the longitudinal resistances show an additional time dependence, which is due to the cooling of the sample after the writing

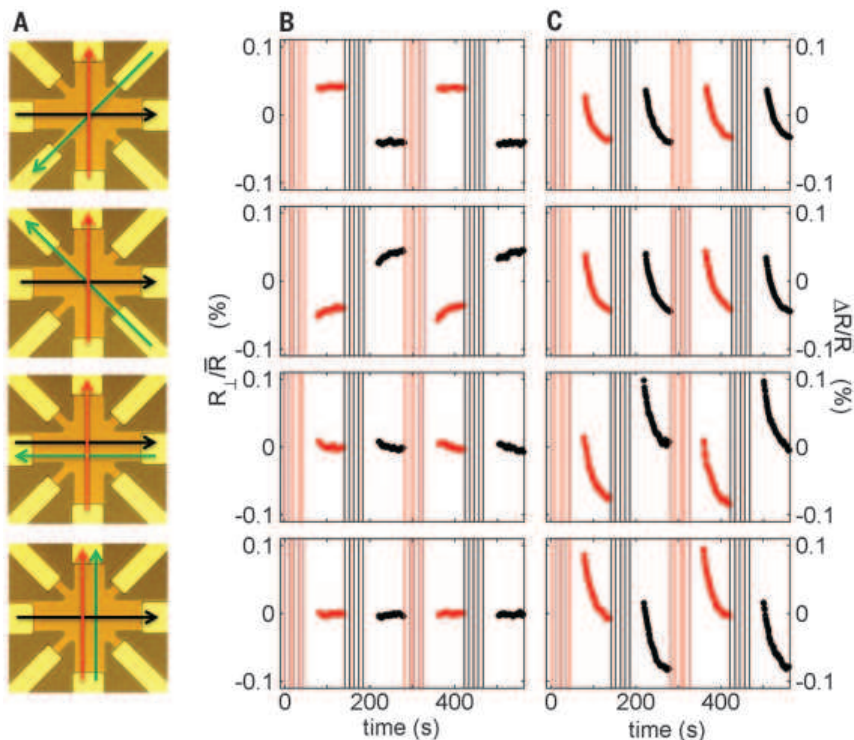


Fig. 4. AMR symmetry of the electrical readout signals. (A) Optical microscopy image of the device and of the measurement geometries with different probe current directions (green arrows). The writing current directions are shown by black and red arrows. (B) Normalized transverse resistance R_{\perp}/\bar{R} after five writing current pulses along the [100] axis (black) and five pulses along the [010] axis (red) for the reading current directions shown in (A). Vertical lines indicate the times of the pulses. The pulse length is 275 ms and amplitude $J_{\text{write}} = 4.5 \times 10^6$ Acm⁻². Measurements were done at a sample temperature of 150 K. A constant offset is subtracted from R_{\perp} . (C) As for (B) but for the normalized longitudinal resistance change, $\Delta R/\bar{R}$, where $\Delta R = R - \bar{R}$.

pulses. These isotropic changes in R correspond to a temperature change of a fraction of a Kelvin over the probing time interval.

We also observe these AMR symmetries in higher-temperature measurements. However, the AMR changes sign between the higher- and lower-temperature data, as seen when comparing the transverse resistance signals in Figs. 2 and 3 with the corresponding measurements in the first row of Fig. 4. The change in sign of the AMR is further confirmed in fig. S3 (see also the supplementary text), where the measured temperature dependence of AMR is shown and compared to calculations. From this comparison, we can infer the preferred AFM spin-axis direction for the given writing current direction. The experimental and theoretical AMR signs match if the AFM spin axis aligns perpendicular to the writing current. This is consistent with the predicted direction of the spin-orbit current-induced fields and with the XMLD-PEEM results. Measurements at high magnetic fields shown in fig. S3 (see also supplementary text) give further confirmation that the AFM spin axis aligns perpendicular to the setting current pulses. These measurements also highlight that our AFM memory can be read and written by the staggered current-induced fields and the memory state retained even in the presence of strong magnetic fields.

The staggered current-induced fields that we observe are not unique to CuMnAs. The high-Néel temperature AFM Mn_2Au (37) is another example in which the spin sublattices form inversion partners and where theory predicts large field-like torques of the form $dM_{A,B}/dt \sim M_{A,B} \times p_{A,B}$ with $p_A = -p_B$ (19). From our microscopic density-functional calculations, we obtain a current-induced field of around 20 Oe per 10^7 A cm^{-2} in Mn_2Au , which, combined with its higher conductivity, may make this a favorable system for observing current-driven AFM switching. AFMs that do not possess these specific symmetries can in principle be switched by injecting a spin current into the AFM from a spin-orbit-coupled nonmagnetic (NM) layer using an applied in-plane electrical current via the spin Hall effect, generating the antidamping-like torque $dM_{A,B}/dt \sim M_{A,B} \times (M_{A,B} \times p)$ (19). The same type of torque can be generated by the spin-orbit Berry-curvature mechanism acting at the inversion-asymmetric AFM/NM interface or in bare AFM crystals with globally noncentrosymmetric unit cells like CuMnSb (19). Our experiments in CuMnAs, combined with the prospect of other realizations of these relativistic non-equilibrium phenomena in AFMs, indicate that AFMs are now ready to join the rapidly developing fields of basic and applied spintronics, enriching this area of solid-state physics and microelectronics by the range of unique characteristics of AFMs.

REFERENCES AND NOTES

- C. Chappert, A. Fert, F. N. Van Dau, *Nat. Mater.* **6**, 813–823 (2007).
- A. V. Kimmel, A. Kirilyuk, A. Tsvetkov, R. V. Pisarev, T. Rasing, *Nature* **429**, 850–853 (2004).
- M. Fiebig *et al.*, *J. Phys. D Appl. Phys.* **41**, 164005 (2008).
- T. Yamaoka, *J. Phys. Soc. Jpn.* **36**, 445–450 (1974).
- W. Zhang *et al.*, *Phys. Rev. Lett.* **113**, 196602 (2014).
- T. Jungwirth *et al.*, *Phys. Rev. B* **83**, 035321 (2011).
- F. Măca *et al.*, *J. Magn. Magn. Mater.* **324**, 1606–1612 (2012).
- L. Néel, www.nobelprize.org/nobel_prizes/physics/laureates/1970/nel-lecture.pdf.
- R. Y. Umetsu, A. Sakuma, K. Fukamichi, *Appl. Phys. Lett.* **89**, 052504 (2006).
- J. Daughton, *Thin Solid Films* **216**, 162–168 (1992).
- A. B. Shick, S. Khmelevskiy, O. N. Mryasov, J. Wunderlich, T. Jungwirth, *Phys. Rev. B* **81**, 212409 (2010).
- B. G. Park *et al.*, *Nat. Mater.* **10**, 347–351 (2011).
- Y. Y. Wang *et al.*, *Phys. Rev. Lett.* **109**, 137201 (2012).
- X. Marti *et al.*, *Nat. Mater.* **13**, 367–374 (2014).
- I. Fina *et al.*, *Nat. Commun.* **5**, 4671 (2014).
- T. Moriyama *et al.*, *Appl. Phys. Lett.* **107**, 122403 (2015).
- D. Kriegner *et al.*, <http://arxiv.org/abs/1508.04877>.
- H. V. Gomonay, V. M. Loktev, *Phys. Rev. B* **81**, 144427 (2010).
- J. Zeleznyj *et al.*, *Phys. Rev. Lett.* **113**, 157201 (2014).
- P. Wadley *et al.*, *Nat. Commun.* **4**, 2322 (2013).
- B. Bernevig, O. Vafeck, *Phys. Rev. B* **72**, 033203 (2005).
- A. Chernyshov *et al.*, *Nat. Phys.* **5**, 656–659 (2009).
- M. Endo, F. Matsukura, H. Ohno, *Appl. Phys. Lett.* **97**, 222501 (2010).
- D. Fang *et al.*, *Nat. Nanotechnol.* **6**, 413–417 (2011).
- A. Manchon, S. Zhang, *Phys. Rev. B* **78**, 212405 (2008).
- I. M. Miron *et al.*, *Nat. Mater.* **9**, 230–234 (2010).
- U. H. Pi *et al.*, *Appl. Phys. Lett.* **97**, 162507 (2010).
- T. Suzuki *et al.*, *Appl. Phys. Lett.* **98**, 142505 (2011).
- I. M. Miron *et al.*, *Nature* **476**, 189–193 (2011).
- A. Y. Silov *et al.*, *Appl. Phys. Lett.* **85**, 5929 (2004).
- Y. K. Kato, R. C. Myers, A. C. Gossard, D. D. Awschalom, *Phys. Rev. Lett.* **93**, 176601 (2004).
- S. D. Ganichev *et al.*, <http://arxiv.org/abs/cond-mat/0403641> (2004).
- J. Wunderlich, B. Kaestner, J. Sinova, T. Jungwirth, <http://arxiv.org/abs/cond-mat/0410295v1> (2004).
- J. Wunderlich, B. Kaestner, J. Sinova, T. Jungwirth, *Phys. Rev. Lett.* **94**, 047204 (2005).
- F. Freimuth, S. Blügel, Y. Mokrousov, *Phys. Rev. B* **90**, 174423 (2014).
- V. Hills *et al.*, *J. Appl. Phys.* **117**, 172608 (2015).
- V. M. T. S. Barthem, C. V. Colin, H. Mayaffre, M.-H. Julien, D. Givord, *Nat. Commun.* **4**, 2892 (2013).

ACKNOWLEDGMENTS

We acknowledge support from the European Union (EU) European Research Council Advanced (grant 268066); the Ministry of Education of the Czech Republic (grant LM2011026); the Grant Agency of the Czech Republic (grant 14-37427); the UK Engineering and Physical Sciences Research Council (grant EP/K027808/1); the EU 7th Framework Programme (grant REGPOT-CT-2013-316014 and FP7-People-2012-ITN-316657); HGF Programme VH-NG 513 and Deutsche Forschungsgemeinschaft SPP 1568; supercomputing resources at Jülich Supercomputing Centre and RWTH Aachen University; and Diamond Light Source for the allocation of beamtime under proposal number SI-12504. We thank C. Nelson for providing the scanning transmission electron microscopy measurement.

SUPPLEMENTARY MATERIALS

www.sciencemag.org/content/351/6273/587/suppl/DC1
Supplementary Text
Figs. S1 to S3
References (38, 39)

11 March 2015; accepted 4 January 2016
Published online 14 January 2016
10.1126/science.aab1031

ICE SHEETS

Holocene deceleration of the Greenland Ice Sheet

Joseph A. MacGregor,^{1*} William T. Colgan,^{2†} Mark A. Fahnestock,³ Mathieu Morlighem,⁴ Ginny A. Catania,^{1,5} John D. Paden,⁶ S. Prasad Gogineni⁶

Recent peripheral thinning of the Greenland Ice Sheet is partly offset by interior thickening and is overprinted on its poorly constrained Holocene evolution. On the basis of the ice sheet's radiostratigraphy, ice flow in its interior is slower now than the average speed over the past nine millennia. Generally higher Holocene accumulation rates relative to modern estimates can only partially explain this millennial-scale deceleration. The ice sheet's dynamic response to the decreasing proportion of softer ice from the last glacial period and the deglacial collapse of the ice bridge across Nares Strait also contributed to this pattern. Thus, recent interior thickening of the Greenland Ice Sheet is partly an ongoing dynamic response to the last deglaciation that is large enough to affect interpretation of its mass balance from altimetry.

The dynamics of the Greenland Ice Sheet (GrIS) are coupled intimately with the surrounding ocean (1), overlying atmosphere (2), and underlying lithosphere (3). The large range of time scales spanned by these interactions and the GrIS's own internal dynamics (4) challenge our ability to predict GrIS evolution within the context of ongoing Holocene climate change (5, 6).

Despite a rapidly warming climate (6), recent dramatic changes in ocean-terminating outlet

glaciers along the margin of the GrIS (7–9), its vulnerability to further oceanic erosion (10), and a sustained negative total mass balance (11–13), more than half of the GrIS interior is presently thickening (8, 14–16), and a portion of its southwestern margin is decelerating (17). Climate histories reconstructed from ice cores show that the GrIS persisted even when atmospheric temperatures were higher by several degrees Celsius (18) and insolation forcing was larger than at present (19). Reconciling these observations is critical to

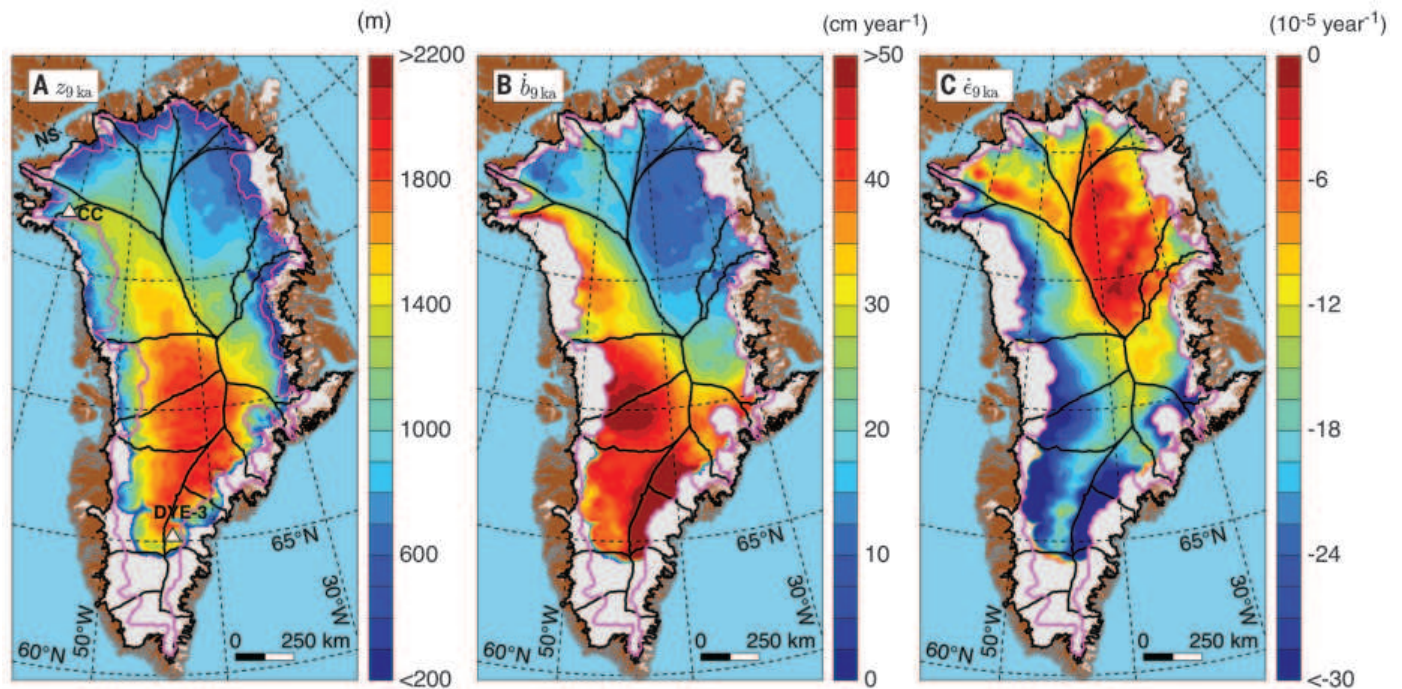


Fig. 1. Constraints on the Holocene-averaged balance ice flux across the GrIS from dated radiostratigraphy. (A) Ice-equivalent depth of the 9-ka isochrone (Z_{9ka}) [determined as in (21)]. Black lines denote major ice-drainage basins (36). NS, Nares Strait. White triangles denote Camp Century (CC) and DYE-3 ice core sites. The magenta line represents the outer limit of reliable 1D modeling of depth-age relations to 9 ka (fig. S4). (B) Mean ice-equivalent accumulation rate over the past 9000 years (\hat{b}_{9ka}). (C) Mean vertical strain rate within the 9- to 0-ka portion of the ice column ($\hat{\epsilon}_{9ka}$).

predicting the future of the GrIS amid ongoing climate change.

The internal stratigraphy of an ice sheet, as observed by ice-penetrating radar, provides a valuable constraint upon its history (3, 20). This radiostratigraphy records the spatial variation of an ice sheet's response to the combination of both external forcings and its internal dynamics. Here we use a dated radiostratigraphy for the whole of the GrIS (21) to calculate the ice sheet's balance velocity during the last three quarters of the Holocene epoch [9 to 0 thousand years ago (ka)].

Balance velocities represent the pattern of depth-averaged ice flow (22). Instead of calculating the balance velocity for the entire ice column, we restrict our analysis to the portion of the ice sheet between the subaerial ice surface and the depth of the 9-ka isochrone (Fig. 1A and fig. S1). This approach avoids the complexity inherent to the interpretation of deeper radiostratigraphy, which is more likely to have experienced substantial horizontal shear and nonsteady flow.

The input ice flux during the Holocene is estimated using the mean accumulation rate over the past 9000 years from one-dimensional (1D) modeling of the depth-age relation of dated reflections (Fig. 1B and figs. S2 and S3) (3), instead of using a compilation or model of modern accumulation rates. During this period, the accumulation-rate history of Greenland's interior was stable across millennial time scales (23), except more than 7 ka in the northwest region, where it was lower (24). Holocene thinning of the GrIS (5) would have increased vertical strain rates, but this effect is small compared with the relative change in accumulation rate between our period of interest and modern values (fig. S8).

When calculating a full-thickness balance velocity, the basal mass balance is assumed to be negligible. In our analysis, the equivalent quantity is the vertical velocity at the depth of the 9-ka isochrone, which is rarely negligible but readily estimated using the same 1D models. Because the ratio between the Holocene-averaged balance and surface speeds is often close to unity (figs. S5 and S6), we can directly compare maps of Holocene-averaged and modern surface velocity. These 1D models and the balance velocity are evaluated only in the ice-sheet interior, where the paths of the particles that form these Holocene-aged reflections are less likely to have been distorted drastically by horizontal gradients in ice flow (25) (fig. S4).

We find that most of the GrIS interior (95%) is slower now than it was, on average, during the Holocene (Fig. 2). Even near the central ice divide, where the absolute decrease in surface

speed is low, the relative decrease in speed is also large (>50%). Considering modeling uncertainty, >87% of the ice-sheet interior has decelerated significantly (fig. S7). Generally higher accumulation rates during this period can explain this pattern only in northeastern Greenland (Fig. 3A and figs. S7 and S8), indicating that the inferred deceleration includes a dynamic component elsewhere. This widespread Holocene deceleration of the GrIS suggests that its dynamic response to the last deglaciation continues to propagate throughout the ice sheet.

The millennial-scale evolution of GrIS rheology can partly explain this response. Ice deposited during the last glacial period (LGP) is approximately three times less viscous ("softer") than ice deposited during the Holocene (26). To explain observations of subtle thickening (~ 1 cm year $^{-1}$) at DYE-3, Reeh (4) hypothesized that, as softer LGP ice is buried by stiffer Holocene ice, the GrIS interior will thicken (hereafter referred to as "Reeh thickening"). Reeh thickening is distinct from that induced by increased accumulation rate, decreased rate of firn densification, post-LGP isostatic adjustment, or horizontal deceleration due to other poorly constrained mechanisms (e.g., increasing basal friction). By continuity, it follows that this transient viscosity change would also have caused the GrIS interior to decelerate after deglaciation.

We assess the modern ice-sheet-wide deceleration associated with the LGP-Holocene viscosity contrast by modeling this deceleration at the GrIS surface with a second, independent 1D ice-flow model. This model includes a 3:1

¹Institute for Geophysics, The University of Texas at Austin, Austin, TX 78758, USA. ²Geological Survey of Denmark and Greenland, Copenhagen DK-1350, Denmark. ³Geophysical Institute, University of Alaska Fairbanks, Fairbanks, AK 99775, USA. ⁴Department of Earth System Science, University of California, Irvine, Irvine, CA 92697, USA. ⁵Department of Geological Sciences, The University of Texas at Austin, Austin, TX 78712, USA. ⁶Center for Remote Sensing of Ice Sheets, The University of Kansas, Lawrence, KS 66045, USA.
*Corresponding author. E-mail: joemac@ig.utexas.edu †Present address: Department of Earth and Space Science and Engineering, York University, Toronto, Ontario M3J 1P3, Canada.

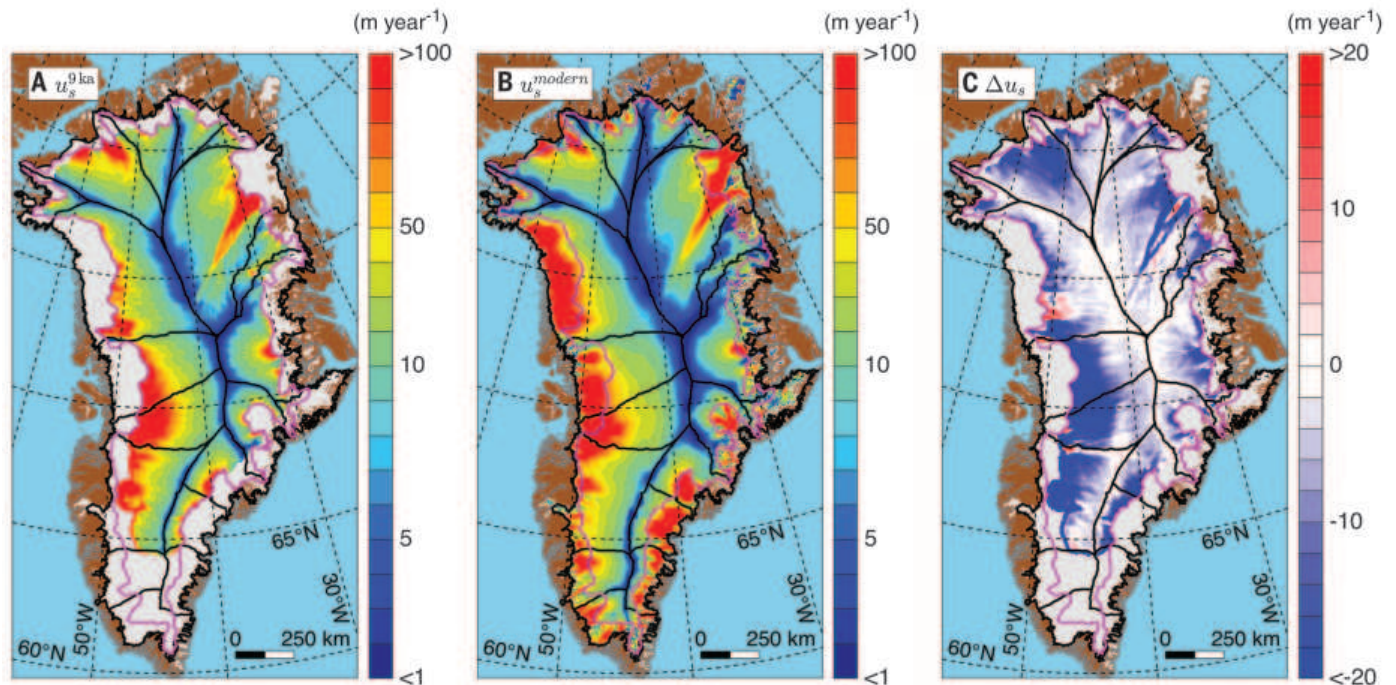


Fig. 2. Holocene-averaged and modern surface speed across the GrIS. (A) Holocene-averaged surface speed u_s^{9ka} (i.e., Holocene balance speed divided by shape factor) (fig. S5B). **(B)** Composite surface speed, u_s^{modern} , from 1995–2013 (37). **(C)** Change in surface speed between the present and the Holocene average ($\Delta u_s = u_s^{modern} - u_s^{9ka}$).

viscosity contrast (26) at the present depth of the beginning of the Holocene (11.7 ka) (21) and is consistent with modern surface velocity and ice temperature estimated by a higher-order ice-sheet model (27). The modeled horizontal deceleration rate (Fig. 3B), resulting from the downward advection of the LGP-Holocene transition (fig. S9), is most comparable to that which we observed in southern Greenland (south of 68°N) (Fig. 3C). There, Holocene-averaged accumulation rates are relatively high (fig. S8), so the rate of burial of LGP ice by Holocene ice is higher, the LGP-Holocene transition is deeper, and its associated viscosity contrast exerts a greater influence upon ice flow. Holocene-averaged accumulation rates in the southern GrIS are higher than modern values only in a narrow region along the central ice divide and are lower on the flanks (fig. S8), further supporting the notion of a dynamic component to the inferred deceleration (Fig. 3A).

Corroborating and expanding upon Reeh's original hypothesis, we suggest that downward advection of the LGP-Holocene transition partly explains the subtle deceleration we infer in the interior of the southern GrIS. The dynamic consequences of this effect are predicted to have increased nonlinearly within the GrIS interior during the Holocene and to continue for tens of millennia (4).

The rheological evolution of the GrIS occurred in conjunction with substantial peripheral changes during the last deglaciation, as it retreated from the continental shelf, with subsequent effects on the interior. In particular, during the LGP, the

northwestern sector of the GrIS was connected to the Innuitian Ice Sheet across Nares Strait (28). After the last deglaciation, the GrIS thinned rapidly at Camp Century (5). This thinning was attributed to the collapse of the Nares Strait ice bridge ~10 ka (5, 29), and residual thinning may be ongoing (30). The Holocene-averaged flow of this sector of the ice sheet was significantly faster than at present (Fig. 2C), and its subsequent dynamic deceleration is at least an order of magnitude greater than can be attributed to the LGP-Holocene viscosity contrast (Fig. 3). This sector's Holocene-averaged accumulation rate was significantly lower than at present (fig. S8) (24), which also suggests that substantial dynamic thinning occurred there. Together, these patterns indicate that faster ice flow in northwestern Greenland during the Holocene included a dynamic response to ice-bridge collapse.

The Holocene deceleration of the northeastern GrIS is similar in magnitude to that of the northwestern region, but it is more likely related to higher Holocene-averaged accumulation rates than to modern rates (Fig. 3A and fig. S8D). Accumulation rates in this region are low (<20 cm year⁻¹) (Fig. 1B), so the dynamic component of this deceleration is harder to constrain, given the difference between Holocene-averaged and modern patterns of accumulation rates. Substantial burial of LGP ice by Holocene ice has yet to occur there (Fig. 1A), so the predicted deceleration due to the LGP-Holocene viscosity contrast is negligible (Fig. 3B). This sector is partially grounded below sea level (10) and recently experienced rapid grounding-line retreat (9).

This vulnerable configuration probably existed throughout the Holocene and may have produced repeated rapid dynamic changes that we cannot resolve from a multimillennial mean balance velocity.

Assuming conservation of mass, the modern horizontal deceleration rates we infer are proportional to dynamically induced rates of ice-sheet thickening. Multiyear to multidecadal altimetric and mass balance observations from multiple platforms show that the interiors of most major GrIS drainage basins have thickened, particularly in southwestern and northeastern Greenland (8, 11, 14–16, 30). These changes could be related to a warming-induced increase in precipitation in the interior (31) or decadal-scale variability in accumulation rate (32), but there is low confidence in these possibilities (33). We propose that this thickening is partly due to ongoing subtle deceleration of the GrIS interior and transient multimillennial-scale processes that are not directly related to modern climate. The region of greatest observed thickening is the southern GrIS interior (south of 70°N) (Fig. 3C), where inferred and modeled rates of horizontal deceleration are also best correlated (Fig. 3C), strongly suggesting that non-negligible Reeh thickening is occurring there.

Gravimetric and input-output-method estimates of ice-sheet mass balance should be less sensitive to Reeh thickening, which may explain the good agreement between these two methods for the GrIS (11, 34). Analyses of altimetric observations of the southern GrIS that do not account for Reeh thickening risk misattribution of

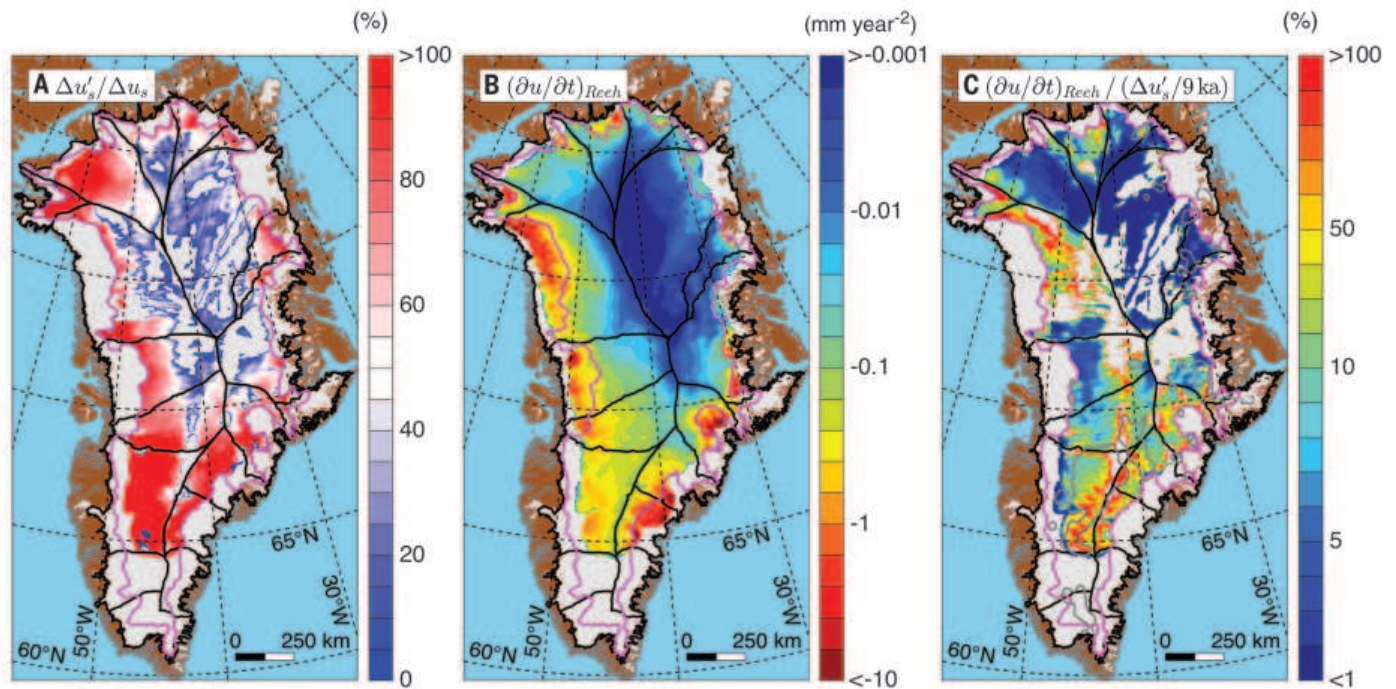


Fig. 3. Dynamic Holocene deceleration of the GrIS. (A) Relative contribution of ice dynamics to change in surface speed ($\Delta u'_s/\Delta u_s$). Gaps in coverage are due to positive $\Delta u'_s$ values. (B) Modeled horizontal deceleration rate due to the LGP-Holocene viscosity contrast [$(\partial u/\partial t)_{Reeh}$] over the past 1000 years, where $Z_{11.7ka}$ is available (21). (C) Ratio of modeled to inferred dynamic deceleration rate [$(\partial u/\partial t)_{Reeh}/(\Delta u'_s/9 \text{ ka})$]. Gray contours outline regions where the mean 2003–2009 thickening rate was $>10 \text{ cm year}^{-1}$ (16).

long-term dynamic thickening as overestimated accumulation rate and, hence, also as overestimated total ice-sheet mass balance. Indeed, in a recent intercomparison study, laser altimetry estimates of GrIS mass balance exceed those of the other two methods (11).

Our results demonstrate that the GrIS's multimillennial-scale response to the last deglaciation is elucidated by its radiostratigraphy and that this response continues to influence its present dynamics. Whereas recent decadal-to-centennial-scale climate forcings are likely the primary cause of the GrIS's present negative mass balance (13), this more recent response is overprinted on the ice sheet's millennial-scale evolution. For southern Greenland in particular, ignoring this long-term dynamic signal risks underestimating recent mass loss when invoking the common assumption of reference-period steady state (35). Separately, the Holocene deceleration of the northwestern sector of the GrIS is further evidence of both the sensitivity and long-term memory of the ice sheet to evolving boundary conditions.

REFERENCES AND NOTES

- Joughin, R. B. Alley, D. M. Holland, *Science* **338**, 1172–1176 (2012).
- L. C. Andrews *et al.*, *Nature* **514**, 80–83 (2014).
- M. Fahnestock, W. Abdalati, I. Joughin, J. Brozena, P. Gogineni, *Science* **294**, 2338–2342 (2001).
- N. Reeh, *Nature* **317**, 797–799 (1985).
- B. M. Vinther *et al.*, *Nature* **461**, 385–388 (2009).
- S. A. Marcott, J. D. Shakun, P. U. Clark, A. C. Mix, *Science* **339**, 1198–1201 (2013).
- T. Moon, I. Joughin, B. Smith, I. Howat, *Science* **336**, 576–578 (2012).
- B. M. Csatho *et al.*, *Proc. Natl. Acad. Sci. U.S.A.* **111**, 18478–18483 (2014).
- J. Mouginot *et al.*, *Science* **350**, 1357–1361 (2015).
- M. Morlighem, E. Rignot, J. Mouginot, H. Seroussi, E. Larour, *Nat. Geosci.* **7**, 418–422 (2014).
- A. Shepherd *et al.*, *Science* **338**, 1183–1189 (2012).
- J. E. Box, W. Colgan, *J. Clim.* **26**, 6990–7002 (2013).
- K. K. Kjeldsen *et al.*, *Nature* **528**, 396–400 (2015).
- R. Thomas *et al.*, *Science* **289**, 426–428 (2000).
- O. M. Johannessen, K. Khvorostovsky, M. W. Miles, L. P. Bobylev, *Science* **310**, 1013–1016 (2005).
- T. Schenk, B. Csáthó, *IEEE Trans. Geosci. Rem. Sens.* **50**, 3302–3316 (2012).
- A. J. Tedstone *et al.*, *Nature* **526**, 692–695 (2015).
- NEEM community members, *Nature* **493**, 489–494 (2013).
- W. J. van de Berg, M. van den Broeke, J. Ettema, E. van Meijgaard, F. Kaspar, *Nat. Geosci.* **4**, 679–683 (2011).
- I. M. Whillans, *Nature* **264**, 152–155 (1976).
- J. A. MacGregor *et al.*, *J. Geophys. Res. Earth Surf.* **120**, 212–241 (2015).
- A. M. Le Brocq, A. J. Payne, M. J. Siegert, *Comput. Geosci.* **32**, 1780–1795 (2006).
- D. A. Meese *et al.*, *Science* **266**, 1680–1682 (1994).
- S. O. Rasmussen *et al.*, *Clim. Past* **9**, 2713–2730 (2013).
- E. D. Waddington, T. A. Neumann, M. R. Koutnik, H.-P. Marshall, D. L. Morse, *J. Glaciol.* **53**, 694–712 (2007).
- W. S. B. Paterson, *Cold Reg. Sci. Technol.* **20**, 75–98 (1991).
- H. Seroussi *et al.*, *J. Glaciol.* **59**, 1024–1034 (2013).
- J. England *et al.*, *Quat. Sci. Rev.* **25**, 689–703 (2006).
- M. Zreda, J. England, F. Phillips, D. Elmore, P. Sharma, *Nature* **398**, 139–142 (1999).
- W. S. B. Paterson, N. Reeh, *Nature* **414**, 60–62 (2001).
- J. Ettema *et al.*, *Geophys. Res. Lett.* **36**, L12501 (2009).
- J. R. McConnell *et al.*, *Nature* **406**, 877–879 (2000).
- D. G. Vaughan *et al.*, in *Observations: Cryosphere*, T. F. Stocker *et al.*, Eds. (Cambridge Univ. Press, 2013), pp. 317–382.
- M. van den Broeke *et al.*, *Science* **326**, 984–986 (2009).
- W. Colgan *et al.*, *Ann. Glaciol.* **56**, 105–117 (2015).
- H. J. Zwally, M. B. Giovinetto, M. A. Beckley, J. L. Saba, Antarctic and Greenland Drainage Systems (GSFC Cryospheric Sciences Laboratory, 2012); http://icesat4.gsfc.nasa.gov/cryo_data/ant_grn_drainage_systems.php.
- I. Joughin, B. Smith, I. M. Howat, T. Scambos, T. Moon, *J. Glaciol.* **56**, 415–430 (2010).

ACKNOWLEDGMENTS

This work was supported by NSF (grants ARC 1107753, ARC 1108058, and ANT 0424589) and NASA (grants NNX12AB71G and NNX15AD55G). We thank the organizations (Center for Remote Sensing of Ice Sheets and Operation IceBridge) and innumerable individuals who aided in the collection and processing of radar data used in this study. Most of the early radar data used in this study were collected as part of NASA's Program for Arctic Regional Climate Assessment, which was initiated by Dr. Robert Thomas. We also thank I. Joughin for providing the updated surface-velocity composite. J.A.M., M.A.F., and G.A.C. designed this study; J.D.P. and S.P.G. contributed to the collection and processing of the radar data; J.A.M., W.T.C., M.A.F., M.M., and G.A.C. analyzed the results and wrote the manuscript; and all authors discussed the results and edited the manuscript. Data are archived at the National Snow and Ice Data Center (<http://nsidc.org/data/rrrag4>).

SUPPLEMENTARY MATERIALS

www.sciencemag.org/content/351/6273/590/suppl/DC1
Materials and Methods
Figs. S1 to S9
References (38–46)

23 March 2015; accepted 7 January 2016
10.1126/science.aab1702

HONEYBEE DISEASE

Deformed wing virus is a recent global epidemic in honeybees driven by *Varroa* mites

L. Wilfert,^{1*} G. Long,² H. C. Leggett,^{2†} P. Schmid-Hempel,³ R. Butlin,² S. J. M. Martin,⁴ M. Boots^{1‡}

Deformed wing virus (DWV) and its vector, the mite *Varroa destructor*, are a major threat to the world's honeybees. Although the impact of *Varroa* on colony-level DWV epidemiology is evident, we have little understanding of wider DWV epidemiology and the role that *Varroa* has played in its global spread. A phylogeographic analysis shows that DWV is globally distributed in honeybees, having recently spread from a common source, the European honeybee *Apis mellifera*. DWV exhibits epidemic growth and transmission that is predominantly mediated by European and North American honeybee populations and driven by trade and movement of honeybee colonies. DWV is now an important reemerging pathogen of honeybees, which are undergoing a worldwide manmade epidemic fueled by the direct transmission route that the *Varroa* mite provides.

The European honeybee *Apis mellifera* is an important domesticated animal that is used worldwide for commercial pollination of intensive and high-value crops, such as nuts and fruit, as well as for honey production. *A. mellifera*, originally from East Asia (1), has been intensively managed by beekeepers and exported from its native origins in Europe and Africa to the New World (North and South America and Hawaii) and Oceania (Australia and New Zealand) by European settlers, where beekeeping accompanied agricultural intensification. Although wild pollinators play an important role in the pollination of wild flowering and crop plants (2), our current horticultural systems also rely on managed honeybees. However, the global stock of domesticated honeybees is growing more slowly than the agricultural demand for pollination (3). Understanding the key threats to *A. mellifera* is important if we are to maintain large populations of bees for honey production and crop pollination services. Although the number of honeybee hives has increased by 45% on a global scale, there have been major regional declines (e.g., a reduction of 59% in the United States from 1947 to 2005), and globally beekeepers have been reporting high overwintering colony mortalities, which threaten the sustainability of bee husbandry (4). Although many factors, ranging from agricultural intensification to the use of pesticides, have been implicated in pollinator declines (5), RNA viral

infections transmitted by the ectoparasitic mite *Varroa destructor* have the potential to be major contributors to global honeybee colony mor-

talities (6). In particular, deformed wing virus (DWV) is the key pathogen associated with overwinter mortality of *Varroa*-infested colonies (7–10). The *Varroa* mite expanded from its native host, the Asian honeybee *A. cerana*, to the European honeybee, *A. mellifera*, in the mid-20th century and now has a global distribution (11). Although DWV occurs in *Varroa*-free natural populations (12–14), DWV appears to amplify in the presence of the mite, either because it can replicate in *Varroa* (15, 16) or because virus particles accumulate in the mites' guts [(17), but see (18)]. Moreover, *Varroa* can inject the virus directly into the bee's hemolymph (15, 19), thus circumventing some of the natural barriers to vertical or horizontal transmission between bees, such as the exoskeleton and the peritrophic membranes lining the digestive tract (20). The recent *Varroa* invasions in Hawaii (12) and New Zealand (13) led to an increase in DWV prevalence among colonies and increased viral loads in infected individuals. Simultaneously, there has been a loss in viral diversity. The Hawaiian and New Zealand invasions (12, 13) indicate that the presence of *Varroa* increases the spread of DWV across honeybee populations. There is also evidence that *Varroa* not only acts as a vector but also increases the virulence of DWV infections,

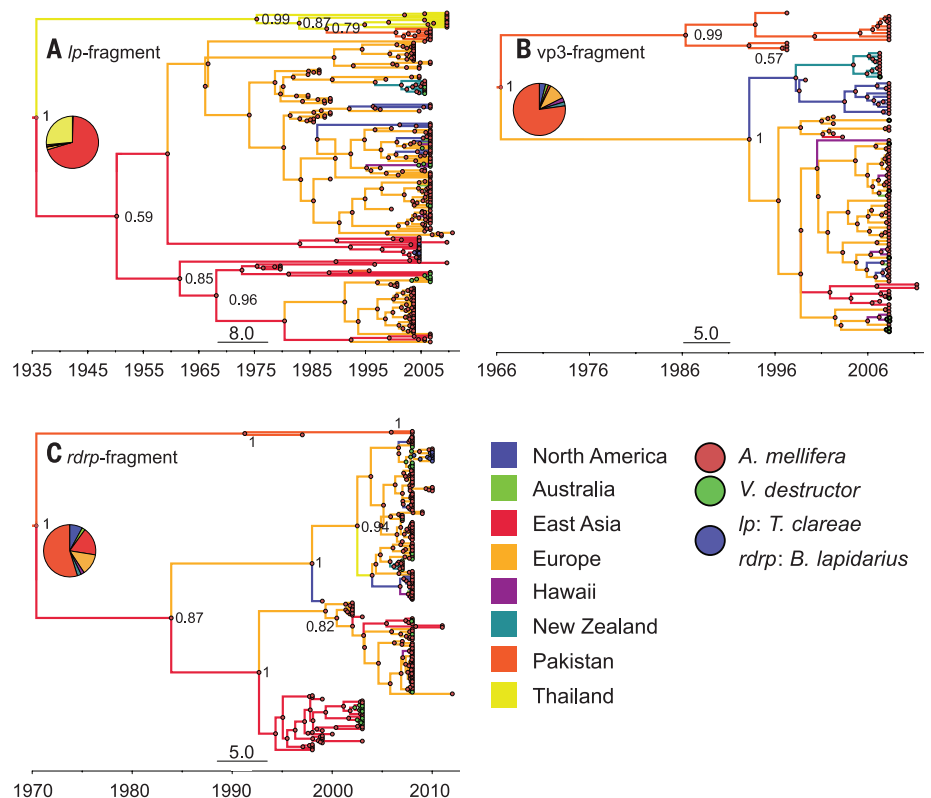


Fig. 1. Phylogenetic reconstruction of three fragments of DWV, showing host and geographic structure. The figure shows maximum clade credibility trees for the *Lp* fragment (A), *Vp3* fragment (B), and the *RdRp* fragment (C) of DWV. The branches are colored according to the lineages' inferred geographic origin, and the nodes are colored according to the inferred host species. Posterior support >0.5 is indicated for nodes up to the fourth order; horizontal bars indicate the time scale in years. The x axis shows time in years. The pie charts show the inferred posterior distribution of the root's geographic location state. Fig. S3 provides an alternative visualization of this graph.

¹Centre for Ecology and Conservation, University of Exeter, Penryn Campus, Penryn TR11 9FE, UK. ²Department of Animal and Plant Sciences, University of Sheffield, Sheffield S10 2TN, UK. ³Institute of Integrative Biology, ETH Zürich, 8092 Zürich, Switzerland. ⁴School of Environment and Life Sciences, University of Salford, Manchester M5 4WT, UK.

*Corresponding author. E-mail: lena.wilfert@ex.ac.uk †Present address: Department of Genetics, University of Cambridge, Cambridge CB2 3EH, UK. ‡Present address: Department of Integrative Biology, University of California, Berkeley, CA 94720, USA.

turning relatively asymptomatic infections into “overt” infections associated with clinical disease symptoms (15, 21–23) and increasing colony mortalities in winter (7–10). There is strong evidence that *Varroa* affects individual and colony-level DWV epidemiology in honeybees, but its importance to the global spread and ongoing worldwide transmission of DWV is less well understood. This is an important problem because of the crucial role that honeybees play in global food production. Furthermore, honeybee diseases also pose risks for the wider pollinator community (24, 25), and we need to understand the global drivers of disease spread in order to manage the transfer of disease to novel hosts.

In this study, we used a phylogeographic approach to test whether *Varroa*-vectored DWV is a globally emerging honeybee pathogen and to determine the dominant routes of DWV spread. There are two main scenarios for DWV's origin that can be distinguished based on its phylogeography. The first scenario is that *Varroa* introduced DWV to the European honeybee *A. mellifera* and caused a global epidemic. Under this scenario, we would expect East Asian *Varroa* populations to be the ancestral host of DWV. The second scenario is that DWV is a reemerging disease whose current pandemic is promoted by *Varroa*, in which case we would expect *A. mellifera* as the ancestral host. We estimated the major routes of global transmission by compar-

ing geographic and host-specific patterns, dated by the viral evolutionary rate, which we derived for three genomic fragments. We collected a total of 246 DWV sequences from honeybees and *Varroa* mites in 32 geographic locations in 17 countries worldwide and supplemented these with all known publicly available DWV sequence data; together, these data were used to infer the epidemic and migration history driving present-day global DWV dynamics.

Our analysis shows a recent global radiation and pandemic of DWV, with the most recent common ancestor coinciding in time with the global emergence of the *Varroa* mite as a honeybee ectoparasite in the mid-20th century (11). The most recent common ancestor for each fragment dates back to the mid-20th century, with mean root heights of 44 years [*RdRp* fragment; 95% Highest Posterior Density (HPD), 27 to 63 years), 47 years (*Vp3* fragment; 95% HPD, 28 to 74 years), and 78 years (*Lp* fragment; 95% HPD, 45 to 118 years). All fragments show significant exponential growth over past decades, with doubling intervals of ~13 years [*Lp* fragment, 16.4 years (95% HPD, 9.9 to 46.8 years); *RdRp* fragment, 11.6 years (95% HPD, 6 to 96.6 years); *Vp3* fragment, 12.4 years (95% HPD, 6.1 to 262.8 years)]. This finding is supported by a Gaussian Markov random field Skyride analysis (fig. S4). Because population structure tends to produce a spurious signature of declining effective population sizes (26), we excluded the small number of geographically disparate samples available in GenBank from 2010 for our demographic analyses (database S1). With the exception of the *RdRp* fragment, exponential growth is also significant when including samples from 2010 to 2013. In combination, these results lend support to the hypothesis that DWV radiated recently from a common source and spread exponentially around the globe (27).

This demographic pattern is consistent with *Varroa* having an important temporal role in the recent expansion of DWV, but the global distribution and the ancestral host state of this virus is also consistent with DWV being a reemerging honeybee virus. DWV has been isolated from honeybee populations that had not been exposed to *Varroa* [Australia (GenBank accession numbers HQ655496 to HQ655501) (28) and present study; fig. S5); Colonsay Island, Scotland (14); Hawaii (12); Ile d'Ouessant, France (14); Isle of Man (present study); Newfoundland (29); and New Zealand (13)]. Emerging pathogens can spread ahead or independently of the initial host if they can replicate in newly encountered hosts, as is the case for many human zoonoses such as SARS (severe acute respiratory syndrome) and wildlife diseases such as squirrel pox (30, 31). In this case, because *Varroa* increases DWV prevalence and titer in honeybees overall (12, 13), it may promote human-mediated viral spread by increasing the number of infected bees and their transmission potential, even without the mite being spread itself. In addition to the presence of DWV in *Varroa*-free populations, the phylogenetic reconstruction also contradicts *Varroa*

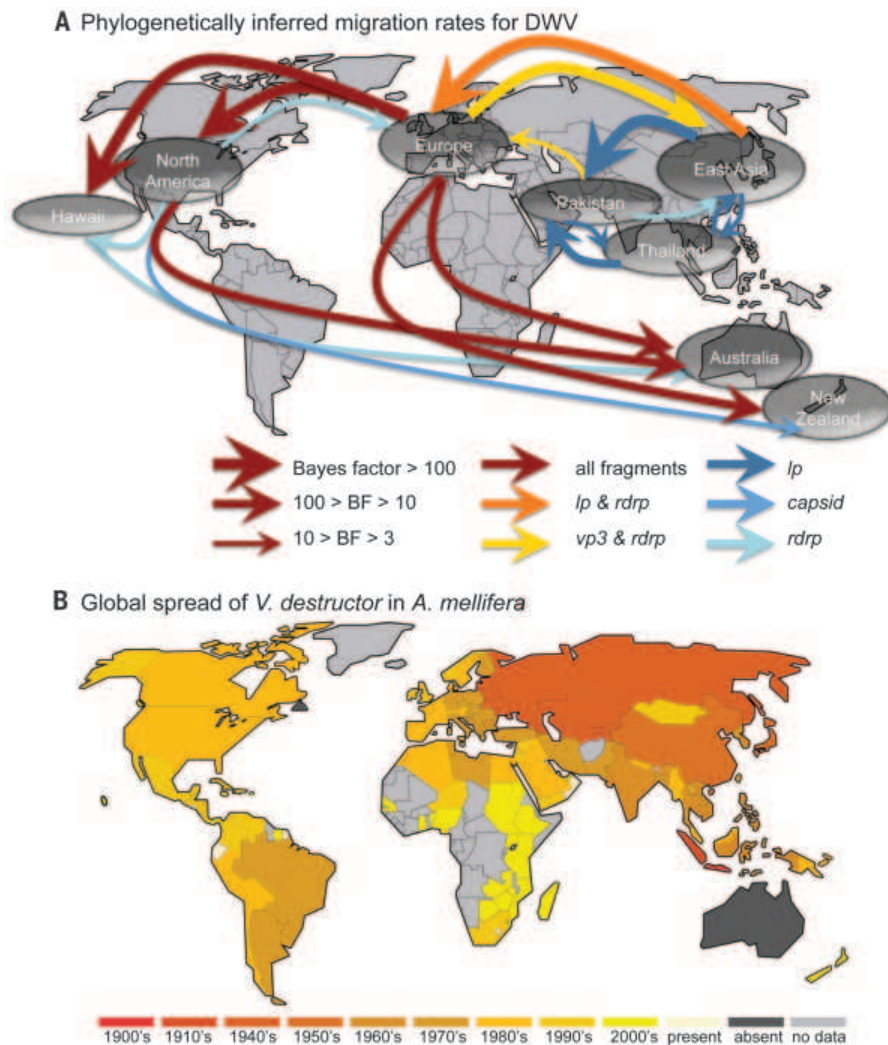


Fig. 2. Global migration patterns of DWV and *V. destructor*. (A) Phylogenetically inferred major migration patterns of DWV. The weight of the line indicates the Bayes factor support for nonzero transition rates (arrows, from thin to thick, indicate BFs of 3 to 10, 10 to 100, and >100); the color indicates the fragments for which these routes were supported (note that the Thai population was only available for the *Lp* fragment; table S5 includes detailed results). (B) Temporal spread of *V. destructor* in *A. mellifera*, based on first records per country (see the supplementary materials); to reflect the coarseness in the data, the temporal spread is shown by decade. Currently, the only remaining *Varroa*-free large land masses with substantial honeybee populations are Australia and Newfoundland; mounting evidence indicates that sub-Saharan Africa has been invaded since the turn of the century.

as the ancestral host of the virus. The ancestral host is unambiguously identified as *A. mellifera* (state probability $P_{Lp} = 99.43\%$, $P_{Vp3} = 97.18\%$, $P_{RdRp} = 92.7\%$) and not *V. destructor* (Fig. 1) or *A. cerana* (figs. S6 and S7). The geographic origin is less certain, with ancestral states being reconstructed with low probabilities (Lp fragment, East Asia, $P_{Lp} = 69.77\%$; $Vp3$ and $RdRp$ fragments, Pakistan, $P_{Vp3} = 77.25\%$, $P_{RdRp} = 54.84\%$). Although we cannot categorically rule out the possibility that DWV was introduced to honeybees from an entirely unknown host, this pattern does rule out *Varroa* and *A. cerana* as the ancestral DWV hosts.

The most parsimonious explanation for the phylogenetic pattern is our second scenario: DWV is an endemic honeybee pathogen that has recently reemerged through ecological change and the spread of *Varroa* as a vector, alongside increased global movement of infected bees or other contaminated material, such as pollen. This conclusion supports previous work that postulated that the ancestral form of DWV may have been associated with *A. mellifera* (32) and that similarities between DWV lineages may represent a recent introduction from *A. mellifera* into other *Apis* species (33).

Our data show that the recent spread of DWV is driven by European *A. mellifera* populations (Figs. 1 and 2A) and follows a similar pattern to the spread of *Varroa* (Fig. 2B), despite increased regulation and control of the global trade in honeybees (11). Combining results from the three fragment subsamples, Europe then North America emerge as the main hubs of DWV transmission to the New World and Oceania (Fig. 2 and table S5). Additionally, there is strong support for migration between East Asia and Europe, in both directions, as well as from Pakistan to Europe in the case of the $Vp3$ and $RdRp$ fragments. This pattern reflects the invasion pattern of the *Varroa* mite (Fig. 2). Small differences in migration patterns between the fragments may be caused by biological differences: DWV shows evidence of frequent recombination (15), and thus genes may differ in their evolutionary history, as well as in their evolutionary rate. However, these differences can also potentially be explained by the different subsets of samples available across fragments (table S4). Additional analyses to address unequal sample distribution and a sampling bias toward European populations confirmed the predominant pattern of European and North American populations as the main transmission hubs, with some evidence for transmission from Asia to these hubs (table S6). This analysis also shows strong support for transmission from *A. mellifera* to *V. destructor* for all fragments (Bayes factor $BF_{Lp} = 12281.21$, $BF_{Vp3} = 1813.53$, $BF_{RdRp} = 12281.21$), as well as to other hosts [the common Asian honeybee ectoparasite *Tropilaelaps calreae* ($BF_{Lp} = 11051.99$) and the bumblebee *Bombus lapidarius* ($BF_{RdRp} = 4.62$)] (Fig. 3). These are not dead-end hosts, and there is limited evidence for transmission to *A. mellifera* from *V. destructor* ($BF_{Lp} = 3.97$, $BF_{Vp3} = 1813.53$, $BF_{RdRp} = 3.09$), from *B. lapidarius* ($BF_{RdRp} = 3.74$), and from *T. clareae*

($BF_{Lp} = 3.93$). DWV shows very little host specificity, because the viral population is not structured by host species: The K_{ST} statistic, which measures the proportion of genetic variation among populations, is nonsignificant or close to zero ($K_{ST-Lp} = 0.023$, $K_{ST-RdRp} = 0.02$, both $P < 0.05$; K_{ST-Vp3} , not significant). In contrast, there is significant but overall moderate geographic population differentiation among all fragments ($K_{ST-Lp} = 0.305$, $K_{ST-Vp3} = 0.703$, $K_{ST-RdRp} = 0.42$; all $P < 0.001$). Population differentiation is significant but less pronounced within Europe ($K_{ST-Lp} = 0.319$, $K_{ST-Vp3} = 0.135$, $K_{ST-RdRp} = 0.181$; all $P < 0.001$) and East Asia ($K_{ST-Lp} = 0.301$, $P < 0.001$); other areas and fragments provided too few samples to be informative). Samples that are genetic nearest neighbors (NN) largely come from the same population, as indicated by Hudson's NN statistic at the continent level ($S_{NN-Lp} = 0.831$, $S_{NN-Vp3} = 0.679$, $S_{NN-RdRp} = 0.65$; all $P < 0.001$), within Europe ($S_{NN-Lp} = 0.772$, $S_{NN-Vp3} = 0.771$, $S_{NN-RdRp} = 0.628$; all $P < 0.001$), and within East Asia ($S_{NN-Lp} = 0.923$, $P < 0.001$). This result shows that DWV has accrued geographic variation since the origin of the epidemic ~80 years ago, but it indicates that high rates of human-mediated migration within Europe and East Asia obscured population differentiation. The phylogenetic trees (Fig. 1) also show that *A. mellifera* is the reservoir host for DWV, with other host species clustered at the terminal nodes. Thus, DWV apparently has little host specificity, being readily transmitted between different host species, but its

primary host is *A. mellifera*, with global transmission having been driven largely by European populations (Fig. 2).

DWV not only causes colony mortality in managed *A. mellifera* populations but also affects feral populations (34) and has been identified as an emerging disease in wild pollinators (24, 25, 35), with dramatic impacts on survival in bumblebees (24). As such, DWV may pose a threat not only to managed honeybees but also to pollinators more generally. Wild pollinators, such as bumblebees and solitary bees, have experienced a loss of species richness and diversity during recent decades, which can be attributed partly to infectious diseases (4, 36–39). Our results show that there is a global pandemic of DWV, with transmission mediated by European populations of *A. mellifera*. Transmission has been amplified by human-mediated movement of honeybees or other infected material and fueled by the concurrent emergence of *V. destructor* mites. Pollinator populations are interconnected via trade and movement of managed pollinators, which offers the potential for rapid spread of pathogens and parasites around the globe and between species. To reduce the negative effects of DWV on beekeeping and wild pollinators, tighter controls, such as mandatory health screenings and regulated movement of honeybees across borders, should be imposed, with every effort made to maintain the current *Varroa*-free refugia for the conservation of wild and managed pollinators.

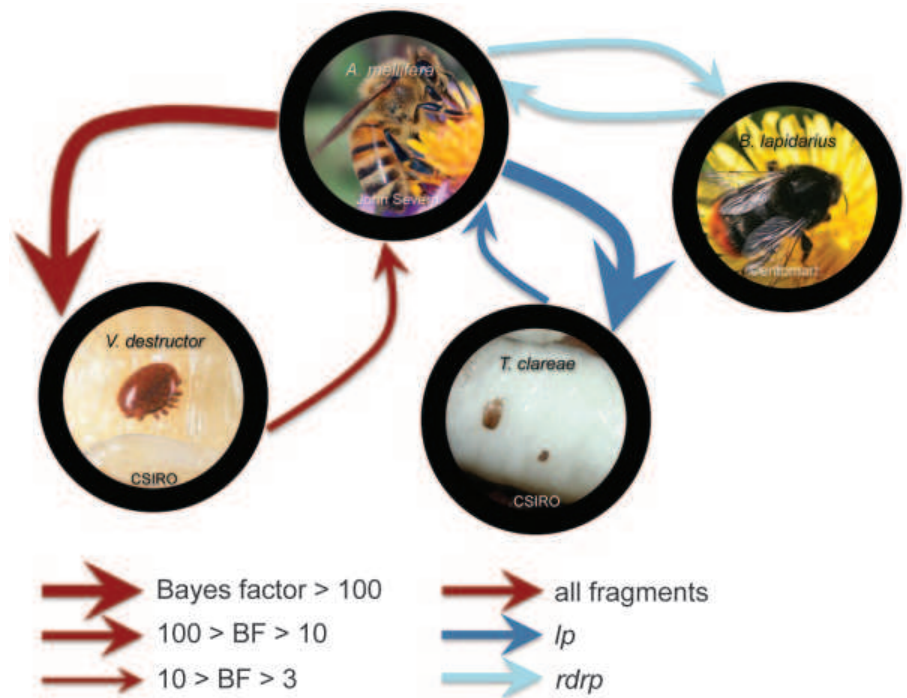


Fig. 3. Phylogenetically inferred DWV-host switching patterns. The weight of the line indicates the Bayes factor support for nonzero transition rates (as in Fig. 2), and the color indicates the fragments for which these routes were supported. Photo credits are indicated in the figure (CSIRO, Commonwealth Scientific and Industrial Research Organisation).

REFERENCES AND NOTES

1. A. Wallberg *et al.*, *Nat. Genet.* **46**, 1081–1088 (2014).
2. L. A. Garibaldi *et al.*, *Science* **339**, 1608–1611 (2013).
3. M. A. Aizen, L. D. Harder, *Curr. Biol.* **19**, 915–918 (2009).
4. S. G. Potts *et al.*, *Trends Ecol. Evol.* **25**, 345–353 (2010).
5. A. J. Vanbergen, I. P. Initiative, *Front. Ecol. Environ.* **11**, 251–259 (2013).
6. E. Genersch, M. Aubert, *Vet. Res.* **41**, 54 (2010).
7. A. C. Highfield *et al.*, *Appl. Environ. Microbiol.* **75**, 7212–7220 (2009).
8. H. Berthoud, A. Imdorf, M. Haueter, S. Radloff, P. Neumann, *J. Apic. Res.* **49**, 60–65 (2010).
9. B. Dainat, J. D. Evans, Y. P. Chen, L. Gauthier, P. Neumann, *Appl. Environ. Microbiol.* **78**, 981–987 (2012).
10. E. Genersch *et al.*, *Apidologie (Celle)* **41**, 332–352 (2010).
11. B. P. Oldroyd, *Trends Ecol. Evol.* **14**, 312–315 (1999).
12. S. J. Martin *et al.*, *Science* **336**, 1304–1306 (2012).
13. F. Mondet, J. R. de Miranda, A. Kretzschmar, Y. Le Conte, A. R. Mercer, *PLOS Pathog.* **10**, e1004323 (2014).
14. C. Mouret *et al.*, *Rev. Met. Vet.* **164**, 577–582 (2013).
15. E. V. Ryabov *et al.*, *PLOS Pathog.* **10**, e1004230 (2014).
16. S. Gisder, P. Aumeier, E. Genersch, *J. Gen. Virol.* **90**, 463–467 (2009).
17. T. Erban *et al.*, *Sci. Rep.* **5**, 13907 (2015).
18. D. Cardoen *et al.*, *PLOS ONE* **6**, e20043 (2011).
19. J. R. de Miranda, E. Genersch, *J. Invertebr. Pathol.* **103**, S48–S61 (2010).
20. J. D. Evans, M. Spivak, *J. Invertebr. Pathol.* **103**, S62–S72 (2010).
21. P. L. Bowen-Walker, S. J. Martin, A. Gunn, *J. Invertebr. Pathol.* **73**, 101–106 (1999).
22. S. J. Martin, *J. Appl. Ecol.* **38**, 1082–1093 (2001).
23. C. Yue, E. Genersch, *J. Gen. Virol.* **86**, 3419–3424 (2005).
24. M. A. Fürst, D. P. McMahon, J. L. Osborne, R. J. Paxton, M. J. Brown, *Nature* **506**, 364–366 (2014).
25. R. Manley, M. Boots, L. Wilfert, *J. Appl. Ecol.* **52**, 331–340 (2015).
26. R. Heller, L. Chikhi, H. R. Siegmund, *PLOS ONE* **8**, e62992 (2013).
27. O. Berényi *et al.*, *Appl. Environ. Microbiol.* **73**, 3605–3611 (2007).
28. R. Singh *et al.*, *PLOS ONE* **5**, e14357 (2010).
29. D. Shuttler *et al.*, *PLOS ONE* **9**, e98599 (2014).
30. D. M. Tompkins, A. W. Sainsbury, P. Nettleton, D. Buxton, J. Gurnell, *Proc. Biol. Sci.* **269**, 529–533 (2002).
31. D. M. Tompkins, A. R. White, M. Boots, *Ecol. Lett.* **6**, 189–196 (2003).
32. X. Zhang *et al.*, *J. Invertebr. Pathol.* **109**, 156–159 (2012).
33. J. Li *et al.*, *PLOS ONE* **7**, e47955 (2012).
34. C. E. Thompson *et al.*, *PLOS ONE* **9**, e105164 (2014).
35. D. P. McMahon *et al.*, *J. Anim. Ecol.* **84**, 615–624 (2015).
36. J. C. Biesmeijer *et al.*, *Science* **313**, 351–354 (2006).
37. S. A. Cameron *et al.*, *Proc. Natl. Acad. Sci. U.S.A.* **108**, 662–667 (2011).
38. L. G. Carvalheiro, W. E. Kunin, J. C. Biesmeijer, *Ecol. Lett.* **16**, 1416–1417 (2013).
39. J. Ollerton, H. Erenler, M. Edwards, R. Crockett, *Science* **346**, 1360–1362 (2014).

ACKNOWLEDGMENTS

The data reported in this paper are available on GenBank (accession numbers KP734326 to KP734846 and KP765048 to KP765235), in the supplementary materials, and in database S1. We thank numerous beekeepers for samples (see supplementary materials). We are grateful to A. Cowley and M. D. Sharma for informatics support and to F. Bayer for help in the laboratory. This work was funded by a Natural Environment Research Council grant to M.B., S.M., and R.B. (NE/F019610/1); L.W. was funded by a Royal Society Dorothy Hodgkin Fellowship. G.L. has been employed by Roche Pharmaceuticals since July 2014; all the work reported here was conducted while she was at the University of Sheffield.

SUPPLEMENTARY MATERIALS

www.sciencemag.org/content/351/6273/594/suppl/DC1

Materials and Methods

Figs. S1 to S7

Tables S1 to S6

References (40–82)

Databases S1 to S5

10 July 2015; accepted 8 January 2016

10.1126/science.aac9976

FOREST MANAGEMENT

Europe's forest management did not mitigate climate warming

Kim Naudts,^{1*}† Yiying Chen,^{1‡} Matthew J. McGrath,¹ James Ryder,¹ Aude Valade,² Juliane Otto,^{1§} Sebastiaan Luyssaert^{1||}

Afforestation and forest management are considered to be key instruments in mitigating climate change. Here we show that since 1750, in spite of considerable afforestation, wood extraction has led to Europe's forests accumulating a carbon debt of 3.1 petagrams of carbon. We found that afforestation is responsible for an increase of 0.12 watts per square meter in the radiative imbalance at the top of the atmosphere, whereas an increase of 0.12 kelvin in summertime atmospheric boundary layer temperature was mainly caused by species conversion. Thus, two and a half centuries of forest management in Europe have not cooled the climate. The political imperative to mitigate climate change through afforestation and forest management therefore risks failure, unless it is recognized that not all forestry contributes to climate change mitigation.

During the past few decades, European forests have acted as a carbon sink (1). Forest management, however, can enhance (2) or weaken (3) this sink, which has put it on the political agenda as a mechanism for mitigating climate change (4). However, forest management not only influences the sink strength, it also changes forest structure, which affects the exchange of energy and water vapor with the overlying atmosphere (5–8). Therefore, the potential of forest management to mitigate climate change can only be fully assessed by accounting for the effects from both biogeochemical changes (greenhouse gas emissions) and biophysical changes (water and energy fluxes) (9, 10).

Whereas the effects of historical anthropogenic land-cover changes, such as deforestation and afforestation, on the carbon cycle and the contemporary climate are relatively well documented (11–13), the impacts of land-use changes that do not involve a change in land cover, such as forest management, are far less well understood. Forest management has been reported to affect water and energy fluxes to the atmosphere to the same extent as changes in land cover do (8), suggesting that centuries of forest management may have contributed to Europe's present-day climate.

Despite the well-known impact of forest management on site-level carbon, energy, and water exchanges (5–8), large-scale studies of the climate

effects of forest management were, until recently, hampered by restrictive model approaches and a lack of sufficiently detailed land-use reconstructions. We have addressed both of these limitations. We reconstructed the land-use history of Europe (defined as the land mass west of the Russian border) to take account of both land-cover changes (afforestation and deforestation) and forest management changes (tree species conversion, wood extraction via thinning and harvesting, and litter raking) (14). Among other developments [section 1 of (15)], we then replaced the big-leaf approach in the land-surface model ORCHIDEE-CAN (Organising Carbon and Hydrology In Dynamic Ecosystems–Canopy) with an explicit canopy representation to simulate the biogeochemical and biophysical effects of land-use change (16). The improved land-surface model was coupled to the atmospheric circulation model LMDZ (Laboratoire de Météorologie Dynamique Zoom) [section 2 of (15)] in a factorial simulation experiment to attribute climate change to global anthropogenic greenhouse gas emissions and European land-use change since 1750.

Increased atmospheric greenhouse gas concentrations from global fossil-fuel burning and land-use changes outside Europe are responsible for a change of 2.98 W m⁻² in the radiative imbalance at the top of the atmosphere, a significant increase of 1.71 K in summertime boundary layer temperature ($P < 0.05$, modified t test; Table 1), and an insignificant decrease of 6 mm in summertime precipitation ($P > 0.05$, modified t test; Table 1), relative to 1750. Enhanced plant growth caused by global warming and increased atmospheric CO₂ has resulted in a European forest-based carbon sink of 0.13 Pg C since 1750 (eq. S1), which is a negligible compensation for the contribution of 247 Pg C or 117 ppm CO₂ from global anthropogenic emissions (Table 1).

From 1750 to 1850, deforestation reduced Europe's forest area by 190,000 km². In the mid-19th century, the increasing use of fossil fuels

¹Laboratoire des Sciences du Climat et de l'Environnement–Institut Pierre Simon Laplace, Commissariat à l'Énergie Atomique et aux Énergies Alternatives (CEA)–Centre National de la Recherche Scientifique (CNRS)–Université de Versailles Saint Quentin, Université Paris-Saclay, 91191 Gif-sur-Yvette, France. ²Institut Pierre Simon Laplace, 75010 Paris, France.

*Corresponding author. E-mail: kim.naudts@mpimet.mpg.de

†Present address: Max Planck Institute for Meteorology, 20146 Hamburg, Germany. ‡Present address: National University of Singapore, 119077 Singapore. §Present address: Climate Service Center Germany, Helmholtz-Zentrum Geesthacht, 20095 Hamburg, Germany. ||Present address: Department of Ecological Science, VU University Amsterdam, 1081 HV Amsterdam, Netherlands.

for energy and, later, agricultural intensification halted net deforestation and even reverted the trend. In subsequent centuries, 386,000 km² of agricultural land was afforested (14), resulting in a net gain of forest area between 1750 and 2010 (17). Whereas deforestation between 1750 and 1850 mainly replaced broadleaved forests with agricultural land, afforestation from 1850 onward was often with coniferous species. Broadleaved forests were also directly converted to coniferous forests (18), resulting in a total increase of 633,000 km² in conifers at the expense of broadleaved forests (decreasing by 436,000 km²) (14). For centuries, foresters have favored a handful of commercially successful tree species (Scots pine, Norway spruce, and beech) and, in doing so, are largely responsible for the current distribution of conifers and broadleaved species in Europe (Fig. 1, A and B).

The species change thus reflects the onset of a more scientific and production-oriented approach to forestry (19). Through local production and trade, Europe tried to satisfy the wood demands of a population that grew from 140 million in 1750 to 580 million by 2010 (20). As a result, 417,000 km² of previously unmanaged forests were taken into production (Fig. 1, C and D), and 218,000 km² of coppices were converted to high stands, which, together with the 196,000 km² of afforestation, resulted in an 833,000 km² increase

in high-stand management (14). Within the same 260-year period, litter raking came into practice. It peaked around 1850, having transferred about 50 Tg of carbon from forests to agricultural land, and was progressively abandoned afterward with the increased availability of straw (21). Below, we discuss the climate effects of this afforestation, species conversion, and wood extraction in Europe between 1750 and 2010.

The net gain of 196,000 km² in forest area, with eastern Ukraine being a noteworthy exception, resulted in a 0.7-Pg carbon sink. At the same time, afforestation decreased the albedo of the land surface by 0.01 (i.e., 1% more solar radiation was absorbed). The decrease in albedo was not offset by the carbon sink, resulting in a net radiative imbalance of 0.11 W m⁻² ($P < 0.05$, modified t test; Table 1). After afforestation, atmospheric warming from changes in vegetation albedo and latent heat flux was largely offset by cooling from changes in sensible heat flux (fig. S1), resulting in a small summertime temperature increase of 0.02 K ($P < 0.05$, modified t test; Table 1). For temperate regions such as Europe, a small to nonexistent temperature effect after afforestation is consistent with observational studies (22–24).

Replacing broadleaved forests with conifers resulted in a simulated carbon sink of 0.6 Pg C (Table 1). Yet the summertime temperature in

the boundary layer increased by 0.08 K ($P < 0.05$, modified t test; Table 1). Temperature changes related to changes in sensible and latent heat flux, which can be triggered by species-specific changes in albedo (Fig. 2B) and canopy structure, were large but offset each other. However, a decrease in water vapor pressure due to reduced evapotranspiration decreased the atmosphere's ability to release thermal heat (atmospheric emissivity) (25), which explains the 0.08-K warming (Fig. 2A). Temperature changes follow a clear spatial pattern, with significant warming over central and eastern Europe (Fig. 2C). The strong correlation [coefficient of determination (R^2) = 0.56, $P < 0.05$, modified Pearson correlation] of the spatial patterns of land-use and species change suggests that the temperature effect of anthropogenic land use is largely determined by tree species conversion (Fig. 2D).

Almost 25% of the 633,000-km² increase in conifers occurred in northern Europe. Despite the lower albedo for coniferous relative to deciduous trees, the albedo over this region increased (Fig. 2B) due to a more than doubling of the surface area of young forests (forests with an average tree diameter <0.07 m) after the onset of widespread forest management. The sparse tree canopy of young forests allows more light to penetrate to the forest floor, which is generally more reflective than the tree cover (26), resulting in a higher albedo.

Putting 417,000 km² of previously unmanaged forest into production is estimated to have released 3.5 Pg of carbon to the atmosphere, because the carbon stock in living biomass, coarse woody debris, litter, and soil was simulated to be, respectively, 24, 43, 8, and 6% lower in managed forests compared with unmanaged forests. Differences in standing biomass between managed and unmanaged forests explain 38% of the total simulated 2.7-Pg increase in atmospheric carbon

Table 1. Attribution of biogeochemical, biophysical, and climatic effects between 1750 and 2010 to global greenhouse gas emissions and different factors of European anthropogenic land-use change. Land-use change includes both land-cover change and forest management, which was separated into species conversion and wood extraction (thinning, harvest, and litter raking). Contributions were calculated from eqs. S1 to S9 [section 3 of (15)]. The footnotes provide statistical information and indicate the main causes of the significant changes. Biogeochemical effects were discounted for the CO₂ emissions from the pressure-driven equilibrium between the oceans and the atmosphere. RF, radiative forcing; GHGs, greenhouse gases.

	Contribution to changes since 1750				
	Δ RF due to GHGs (W m ⁻²)	Δ RF due to surface change (W m ⁻²)	ΔT_a , summer (K)	Δ Precipitation, summer (mm per season)	Δ Atmospheric carbon (Pg C)†
Global					
Greenhouse gas emissions	2.98*‡	0.00	1.71*‡	-6	247§
European					
Land-use change	0.01*	0.11*¶	0.12*#	-3	3.1
Land-cover change	-0.01	0.12*¶	0.02*¶	0	-0.7**
Forest management	0.02	-0.01	0.10*#	-3*‡‡	1.9
Species conversion	-0.01	0.00	0.08*#	-4*‡‡	-0.6‡‡
Wood extraction	0.03	-0.01	0.02*	1	2.7

*Significant effects at the 0.05 significance level, as determined by a modified paired one-sample t test. †Effects for which statistical testing was not possible, because only a single realization was available. ‡Increased radiative forcing from increased atmospheric CO₂ concentrations due to fossil-fuel burning and land-use change. §Increased atmospheric CO₂ concentrations due to fossil-fuel burning and land-use change. ||Decreased carbon storage in vegetation caused by taking unmanaged forests into production. ¶Decreased vegetation albedo caused by large-scale afforestation. #Decreased atmospheric emissivity due to changes in albedo and canopy structure caused by replacing broadleaved deciduous with evergreen coniferous tree species. **Increased carbon sequestration in vegetation through large-scale afforestation. ††Although statistically significant, these changes are unlikely to be relevant. ‡‡Increased carbon sequestration in vegetation caused by replacing broadleaved with fast-growing coniferous tree species.

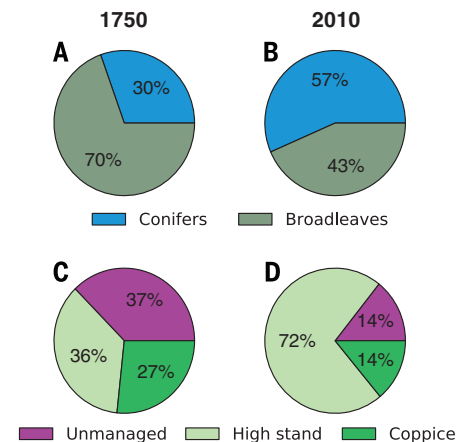


Fig. 1. Main changes in European forest management between 1750 and 2010. (A) Relative distribution (percent) of tree growth forms in 1750 and (B) 2010. Total forest area in 1750 was 1,929,000 km² and increased to 2,126,000 km² by 2010. (C) Relative distribution (percent) of wood extraction strategies in 1750 and (D) 2010.

due to wood extraction (Table 1). The decrease in carbon stocks caused by extracting wood from previously unmanaged forests could not be compensated for by building up a carbon stock in the wood-product pools (only 0.05 Pg C would be offset). The carbon released from wood extraction was, however, partly compensated for by the conversion from broadleaved to faster-growing coniferous species. Nevertheless, the combination of wood extraction and species conversion emitted 1.9 Pg C to the atmosphere (Table 1). Wood extraction only had minor effects on albedo ($P > 0.1$, modified t test), surface roughness, and evapotranspiration; the climate effect of wood extraction is therefore controlled by its carbon release.

Despite their present-day strength as carbon sinks (1), the distinctive history of afforestation, species conversion, and wood extraction from previously unmanaged forests nevertheless has resulted in European forests having a carbon debt of 3.1 Pg C, compared with 1750 (Table 1). A concurrent 0.12-K increase in summertime boundary layer temperature ($P < 0.05$, modified t test; Table 1) can be attributed only to a minor extent to afforestation (0.02 K) and is mainly due to

forest management (0.10 K; $P < 0.05$, modified t test; Table 1), more specifically to the conversion from broadleaved to coniferous species (0.08 K; $P < 0.05$, modified t test; Table 1). The radiative imbalance at the top of the atmosphere increased by 0.12 W m^{-2} as a result of land-use change ($P < 0.05$, modified t test; Table 1). Contrary to the temperature effect from land-use change that was largely explained by species conversion, the radiative imbalance can mainly be attributed to afforestation (0.11 W m^{-2}).

Although our analysis is restricted to Europe, similar effects are likely for regions where similar underlying processes are or have been occurring. Large-scale afforestation is ongoing in China (772,000 km²), the United States (254,000 km²), and the Russian Federation (170,000 km²) (17, 27). Wood extraction occurs in 64 to 72% of the 26.5 to 29.4 million km² of global forest area (8), and substantial species changes have occurred in China (216,000 km²), Brazil (71,000 km²), Chile (24,000 km²), New Zealand (18,000 km²), and South Africa (17,000 km²) (27).

Afforestation and forest management to maximize carbon sequestration are recognized as key strategies for climate mitigation by the Paris

agreement of the United Nations Framework Convention on Climate Change, because forest management and wood use are expected to slow global warming by removing CO₂ from the atmosphere. In Europe, two and a half centuries of land-use change increased the forest area by 10% and has put over 85% of the forests under management, but it has failed to result in net CO₂ removal from the atmosphere, because wood extraction released carbon otherwise stored in the biomass, litter, dead wood, and soil carbon pools. In addition, converting deciduous forests into coniferous forests resulted in changes in albedo, canopy roughness, and evapotranspiration from the land surface, which contributed to warming rather than mitigating it. Hence, any climate framework that includes land management as a pathway for climate mitigation should not only account for land-cover changes but also should equally address changes in forest management, because not all forest management contributes to climate change mitigation. The key question now is whether it is possible to design a forest management strategy that cools the climate and, at the same time, sustains wood production and other ecosystem services.

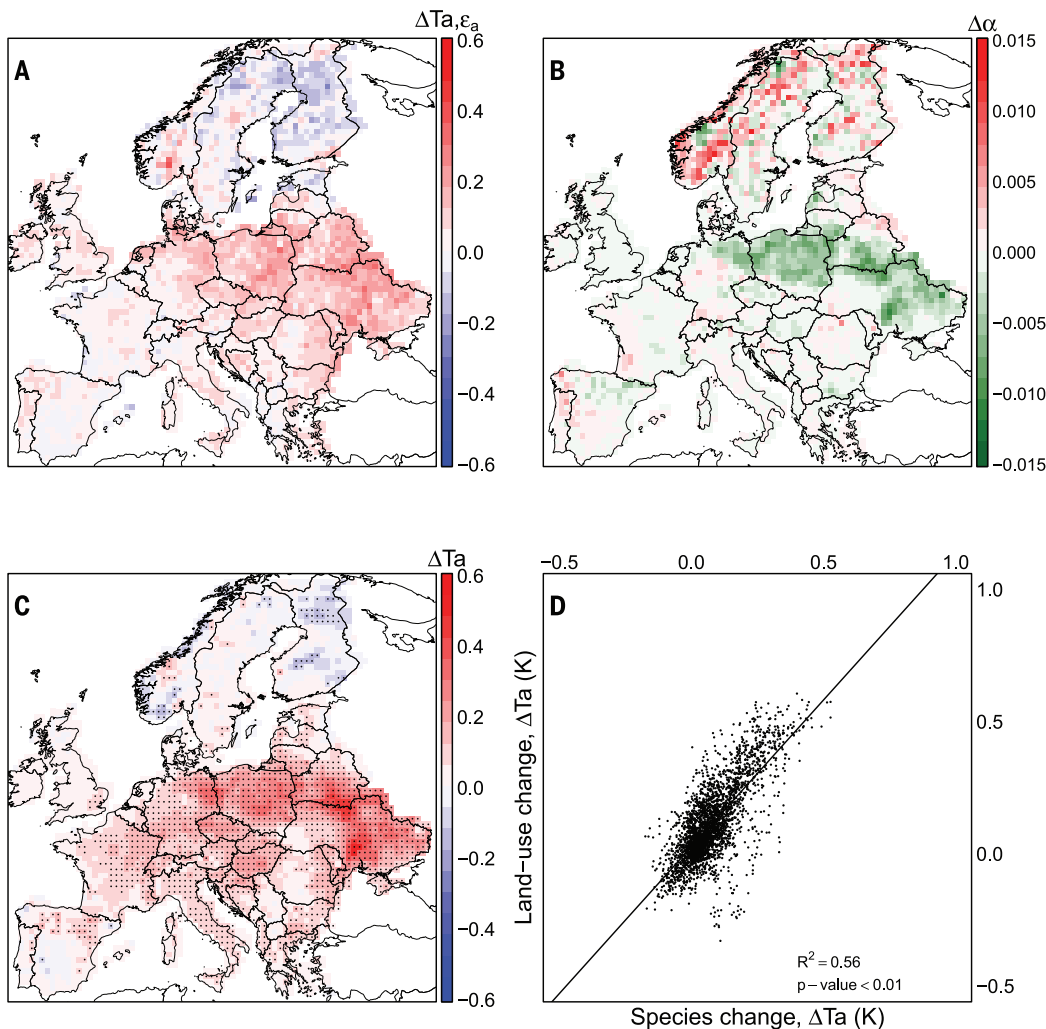


Fig. 2. Effects of species conversion in Europe since 1750. Temperature changes are for boundary layer temperature during summer (kelvin). (A) Temperature change due to changes in emissivity ($\Delta T_a, \epsilon_a$) caused by species conversion, (B) changes in albedo ($\Delta \alpha$) due to species conversion, (C) total temperature change (ΔT_a) due to species conversion, and (D) correlation between species-induced and land use-induced temperature change. In (C), black dots denote significant temperature changes at the 0.05 significance level, as determined by a modified paired one-sample t test.

REFERENCES AND NOTES

1. S. Luysaert et al., *Glob. Change Biol.* **16**, 1429–1450 (2010).
2. B. Schlamadinger, G. Marland, *Biomass Bioenergy* **10**, 275–300 (1996).
3. T. W. Hudiburg, B. E. Law, C. Wirth, S. Luysaert, *Nat. Clim. Change* **1**, 419–423 (2011).
4. UN, *Kyoto Protocol to the United Nations Framework Convention on Climate Change* (1998); http://unfccc.int/kyoto_protocol/items/2830.php.
5. B. Amiro et al., *Agric. For. Meteorol.* **136**, 237–251 (2006).
6. J.-Y. Juang, G. Katul, M. Siqueira, P. Stoy, K. Novick, *Geophys. Res. Lett.* **34**, L21408 (2007).
7. E. Rotenberg, D. Yakir, *Science* **327**, 451–454 (2010).
8. S. Luysaert et al., *Nat. Clim. Change* **4**, 389–393 (2014).
9. R. A. Pielke Sr. et al., *Philos. Trans. A Math. Phys. Eng. Sci.* **360**, 1705–1719 (2002).
10. R. A. Pielke et al., *WIREs Clim. Change* **2**, 828 (2011).
11. A. J. Pitman et al., *Geophys. Res. Lett.* **36**, L14814 (2009).
12. J. Pongratz, T. Raddatz, C. H. Reick, M. Esch, M. Claussen, *Geophys. Res. Lett.* **36**, GB3018 (2009).
13. R. Mahmood et al., *Int. J. Climatol.* **34**, 929–953 (2014).
14. M. J. McGrath et al., *Biogeosciences* **12**, 4291–4316 (2015).
15. Materials and methods are available as supplementary materials on Science Online.
16. K. Naudts et al., *Geosci. Model Dev.* **8**, 2035–2065 (2015).
17. P. Meyfroidt, E. F. Lambin, *Annu. Rev. Environ. Resour.* **36**, 343–371 (2011).
18. M. Bürgi, A. Schuler, *For. Ecol. Manage.* **176**, 173–183 (2003).
19. E. P. Farrell et al., *For. Ecol. Manage.* **132**, 5–20 (2000).
20. K. Klein Goldewijk, A. Beusen, P. Janssen, *Holocene* **20**, 565–573 (2010).
21. U. Gimmi, M. Bürgi, M. Stuber, *Ecosystems* **11**, 113–124 (2008).
22. X. Lee et al., *Nature* **479**, 384–387 (2011).
23. Y. Li et al., *Nat. Commun.* **6**, 6603 (2015).
24. M. Zhang et al., *Environ. Res. Lett.* **9**, 034002 (2014).
25. W. Brutsaert, *Water Resour. Res.* **11**, 742–744 (1975).
26. J. Otto et al., *Biogeosciences* **11**, 2411–2427 (2014).
27. Food and Agriculture Organization of the United Nations (FAO), *Global Forest Resources Assessment 2005. Progress Towards Sustainable Forest Management* (FAO Forestry Paper 147, FAO, 2006).

ACKNOWLEDGMENTS

K.N., J.R., Y.C., M.J.M., J.O., and S.L. were funded through European Research Council starting grant 242564 [DOFOCO (Do Forests Cool the Earth) program]. A.V. was funded through the French Environment and Energy Management Agency (ADEME, Bilan Carbone de la Forêt Française program). K.N. received additional funding through the Essential Climate Variables land cover program and the German Research Foundation's Emmy Noether Program (grant PO 1751/1-1). The study benefited from a Short-Term Scientific Mission [COST (European Cooperation in Science and Technology) TERRABITES (Terrestrial Biosphere in the Earth System) grant ES805] offered to K.N. Precipitation data from the Global Precipitation Climatology Centre were made available by the National Oceanic and Atmospheric Administration's Earth System Research Laboratory (Physical Science Division), Boulder, CO (www.esrl.noaa.gov/psd/). The ORCHIDEE and LMDZ project teams as well as the Centre de Calcul Recherche et Technologie provided the run environment that is essential for the type of coupled land-atmosphere simulations that were conducted in this study. The code and the run environment are open source and distributed under the CeCILL (CEA CNRS INRIA Logiciel Libre) license (<http://labex.ipsl.fr/orchidee/>). M.J.M., J.O., J.R., Y.C., K.N., A.V., and S.L. designed the study and/or contributed to the interpretation of the results. M.J.M., J.O., J.R., Y.C., K.N., A.V., and S.L. developed, parameterized, and validated ORCHIDEE-CAN. M.J.M., Y.C., and S.L. conducted the simulation experiment. K.N., Y.C., M.J.M., J.O., S.L., and J.R. analyzed the data.

SUPPLEMENTARY MATERIALS

www.sciencemag.org/content/351/6273/597/suppl/DC1
Materials and Methods
Figs. S1 to S6
Tables S1 to S3
References (28–75)

26 October 2015; accepted 8 January 2016
10.1126/science.aad7270

CLIMATE CHANGE

Biophysical climate impacts of recent changes in global forest cover

Ramdane Alkama and Alessandro Cescatti*

Changes in forest cover affect the local climate by modulating the land-atmosphere fluxes of energy and water. The magnitude of this biophysical effect is still debated in the scientific community and currently ignored in climate treaties. Here we present an observation-driven assessment of the climate impacts of recent forest losses and gains, based on Earth observations of global forest cover and land surface temperatures. Our results show that forest losses amplify the diurnal temperature variation and increase the mean and maximum air temperature, with the largest signal in arid zones, followed by temperate, tropical, and boreal zones. In the decade 2003–2012, variations of forest cover generated a mean biophysical warming on land corresponding to about 18% of the global biogeochemical signal due to CO₂ emission from land-use change.

Forests play a relevant role in the climate system by absorbing approximately one-fourth of anthropogenic CO₂ emissions (1), storing large carbon pools in tree biomass and forest soils (2), and modulating the land-atmosphere exchange of energy and water vapor (3). Given the important role of forests in the global carbon cycle, climate treaties account for land-based mitigation options such as afforestation, reforestation, and avoided deforestation or forest degradation (4, 5). On the contrary, the climate impacts of biophysical processes, such as the surface exchange of energy and water vapor (6), are still uncertain in sign and magnitude and therefore have not been considered in climate negotiations to date.

Over the past two decades, the biophysical effects of deforestation on climate have been assessed mainly by comparing paired model simulations with contrasting forest cover (7–12). These analyses have shown that, despite the increase in surface albedo, the net biophysical effects of tropical deforestation may increase surface temperature through the reduction of evapotranspiration (9, 13). On the contrary, boreal deforestation may lead to net climate cooling due to the high snow albedo in cleared areas during winter/spring and to the land-albedo/sea-temperature feedback (11, 12, 14). However, results of these numerical experiments are model-dependent, and the uncertainties in sign, magnitude, and spatial distribution of the predicted effects are very large (15–17). Therefore, direct observations of the biophysical climate effects of recent forest losses and gains are required to constrain predictions, reduce the uncertainty of model ensembles, and provide robust recommendations to climate policy.

To date, data-driven assessments based on in situ (18–20) or satellite observations (3, 21, 22) have adopted the space-for-time analogy, mean-

ing that spatial differences in surface temperature between areas with contrasting forest cover have been interpreted as the climate signal of hypothetical deforestation/afforestation. The substitution of space for time produces unbiased results only if forests are randomly distributed in the landscape. Conversely, the systematic location of forests in less favorable areas (such as steeper or colder slopes, shallow soils, etc.) may produce spatial gradients in surface climate that should not be attributed to changes in land cover (18). In addition, both model-based and observation-based assessments have focused so far on idealized scenarios of deforestation (10, 11) and on the estimation of climate sensitivities to land-use change (3, 18, 22), but the climate signal generated by the ongoing changes in forest cover has not yet been quantified.

To overcome the limits and uncertainties of past assessments, in this work we focused on areas that underwent recent land cover transitions, with the objective of providing a global, robust, and data-driven assessment of the biophysical climate impacts of observed forest gains and losses. The analysis builds on overlapping satellite retrievals of surface radiometric temperature (23) and of high-resolution variations in forest cover (24). A novel methodology has been developed to disentangle the effect of forest cover change from the global climate signal [details in supplementary materials (SM) text S1.2]. For this purpose, the temperature difference (ΔT) between two years at a given location is expressed as the effect of forest cover change (ΔT_{fcc}) plus the residual signal (ΔT_{res}) due to climate variability (Eq. 1)

$$\Delta T = \Delta T_{\text{fcc}} + \Delta T_{\text{res}} \rightarrow \Delta T_{\text{fcc}} = \Delta T - \Delta T_{\text{res}} \quad (1)$$

The temporal variation in air surface temperature (ΔT) is estimated from satellite retrievals of radiometric land surface temperature, evapotranspiration, and albedo, with semi-empirical models calibrated against in situ measurements of air temperature (SM text S1.1 and figs. S1 and S2). For a given location, we derive ΔT_{fcc} from Eq. 1 by estimating ΔT_{res} from adjacent areas with stable forest cover and therefore where $\Delta T_{\text{fcc}} \approx 0$

European Commission, Joint Research Centre, Institute for Environment and Sustainability, Ispra, Italy.

*Corresponding author. E-mail: alessandro.cescatti@jrc.ec.europa.eu

and $\Delta T \approx \Delta T_{\text{res}}$ (fig. S4). To estimate ΔT_{res} , areas located within 50 km of the target location were considered, using the inverse distance as a weighting factor (methods in SM text S1.2). At a seasonal time scale, the residual signal ΔT_{res} is typically in the range $\pm 1.5^\circ\text{C}$, as the temperature signal of forest cover changes (fig. S4). We focused the analysis on the first and last year of the available time series (i.e., 2003 and 2012) in order to maximize the observed land cover change and therefore the spatial extent and robustness of the estimates. In parallel, the interannual variability of the climate signal was investigated by comparing 2003 with each of the other years, and the robustness of the signal was estimated on an ensemble of nine pairs of years (2003–2005 versus 2010–2012; methods in SM text S1.2.2).

Results show that in all climate zones, forest clearing produces a marked increase of mean annual maximum air surface temperatures, slight changes in minimum temperatures, and an overall increase of mean temperatures, except at the northernmost latitudes (Fig. 1, B and C). In fact, the removal of forest cover does not significantly affect the mean air temperature in the boreal zone, whereas it increases the temperature by about 1°C in the temperate and tropical zones and by more than 2°C in the arid zone (Fig. 1C). These signals show limited interannual variability and a decreasing uncertainty at the increase of the time interval and therefore of the area affected by cover change (fig. S9). In the temperate and boreal zones, the warming induced by forest losses declines over time, presumably because of

the progressive recovery of vegetation in forest clearings. On the contrary, tropical areas show a stable signal, likely due to the conversion of forests to agriculture (fig. S9).

The methodology used in Fig. 1 to investigate mean annual temperatures has been replicated at a monthly time scale to explore the seasonal temperature sensitivity (Fig. 2 and figs. S5 and S6). These monthly signals show a limited variability between years in the different climate zones and latitudinal bands (figs. S10 and S11). The climate impact of deforestation is modulated by the incoming radiation and, as a consequence, the largest warming occurs during the summer solstice at maximum temperatures, whereas changes in air temperatures during nighttime are negligible. The substantial reduction of evapotranspiration

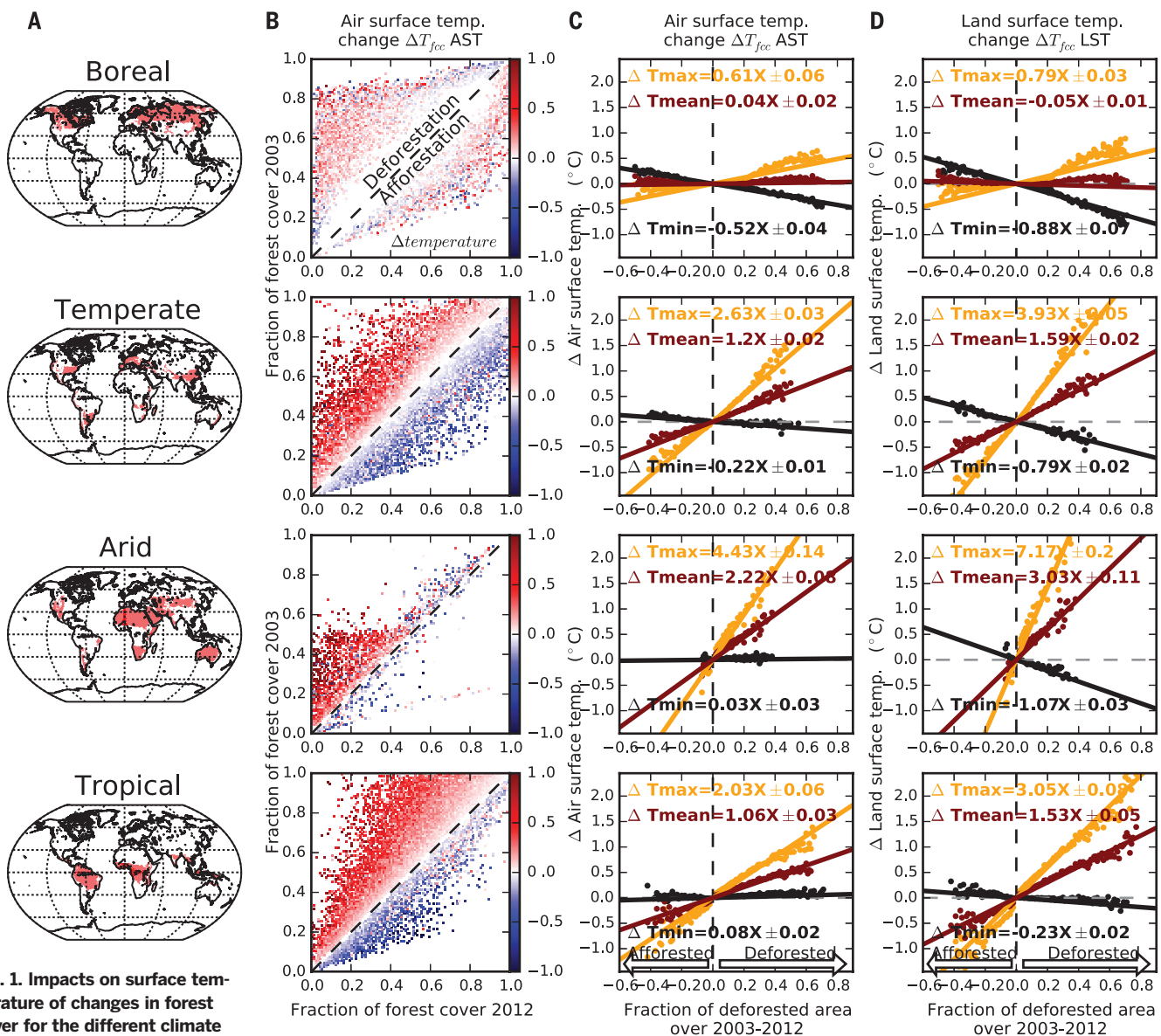


Fig. 1. Impacts on surface temperature of changes in forest cover for the different climate zones. The panels in rows 1 to 4

show the observed climate impacts of changes in forest cover between 2003 and 2012 in the climate zones defined in (A). (B) Observed variations in mean annual air surface temperature due to observed changes in forest cover (seasonal plots are reported in figs. S5 and S6). The sensitivity of the mean (dark red), minimum (black), and maximum (orange) air surface temperatures (C) and land surface temperature (D) to the fraction of the deforested area is shown.

Fig. 2. Seasonal changes in air and land surface temperature due to losses of forest cover. Expected changes in the monthly maximum, minimum, and mean air (A) and land (B) surface temperature due to the total clearing of a 0.05° grid cell in the different climate zones are shown (mean ± weighted root mean square error, WRMSE).

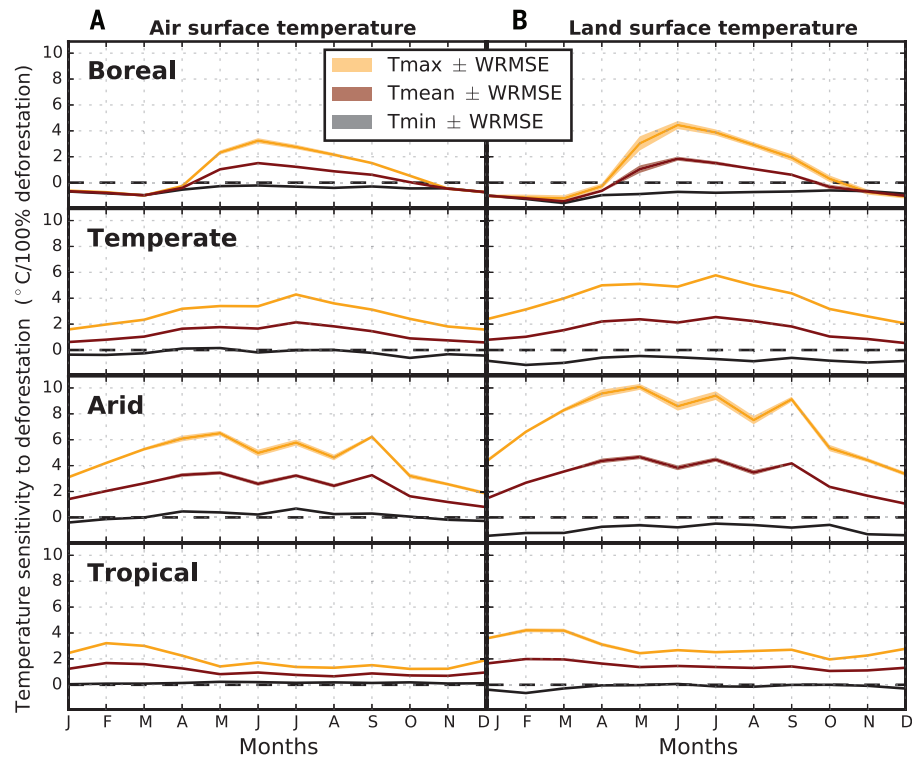
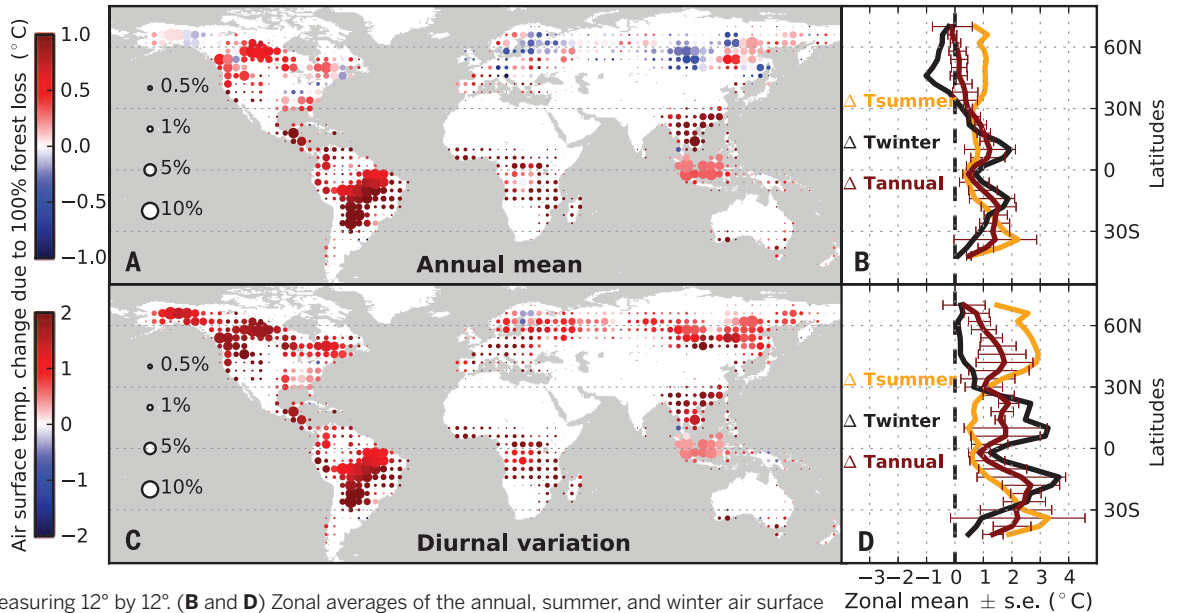


Fig. 3. Regional changes in air surface temperature due to losses in forest cover between 2003 and 2012.

Changes in mean annual air temperature (A) and diurnal variations (C) due to forest losses are shown. The symbol size indicates the magnitude of forest cover losses, and the color specifies the average temperature sensitivity to total deforestation. Points are spaced 4° in both latitude and longitude, and statistics were



computed in windows measuring 12° by 12° (B and D) Zonal averages of the annual, summer, and winter air surface temperature statistics at 4° of latitudinal resolution (the equivalent image for land surface temperature is reported in fig. S7).

and surface roughness with forest clearing (11, 13) is the most plausible explanation for the substantial local warming under high radiation load. The remarkable daytime warming ultimately leads to an increase in the diurnal variation (the difference between the daily maximum and minimum temperature) of about $1.13 \pm 0.1^\circ\text{C}$, $2.85 \pm 0.04^\circ\text{C}$, $4.4 \pm 0.17^\circ\text{C}$, and $1.95 \pm 0.08^\circ\text{C}$ over the boreal, temperate, arid, and tropical climate zones, respectively. In summary, forests show

important biophysical mitigation effects on local maximum temperature in all climate zones, by reducing local daytime summer temperatures and substantially decreasing the diurnal and annual temperature variations. The key role of evapotranspiration in the biophysical impacts of forest clearing emerges from the ranking of the climate zones, with the arid areas showing the strongest signal, followed by the temperate, the tropical, and the boreal zones.

Climate sensitivity to losses of forest cover was investigated at the regional scale by applying in a 12°-by-12° moving window the same methodology used to investigate the climate zones (Fig. 3 and fig. S7; methods in SM text S1.2.1). This analysis shows that forest losses in tropical areas generate warming across all seasons. Contrasting effects occur at northern latitudes between seasons (winter cooling and summer warming) and continents (warming in North America and cooling in

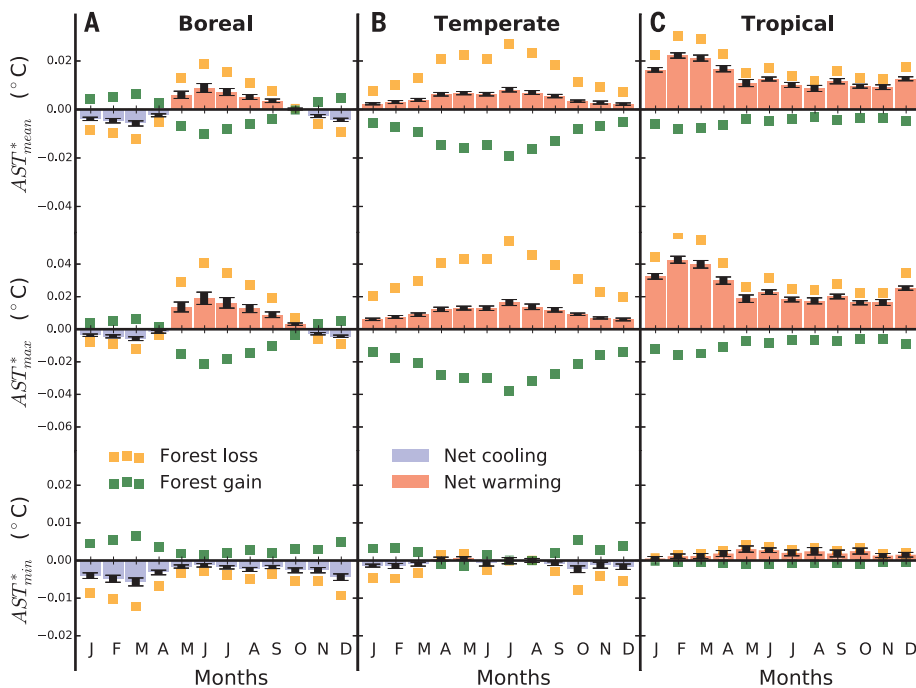


Fig. 4. Net impact of deforestation and afforestation on monthly air surface temperatures.

Changes in monthly mean, maximum, and minimum air surface temperature due to forest cover change over the (A) boreal, (B) temperate, and (C) tropical climate zones (the arid zone has experienced minor changes in forest cover) are shown. Yellow and green squares represent the global temperature signal of forest cover losses and gains, and light red and blue bars indicate the warming and cooling due to the net change in forest cover (the equivalent image for land surface temperature is shown in fig. S8).

northern Eurasia, Fig. 3, A and B). In accordance with observations performed in North America (18, 20), forest clearing increases the diurnal temperature variation during summer months at all latitudes (Fig. 3, C and D), whereas it has no effects on the diurnal variation during the boreal winter, because of the dominant effect of snow albedo. The changes in diurnal temperature variation (Fig. 3D) are substantially larger than those in mean annual temperature (Fig. 3B). These results highlight the fact that local biophysical processes triggered by forest losses can effectively increase summer temperatures in all world regions, further amplifying the climate trends driven by the increasing greenhouse gas concentrations.

The estimated rate of local warming after forest losses is lower than that predicted by observation-driven studies focused on land surface temperature (22). In addition, the low sensitivity of the mean annual temperature observed at northern latitudes is in contrast with model simulations of large-scale deforestation that typically predict a sharp reduction in boreal temperatures (8, 10), possibly amplified by land-ocean interactions (11). Differently from previous assessments (3, 22), our analysis focused on air surface temperature instead of land surface temperature, given the greater relevance of the first parameter in climate science. On this aspect Figs. 1, C and D, and 2 show that the sensitivity of land surface temperature to changes in forest cover is about 50% larger than that of air temperature. This large difference is probably driven by satellite retrievals of land surface temperature that are biased toward clear sky conditions, when the biophysical differences between land covers are maximized. In addition, it is important to consider that our analysis quantifies the local im-

pacts of fine-scale variations in forest cover that are primarily driven by changes in the surface energy budget and related first-order interactions with the boundary layer. Therefore, this assessment cannot capture the signal of large-scale land-atmosphere interactions and regional teleconnections. On the contrary, model experiments of idealized large-scale deforestation also account for second-order effects and feedbacks (such as changes in cloud cover, rainfall, sea surface temperature, etc.) that may amplify and eventually override the local temperature signal of deforestation (25). In particular, significant feedbacks between land surface albedo and sea temperature seem to drive the temperate/boreal cooling in model experiments of global deforestation (11).

Afforestation or reforestation can significantly attenuate the biophysical effect of forest clearing on surface temperature, especially over boreal and temperate zones, where gains in forest cover compensated for more than 60% of forest losses in the decade 2003–2012 (Fig. 4A). On the contrary, over the same period, forest gains offset less than 30% of the losses in the tropics, leading to a significant net deforestation (24, 26) (Fig. 4C). The strong local effect of the changes in forest cover on air surface temperature turns out to be rather minor when averaged over the year at the global scale (0.0062°C, Fig. 4), due to the attenuation effect of the boreal winter and of nighttime temperatures, to the compensatory effect of forest gains, and to the limited extent of forest losses. On average, in the analyzed decade, the global biophysical warming due to changes in forest cover is equal to about 18% (12 to 42%) of the biogeochemical warming due to CO₂ emissions from land-use change (methods in SM text S1.3).

This analysis reveals that the biophysical effects of changes in forest cover can substantially affect the local climate by altering the average temperature and, even more markedly, the maximum summer temperatures and the diurnal and annual variations (18, 20). In addition to the global mitigation effects of the terrestrial carbon sink (1), the biophysical properties of forests can therefore contribute to the mitigation of climate extremes, in particular by reducing daytime temperatures during summer months (27). These effects are relevant both in the tropics, where deforestation rates are still substantial and forest clearing generates warming throughout the whole year, and in the boreal zone, where forests contribute to the mitigation of rapidly increasing summer temperatures. Overall, the observation-driven global quantification of the biophysical signal of deforestation provided in this study may support accounting for land biophysics in climate negotiations, as well as the definition of novel protocols for the measurement, reporting, and verification of these relevant effects.

REFERENCES AND NOTES

1. C. Le Quéré et al., *Earth Syst. Sci. Data*, **6**, 235–263 (2014).
2. N. Carvalhais et al., *Nature*, **514**, 213–217 (2014).
3. K. Zhao, R. B. Jackson, *Ecol. Monogr.*, **84**, 329–353 (2014).
4. D. E. Schulze, C. Wirth, M. Heimann, *Science*, **289**, 2058–2059 (2000).
5. H. K. Gibbs, S. Brown, J. O. Niles, J. A. Foley, *Environ. Res. Lett.*, **2**, 045023 (2007).
6. G. B. Bonan, *Science*, **320**, 1444–1449 (2008).
7. J. Lean, D. Warrilow, *Nature*, **342**, 411–413 (1989).
8. P. K. Snyder, C. Delire, J. Foley, *Clim. Dyn.*, **23**, 279–302 (2004).
9. J. J. Feddema et al., *Science*, **310**, 1674–1678 (2005).
10. G. Bala et al., *Proc. Natl. Acad. Sci. U.S.A.*, **104**, 6550–6555 (2007).
11. E. L. Davin, N. de Noblet-Ducoudre, *J. Clim.*, **23**, 97–112 (2010).
12. N. de Noblet-Ducoudre et al., *J. Clim.*, **25**, 3261–3281 (2012).
13. G. A. Ban-Weiss, G. Bala, L. Cao, J. Pongratz, K. Caldeira, *Environ. Res. Lett.*, **6**, 034032 (2011).

14. M. M. Lorant, L. T. Berner, S. J. Goetz, Y. Jin, J. T. Randerson, *Glob. Change Biol.* **20**, 594–606 (2014).
15. A. J. Pitman et al., *Geophys. Res. Lett.* **36**, L14814 (2009).
16. V. Brovkin et al., *J. Adv. Model. Earth Syst.* **5**, 48–57 (2013).
17. L. R. Boysen et al., *Earth Syst. Dyn. Discuss.* **5**, 443–472 (2014).
18. X. Lee et al., *Nature* **479**, 384–387 (2011).
19. S. Luyssaert et al., *Nat. Clim. Change* **4**, 389–393 (2014).
20. M. Zhang et al., *Environ. Res. Lett.* **9**, 034002 (2014).
21. S.-S. Peng et al., *Proc. Natl. Acad. Sci. U.S.A.* **111**, 2915–2919 (2014).
22. Y. Li et al., *Nat. Commun.* **6**, 6603 (2015).
23. Z. Wan, *Remote Sens. Environ.* **140**, 36–45 (2014).
24. M. C. Hansen et al., *Science* **342**, 850–853 (2013).
25. P. K. Snyder, *Earth Interact.* **14**, 1–34 (2010).
26. F. Achard et al., *Glob. Change Biol.* **20**, 2540–2554 (2014).
27. A. J. Teuling et al., *Nat. Geosci.* **3**, 722–727 (2010).

ACKNOWLEDGMENTS

The authors gratefully acknowledge G. Duveiller and F. Achard for inspiring discussions and valuable inputs. The authors acknowledge the use of forest cover data from the University of Maryland (<http://earthenginepartners.appspot.com/science-2013-global-forest>); gridded air surface temperature data TS.3.22 from the Climatic Research Unit, University of East Anglia (<http://catalogue.ceda.ac.uk/uuid/3f894480cc48e1cbc29a5ee12d8542d>); and in situ monthly data of air temperature from the Global Historical Climatology Network (GHCN-Monthly, <http://www.ncdc.noaa.gov/ghcnm/v3.php>) of the National Oceanic and Atmospheric Administration's National Climatic Data Center. The MODIS products LST MYD11C3 and NDVI MYD13C2 were retrieved through the online data pool of the NASA Land Processes Distributed Active Archive Center (<https://lpdaac.usgs.gov>). The authors are grateful to C. Martinez for the linguistic revision. The work was supported by the European Commission JRC-IES-H07 ClimEcos

(995) and EU-FP7-LUC4C (603542). The authors contributed equally to the conception of the work, design of the analysis, development of the methodology, and interpretation of results. R.A. was responsible for the data processing and artwork, and A.C. finalized the writing of the text.

SUPPLEMENTARY MATERIALS

www.sciencemag.org/content/351/6273/600/suppl/DC1
Materials and Methods
Supplementary Text
Figs. S1 to S11
Table S1
References (28–39)

17 June 2015; accepted 7 January 2016
10.1126/science.aac8083

CANCER THERAPEUTICS

Allele-specific inhibitors inactivate mutant KRAS G12C by a trapping mechanism

Piro Lito,^{1*} Martha Solomon,² Lian-Sheng Li,³ Rasmus Hansen,³ Neal Rosen^{1,2*}

It is thought that KRAS oncoproteins are constitutively active because their guanosine triphosphatase (GTPase) activity is disabled. Consequently, drugs targeting the inactive or guanosine 5'-diphosphate-bound conformation are not expected to be effective. We describe a mechanism that enables such drugs to inhibit KRAS^{G12C} signaling and cancer cell growth. Inhibition requires intact GTPase activity and occurs because drug-bound KRAS^{G12C} is insusceptible to nucleotide exchange factors and thus trapped in its inactive state. Indeed, mutants completely lacking GTPase activity and those promoting exchange reduced the potency of the drug. Suppressing nucleotide exchange activity downstream of various tyrosine kinases enhanced KRAS^{G12C} inhibition, whereas its potentiation had the opposite effect. These findings reveal that KRAS^{G12C} undergoes nucleotide cycling in cancer cells and provide a basis for developing effective therapies to treat KRAS^{G12C}-driven cancers.

Wild-type RAS guanosine triphosphatases (GTPases) cycle between an active, guanosine 5'-triphosphate (GTP)-bound, and an inactive, guanosine 5'-diphosphate (GDP)-bound, state (1, 2). This is mediated by nucleotide exchange factors, which catalyze the exchange of GDP for GTP, and GTPase-activating proteins, which potentiate a weak intrinsic GTPase activity (3). Cancer-causing mutations impair the GTPase activity of RAS, causing it to accumulate in the activated state (4–6). Despite the prevalence of these mutations, no therapies that directly target this oncoprotein are currently available in the clinic (7–9). A recently identified binding pocket in KRAS^{G12C} (10) now enables the discovery of compounds that potentially inhibit KRAS-GTP or effector signaling by this mutant.

Here we characterize a novel compound, ARS853, designed to bind KRAS^{G12C} with high affinity (11). The structures of ARS853 and previously reported (10) compounds (cmpds) 6 and 12 are shown in fig. S1A. Treatment of KRAS^{G12C}-mutant lung cancer cells with ARS853 reduced the level of GTP-bound KRAS by more than 95% (Fig. 1A, 10 μM). This caused decreased phosphorylation of CRAF, ERK (extracellular signal-regulated kinase), and AKT. In contrast, even at the highest concentration tested, cmpd 6 or 12 had only a minimal effect on pCRAF and pERK, without affecting KRAS-GTP levels (Fig. 1A and fig. S1B). ARS853 inhibited proliferation with an inhibitory concentration 50% (IC₅₀) of 2.5 μM, which was similar to its IC₅₀ for target inhibition (Fig. 1, A and B). ARS853 (10 μM) inhibited effector signaling (Fig. 1C and fig. S1C) and cell proliferation (Fig. 1D and fig. S2) to varying degrees in six KRAS^{G12C} mutant lung cancer cell lines, but not in non-KRAS^{G12C} models (Fig. 1E and fig. S1, C and D). Similarly, it completely suppressed the effects of exogenous KRAS^{G12C} expression on KRAS-GTP levels, KRAS-BRAF interaction, and ERK signaling (fig. S1E). Inhib-

itor treatment also induced apoptosis in four KRAS^{G12C} mutant cell lines (Fig. 1, F to H). Thus, ARS853 selectively reduces KRAS-GTP levels and RAS-effector signaling in KRAS^{G12C}-mutant cells, while inhibiting their proliferation and inducing cell death.

In contrast to the rapid inhibition of signaling by kinase inhibitors, inhibition of KRAS^{G12C} by ARS853 occurred slowly (Fig. 2A and fig. S3). In some cell lines, maximal inhibition of KRAS-GTP occurred in 6 hours; in others, in 48 to 72 hours. To understand this phenomenon, we examined the mechanism of KRAS^{G12C} inhibition in more detail. To determine whether ARS853 binds to the active or the inactive conformation of KRAS^{G12C}, we used differential scanning fluorimetry, which assays ligand-induced changes in protein thermal stability (12). Recombinant KRAS^{G12C} was loaded with either GTPγS or GDP (fig. S4A) and then incubated with ARS853. Samples were incubated at increasing temperatures in the presence of a fluorescent dye that binds to hydrophobic surfaces exposed during thermal denaturation. ARS853 increased the amplitude of the thermal denaturation curve of KRAS^{G12C} loaded with GDP but not with GTPγS (Fig. 2B and fig. S4B). ARS853 did not alter the denaturation curve of GDP-loaded KRAS^{WT} (fig. S4C). These data suggest that ARS853 preferentially interacts with inactive, or GDP-bound, KRAS^{G12C}.

KRAS mutants are thought to exist in a “constitutively” active (GTP-bound) state in cancer cells (13). Thus, inhibition of KRAS-GTP levels by a drug that preferentially interacts with GDP-bound mutant KRAS is puzzling. Codon 12 mutations disable the activation of RAS GTPase by GTPase-activating proteins (14–16). It is possible, however, that the basal GTPase activity of KRAS^{G12C} is sufficient to enable nucleotide cycling in cancer cells. Consequently, we hypothesized that binding of the inhibitor to KRAS^{G12C} traps it in an inactive (GDP-bound) conformation by reducing its susceptibility to exchange, which then results in the observed time-dependent reduction in cellular KRAS-GTP levels. For this to be the case, (i) inhibition by the drug should require KRAS^{G12C} GTPase activity. (ii) If KRAS^{G12C} GTPase activity is constant, the rate of RAS inhibition by the drug should depend on exchange factor activity. (iii) Regulating exchange factor activity

¹Department of Medicine, Memorial Sloan Kettering Cancer Center, New York, NY, USA. ²Molecular Pharmacology Program, Memorial Sloan Kettering Cancer Center, New York, NY, USA. ³Wellspring Biosciences, La Jolla, CA, USA. *Corresponding author. E-mail: rosenn@mskcc.org (N.R.); lito@mskcc.org (P.L.)

should affect drug potency and the kinetics of inhibition.

We tested this hypothesis by using mutations that occur in cancer patients and affect the gua-

nine nucleotide cycle of RAS (Fig. 3A and fig. S5A). A59G is a “transition state” mutant that abrogates GTPase activity (17, 18). When assayed for their GTPase activity (Fig. 3B), KRAS^{WT} and

KRAS^{G12C} generated approximately three times as much hydrolysis product as the control reactions, whereas KRAS^{A59G} or KRAS^{G12C/A59G} had little activity. Thus, KRAS^{G12C} has basal GTPase

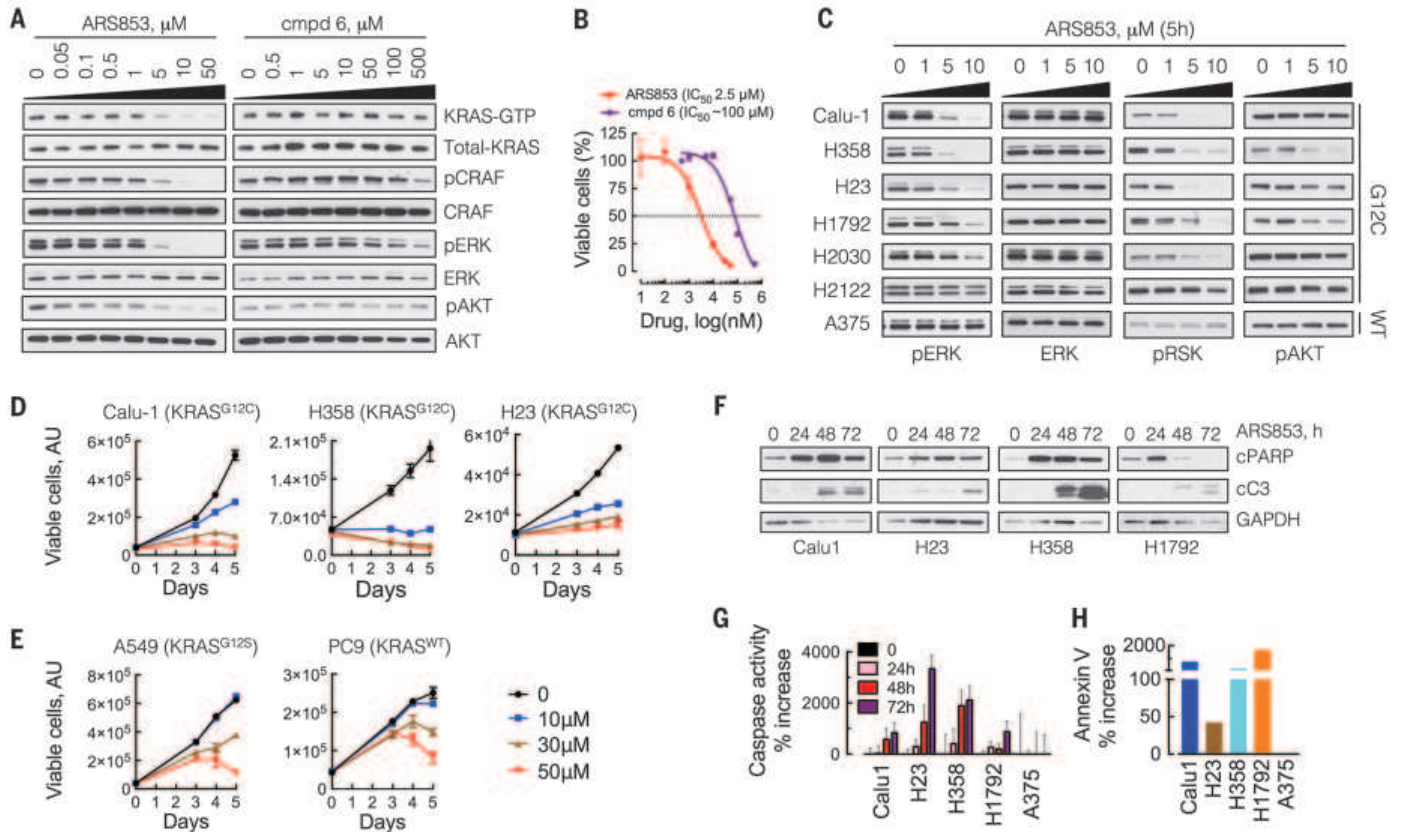


Fig. 1. Selective inhibition of KRAS^{G12C} signaling and cancer cell growth by ARS853. (A) KRAS^{G12C} mutant cells (H358) were treated with a novel (ARS853) or a previously described (cmpd 6) compound for 5 hours. The effect on the level of active, or GTP-bound, KRAS was determined by a RAS-binding domain pull-down (RBD:PD) assay and immunoblotting with a KRAS-specific antibody. The effect on ERK and AKT signaling was determined by immunoblotting with the indicated antibodies. A representative of at least two independent experiments for each compound is shown. (B) H358 cells were treated for 72 hours with increasing concentrations of the indicated inhibitors, followed by determination of viable cells by the ATP glow assay ($n = 3$ replicates). (C) The effect of ARS853 treatment on the inhibition of signaling intermediates in a panel of KRAS^{G12C}-mutant lung cancer cell lines. KRAS^{WT} A375 cells were used

as a control. A representative of at least two independent experiments for each cell line is shown. (D and E) The cell lines were treated over time to determine the effect of ARS853 on the proliferation of G12C (D) or non-G12C (E) KRAS models ($n = 3$ replicates). (F) The effect of ARS853 treatment on the cleavage of apoptotic intermediates was determined by immunoblotting with the indicated antibodies. A representative of two independent experiments is shown. (G) Cell extracts from the indicated cell lines treated with ARS853 were subjected to a caspase activation assay with the Z-DEVD-AMC reporter substrate. The increase in fluorescence relative to untreated (0) is shown ($n = 3$ replicates). (H) Following treatment with ARS853 for 24 hours, the cells were stained with annexin V and evaluated by flow cytometry to determine the increase in annexin V-positive cells relative to untreated cells. Data in (B), (D), (E), and (G) are mean and SEM.

Fig. 2. Inhibition of active KRAS levels despite an interaction with GDP-bound KRAS^{G12C}.

(A) KRAS^{G12C} mutant lung cancer cell lines were treated with ARS853 (10 μ M) over time, and cellular extracts were analyzed to determine the effect on KRAS-GTP as in Fig. 1A.

(B) Recombinant KRAS^{G12C} was loaded with GDP or nonhydrolyzable GTP γ S and then reacted with ARS853 at a 1:1 molar ratio for 1 hour, at room temperature. The samples were analyzed by differential scanning fluorimetry to determine the shift in thermal denaturation curve induced by ARS853 binding ($n = 4$ replicates for GDP and $n = 3$ replicates for GTP γ S). Mean and SEM are shown.

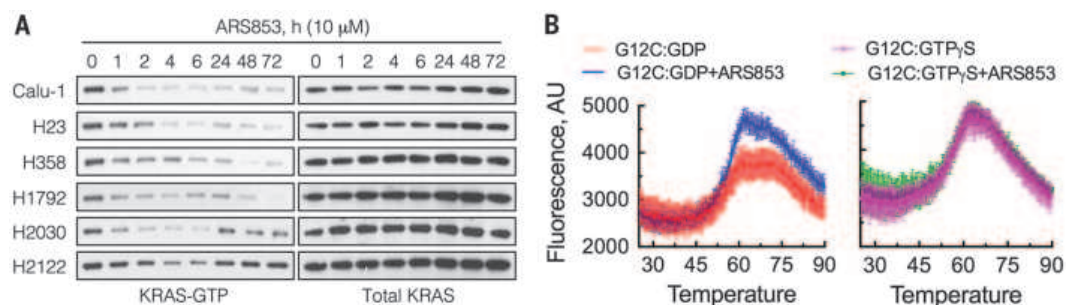
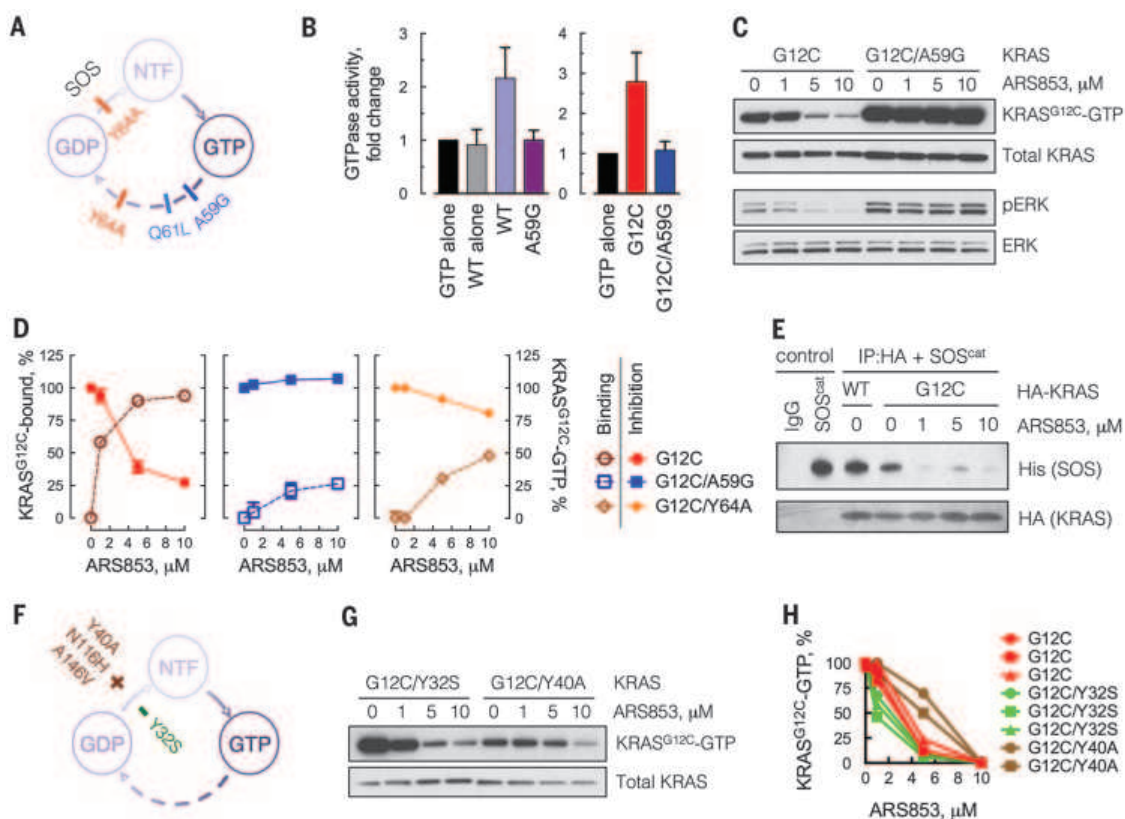


Fig. 3. Inhibition of KRAS^{G12C} requires GTPase activity and is attenuated by nucleotide exchange.

(A) Schematic of the mutations used to block the GTPase activity of KRAS. NTF, nucleotide free. (B) KRAS mutants, expressed and affinity purified from HEK293 cells, were subjected to a GTPase reaction. The orthophosphate product was measured by the Cytophos reagent and expressed as fold change over GTP alone ($n = 3$, mean and SEM). (C) HEK293 cells expressing HA-tagged KRAS constructs were treated with ARS853 for 5 hours. Cell extracts were evaluated by RBD:PD and immunoblotting with an anti-HA antibody, to determine the effect on GTP-bound mutant KRAS^{G12C}. A representative of three independent experiments is shown. (D) Extracts from cells expressing the KRAS constructs treated as shown were evaluated by mass spectrometry to determine the percentage of KRAS^{G12C} bound to the drug. KRAS^{G12C}-GTP levels in the same extracts were determined as in (C) and quantified by densitometry ($n = 3$, mean and SEM). (E) HEK293 cells expressing the constructs shown were treated with ARS853 for 5 hours. HA-tagged KRAS was immunoprecipitated (IP) and subjected to a binding assay with the catalytic domain of SOS (SOS^{cat}). (F) Schematic of the mutations used to biochemically increase (+) or decrease (-) the nucleotide



exchange function of KRAS^{G12C}. (G) HEK293 cells expressing the indicated constructs were analyzed as in (C). (H) The level of active KRAS-GTP was quantified by densitometry. Each replicate is shown. A similar result was obtained in H358 cells (fig. S6F). The baseline level of KRAS^{G12C/Y40A} detected by the RBD:PD is low because the Y40 mutation impairs the interaction of RAS with RAF (33). See also the effects of N116H and A146V mutations, which increase nucleotide exchange without affecting RAS-RAF interaction (fig. S6G).

activity that is suppressed by the A59G mutation (see also Fig. 3C, lane 5 versus lane 1). ARS853 reduced KRAS-GTP levels and ERK phosphorylation in human embryonic kidney 293 (HEK293) or H358 cells engineered to express KRAS^{G12C} but not in those expressing KRAS^{G12C/A59G} (Fig. 3C and fig. S5B). The crystal structure of HRAS^{A59G} shows that Q61, a critical residue for GTP hydrolysis, is displaced in this mutant (fig. S5C). Q61L impairs in vitro GTP hydrolysis by HRAS (19), and, when expressed in HEK293 cells, KRAS^{G12C/Q61L} was less sensitive to ARS853 than KRAS^{G12C} (fig. S5D). Y64A both reduces RAS GTPase activity and impairs the interaction of HRAS with the active site of the guanine nucleotide exchange factor (GEF) SOS (18, 20, 21) (fig. S6, A to C). As expected, ARS853 caused only minimal inhibition of GTP-bound KRAS^{G12C/Y64A} or signaling driven by this mutant (fig. S6D). Thus, KRAS^{G12C} GTPase activity is required for its inhibition by ARS853.

The percentage of KRAS^{G12C} bound to ARS853 in cells was evaluated by mass spectrometry (Fig. 3D, dotted line). GTPase-impairing mutations A59G or Y64A diminished the cellular

interaction of ARS853 with KRAS^{G12C} by ~75 and ~50%, respectively. This effect was inversely proportional to their effect on KRAS^{G12C}-GTP inhibition (Fig. 3D, solid line), supporting the conclusions that ARS853 interacts preferentially with GDP-bound KRAS^{G12C} in cells and that GTPase activity is required for the drug to bind and inhibit KRAS^{G12C}.

ARS853 reduced the interaction of KRAS^{G12C} with the catalytic subunit of SOS (Fig. 3E) and attenuated SOS-mediated nucleotide exchange by KRAS^{G12C} (fig. S6E). These findings suggest that ARS853 traps KRAS^{G12C} in a GDP-bound conformation by lowering its affinity for nucleotide exchange factors. It is therefore possible that nucleotide exchange activity modulates the effect of ARS853. We tested whether RAS mutations that affect nucleotide exchange alter the sensitivity of KRAS^{G12C} to ARS853 (Fig. 3F). Y40A, N116H, and A146V increase, whereas Y32S decreases, nucleotide exchange (22–24). Mutations that increase exchange attenuated the effect of ARS853 on KRAS^{G12C}-GTP, whereas Y32S caused a small augmentation of its effect (Fig. 3, G and H, and fig. S6, F and G). These data imply that

potentiation of nucleotide exchange reduces sensitivity to ARS853, by lowering the levels of GDP-bound KRAS^{G12C} available for drug binding.

If the inhibitor works by the trapping mechanism suggested by these data (Fig. 4A), then cellular parameters regulating nucleotide exchange ought to modulate the inhibition of KRAS^{G12C}. Exposure to epidermal growth factor (EGF), an activator of SOS (25), delayed the inhibition of KRAS^{G12C} by ARS853 by several hours compared to inhibition in serum-free medium (Fig. 4B and fig. S7A). Treatment with an EGF receptor (EGFR) inhibitor (fig. S7, B and C) or SOS-specific small interfering RNAs (fig. S7D) had the opposite effect. We determined if EGFR signaling affects the inhibition of the mutant KRAS^{G12C} allele, by expressing hemagglutinin (HA)-tagged KRAS^{G12C} in EGFR-mutant PC9 cells, in which nucleotide exchange depends on EGFR (26, 27). The specific effect on the mutant allele was determined by pulling down active KRAS and then immunoblotting for HA-tagged KRAS^{G12C}. ARS853 inhibited GTP-bound KRAS^{G12C} more potently in the presence of gefitinib, as compared to its absence (fig. S7E). Furthermore, EGFR inhibition

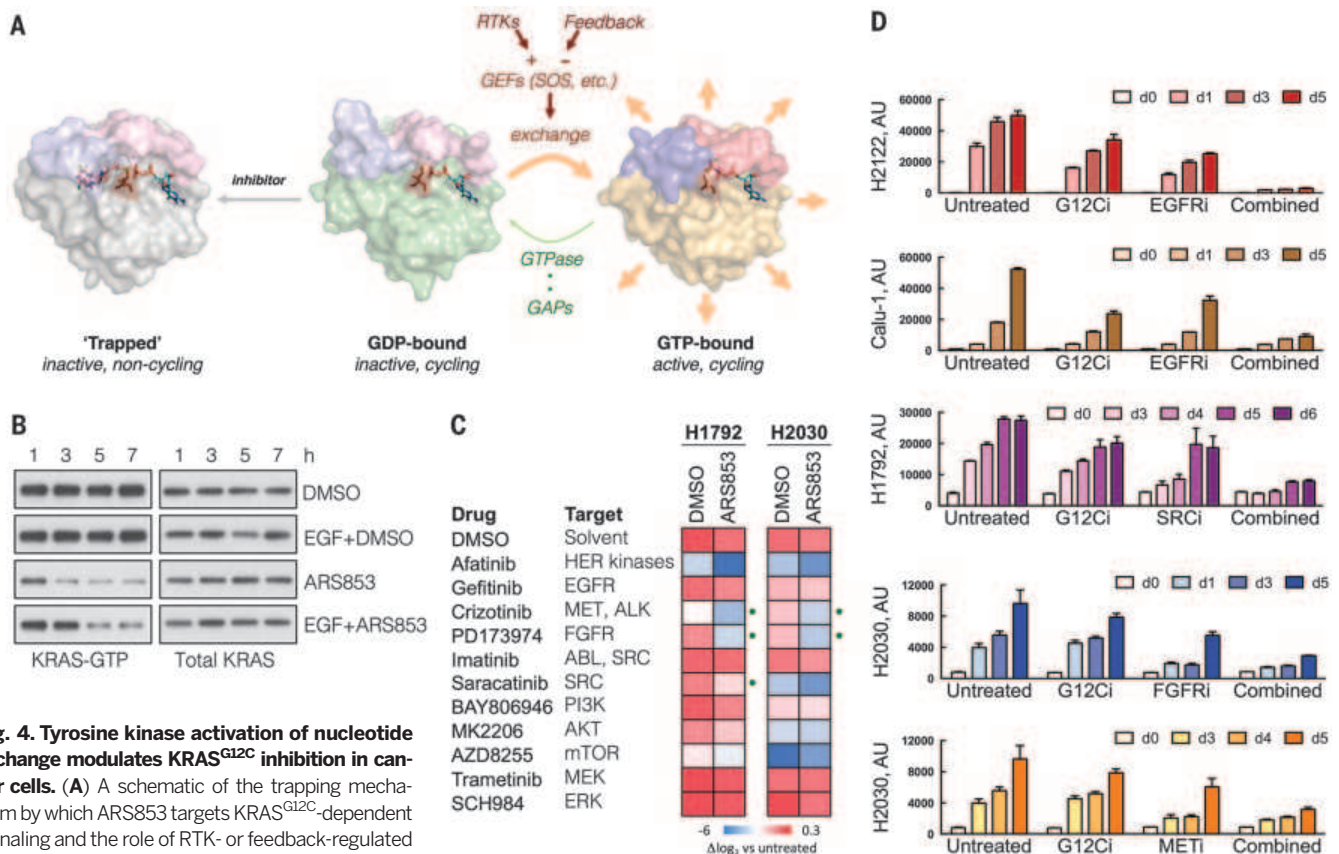


Fig. 4. Tyrosine kinase activation of nucleotide exchange modulates KRAS^{G12C} inhibition in cancer cells. (A) A schematic of the trapping mechanism by which ARS853 targets KRAS^{G12C}-dependent signaling and the role of RTK- or feedback-regulated nucleotide exchange in this process. Structures were adapted from Protein Data Bank accessions 4luc (inhibitor-bound KRAS^{G12C}-GDP), 4ldj (KRAS^{G12C}-GDP), and 4l9w (HRAS^{G12C}-GTP). (B) H358 cells were serum starved overnight followed by treatment with ARS853 (10 μ M), with or without EGF (100 ng/ml) for the indicated times, to determine the effect on KRAS-GTP. A representative of two independent experiments is shown. (C) The indicated cell lines, selected because of their relative insensitivity to KRAS^{G12C} inhibition, were treated with inhibitors of RTK signaling, alone or in combination with ARS853 for 5 days, in order

to determine the most effective combinations. The effect of treatment is shown relative to the proliferation of untreated cells. The dots indicate combination treatments resulting in significantly more pronounced inhibition, compared to either drug alone ($n = 3$ replicates, mean). DMSO, dimethyl sulfoxide. (D) The effect of inhibitors targeting tyrosine kinases on the antiproliferative effect of KRAS^{G12C} inhibition in KRAS^{G12C} mutant cell lines ($n = 3$ replicates, mean and SEM). The concentrations of the inhibitors used in (C) and (D) are noted in Materials and Methods.

enhanced the suppression of KRAS-GTP levels by ARS853 in both KRAS^{G12C} homozygous and heterozygous cells (fig. S7F). Receptor tyrosine kinase (RTK) signaling and nucleotide exchange are also subject to feedback inhibition by ERK or AKT (28). Mitogen-activated protein kinase (MEK) or AKT inhibitors relieve this feedback and activated RTK signaling (29, 30). Inhibiting these pathways also attenuated the inhibitory effect of ARS853 (fig. S7, G and H). Taken together, these findings show that RTK-mediated nucleotide exchange regulates the kinetics and potency of KRAS^{G12C} inhibition in cancer cells.

The above results also suggest that pharmacologic inhibition of the exchange reaction, as achieved, for example, with inhibitors of RTK signaling, ought to potentiate the antiproliferative effect of KRAS^{G12C} inhibitors. To test this hypothesis, we evaluated the effects of 11 inhibitors targeting RTKs, or their downstream signaling pathways, in KRAS^{G12C}-mutant cell lines. In agreement with our model, inhibiting the tyrosine kinase activities of MET, SRC, or FGFR (fibroblast growth factor receptor) enhanced

growth inhibition by ARS853 in H1792 and H2030 cells, whereas MEK, ERK, phosphatidylinositol 3-kinase (PI3K), or AKT inhibitor treatment did not have a significant effect (Fig. 4, C and D). In H2122 and Calu-1 cells, the effect of ARS853 was potentiated by concurrent inhibition of EGFR (Fig. 4D). Inhibition of EGFR also enhanced the induction of caspase activity by ARS853 (fig. S7I). These findings support another report showing that EGFR is required for KRAS-driven cancer formation (31) and suggest that the RTKs responsible for modulating the timing of KRAS^{G12C} inhibition in lung cancer vary from tumor to tumor. They also provide a rationale for selecting optimal combination treatments to achieve maximal KRAS^{G12C} inhibition in patients.

We thus report an inhibitor that suppresses KRAS^{G12C} signaling and tumor cell growth by binding to the GDP-bound form of the protein. This reduces the levels of KRAS^{G12C}-GTP, because the protein retains GTPase activity and undergoes nucleotide cycling in cells. Some RAS mutants have low levels of basal GTPase activity in vitro; yet, perhaps owing to an inability to

directly test such activity in vivo, these oncoproteins are assumed to be constitutively GTP-bound in cancer cells. The data presented here, however, indicate that inhibition by ARS853 requires GTPase activity and that nucleotide exchange activity is inversely related to the kinetics and/or magnitude of inhibition. The model suggests that the RAS inhibitor and exchange factors compete for binding to KRAS^{G12C}-GDP. Drug-bound KRAS^{G12C}-GDP is not susceptible to exchange and exits the cycle, thus lowering the levels of KRAS^{G12C}-GTP.

This model also predicts that genetic alterations that completely disable KRAS^{G12C} GTPase activity, or those that activate nucleotide exchange function, will confer resistance to this class of drugs. Careful selection of combination therapies may in turn prevent or delay the emergence of resistance by enabling a more potent inhibition of KRAS^{G12C}. The mechanism of action elucidated here establishes a basis for such combination therapies. Inhibitors of receptors dominantly responsible for activation of RAS nucleotide exchange are predicted to enhance activity, whereas inhibitors of downstream

pathways that reactivate these receptors are likely to blunt inhibition of mutant KRAS.

KRAS^{G12C} mutations occur in 16% of lung adenocarcinomas (32), making them one of the most frequent activating genetic alterations in lung cancer, a disease responsible for approximately 1.6 million annual deaths worldwide. No effective inhibitor of mutant KRAS has yet been developed for use in the clinic. Our results suggest that KRAS^{G12C} allele-specific inhibitors, such as the one described here, merit investigation as potential therapeutics for KRAS^{G12C} lung cancers.

REFERENCES AND NOTES

1. Y. Pylayeva-Gupta, E. Grabocka, D. Bar-Sagi, *Nat. Rev. Cancer* **11**, 761–774 (2011).
2. A. G. Stephen, D. Esposito, R. K. Bagni, F. McCormick, *Cancer Cell* **25**, 272–281 (2014).
3. J. L. Bos, H. Rehmann, A. Wittinghofer, *Cell* **129**, 865–877 (2007).
4. L. F. Parada, C. J. Tabin, C. Shih, R. A. Weinberg, *Nature* **297**, 474–478 (1982).
5. E. Santos, S. R. Tronick, S. A. Aaronson, S. Pulcinani, M. Barbacid, *Nature* **298**, 343–347 (1982).
6. E. Taparowsky *et al.*, *Nature* **300**, 762–765 (1982).
7. G. Bollag, C. Zhang, *Nature* **503**, 475–476 (2013).
8. A. D. Cox, S. W. Fesik, A. C. Kimmelman, J. Luo, C. J. Der, *Nat. Rev. Drug Discov.* **13**, 828–851 (2014).
9. J. Spiegel, P. M. Cromm, G. Zimmermann, T. N. Grossmann, H. Waldmann, *Nat. Chem. Biol.* **10**, 613–622 (2014).
10. J. M. Ostrem, U. Peters, M. L. Sos, J. A. Wells, K. M. Shokat, *Nature* **503**, 548–551 (2013).
11. M. P. Patricelli *et al.*, *Cancer Discov.* CD-15-1105 (2016).
12. F. H. Niesen, H. Berglund, M. Vedadi, *Nat. Protoc.* **2**, 2212–2221 (2007).
13. S. Gysin, M. Salt, A. Young, F. McCormick, *Genes Cancer* **2**, 359–372 (2011).
14. G. Bollag, F. McCormick, *Nature* **351**, 576–579 (1991).
15. K. Scheffzek *et al.*, *Science* **277**, 333–338 (1997).
16. I. R. Vetter, A. Wittinghofer, *Science* **294**, 1299–1304 (2001).
17. B. E. Hall, D. Bar-Sagi, N. Nassar, *Proc. Natl. Acad. Sci. U.S.A.* **99**, 12138–12142 (2002).
18. S. M. Margarit *et al.*, *Cell* **112**, 685–695 (2003).
19. M. J. Smith, B. G. Neel, M. Ikura, *Proc. Natl. Acad. Sci. U.S.A.* **110**, 4574–4579 (2013).
20. P. A. Boriack-Sjodin, S. M. Margarit, D. Bar-Sagi, J. Kuriyan, *Nature* **394**, 337–343 (1998).
21. H. Sondermann *et al.*, *Cell* **119**, 393–405 (2004).
22. L. A. Feig, G. M. Cooper, *Mol. Cell. Biol.* **8**, 2472–2478 (1988).
23. B. E. Hall, S. S. Yang, P. A. Boriack-Sjodin, J. Kuriyan, D. Bar-Sagi, *J. Biol. Chem.* **276**, 27629–27637 (2001).
24. G. Patel, M. J. MacDonald, R. Khosravi-Far, M. M. Hisaka, C. J. Der, *Oncogene* **7**, 283–288 (1992).
25. M. A. Lemmon, J. Schlessinger, *Cell* **111**, 1117–1134 (2010).
26. W. Pao, J. Chmielecki, *Nat. Rev. Cancer* **10**, 760–774 (2010).
27. T. M. Chin *et al.*, *Clin. Cancer Res.* **14**, 6867–6876 (2008).
28. P. Lito, N. Rosen, D. B. Solit, *Nat. Med.* **19**, 1401–1409 (2013).
29. S. Chandralapaty *et al.*, *Cancer Cell* **19**, 58–71 (2011).
30. P. Lito *et al.*, *Cancer Cell* **22**, 668–682 (2012).
31. C. Navas *et al.*, *Cancer Cell* **22**, 318–330 (2012).
32. E. A. Collisson *et al.*, *Nature* **511**, 543–550 (2014).
33. P. Rodriguez-Viciana *et al.*, *Cell* **89**, 457–467 (1997).

ACKNOWLEDGMENTS

We thank C. Sawyers and M. Mroczkowski for reviewing the manuscript. This work has been funded by the National Institutes of Health (PO1CA129243-06 to N.R. and P.L.; K08CA191082-01A1 to P.L.), the Memorial Sloan Kettering Cancer Center Experimental Therapeutics “Big Bets” program

(SK112103 to N.R. and P.L.), the LUNgevity Foundation Career Development Award (P.L.) and the V Foundation Translational Grant (P.L.). N.R. is a member of the Scientific Advisory Board of Wellspring Biosciences and has received grant support from this organization. L.-S.L. and R.H. are employees of Wellspring Biosciences. ARS853 was obtained from Wellspring Biosciences under a material transfer agreement. L.-S.L. is an inventor on a patent held by Araxes Pharma LLC (an affiliate of Wellspring Biosciences) that covers ARS853.

SUPPLEMENTARY MATERIALS

www.sciencemag.org/content/351/6273/604/suppl/DC1
Materials and Methods
Figs. S1 to S7
References (34–36)

12 October 2015; accepted 6 January 2016
Published online 14 January 2016
10.1126/science.aad6204

STRUCTURAL BIOLOGY

Structures of aminoarabinose transferase ArnT suggest a molecular basis for lipid A glycosylation

Vasileios I. Petrou,¹ Carmen M. Herrera,^{2*} Kathryn M. Schultz,^{3*} Oliver B. Clarke,⁴ Jérémie Vendome,^{4,5} David Tomasek,¹ Surajit Banerjee,⁶ Kanagalaghatta R. Rajashankar,⁶ Meagan Belcher Dufresne,¹ Brian Kloss,⁷ Edda Kloppmann,⁸ Burkhard Rost,^{8,9} Candice S. Klug,³ M. Stephen Trent,² Lawrence Shapiro,⁴ Filippo Mancini^{1†}

Polymyxins are antibiotics used in the last line of defense to combat multidrug-resistant infections by Gram-negative bacteria. Polymyxin resistance arises through charge modification of the bacterial outer membrane with the attachment of the cationic sugar 4-amino-4-deoxy-L-arabinose to lipid A, a reaction catalyzed by the integral membrane lipid-to-lipid glycosyltransferase 4-amino-4-deoxy-L-arabinose transferase (ArnT). Here, we report crystal structures of ArnT from *Cupriavidus metallidurans*, alone and in complex with the lipid carrier undecaprenyl phosphate, at 2.8 and 3.2 angstrom resolution, respectively. The structures show cavities for both lipidic substrates, which converge at the active site. A structural rearrangement occurs on undecaprenyl phosphate binding, which stabilizes the active site and likely allows lipid A binding. Functional mutagenesis experiments based on these structures suggest a mechanistic model for ArnT family enzymes.

Polymyxins are last-resort antibiotics used to combat multidrug-resistant infections by Gram-negative bacteria (1, 2). They are thought to act by permeabilizing the membranes of Gram-negative bacteria, after binding to the lipopolysaccharide (LPS) of the outer membrane (1, 2). This association with the outer membrane is primarily achieved through electrostatic interactions between amino groups of polymyxins and negatively charged moieties of

the backbone glucosamine and 3-deoxy-D-manno-oct-2-ulosonic acid (Kdo) sugars of lipid A, an amphipathic saccharolipid that anchors LPS to the outer leaflet of the outer membrane (3). Resistance to polymyxins develops through active modifications of lipid A, which cap the glucosamine sugar phosphates and thus reduce negative membrane charge (4). Lipid A modification is also relevant for evasion of naturally occurring cationic antimicrobial peptides by Gram-negative bacteria (5, 6).

In *Escherichia coli* and *Salmonella enterica*, the most effective modification for reduction of negative membrane charge is the attachment of the cationic sugar 4-amino-4-deoxy-L-arabinose (L-Ara4N) to lipid A phosphate groups at the 1 and 4' positions (7). L-Ara4N is provided by the lipid carrier undecaprenyl phosphate (UndP). The reaction is catalyzed on the periplasmic side of the inner membrane by ArnT (PmrK), an integral membrane lipid-to-lipid glycosyltransferase and the last enzyme in the aminoarabinose biosynthetic pathway of Gram-negative bacteria (4, 7, 8) (Fig. 1A). The lipid A 1-phosphate group is also modified by EptA (PmrC), which adds phosphoethanolamine (pEtN), competing with ArnT for the 1-phosphate site (9, 10).

To gain insight into the structure and mechanistic basis of ArnT function, we screened 12

¹Department of Physiology and Cellular Biophysics, Columbia University, New York, NY 10032, USA. ²Department of Infectious Diseases, University of Georgia, College of Veterinary Medicine, Athens, GA 30602, USA. ³Department of Biophysics, Medical College of Wisconsin, Milwaukee, WI 53226, USA. ⁴Department of Biochemistry and Molecular Biophysics, Columbia University, New York, NY 10032, USA. ⁵Department of Systems Biology, Columbia University, New York, NY 10032, USA. ⁶Department of Chemistry and Chemical Biology, Cornell University, Northeastern Collaborative Access Team, Advanced Photon Source, Argonne, IL 60439, USA. ⁷New York Consortium on Membrane Protein Structure, New York Structural Biology Center, 89 Convent Avenue, New York, NY 10027, USA. ⁸Department of Informatics, Bioinformatics and Computational Biology, Technische Universität München, Boltzmannstrasse 3, 85748 Garching, Germany.

⁹Institute for Advanced Study (TUM-IAS), Technische Universität München, Boltzmannstrasse 3, 85748 Garching, Germany.

*These authors contributed equally to this work.

†Corresponding author. E-mail: fmi23@cumc.columbia.edu

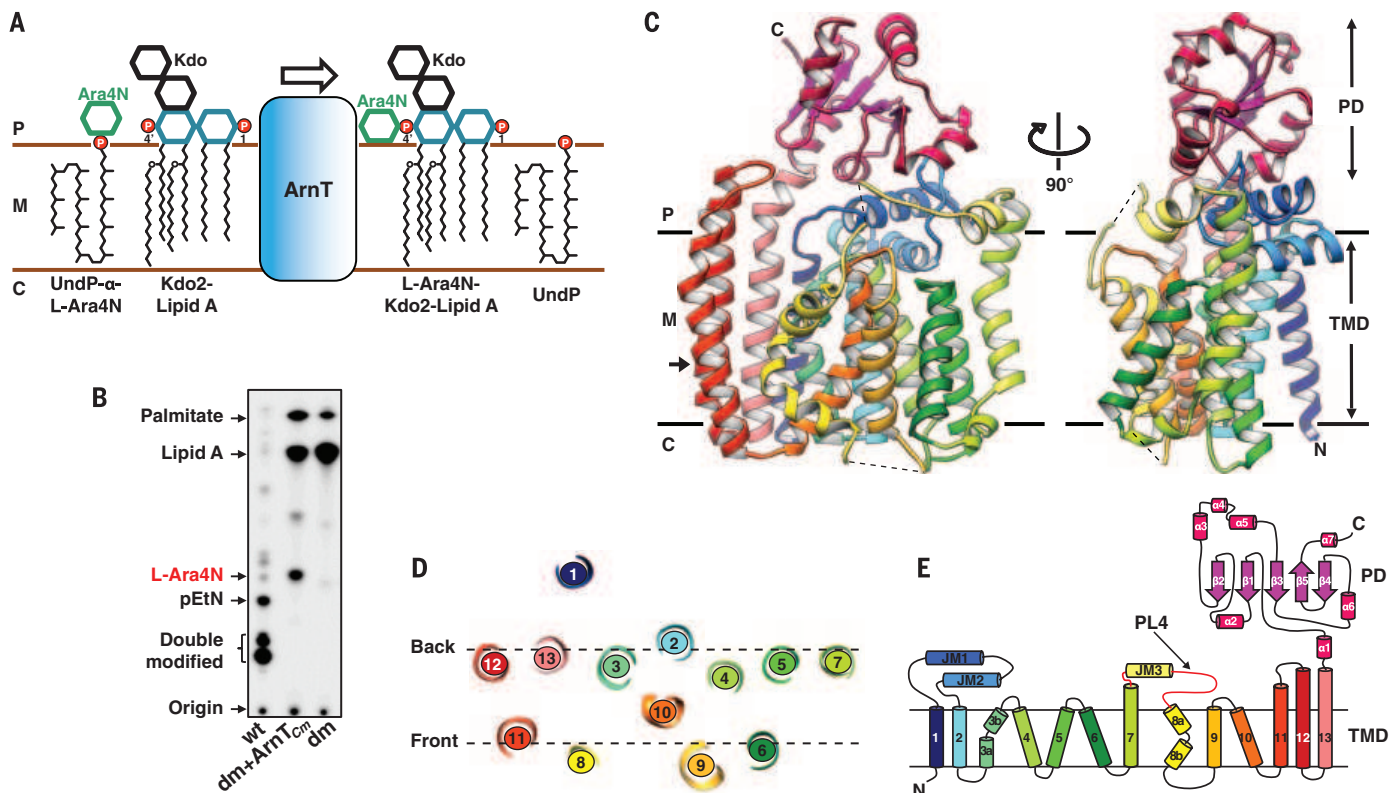


Fig. 1. Structure and function of ArnT from *Cupriavidus metallidurans* CH34. (A) Schematic representation of the reaction catalyzed by ArnT. The sugar L-Ara4N is transferred from the carrier UndP to lipid A. 1 and 4' phosphate positions on lipid A are marked. (B) Analysis of ^{32}P -labeled lipid A species by TLC showing rescue of lipid A modification with L-Ara4N when ArnT_{Cm} is expressed in the $\Delta\text{arnT}\Delta\text{eptA}$ double-knockout *E. coli* strain (dm). The background *E. coli* strain (WD101; wt, wild type) has a pmrA constitutive phenotype (pmrA^C), enabling it to synthesize L-Ara4N- and pEtN-modified lipid A and to exhibit resistance to polymyxins (8). (C) Crystal structure of ArnT_{Cm}. Two

orthogonal views, perpendicular to the plane of the membrane, are presented in ribbon representation with rainbow coloring starting from the N terminus (blue) to the C terminus (purple). The approximate dimensions of the monomer are 55, 79, and 42 Å (width, height, and depth). Membrane boundaries shown were calculated using the PPM server (21). Dashed lines represent missing segments in the structure. (D) Arrangement of TM helices in ArnT_{Cm} shown as a slice of the TM domain at the level indicated by the arrow in (C). (E) Schematic representation of the connectivity and structural elements of ArnT_{Cm}. P, periplasm; M, membrane (inner); C, cytoplasm; TMD: TM domain; PL4 (shown in red).

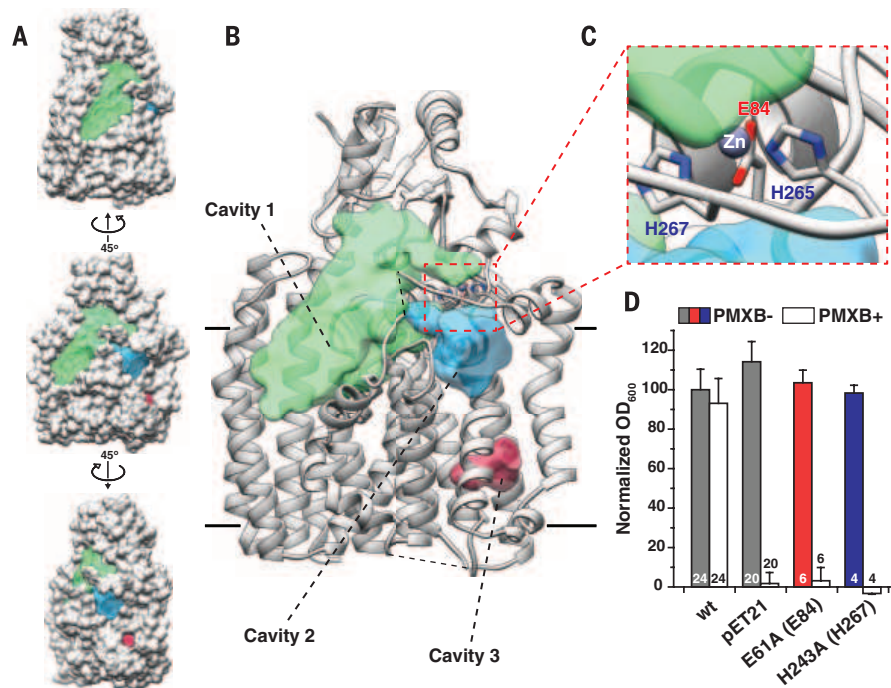


Fig. 2. Significant structural features of ArnT_{Cm}.

(A) Three views of ArnT_{Cm} in spacefill representation showing the location of notable cavities in the structure. The middle view has the same orientation as the view in (B). The other two are obtained by 45° rotation in opposite directions around a vertical axis. Cavities are color coded as in (B), where their identity is labeled. (B) Ribbon representation of ArnT_{Cm} showing the volumes of notable cavities in the structure. Volumes were calculated using the Voss Volume Voxelator server (22), using probes with 15 and 1.75 Å radii, corresponding to the outer and inner probe, respectively. The approximate membrane boundaries are shown as black lines. (C) Close-up of the metal coordination site in ArnT_{Cm} showing Zn²⁺ as a purple sphere and the coordinating residues colored by heteroatom. The dashed red line box in (B) shows the overall location of the coordination site. (D) The effect of mutations in Zn²⁺ coordinating residues on ArnT_{Se} expressed in a BL21(DE3) ΔarnT *E. coli* strain for rescue of polymyxin B (PMXB) resistance (13). Corresponding residue numbers in ArnT_{Cm} are shown in parentheses here and in all subsequent figures. OD₆₀₀, optical density at 600 nm. Data presented are means + SD. *N* is shown for each data column.

prokaryotic putative ArnTs from diverse species to find a candidate for crystallization (11). ArnT from *Cupriavidus metallidurans* CH34 (ArnT_{Cm}) emerged as the most promising based on expression levels (fig. S1A) and behavior in size-exclusion chromatography in detergent (fig. S1B). This protein yielded crystals in lipidic cubic phase (LCP) (12) (fig. S1, C and D) that were suitable for structure determination.

We characterized ArnT_{Cm} to determine whether it was a true ArnT capable of transferring 1-Ara4N to lipid A. Thin-layer chromatography (TLC) of ³²P-labeled lipid A isolated from *E. coli* showed that heterologous expression of ArnT_{Cm} in an *E. coli* strain lacking endogenous *arnT* and *eptA* (Δ arnT Δ eptA) resulted in lipid A modification by 1-Ara4N (Fig. 1B). The identity of the transferred sugar was confirmed by mass spectrometry (fig. S2A). Unlike ArnT from *Salmonella enterica* serovar Typhimurium (ArnT_{Se}), ArnT_{Cm} failed to rescue resistance to polymyxin in Δ arnT (13, 14) (fig. S2B) and in Δ arnT Δ eptA (fig. S2C) *E. coli* strains. Although it is known that ArnT_{Se} adds 1-Ara4N to both the 1 and 4' phosphates of lipid A (7), ArnT_{Cm} appears only to yield a single lipid A species modified at the 1-phosphate position (fig. S2D), which suggests that modification at the 1-position does not confer protection to polymyxin in *E. coli*. Consistent with this, removal or modification of the 4'-phosphate confers polymyxin resistance in other species (15, 16). Therefore, functional hypotheses derived from the structures of ArnT_{Cm} were tested on ArnT_{Se} by using a polymyxin growth assay previously established in *E. coli* (13, 14) and with a direct assay on ArnT_{Cm} for some mutants. The overall sequence identity between ArnT_{Se} and ArnT_{Cm} is 23%, but the degree of conservation in and around the key regions for activity is substantially higher, which suggests that their structure and function are likely conserved (fig. S3).

The structure of ArnT_{Cm} was determined to 2.8 Å resolution by the single-wavelength anomalous diffraction method using SeMet-substituted protein (fig. S4 and Table 1). ArnT_{Cm} is a monomer, consisting of a transmembrane (TM) domain and a soluble periplasmic domain (PD) positioned above it (Fig. 1C). The TM domain, demarcated by a clear hydrophobic belt (fig. S5A), shows 13 TM helices, as recently predicted for ArnT from *Burkholderia cenocepacia* (17), in an intricate arrangement (Fig. 1, D and E). The structure has three juxtamembrane (JM) helices (JM1 to JM3). JM1 and JM2 are both part of the first periplasmic loop and are perpendicular to each other, creating a distinctive cross-shaped structure (Fig. 1C). JM3 leads into a flexible periplasmic loop between TM7 and TM8 [periplasmic loop 4 (PL4), partially disordered in the structure], previously shown to be functionally important (13, 17). TM13 leads into the PD, which has an $\alpha/\beta/\alpha$ arrangement (Fig. 1E).

ArnT is a member of the GT-C family of glycosyltransferases (18), and it has a similar fold to a bacterial oligosaccharyltransferase (OST) from *Campylobacter lari* (PglB) and to an archaeal OST from *Archaeoglobus fulgidus* (AglB) (19, 20) (fig.

S6A). The topology differs among the three (fig. S6B), but an inner core of AglB's TM domain aligns well with that of ArnT_{Cm} (fig. S6C) and a part of the PDs of ArnT_{Cm} and PglB is similar (fig. S6, D and E). These similarities in fold may underscore an evolutionary relationship, but the functions of the

three enzymes are markedly different. Only ArnT has a lipid as glycosyl acceptor (lipid A). Because both substrates are lipidic, ArnT must bring both from the membrane to the active site for catalysis.

The structure of ArnT_{Cm} shows three major cavities (Fig. 2, A and B), which differ in their

Table 1. Data collection and refinement statistics for ArnT. $I/\sigma(I)$, the empirical signal-to-noise ratio; $CC_{1/2}$, a correlation coefficient; N/A, not applicable; h , k , and l , indices that define the lattice planes; R_{meas} , multiplicity-corrected R ; R_{pim} , expected precision; RMS, root mean square; clashscore is a validation tool in Phenix; TLS, translation/libration/screw, a mathematical model. Note that the apo data set was collected from crystals grown in the presence of decaprenyl phosphate. The presence of this compound in the crystallization mix does not lead to the conformational change observed in the ligand-bound form (see Materials and Methods).

	apo	bound (UndP)	SeMet
Data collection			
Wavelength (Å)	0.979	0.979	0.979
Resolution range (Å)	46.2–2.7 (2.8–2.7)	47.9–3.2 (3.3–3.2)	75.5–3.3 (3.4–3.3)
Space group	P2 ₁ 2 ₁ 2 ₁	P2 ₁ 2 ₁ 2 ₁	P2 ₁ 2 ₁ 2 ₁
Unit cell: a, b, c (Å)	58.60, 80.63, 150.25	59.65, 80.32, 150.16	58.91, 81.21, 151.63
Total reflections	554,931 (41,515)	89,964 (8,386)	265,697 (25,867)
Unique reflections	20,239 (2,000)	12,427 (1,212)	11,387 (1,120)
Multiplicity	27.4 (20.8)	7.2 (6.9)	23.3 (23.1)
Completeness (%)	99.9 (100.0)	99.8 (99.5)	100 (99.9)
Mean $I/\sigma(I)$	25.5 (0.9)	5.6 (1.3)	11.4 (2.4)
Wilson B-factor (Å ²)	65.2	63.8	81.5
R_{merge}	0.38 (3.5)	0.37 (1.9)	0.23 (1.3)
R_{meas}	0.39 (3.6)	0.40 (2.0)	0.23 (1.3)
R_{pim}	0.075 (0.767)	0.144 (0.748)	0.048 (0.271)
$CC_{1/2}$	0.999 (0.218)	0.994 (0.468)	1.000 (0.839)
Resolution where $I/\sigma(I) > 2.0$ (overall)	2.83	3.40	N/A
Resolution where $I/\sigma(I) > 2.0$ (along h)	2.92	3.20	N/A
Resolution where $I/\sigma(I) > 2.0$ (along k)	2.70	4.11	N/A
Resolution where $I/\sigma(I) > 2.0$ (along l)	2.84	3.58	N/A
Resolution where $CC_{1/2} > 0.5$ (overall)	2.86	3.20	N/A
Resolution where $CC_{1/2} > 0.5$ (along h)	2.81	3.20	N/A
Resolution where $CC_{1/2} > 0.5$ (along k)	2.83	3.85	N/A
Resolution where $CC_{1/2} > 0.5$ (along l)	2.94	3.36	N/A
Refinement			
Reflections used in refinement	20,239 (1,962)	12,427 (1,208)	N/A
Reflections used for R_{free}	1047 (96)	668 (59)	N/A
R_{work}	0.21 (0.41)	0.22 (0.32)	N/A
R_{free}	0.26 (0.42)	0.26 (0.38)	N/A
Number of nonhydrogen atoms	4,562	4,804	N/A
Macromolecules	4,097	4,171	N/A
Ligands	431	627	N/A
Protein residues	537	541	N/A
RMS (bonds)	0.003	0.002	N/A
RMS (angles)	0.56	0.49	N/A
Ramachandran favored (%)	97	96	N/A
Ramachandran allowed (%)	2.8	3.7	N/A
Ramachandran outliers (%)	0	0.2	N/A
Rotamer outliers (%)	0.5	0.5	N/A
Clashscore	4.25	4.96	N/A
Average B-factor	75.8	50.6	N/A
Macromolecules	74.4	49.5	N/A
Ligands	89.6	57.4	N/A
Solvent	65.1	44.2	N/A
Number of TLS groups	2	2	N/A

electrostatic nature. The largest ($>3000 \text{ \AA}^3$ within the membrane), cavity 1, is amphipathic with a lower, primarily hydrophobic portion located below the level of the membrane and an upper hydrophilic one (fig. S5B). We hypothesize that cavity 1 is where lipid A binds to ArnT. Note that the hydrophobic portion of cavity 1 is directly accessible from the outer leaflet of the inner membrane, and it has a volume compatible with the acyl chains and the glucosamine sugar backbone of lipid A. This suggests a simple mechanism for lipophilic substrate recruitment, although entrance to cavity 1 may be occluded by PL4 (Fig. 2, A and B). The Kdo sugars of lipid A could bind to the hydrophilic upper portion of the cavity and possibly interact with the PD. The smaller cavity 2, connected to cavity 1 through a narrow passage, is primarily hydrophilic, despite its position, at least in part, below the boundary of the membrane (Fig. 2, A and B, and fig. S5B). Finally, cavity 3, located close to the cytoplasmic side of the molecule is entirely hydrophobic (Fig. 2, A and B, and fig. S5B).

ArnT_{Cm} binds a metal we identified as Zn between JM1 and PL4 (Fig. 2C and fig. S7). The Zn²⁺ ion is bound with a five-point trigonal bipyramidal coordination by glutamic acid at position 84 (E84) (bidentate), histidines H265 and H267, and likely by a water molecule (Fig. 2C), replaced in our crystals by the carboxy-terminal carbonyl from a symmetry-related molecule (fig. S7B). All three metal-coordinating residues appear to be important for function, as shown by the lack of polymyxin resistance in ArnT_{Se} when mutated (Fig. 2D) (13). However, H265 is a valine (V241) in ArnT_{Se} (fig. S3A), and therefore, its metal coordination must differ.

To investigate how ArnT interacts with its lipid substrates, we cocrystallized ArnT_{Cm} with

UndP by incorporating this hydrophobic compound into the LCP mixture, and we determined the structure to 3.2 Å resolution (Table 1). The ArnT_{Cm}-UndP structure features three discontinuous densities compatible with a poly-prenyl ligand, which allowed us to model the entire carrier lipid (Fig. 3A and fig. S8). The upper density (Fig. 3A), stemming from inside cavity 2, corresponds to the phosphate head group and five prenyl groups and defines the approximate location of the active site within the hydrophilic cavity 2 (Fig. 3B). The lower region of density (Fig. 3A), corresponding to the last four prenyls of UndP, extends from cavity 3, which is lined with hydrophobic residues that provide an ideal environment for accommodating the lipid tail (Fig. 3C). Mutations within cavity 3 had only a marginal effect on ArnT_{Se} function (fig. S9). These results may indicate flexibility of the UndP binding mode away from the active site.

Notably, in the UndP-bound structure, we observed a structural rearrangement of PL4. A coil-to-helix transition results in an extension of JM3 by two full turns, which leads to a repositioning of several residues around UndP and the apparent loss of metal coordination (Fig. 3, A and D). The nature of Zn²⁺ coordination is consistent with a role in fixing the loop in a conformation that allows the UndP substrate to bind. The conformation observed in the UndP-bound structure substantially reduces the volume of cavity 2, as the extension of JM3 envelopes the head of the substrate (fig. S10). Furthermore, although the volume of cavity 1 is only marginally changed, the UndP-mediated structural rearrangement enables displacement of PL4 from the cavity 1 surface, which may enable access to lipid A (fig. S10).

The phosphate of UndP is coordinated by lysine K85 and arginine R270, whereas the oxy-

gen of the phosphodiester bond participates in hydrogen bonding with tyrosine Y345 (Fig. 3B). These three residues are absolutely conserved (fig. S11), and their mutation in ArnT_{Se} leads to complete loss of function (Fig. 3E) (13). A sulfate ion identified in the structure of AglB and proposed to occupy the position of the UndP phosphate (20), is superimposable with the phosphate of UndP in our structure (fig. S12), which suggests a common modality for donor substrate orientation.

Naïve docking of 1-Ara4N-tri-prenyl phosphate to the ArnT_{Cm} structure yielded a highly populated pose with favorable energy and positions that matched the experimentally observed UndP (fig. S13). This pose revealed three additional conserved residues (Y59, Y82 and E506) that are likely to interact with 1-Ara4N. We confirmed the importance of Y59 and Y82 in ArnT_{Se} function (Fig. 3E). Residues corresponding to Y59, K85, R270, and E506, have been shown to be functionally relevant in ArnT from *B. cenocepacia* (17). E84, which coordinates Zn²⁺ in apo ArnT_{Cm}, appears to bind the amino group of 1-Ara4N, which suggests a possible role for this residue in transitioning to the substrate-bound form. In ArnT_{Cm}, E84A was also inactive (fig. S14).

Overall, the structures of ArnT_{Cm} suggest that the binding of substrates may be sequential, with UndP- α -1-Ara4N binding stabilizing a conformation accessible to lipid A (Fig. 4A). The active site, situated between the two substrate cavities, is completed by elements of the extended JM3 helix only with UndP bound (Fig. 4, A and B). The structure with bound UndP and modeled 1-Ara4N is consistent with a catalytic mechanism in which two conserved aspartic acid residues, D55 and D158, located at the interface between cavities 1 and 2 (Fig. 4B) and engaged in salt bridges

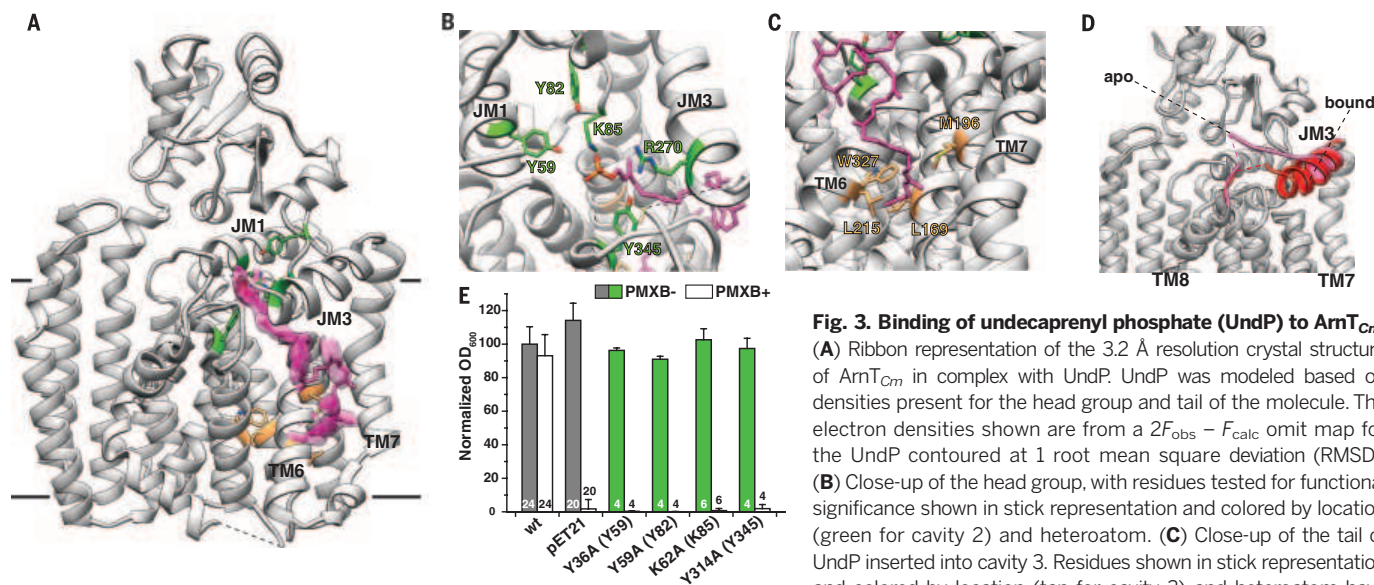


Fig. 3. Binding of undecaprenyl phosphate (UndP) to ArnT_{Cm}. (A) Ribbon representation of the 3.2 Å resolution crystal structure of ArnT_{Cm} in complex with UndP. UndP was modeled based on densities present for the head group and tail of the molecule. The electron densities shown are from a $2F_{\text{obs}} - F_{\text{calc}}$ omit map for the UndP contoured at 1 root mean square deviation (RMSD). (B) Close-up of the head group, with residues tested for functional significance shown in stick representation and colored by location (green for cavity 2) and heteroatom. (C) Close-up of the tail of UndP inserted into cavity 3. Residues shown in stick representation and colored by location (tan for cavity 3) and heteroatom have been tested for functional significance (see fig. S9). (D) Superposition of the apo and UndP-bound structures, where PL4 is colored pink for the apo structure and red for the UndP-bound state. The rearrangement of coil (apo) to helix (bound) shown here is the only substantial change between the two structures. (E) Functional significance of residues around the head group of UndP, tested by using a polymyxin B (PMXB) growth assay (13). Data presented are means + SD. N is shown for each data column.

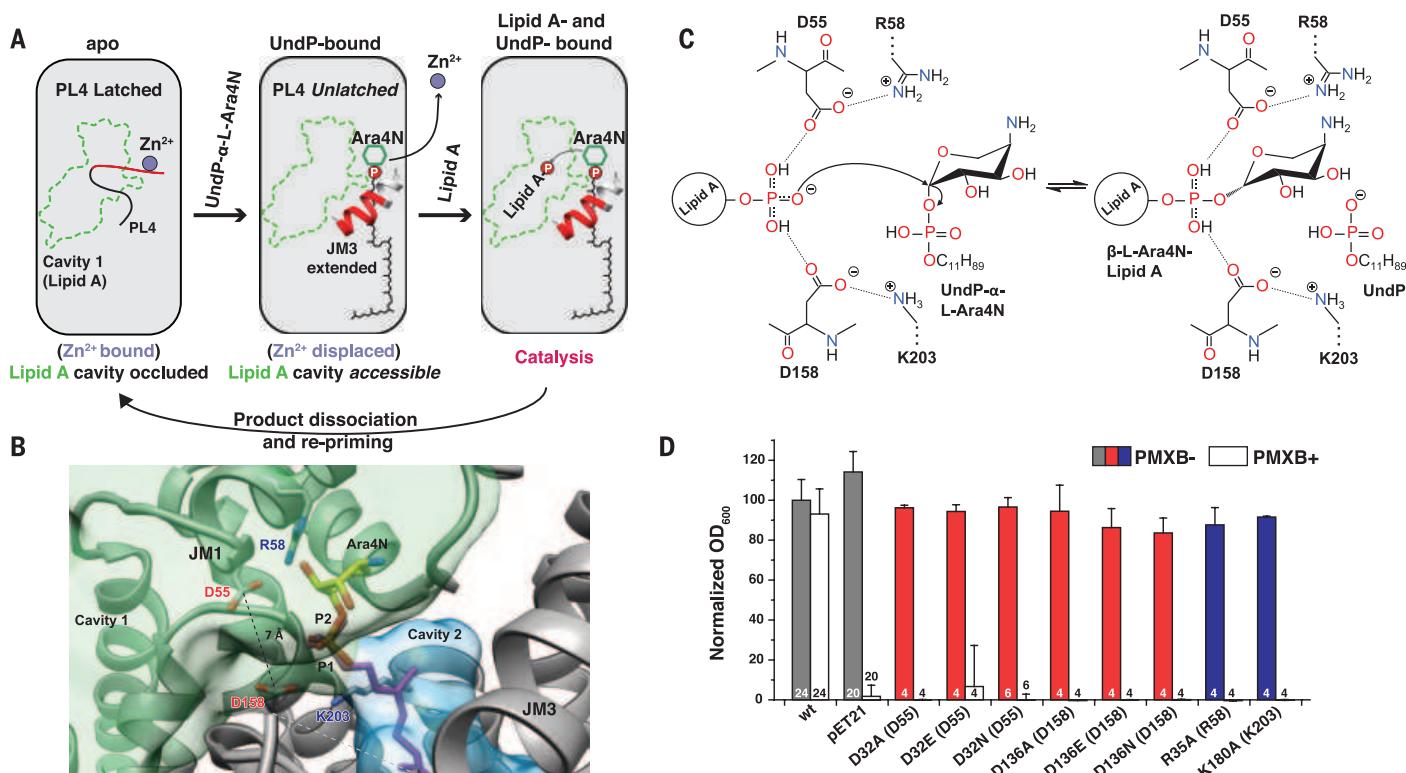


Fig. 4. Putative catalytic mechanism of ArnT. (A) Schematic representation of substrate-binding-induced conformational changes and catalytic cycle of ArnT_{Cm}. The boundaries of cavity 1 are shown in green, and the loop (PL4) that rearranges upon UndP binding is in red. (B) Structural perspective of the active site of ArnT_{Cm}. A putative position for the aminoarabinose sugar determined by docking is shown. The conserved D55 and D158 are located at the interface between the binding site for UndP-L-Ara4N and cavity 1, and have a C_γ-C_γ distance of 7.1 Å. P1 (magenta) is the phosphate of experimentally determined UndP, whereas P2 (heteroatom) is the phosphate from the modeled L-Ara4N-phosphate. (C) Putative catalytic mechanism in which two of the oxy-

gen atoms of the acceptor phosphate are coordinated by D55 and D158, which leaves the third with a net negative charge, primed for a direct nucleophilic attack on the arabinose ring. This mechanism is consistent with inversion of the glycosidic bond, as reported for L-Ara4N attachment to lipid A (23). A precedent for a phosphate acting as a nucleophile exists (24). R58 and K203 appear to act similarly as the catalytic Mg²⁺, in the case of PglB, that localizes the charge of an aspartate and a glutamate, which in turn coordinate the nucleophile acceptor amide (19, 25). (D) Function of putative catalytic aspartates D32 and D136 and positively charged residues R35 and K180 in ArnT_{Se} tested utilizing the PMXB growth assay (13). Data presented are means + SD. N is shown for each data column.

with conserved positively charged residues (R58 and K203, respectively), play a critical role in orienting the lipid A phosphate for a nucleophilic attack on the L-Ara4N donor (Fig. 4C). Indeed, mutations of D55 and D158 in ArnT_{Cm}, and of any of the equivalent residues involved in these two ion pairs in ArnT_{Se}, led to loss of activity (Fig. 4D and fig. S14). This work provides a structural framework for understanding the function of the ArnT family of enzymes, which may inform the design of compounds targeted at reversing resistance to polymyxin-class antibiotics.

REFERENCES AND NOTES

- A. P. Zavascki, L. Z. Goldani, J. Li, R. L. Nation, *J. Antimicrob. Chemother.* **60**, 1206–1215 (2007).
- D. Landman, C. Georgescu, D. A. Martin, J. Quale, *Clin. Microbiol. Rev.* **21**, 449–465 (2008).
- J. Mares, S. Kumaran, M. Gobbo, O. Zerbe, *J. Biol. Chem.* **284**, 11498–11506 (2009).
- C. R. H. Raetz, C. M. Reynolds, M. S. Trent, R. E. Bishop, *Annu. Rev. Biochem.* **76**, 295–329 (2007).
- K. A. Brogden, *Nat. Rev. Microbiol.* **3**, 238–250 (2005).
- B. D. Needham, M. S. Trent, *Nat. Rev. Microbiol.* **11**, 467–481 (2013).
- M. S. Trent, A. A. Ribeiro, S. Lin, R. J. Cotter, C. R. H. Raetz, *J. Biol. Chem.* **276**, 43122–43131 (2001).
- M. S. Trent *et al.*, *J. Biol. Chem.* **276**, 43132–43144 (2001).
- C. M. Herrera, J. V. Hankins, M. S. Trent, *Mol. Microbiol.* **76**, 1444–1460 (2010).
- H. Lee, F.-F. Hsu, J. Turk, E. A. Groisman, *J. Bacteriol.* **186**, 4124–4133 (2004).
- F. Mancia, J. Love, *J. Struct. Biol.* **172**, 85–93 (2010).
- M. Caffrey, *Annu. Rev. Biophys.* **38**, 29–51 (2009).
- N. A. Impellitteri, J. A. Merten, L. E. Bretscher, C. S. Klug, *Biochemistry* **49**, 29–35 (2010).
- L. E. Bretscher, M. T. Morrell, A. L. Funk, C. S. Klug, *Protein Expr. Purif.* **46**, 33–39 (2006).
- T. W. Cullen *et al.*, *PLOS Pathog.* **7**, e1002454 (2011).
- X. Wang, S. C. McGrath, R. J. Cotter, C. R. H. Raetz, *J. Biol. Chem.* **281**, 9321–9330 (2006).
- F. Tavares-Carreón, K. B. Patel, M. A. Valvano, *Sci. Rep.* **5**, 10773 (2015).
- L. L. Lairson, B. Henrissat, G. J. Davies, S. G. Withers, *Annu. Rev. Biochem.* **77**, 521–555 (2008).
- C. Lizak, S. Gerber, S. Numao, M. Aebi, K. P. Locher, *Nature* **474**, 350–355 (2011).
- S. Matsumoto *et al.*, *Proc. Natl. Acad. Sci. U.S.A.* **110**, 17868–17873 (2013).
- M. A. Lomize, I. D. Pogozheva, H. Joo, H. I. Mosberg, A. L. Lomize, *Nucleic Acids Res.* **40** (Database issue), D370–D376 (2012).
- N. R. Voss, M. Gerstein, *Nucleic Acids Res.* **38** (Web Server), W555–W562 (2010).
- Z. Zhou, A. A. Ribeiro, C. R. H. Raetz, *J. Biol. Chem.* **275**, 13542–13551 (2000).
- J. B. Thoden, H. M. Holden, *Protein Sci.* **16**, 1379–1388 (2007).
- C. Lizak *et al.*, *Nat. Commun.* **4**, 2627 (2013).

ACKNOWLEDGMENTS

Crystallographic data for this study were collected at the Northeastern Collaborative Access Team beamlines 24ID-C and E, supported by National Institute of General Medical Sciences (NIGMS), NIH, grant P41 GM103403, at the Advanced Photon Source. The Pilatus 6M detector on 24-ID-C beam line is funded by an Office of Research Infrastructure High-End Instrumentation, NIH, grant S10 RR029205. This work was supported by an NIGMS initiative to the New York Consortium on Membrane Protein Structure (NYCOMP; U54 GM095315) and by NIGMS grant R01 GM11980 (F.M.). Also acknowledged are NIH grants AIO64184 and AIO76322 (M.S.T.), and grant W911NF-12-1-0390 from the Army Research Office (M.S.T.). O.B.C. was supported by a Charles H. Revson Senior Fellowship. We thank W. Hendrickson for his leadership of NYCOMP and continuous support and advice, A. Palmer and P. Loria for helpful discussions, and L. Hamberger for her assistance managing the Mancia laboratory. PDB accession codes: 5EZM (apo ArnT_{Cm}) and 5F15 (UndP-bound ArnT_{Cm}).

SUPPLEMENTARY MATERIALS

www.sciencemag.org/content/351/6273/608/suppl/DC1
Materials and Methods
Figs. S1 to S14
References (26–46)

29 July 2015; accepted 7 January 2016
10.1126/science.aad1172

STEM CELLS

Foxc1 reinforces quiescence in self-renewing hair follicle stem cells

Li Wang,¹ Julie A. Siegenthaler,² Robin D. Dowell,^{1,3} Rui Yi^{1*}

Stem cell quiescence preserves the cell reservoir by minimizing cell division over extended periods of time. Self-renewal of quiescent stem cells (SCs) requires the reentry into the cell cycle. In this study, we show that murine hair follicle SCs induce the *Foxc1* transcription factor when activated. Deleting *Foxc1* in activated, but not quiescent, SCs causes failure of the cells to reestablish quiescence and allows premature activation. Deleting *Foxc1* in the SC niche of gene-targeted mice leads to loss of the old hair without impairing quiescence. In self-renewing SCs, *Foxc1* activates *Nfatc1* and bone morphogenetic protein (BMP) signaling, two key mechanisms that govern quiescence. These findings reveal a dynamic, cell-intrinsic mechanism used by hair follicle SCs to reinforce quiescence upon self-renewal and suggest a unique ability of SCs to maintain cell identity.

Maintaining a pool of adult stem cells (SCs) is critical for tissue homeostasis and wound repair throughout an organism's life. Self-renewal, a defining property of SCs, is achieved by either symmetrical or asymmetrical cell division, through which new generations of SCs are produced to replenish the SC pool (1, 2). Some SCs can also be kept in a quiescent state for a prolonged period of time to minimize cell turnover (3). Although it is well documented that cell extrinsic mechanisms, such

as those mediated by the SC niche, play important roles in governing the transition between quiescence and self-renewal, it is unclear whether there are cell-intrinsic mechanisms that respond to self-renewal and promote dividing SCs to return to quiescence. In this study, we investigated largely synchronized murine hair follicle SC (HFSC) populations during early adulthood to probe this layer of SC regulation.

HFSCs reside in an anatomically distinct compartment of the hair follicle, known as the bulge

(4–6). During the adult hair cycle, HFSCs periodically go through the phases of activation and quiescence to maintain the SC population and to produce new hair follicles (7). The *Foxc1* transcription factor (TF) has been previously identified as one of the few genes with dynamic histone modification patterns in the HFSCs (8), but its expression and function remained unknown. We first monitored *Foxc1* expression during the adult hair cycle using a mouse into which *LacZ* was introduced at the *Foxc1* locus (*Foxc1-LacZ* knock-in mouse) (9) and immunofluorescence staining. We did not observe expression of *Foxc1* in the interfollicular epidermis in any of the stages examined (fig. S1). At the first telogen, about postnatal day 18 (~P18), *Foxc1* was absent from the bulge SC compartment but expressed in the infundibulum and sebaceous gland progenitors (Fig. 1A). By anagen III of the HF cycle, *Foxc1* was induced in both the basal and suprabasal bulge layers and the inner root sheath (IRS) (Fig. 1B). In mature HF of anagen IV, *Foxc1* was strongly expressed in the bulge layers and the IRS (Fig. 1, C to G). When HF progressed through the catagen and reached the second telogen (~P47), *Foxc1* was again absent in the bulge (Fig. 1, H to J). The

¹Department of Molecular, Cellular, and Developmental Biology, University of Colorado, Boulder, CO 80309, USA.

²Department of Pediatrics, Denver-Anschutz Medical Campus, University of Colorado, Aurora, CO 80045, USA.

³BioFrontiers Institute, University of Colorado, Boulder, CO 80309, USA.

*Corresponding author. E-mail: yir@colorado.edu

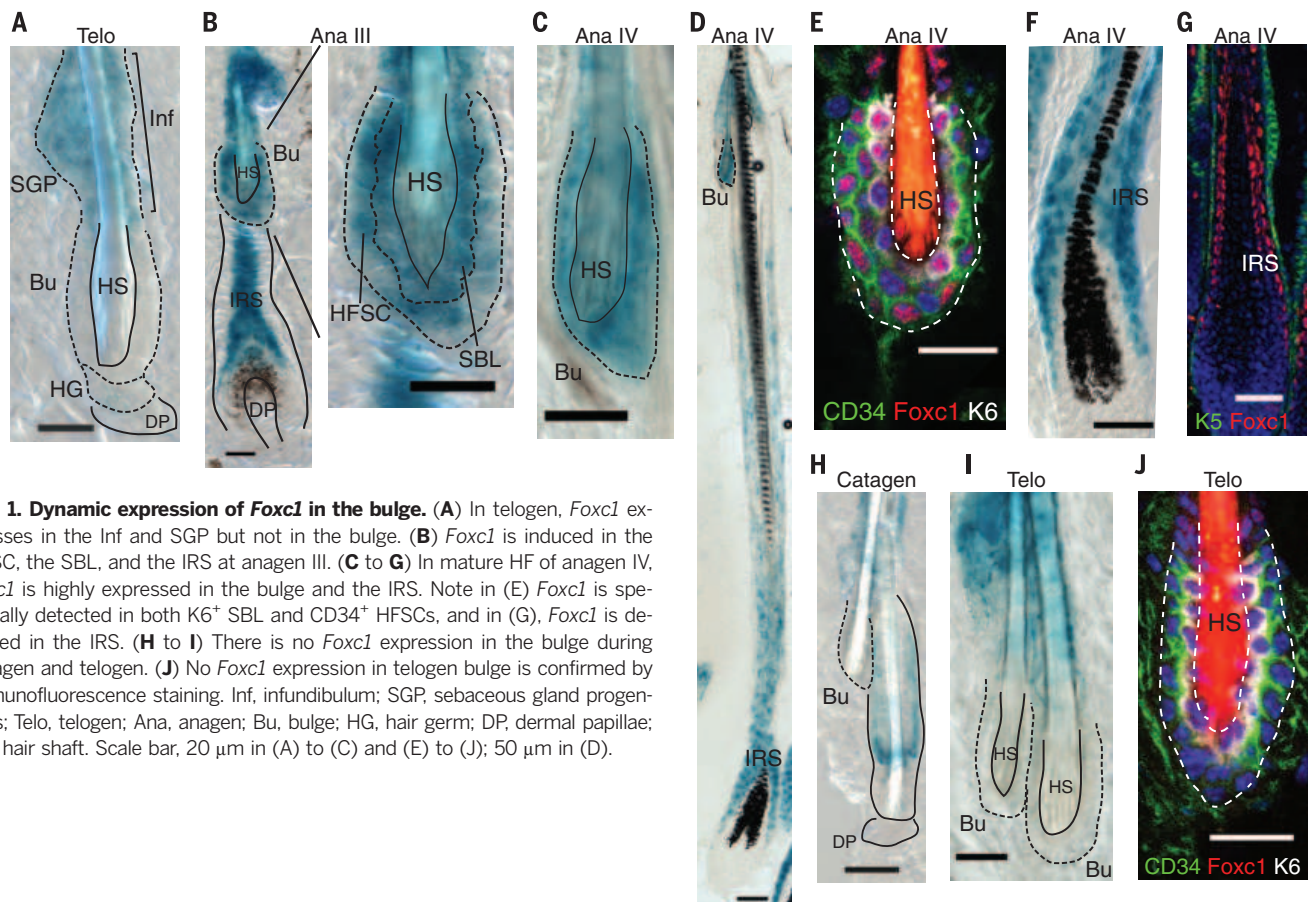


Fig. 1. Dynamic expression of *Foxc1* in the bulge. (A) In telogen, *Foxc1* expresses in the Inf and SGP but not in the bulge. (B) *Foxc1* is induced in the HFSC, the SBL, and the IRS at anagen III. (C to G) In mature HF of anagen IV, *Foxc1* is highly expressed in the bulge and the IRS. Note in (E) *Foxc1* is specifically detected in both K6⁺ SBL and CD34⁺ HFSCs, and in (G), *Foxc1* is detected in the IRS. (H to I) There is no *Foxc1* expression in the bulge during catagen and telogen. (J) No *Foxc1* expression in telogen bulge is confirmed by immunofluorescence staining. Inf, infundibulum; SGP, sebaceous gland progenitors; Telo, telogen; Ana, anagen; Bu, bulge; HG, hair germ; DP, dermal papillae; HS, hair shaft. Scale bar, 20 μm in (A) to (C) and (E) to (J); 50 μm in (D).

induction of *Foxc1* in both those cells positive for keratin 6 ($K6^+$) in the suprabasal bulge layer (SBL), a putative niche for HFSCs (10), and the $CD34^+$ HFSCs at the basal bulge layer in anagen but not in telogen was confirmed by immunofluorescence staining (Fig. 1, E and J). Furthermore, by examining old mice in which the hair cycle became asynchronized and all different hair cycle stages were observed in a single animal, we validated that the expression of *Foxc1* inherently correlates with the hair cycle (fig. S1).

We then investigated *Foxc1* function by conditionally deleting *Foxc1* [conditional knock out (cKO)] in the skin of mice. *K14-Cre* deletes *Foxc1* in all skin lineages. *Foxn1-Cre* deletes *Foxc1* in the SBL but not in the HFSCs. *K15-CrePR* deletes *Foxc1* in the HFSCs but not in the SBL upon induction (Fig. 2A and fig. S2). All wild-type (WT) and cKO animals were born at the expected Mendelian ratios (fig. S3A) and developed normal skin neonatally, consistent with the lack of *Foxc1* expression in embryonic skin progenitors (fig. S3, B and C).

Compared with the WT HFSCs, which usually entered anagen at $\sim P70$ to $P75$, the *K14-Cre*

cKO HFSCs had a much shortened telogen: The HFSCs entered anagen prematurely by the middle of the second telogen at $\sim P64$ (as revealed by the darkened skin) and grew hair coat by $P70$ (Fig. 2B). We then examined HFSC activation in WT and cKO animals during the second adult telogen. At $P47$, we observed no signs of HF growth or HFSC division. However, loss of the old hair follicle (also known as club hair) was evident (Fig. 2C). By $P60$, HF growth was initiated in cKO mice, as indicated by widespread bromodeoxyuridine (BrdU) incorporation into both the HFSCs and hair germs (HG, the progenitors that fuel hair growth) (Fig. 2, D and F). By $P64$, whereas cKO animals produced mature HF, WT animals were still in quiescent telogen (fig. S4A). In the *Foxn1-Cre* cKO mice, in which *Foxc1* was deleted in the SBL but not in the HFSCs, no premature HF growth was observed, although the loss of club hair was evident (Fig. 2E, left). In contrast, in the *K15-CrePR* model in which *Foxc1* was deleted before anagen, premature HF growth was observed without the loss of club hair at $P60$ (Fig. 2E, middle, and 2F). In the *K15-CrePR* model, in which *Foxc1* was de-

leted after anagen, neither premature HF growth nor the loss of club hair was observed at $P60$ (Fig. 2E, right, and 2F). By dyeing hair at $P21$ and observing subsequent loss of the dyed hair, we found that the club hair was lost late in the second anagen ($\sim P33$ to $P35$) in the *K14-Cre* and *Foxn1-Cre* cKO mice (fig. S4, B and C). Morphological examination showed that the loss of club hair was correlated with upward movement of the club hair, likely caused by reduced cell adhesion but not by abnormal apoptosis or proliferation of the SBL (fig. S4, D to F).

The widespread loss of club hair was further confirmed by flow cytometry analysis, by which HFSCs were detected as $H2BGFP^{hi}/CD34^{hi}/\alpha6^{hi}$ and $H2BGFP^{hi}/CD34^{hi}/\alpha6^{lo}$ populations in WT skin (5). The $H2BGFP^{hi}/CD34^{hi}/\alpha6^{lo}$ population marks a cell population sandwiched between the club hair and the new hair follicle, characteristic of the two-bulge formation in WT skin (5) (fig. S5A). Consistent with the morphological results, we observed a progressive loss of the $H2BGFP^{hi}/CD34^{hi}/\alpha6^{lo}$ population in the *K14-Cre* and *Foxn1-Cre* cKO between $P30$ and $P47$ (fig. S5, B and C). $CD34$ expression levels in the KO HFSCs were also

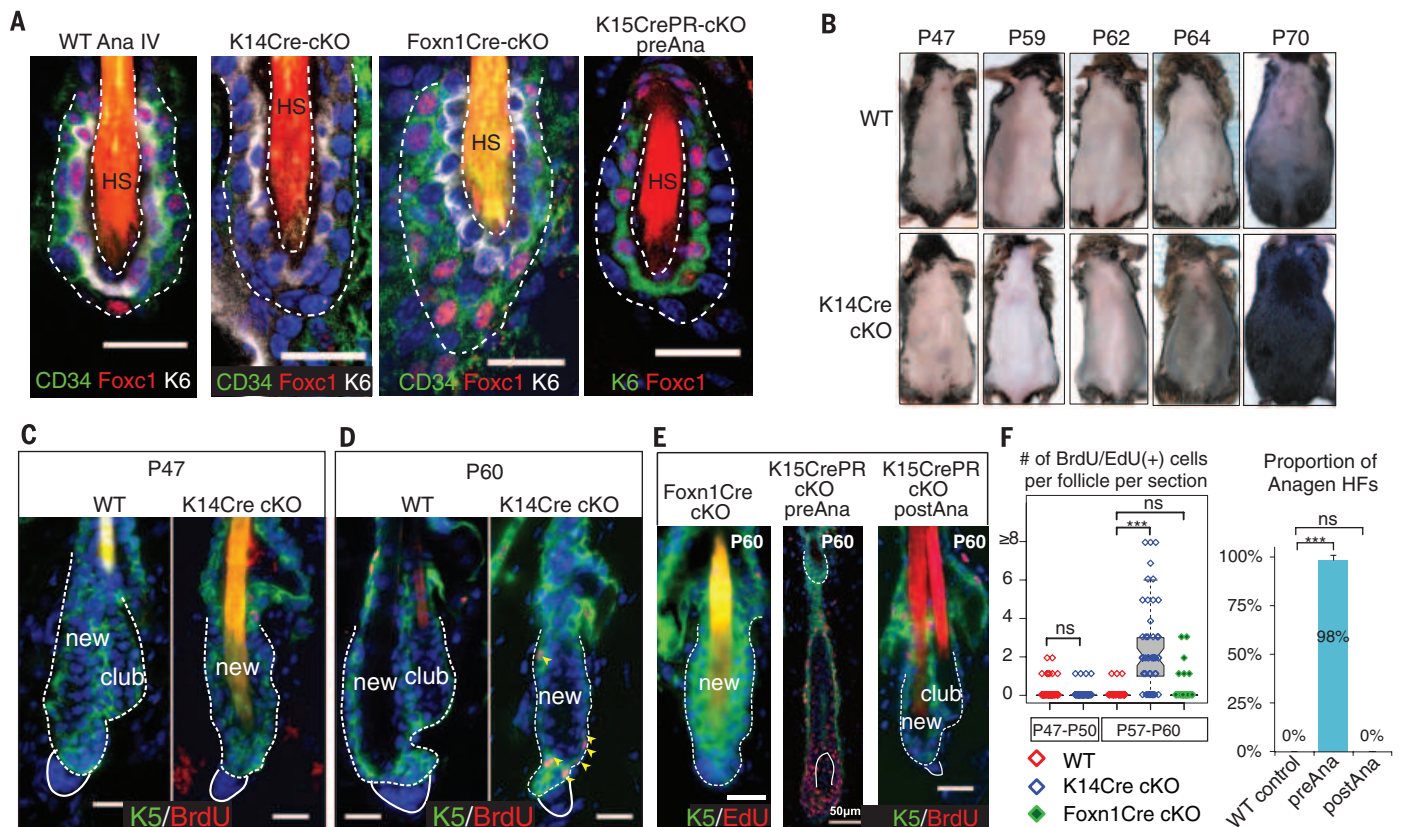


Fig. 2. *Foxc1* is differentially required by the HFSCs and the suprabasal bulge layer. (A) Differential deletion of *Foxc1* by different Cre lines at anagen ($P26$ to $P30$). (B) Premature HF growth of *Foxc1* cKO animals, compared with WT animals, during the second telogen. (C and D) Premature HFSC activation in *Foxc1* cKO mice is shown by BrdU incorporation and HF growth and the loss of club hair in the *K14-Cre* cKO mice. (E) Different defects in club hair loss and compromised quiescence are observed in *Foxn1-Cre* and *K15-CrePR* models. (F) Quantification of BrdU or 5-ethynyl-

2'-deoxyuridine-positive (Edu^+) cells in the HFSCs and HG cells before ($P47$ to $P50$, $n = 3$ for each genotype) and after ($P57$ to $P60$, $n = 3$ for *K14-Cre*, $n = 4$ for *Foxn1-Cre*) the premature HFSC activation and quantification of premature HF growth in the *K15-CrePR* model with preanagen deletion, compared with the WT and the *K15-CrePR* model with postanagen deletion. $***P < 0.001$; ns, not significant. Scale bar, $20 \mu m$ in (A) and (C) to (E) unless otherwise labeled. Dashed lines outline the bulge and solid lines outline the DP.

reduced (fig. S5D). These data indicate that *Foxc1* is required to restrict HFSCs from premature activation and to maintain the club hair. The *Foxn1-Cre* cKO results suggest that *Foxc1* is required by the SBL to maintain the club hair. The *K15-CrePR* cKO results reveal an intrinsic requirement of *Foxc1* by HFSCs and suggest that temporal induction of *Foxc1* in the activated HFSCs during anagen is required to reinforce quiescence.

To determine the effect of loss of *Foxc1* on HFSC quiescence, we performed RNA sequencing (RNA-Seq) at P47 when both WT and *K14-Cre* cKO HFSCs were in telogen. Genes associated with quiescence of HFSCs, including *Bmp6* (11) and *Fgf18* (12, 13), and HFSC markers (4, 5, 14), including *CD34*, were among the substantially down-regulated genes, whereas genes associated with HFSC activation were up-regulated in the cKO mice (Fig. 3A). Signature genes characteristic of quiescent SCs (3) were dysregulated (Fig. 3A). Global analysis revealed that genes involved in cell division were markedly up-regulated (fig. S6A). We then confirmed by quantitative polymerase chain reaction (qPCR) the down-regulation of *Bmp6*, *CD34*, and *Fgf18* and the up-regulation of cell cycle genes in the HFSCs purified from each model. Consistent with the cell-intrinsic requirement of *Foxc1* in the HFSCs during anagen, changes of gene expression were only observed in the *K14-Cre* and *K15-CrePR* models, in which *Foxc1* was constitutively deleted or specifically deleted in the HFSCs before anagen, respectively. Also, changes of gene expression were not seen in the *Foxn1-Cre* and *K15-CrePR*

models, in which *Foxc1* was deleted in the SBL but not in the HFSCs, or specifically deleted in the HFSC after anagen, respectively (Fig. 3B and fig. S7).

Next, we performed gene set enrichment analysis (GSEA) using published HFSC and progenitor data sets (15). Quiescent *Foxc1* KO HFSCs (P47) were more similar to HG progenitors that are poised for activation than to quiescent HFSCs (Fig. 3C and fig. S8). We also observed a strong similarity between *Foxc1* and *Lhx2* cKO HFSCs in their molecular signature (fig. S8). We then performed principal component analysis using data sets from the quiescent or activated HFSCs (8, 12, 16), the HGs (12), the transit-amplifying cells (TACs) (8), and our RNA-Seq data. We found that activated HFSCs (P28) and dividing HFSCs destined for differentiation (P20) (16) were intermediate populations between quiescent HFSCs and HG progenitors. The P47 *Foxc1* KO HFSCs were grouped most closely with activated HFSCs and clearly distinct from quiescent HFSCs (Fig. 3D). These data provide a global view for the sensitized cellular state of the *Foxc1* KO HFSCs before the premature SC activation.

To determine the mechanism of *Foxc1*'s action, we analyzed differentially expressed (DE) genes in *Foxc1* WT and KO HFSCs between P29 and P31, when the HFSCs are activated and when *Foxc1* is highly expressed. Genes associated with HFSC quiescence, HFSC markers, and adhesion were notably down-regulated, and cell cycle regulators were strongly up-regulated in the cKO mice, consistent with the observed phenotypes

(Fig. 4A and fig. S6B). These data suggest that the transient expression of *Foxc1* maintains SC adhesion and promotes the transition back to quiescence when the HFSCs undergo self-renewal.

Next, we mapped open chromatin regions and TF occupancy in the WT and KO HFSCs using an assay for transposase-accessible chromatin using sequencing (ATAC-Seq) (17). We analyzed published chromatin immunoprecipitation sequencing (ChIP-Seq) data for Sox9 (18), Tcf3/4 (19), and Lhx2 (20) in HFSCs and observed strong overlaps between ChIP-Seq and ATAC-Seq peaks, which validated the detection of TF occupancy by ATAC-seq (fig. S9, A to C). To determine *Foxc1* recognition motifs, we analyzed a *Foxc1* ChIP-Seq data set (21). De novo motif discovery retrieved *Foxc1*-binding sites that were best matched by previously determined *Foxa2* and *Foxa1* recognition motifs (fig. S9D). Notably, *Foxa2* and *Foxc1* were validated to bind to the same enhancer sequences (22), consistent with our findings. Both *Foxa1* and *Foxa2* loci are epigenetically silenced in HFSCs (fig. S10), which suggests that *Foxc1* is responsible for these binding sites. We then intersected our ATAC-seq peaks harboring the *Foxc1* recognition motifs with DE genes ($P < 0.01$) in the *Foxc1* KO HFSCs. We identified 104 genes likely to be targeted by *Foxc1* (table S1). Among these putative targets, 85 (81.7%) were down-regulated in the *Foxc1* KO HFSCs (fig. S9E). Several genes involved in regulating HFSC quiescence were found to contain *Foxc1*-binding sites in their promoter or enhancer regions, including *Bmp2* (23), *Foxp1* (24), *Nfatc1* (25, 26), and *Prhr* (26, 27).

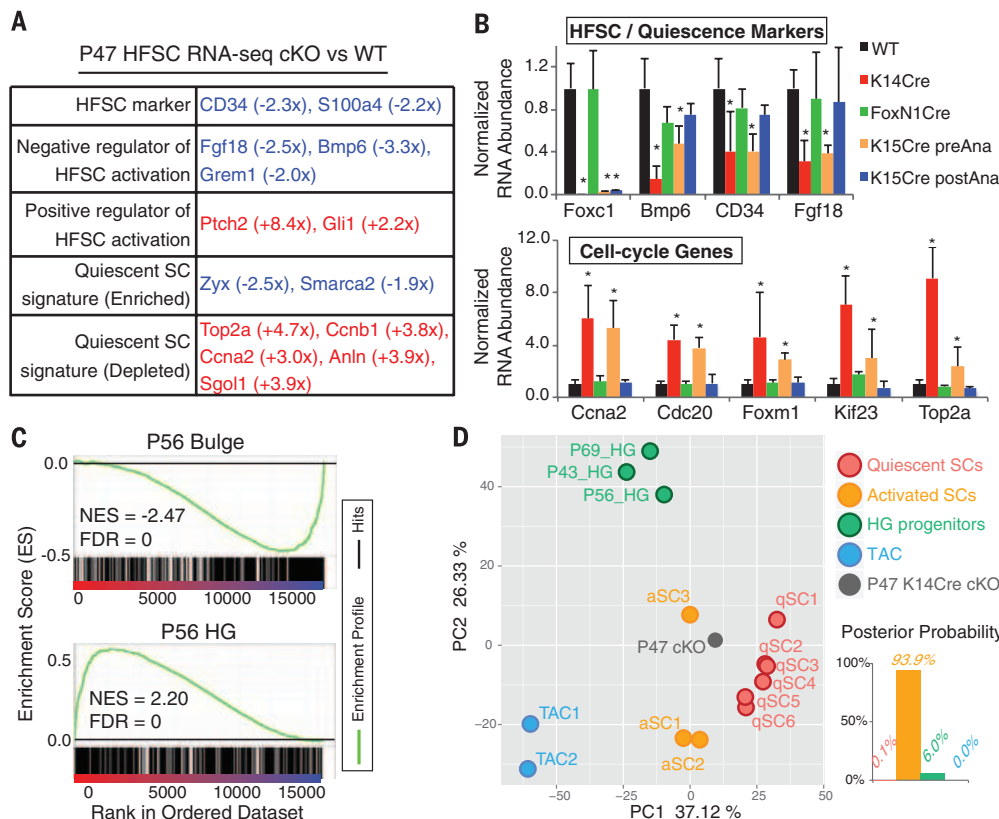


Fig. 3. *Foxc1* KO HFSCs fail to return to quiescence. (A) Functional classification of selected DE gene in P47 KO HFSCs. Red and blue mark up- and down-regulated genes in the KO HFSCs, respectively. (B) qPCR validation of down- and up-regulated genes in the HFSCs isolated from different cKO models at the second telogen (P47 to P60, $n \geq 3$ for each genotype, $*P < 0.05$). (C) GSEA comparison of P47 KO transcriptome to telogen bulge and HG signature genes. NES, normalized enrichment score; FDR, false discovery rate. (D) Principal component analysis of P47 *Foxc1* KO transcriptome and profiling data from WT HFSCs, HGs, and TACs. Linear discriminant analysis groups *Foxc1* KO transcriptome to activated HFSCs.

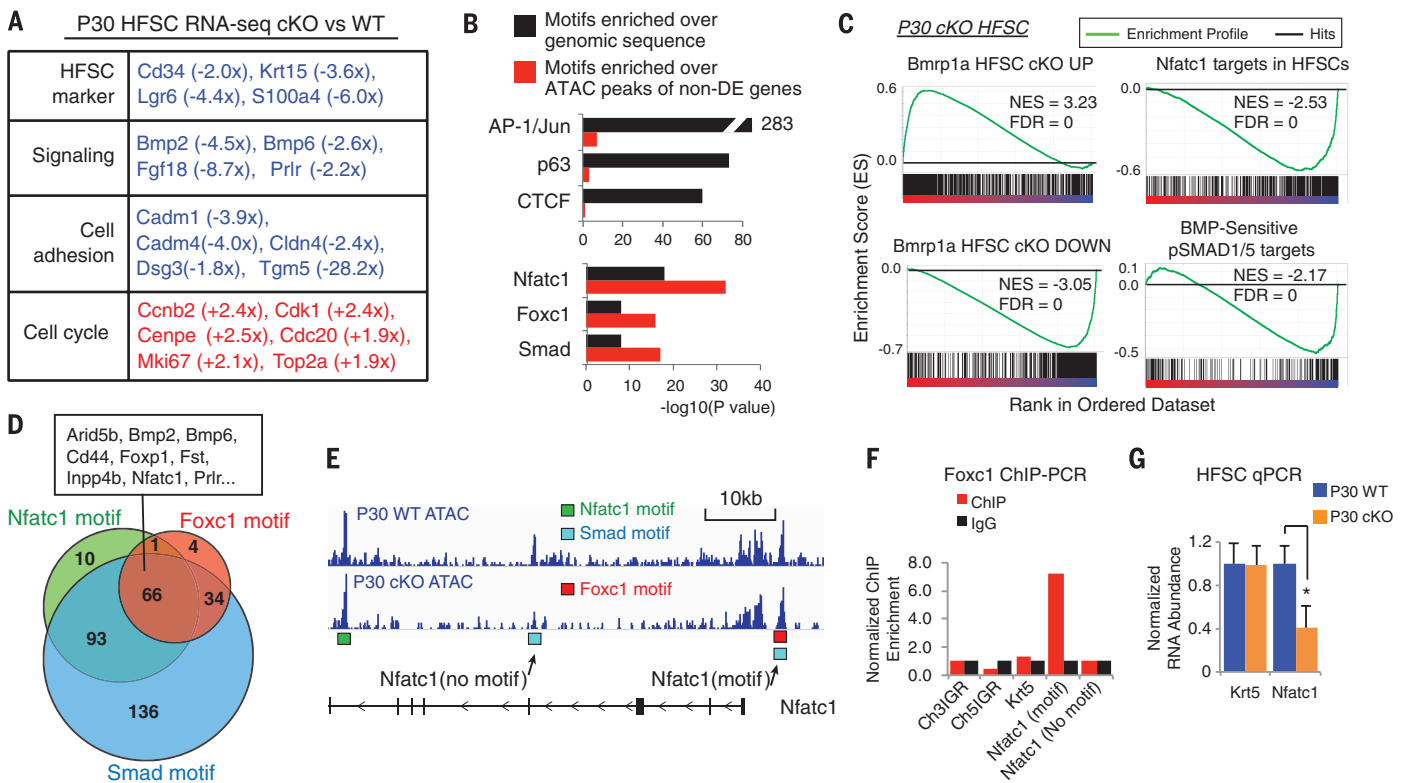


Fig. 4. Foxc1 activates quiescence gene networks. (A) Functional classification of selected DE gene in P30 KO HFSCs. (B) Comparison of enriched TF motifs against genomic sequences and against the peaks covering the non-DE genes in P30 KO HFSCs. (C) GSEA of bone morphogenic proteins (BMP)-responsive genes and Nfatc1 targets in P30 KO HFSCs. (D) Venn diagram of the DE genes in P30 KO HFSCs that contain motifs of Foxc1, Smad, and Nfatc1 shows a coregulated gene network. (E) ATAC-seq track of the *Nfatc1* locus. Location of Nfatc1, Smad, and Foxc1 motifs are shown in the peak region. (F) ChIP-PCR analysis of Foxc1 confirms association of Foxc1 to the predicted binding site in the *Nfatc1* locus. (G) DE of Foxc1 targets, *Krt5* and *Nfatc1*, in the WT and KO HFSCs (**P* < 0.05).

We further dissected pathways that are downstream from *Foxc1*. Because ATAC-seq provided a comprehensive survey for all TF-binding sites in the genome, we analyzed the top TF hits in our ATAC-seq. Overall in the HFSCs, motifs representing AP-1/c-Jun, p63, and CTCF were the most enriched sequences that were detected by ATAC-seq, consistent with high expression levels and the widespread roles of these TFs in the skin (Fig. 4B). However, when we specifically searched the subset of ATAC-seq peaks that cover the DE genes identified in the *Foxc1* KO HFSCs against ATAC peaks of non-DE genes, motifs representing Foxc1, Nfatc1, and Smad, which reflect the BMP signaling pathway, were significantly enriched (Fig. 4B). Furthermore, GSEA comparison showed that direct targets of Nfatc1 (28) and pSMAD1/5 (29) were considerably enriched and largely down-regulated in the *Foxc1* KO HFSCs, which positively linked the *Foxc1* KO HFSCs to the compromised BMP signaling pathway and loss of *Nfatc1* in the HFSCs (29, 30) (Fig. 4C). Sixty-six of these genes—including *Bmp2*, *Bmp6*, *Foxp1*, *Inpp4b*, *Nfatc1*, and *Prlr*—were likely coregulated by Foxc1, Nfatc1, and Smad (Fig. 4D and tables S2 and S3). Such a combinatorial action of these TFs is illustrated by the *Nfatc1* locus (Fig. 4E). The direct regulation of *Nfatc1*, *Bmp6*, and *Hspb8* by Foxc1 was confirmed by ChIP-PCR and qPCR (Fig. 4, F and G, and Fig. S11). Because

Hspb8 was confirmed as a Smad target (29), it is an example coregulated by Foxc1 and Smad. Overall, 343 out of 421 DE genes are likely controlled by *Foxc1* directly (104) or by *Nfatc1* (170) and *Smad* (328) indirectly, which indicates a collaborative gene regulatory network between *Foxc1* and *Nfatc1*, as well as BMP signaling, two critical regulatory networks governing the quiescence of HFSCs (11, 12, 23, 25, 30, 31).

In conclusion, we have uncovered a dynamic and cell-intrinsic mechanism mediated by *Foxc1* that is induced to promote quiescent SC identity in response to SC activation. Our findings also suggest that quiescent SCs actively sense the change of their cellular states and use transient gene expression to reinforce their identity. Investigation of such adaptive mechanisms should provide new insights into SC maintenance during tissue homeostasis and injury repair.

REFERENCES AND NOTES

1. K. W. Orford, D. T. Scadden, *Nat. Rev. Genet.* **9**, 115–128 (2008).
2. S. He, D. Nakada, S. J. Morrison, *Annu. Rev. Cell Dev. Biol.* **25**, 377–406 (2009).
3. T. H. Cheung, T. A. Rando, *Nat. Rev. Mol. Cell Biol.* **14**, 329–340 (2013).
4. T. Tumber et al., *Science* **303**, 359–363 (2004).
5. C. Blanpain, W. E. Lowry, A. Geoghegan, L. Polak, E. Fuchs, *Cell* **118**, 635–648 (2004).
6. G. Cotsarelis, T. T. Sun, R. M. Lavker, *Cell* **61**, 1329–1337 (1990).

7. C. Blanpain, E. Fuchs, *Nat. Rev. Mol. Cell Biol.* **10**, 207–217 (2009).
8. W.-H. Lien et al., *Cell Stem Cell* **9**, 219–232 (2011).
9. T. Kume et al., *Cell* **93**, 985–996 (1998).
10. Y. C. Hsu, H. A. Pasolli, E. Fuchs, *Cell* **144**, 92–105 (2011).
11. N. Oshimori, E. Fuchs, *Cell Stem Cell* **10**, 63–75 (2012).
12. V. Greco et al., *Cell Stem Cell* **4**, 155–169 (2009).
13. M. Kimura-Ueki et al., *J. Invest. Dermatol.* **132**, 1338–1345 (2012).
14. R. J. Morris et al., *Nat. Biotechnol.* **22**, 411–417 (2004).
15. A. Subramanian et al., *Proc. Natl. Acad. Sci. U.S.A.* **102**, 15545–15550 (2005).
16. Y. V. Zhang, J. Cheong, N. Ciapurin, D. J. McDermitt, T. Tumber, *Cell Stem Cell* **5**, 267–278 (2009).
17. J. D. Buenostro, P. G. Giresi, L. C. Zaba, H. Y. Chang, W. J. Greenleaf, *Nat. Methods* **10**, 1213–1218 (2013).
18. M. Kadaja et al., *Genes Dev.* **28**, 328–341 (2014).
19. W.-H. Lien et al., *Nat. Cell Biol.* **16**, 179–190 (2014).
20. A. R. Folgueras et al., *Cell Stem Cell* **13**, 314–327 (2013).
21. S. Amin et al., *Dev. Cell* **32**, 265–277 (2015).
22. H. Yamagishi et al., *Genes Dev.* **17**, 269–281 (2003).
23. M. V. Plikus et al., *Nature* **451**, 340–344 (2008).
24. E. Leishman et al., *Development* **140**, 3809–3818 (2013).
25. V. Horsley, A. O. Aliprantis, L. Polak, L. H. Glimcher, E. Fuchs, *Cell* **132**, 299–310 (2008).
26. J. Goldstein et al., *Genes Dev.* **28**, 983–994 (2014).
27. A. J. Craven et al., *Endocrinology* **142**, 2533–2539 (2001).
28. B. E. Keyes et al., *Proc. Natl. Acad. Sci. U.S.A.* **110**, E4950–E4959 (2013).
29. M. Genander et al., *Cell Stem Cell* **15**, 619–633 (2014).

30. K. Kobiela, N. Stokes, J. de la Cruz, L. Polak, E. Fuchs, *Proc. Natl. Acad. Sci. U.S.A.* **104**, 10063–10068 (2007).
31. V. A. Botchkarev *et al.*, *Nat. Cell Biol.* **1**, 158–164 (1999).

ACKNOWLEDGMENTS

We thank members of the Yi laboratory for discussions, P. Muhlrad and T. Cech for critical reading of the manuscript, Y. Han for FACS, K. Diener and B. Gao for Illumina sequencing, J. Tyler for

imaging, E. Fuchs (Rockefeller University) for *K14-Cre* and *K14-H2BEGFP* mice, H. Chang (Stanford University) for help on ATAC-seq, N. Manley (University of Georgia) for *Foxn1-Cre* mice, and D. Roop and G. Bilousova (University of Colorado, Denver) for Krt6 antibody. This project was partly supported by NIH grant AR066703 and a start-up fund from the University of Colorado Boulder to R.Y. L.W. was supported by an NIH training grant T32GM008759. R.Y. and R.D.D. were coadvisors for L.W. All sequencing data are deposited to GEO with the accession numbers GSE67404 and GSE68288. The authors declare no conflicts of interest.

SUPPLEMENTARY MATERIALS

www.sciencemag.org/content/351/6273/613/suppl/DC1
Materials and Methods
Figs. S1 to S12
Tables S1 to S4
References (32–42)

1 October 2015; accepted 4 January 2016
10.1126/science.aad5440

HEART DISEASE

A small-molecule inhibitor of sarcomere contractility suppresses hypertrophic cardiomyopathy in mice

Eric M. Green,^{1*} Hiroko Wakimoto,^{2*} Robert L. Anderson,¹ Marc J. Evanchik,¹ Joshua M. Gorham,² Brooke C. Harrison,³ Marcus Henze,¹ Raja Kawas,¹ Johan D. Oslob,¹ Hector M. Rodriguez,¹ Yonghong Song,¹ William Wan,³ Leslie A. Leinwand,³ James A. Spudich,⁴ Robert S. McDowell,^{1,††} J. G. Seidman,^{2,†} Christine E. Seidman^{2,5,6,††}

Hypertrophic cardiomyopathy (HCM) is an inherited disease of heart muscle that can be caused by mutations in sarcomere proteins. Clinical diagnosis depends on an abnormal thickening of the heart, but the earliest signs of disease are hyperdynamic contraction and impaired relaxation. Whereas some *in vitro* studies of power generation by mutant and wild-type sarcomere proteins are consistent with mutant sarcomeres exhibiting enhanced contractile power, others are not. We identified a small molecule, MYK-461, that reduces contractility by decreasing the adenosine triphosphatase activity of the cardiac myosin heavy chain. Here we demonstrate that early, chronic administration of MYK-461 suppresses the development of ventricular hypertrophy, cardiomyocyte disarray, and myocardial fibrosis and attenuates hypertrophic and profibrotic gene expression in mice harboring heterozygous human mutations in the myosin heavy chain. These data indicate that hyperdynamic contraction is essential for HCM pathobiology and that inhibitors of sarcomere contraction may be a valuable therapeutic approach for HCM.

Hypertrophic cardiomyopathy (HCM) is the most common inherited disease of the heart muscle and occurs in ~1 in 500 adults (1). Patients are diagnosed with HCM when they present with left ventricular hypertrophy (LVH) that cannot be explained by another cardiac or systemic disease. Associated histopathologic findings include enlarged, disorganized cardiomyocytes and increased amounts of myocardial fibrosis. HCM also perturbs heart function, with characteristically hyperdynamic contraction (2, 3)

and impaired relaxation (4). Both the histopathologic and hemodynamic abnormalities of HCM contribute to patient symptoms (including exertional angina and shortness of breath) and increase the risk for atrial fibrillation, stroke, heart failure, and premature death (5). Contemporary pharmacologic therapy for HCM consists of off-label use of medications that nonspecifically reduce contractile strength by blocking β -adrenergic receptors or calcium channels (6). Although these medications can provide some symptom relief, none alter the progression of disease (7).

Dominant inherited and *de novo* mutations in genes that encode protein components of the sarcomere, the contractile unit of the heart, are identified in 35% of unselected patients who submit to gene-based testing (8) and 80% of patients with familial HCM (9). The two most frequently mutated HCM genes encode β -cardiac myosin heavy chain (*MYH7*), the predominant myosin isoform expressed in the adult human heart, and myosin-binding protein C (*MYBPC3*), a modulator of cardiac contraction. Pathogenic missense mutations in *MYH7* cluster within the globular

motor domain, the head-rod junction region, and the rod domain, whereas most pathogenic *MYBPC3* variants encode truncated proteins (8, 10). Studies of young carriers of either *MYH7* or *MYBPC3* mutations have shown that hyperdynamic contraction and impaired relaxation precede the appearance of LVH (11–13).

To study the role of sarcomere mutations in the development of HCM, we used previously generated mouse models of HCM, which we created by introducing human disease-causing mutations into the murine α -cardiac myosin heavy chain gene (14–17). This is the predominant myosin isoform expressed in the adult mouse ventricle and is 92% identical to human β -cardiac myosin heavy chain. Mice with heterozygous Arg⁴⁰³→Gln⁴⁰³ (R403Q) (within the actin-binding site), Arg⁴⁵³→Cys⁴⁵³ (R453C) (adjacent to the nucleotide-binding site), and Arg⁷¹⁹→Trp⁷¹⁹ (R719W) (within the converter domain) missense residues (fig. S1) recapitulate most morphologic and functional features of human HCM.

Characterizing the biochemical and biophysical effects of these mutations at the molecular level and connecting these properties to the clinical phenotype of HCM is an active field of study. In many biomechanical assays, mutant myosin molecules expressed *in vitro* or isolated from HCM mouse hearts or human myofibrillar preparations have shown enhanced enzymatic [adenosine triphosphatase (ATPase)] activity, increased tension development, and/or increased unloaded actin-filament sliding velocities (10, 18). These molecular phenotypes could explain the hyperdynamic contraction observed in human HCM patients. Furthermore, as cardiac fibroblasts respond to heightened mechanical, paracrine, and electrophysiological signals from cardiomyocytes with increased profibrotic gene expression (19) and production of extracellular matrix proteins (20), the hyperdynamic biomechanical properties of mutant sarcomeres could contribute to the downstream development of HCM histopathology (16). However, some HCM mutant proteins in reconstituted systems do not demonstrate increased power production and appear to slightly decrease force production (21). Such discrepancies highlight the current limitations of the reconstituted systems: single- rather than double-headed myosins, as well as the absence of key protein components and posttranslational modifications. Thus, the question remains as to whether mutations found in HCM increase power output at the molecular level. To test this hypothesis by an alternate approach, we sought a small molecule that could reduce sarcomere power output.

¹MyoKardia, South San Francisco, CA 94080, USA.

²Department of Genetics, Harvard Medical School, Boston, MA 02115, USA. ³Department of Molecular, Cellular, and Developmental Biology and BioFrontiers Institute, University of Colorado, Boulder, CO 80309, USA. ⁴Department of Biochemistry, Stanford University School of Medicine, Stanford, CA 94305, USA. ⁵Division of Cardiovascular Medicine, Brigham and Women's Hospital, Boston, MA 02115, USA. ⁶Howard Hughes Medical Institute, Chevy Chase, MD 20815, USA.

*These authors contributed equally to this work. †These authors contributed equally to this work. ††Corresponding author. E-mail: cseidman@genetics.harvard.edu (C.E.S.); rmcowell@myokardia.com (R.S.M.)

We reasoned that if excess sarcomere power is the primary defect in HCM, small-molecule inhibitors of sarcomere power might ameliorate the disease at its source and abolish hallmark features of HCM such as hypertrophy, cellular disarray, and myocardial fibrosis.

Sarcomere power output is the product of ensemble force generated by myosin heads and their velocity of movement along actin filaments (22). In principle, either component of power output could be a target for modulation, and we initially

sought agents that reduce power by reducing ensemble force generation. Because increases in the cycle time of myosin ATPase reduce ensemble force generation, we conducted a chemical screen for molecules that reduced the maximal actin-activated ATPase rate of myosin in bovine myofibrils (Fig. 1A). Both α - and β -cardiac myosin normally spend $\sim 1/10$ of their ATPase chemomechanical cycle times strongly bound to actin (Fig. 1A, lower two structures). Lengthening the total cycle time reduces this proportion, resulting in fewer myosin

molecules in a force-producing state and an overall reduction in force generation (22). Compounds identified via this screen underwent optimization of potency and pharmaceutical properties to yield MYK-461 (Fig. 1B).

Treatment of mouse cardiac myofibrils with MYK-461 reduced ATPase activity in a dose-dependent manner [median inhibitory concentration (IC_{50}) of 0.3 μM] (Fig. 1C). Maximal doses of MYK-461 ($>10 \mu M$) reduced the maximal ATPase rate by $\sim 90\%$. The potent inhibition of

Fig. 1. MYK-461 inhibits myosin ATPase and contractility of cardiomyocytes.

(A) Chemo-mechanical cycle of myosin, demonstrating the coupling between ATP hydrolysis and the myosin powerstroke. The swinging of the myosin lever arm (gray; bound light chains not shown) in step two is associated with movement of the actin filament (blue). (B) Chemical structure of MYK-461. (C) Decreasing rate of myosin ATPase in mouse cardiac myofibrils treated with increasing concentrations of MYK-461 ($n = 6$ biological replicates, mean \pm SD). (D) Plots of tension versus pCa for skinned cardiac muscle fibers (from rats) exposed to increasing concentrations of MYK-461 ($n = 3$ to 4 fibers per concentration, mean \pm SEM). (E) Decreasing maximal tension of skinned cardiac muscle fibers (from rats) exposed to increasing concentrations of MYK-461 ($n = 3$ to 4 fibers per concentration, mean \pm SEM). (F) Decreasing fractional shortening (FS) of isolated adult rat ventricular cardiomyocytes treated with increasing concentrations of MYK-461 ($n = 3$ to 5 cells per concentration, mean \pm SD).

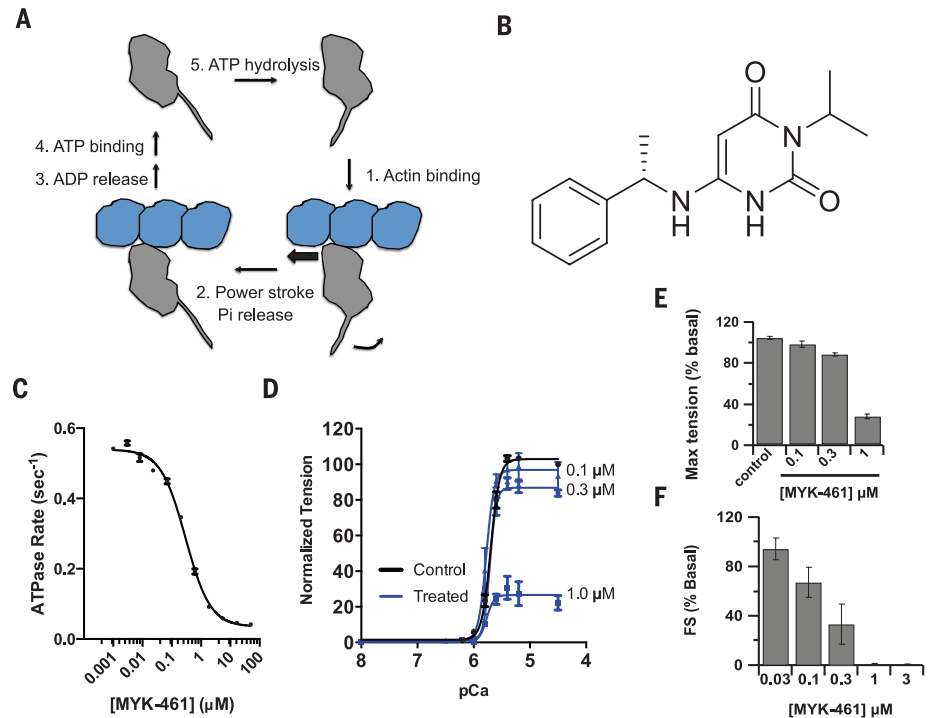
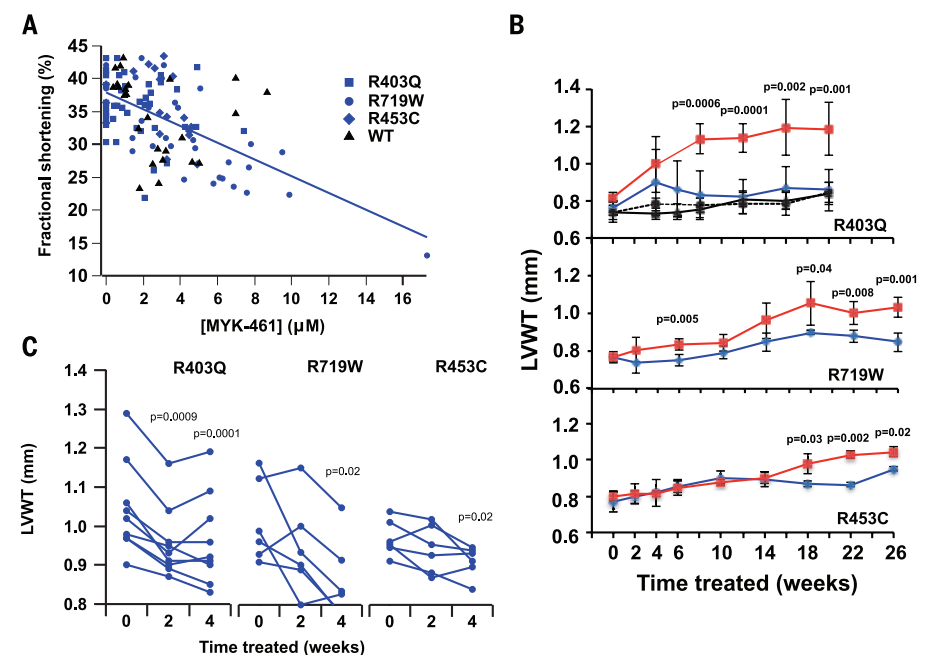


Fig. 2. MYK-461 reduces cardiac contractility in mouse models of HCM and prevents or ameliorates LV hypertrophy.

(A) Reduction in fractional shortening with increasing MYK-461 plasma exposure in hearts from R403Q, R719W, R453C, and WT mice, fit by linear regression ($n = 6$ to 9 mice per background, Pearson's $r = 0.57$, $P < 10^{-5}$). (B) Changes in LVWT over time by echocardiography for WT mice (top panel: dashed black line, untreated; solid black line, treated; $n = 6$ mice each) and the indicated HCM mouse models (blue, treated with MYK-461; red, untreated; $n = 3$ to 6 mice per background). All data are expressed as mean \pm SD, and statistical significance was tested by repeated-measures one-way analysis of variance. (C) Reduction in LVWT for the indicated HCM mouse models treated with MYK-461 after the onset of hypertrophy (15 to 30 weeks of age). Statistical significance was tested by paired t tests compared with baseline values.



ATPase rates in both murine [$>90\%$ α -myosin (23)] and bovine myofibrils [$>90\%$ β -myosin (24)] indicates that MYK-461 is active against both the α and β isoforms of cardiac myosin. Because we observed similar activity (IC_{50} of $0.3 \mu\text{M}$) (fig. S2A) in a basal system consisting of only purified bovine myosin S1, we concluded that MYK-461 acts directly on myosin. We next performed transient kinetic experiments to isolate individual steps of the myosin chemomechanical cycle by which MYK-461 inhibits myosin ATPase. Treatment with MYK-461 reduced the rate of phosphate release (Fig. 1A, step two, and fig. S2B), the rate-limiting step in the chemomechanical cycle, in a dose-dependent manner without slowing adenosine diphosphate (ADP) release (Fig. 1A, step three, and fig. S2C). These data suggest that MYK-461 reduces the myosin duty ratio (i.e., the ratio of strongly bound state time to total cycle time) and thus decreases the ensemble force, power, and contractility produced by the sarcomere.

We also directly studied the effect of MYK-461 on power generation in muscle, by measuring

tension produced by skinned cardiac muscle fibers isolated from adult rats. Exposure to MYK-461 reduced maximal tension in a dose-dependent manner ($\sim 70\%$ reduction at $1.0 \mu\text{M}$) without altering the pCa_{50} (i.e., the pCa at half the maximal activity) or the tension at lower calcium concentrations (Fig. 1, D and E). Similarly, adult rat ventricular cardiomyocytes treated with MYK-461 showed a dose-dependent reduction in fractional shortening (IC_{50} $0.18 \mu\text{M}$) (Fig. 1D) without changing the calcium transient (fig. S3).

To study *in vivo* effects and determine whether MYK-461 decreases fractional shortening, a measure of contractility (fig. S4A), we administered MYK-461 orally (2.5 mg/kg per day via drinking water) to young (ages 6 to 15 weeks) wild-type (WT) and HCM mice expressing α -cardiac myosin heavy chain missense mutations R403Q, R719W, or R453C. Chamber dimensions, fractional shortening, and plasma drug concentrations were measured at baseline and at 2- to 4-week intervals (fig. S4B). WT and mutant mice exhibited decreased fractional shortening that correlated linearly with MYK-461 plasma exposures (correlation coefficient

$r = 0.57$; $P < 10^{-5}$) (Fig. 2A). Although MYK-461 inhibits the ATPase activity of skeletal myosin with a lower affinity (IC_{50} of $4.7 \mu\text{M}$ with rabbit skeletal myosin), treated rodents had no reduction in grip strength or voluntary exercise capacity (fig. S5). Thus, MYK-461 reduced cardiac contractility in a dose-dependent manner in normal and mutant mice without overt impairment of skeletal muscle function.

We next investigated whether MYK-461 administered to young prehypertrophic HCM mice [ages 8 to 15 weeks; left ventricular wall thickness (LVWT) $\leq 0.8 \text{ mm}$] affected the development of LVH, the cardinal manifestation of HCM. Both treated and untreated WT mice maintained stable LVWT throughout the experiment, whereas LVWT increased in placebo-treated HCM mice (Fig. 2B), indicating the emergence of overt disease. In contrast, HCM mice treated with MYK-461 had LVWT comparable to that of WT mice (Fig. 2B).

To determine whether MYK-461 could reverse pathologic remodeling, we administered this drug to older HCM mice (ages 30 to 35 weeks) with

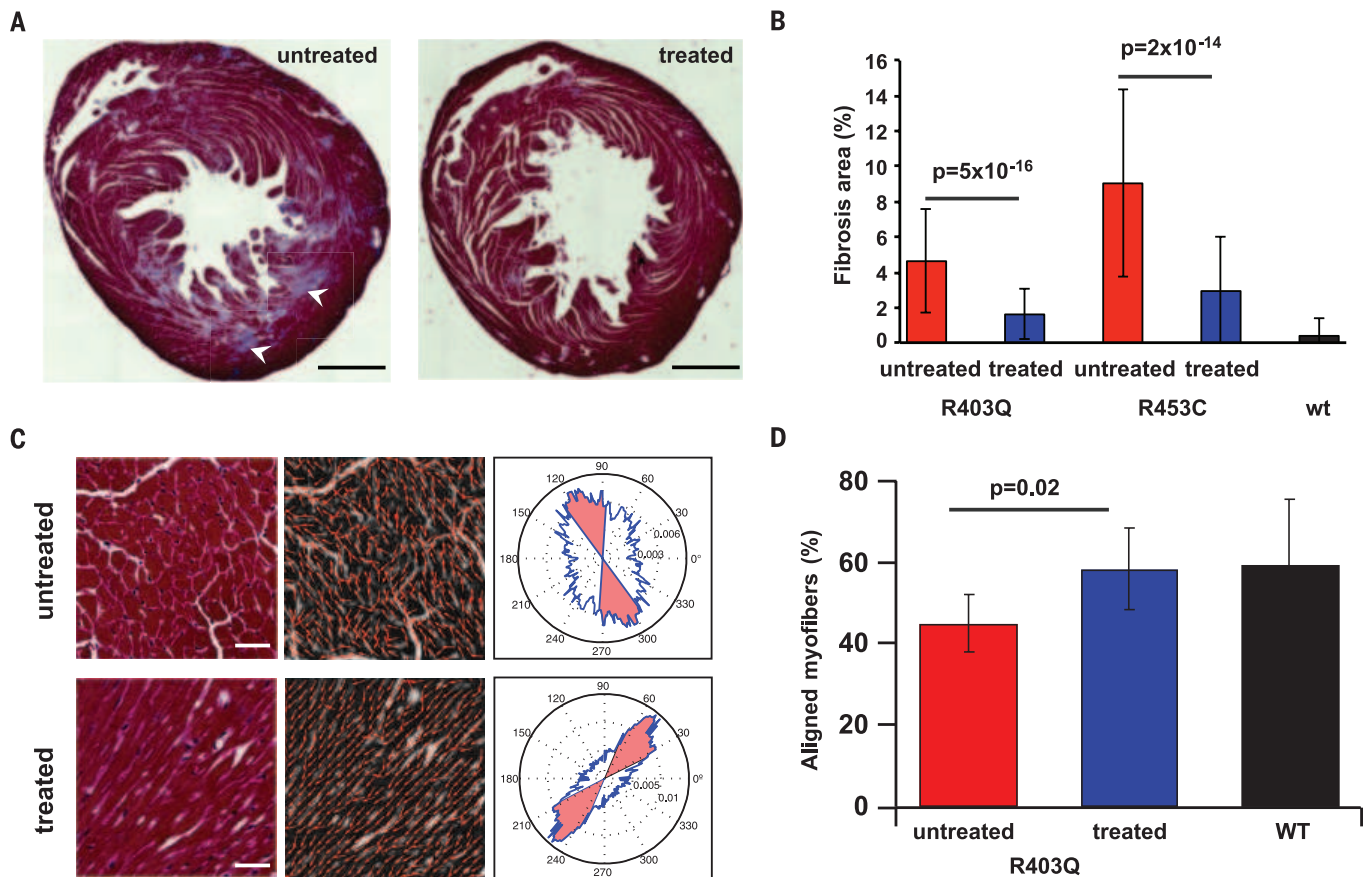


Fig. 3. MYK-461 reduces the development of myocardial disarray and fibrosis in mouse models of HCM. (A) Sections from untreated (left) and MYK-461-treated (right) 30-week-old R403Q mice stained with Masson's trichrome (arrowheads point to fibrotic areas). Scale bars, 1 mm. (B) Reduction in fibrosis area with MYK-461 treatment assessed in more than eight sections per mouse for R403Q and R453C HCM mice ($n = 5$ to 6 animals per group). (C) Representative regions of interest for analysis of cell orientation from R403Q

mouse heart sections. Regions are shown (left) stained with Masson's trichrome (scale bars, $50 \mu\text{m}$), (middle) with local gradient vectors illustrating cell orientations for analysis, and (right) as rose plots of the distribution of myofibril orientation angles (blue line; myofibrils oriented within 20° of the mean are shaded in red). (D) Percentage of aligned myofibers in WT and R403Q mice with and without MYK-461 treatment ($n = 6$ animals per condition). All data expressed are as mean \pm SD; statistical comparisons were performed by *t* test.

overt LVH (LVWT ≥ 0.9 mm). Serial echocardiograms showed a significant reduction in the fractional shortening by week 2 (fig. S4C) and in LVWT by week 4 (Fig. 2C), after which these parameters remained stable with continued treatment. Thus, reduction of the pathologic power generated by the mutant sarcomere blunted the development of LVH and promoted partial regression of hypertrophy in older HCM mice.

Seminal histopathologic features of HCM include cardiomyocyte disarray and fibrosis, which may contribute to ventricular arrhythmias and heart failure (25). We hypothesized that counteracting the biomechanical effects of sarcomere mutations with MYK-461 would normalize these histopathologic phenotypes. Untreated HCM mice (R403Q or R453C) developed variable amounts of patchy fibrosis encompassing ~ 4.5 and $\sim 9.6\%$ of the left ventricle (LV), respectively (Fig. 3, A and B). Prehypertrophic mice treated for 20 to 26 weeks (Fig. 3, A and B, and fig S6) displayed $\sim 80\%$ less fibrosis. However, when MYK-461 was administered after the development of substantial hypertrophy, it did not significantly reduce the occurrence of fibrosis. These data suggest that normalizing sarcomere power output can reduce the fibrotic response to an HCM mutation, but the maximum benefit may be achieved by administering treatment before the onset of overt hypertrophy.

To characterize the effect of MYK-461 on myofibrillar disarray, we used an algorithm (26, 27) that determines the regional orientation of myofibrils across histological sections (Fig. 3C and fig. S7). We defined the mean myofiber orientations for a given region (Fig. 3C) and the percentage of aligned cells (cells oriented within 20° of the mean; see supplementary materials and methods). At 30 weeks of age, untreated HCM R403Q mice had an average of $45 \pm 7\%$ aligned cardiomyocytes per region (Fig. 3D, red). Prehypertrophic R403Q mice treated with MYK-461 had 30% more aligned cardiomyocytes ($59 \pm 10\%$; $P = 0.02$) (Fig. 3D, blue), comparable to the mean alignment of cardiomyocytes observed in WT heart sections (Fig. 3D, black). In contrast, mice treated with MYK-461 after the development of overt hypertrophy showed no significant increase in cardiomyocyte alignment.

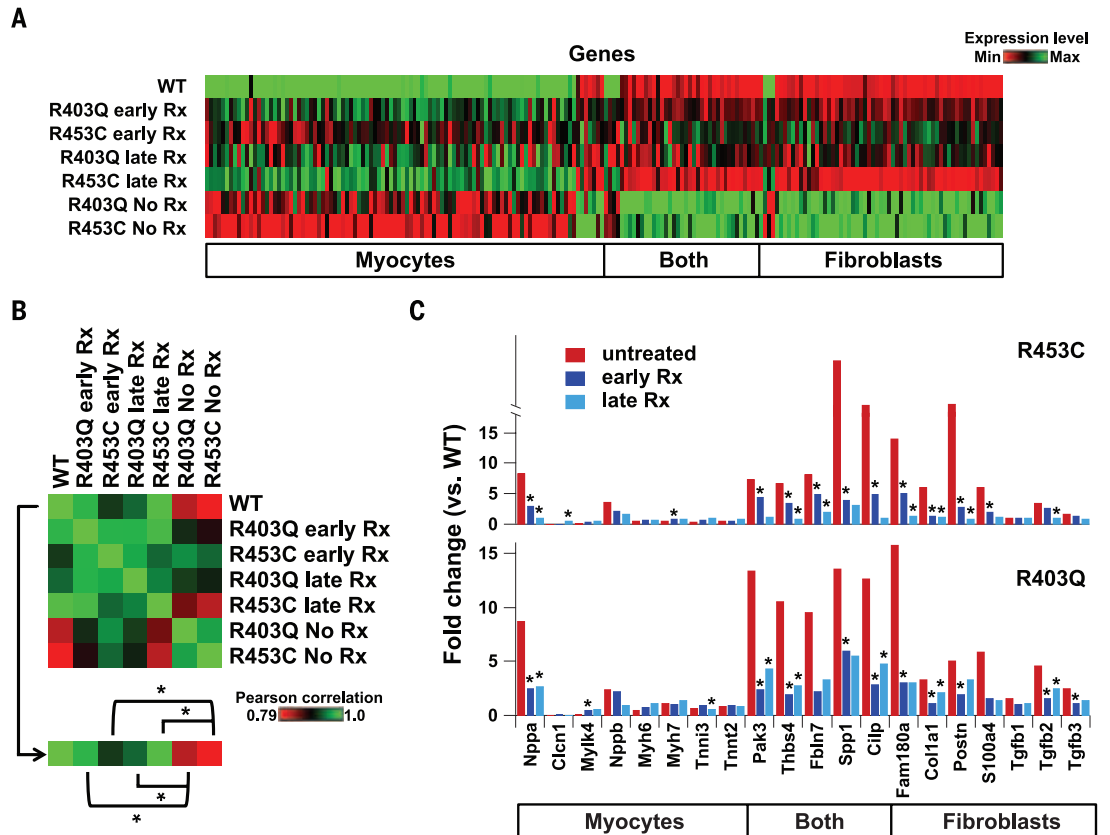
To characterize the cardiac transcriptional responses to reduced contractility from MYK-461 in HCM hearts, we focused on 200 genes with significantly altered expression in hypertrophic R403Q and R453C mice compared with WT controls (table S1). This gene set was enriched for cardiomyocyte-expressed transcripts encoding contractile-associated proteins and for cardiac fibroblast transcripts encoding proteins involved in extracellular matrix production (table S2). RNA

expression of this 200-gene set in R403Q and R453C mice exposed to MYK-461 either before (ages 8 to 15 weeks; early Rx) or after (ages 30 to 35 weeks; late Rx) the development of overt LVH was significantly closer to WT LV levels than to untreated HCM LV levels (Fig. 4, A and B) ($P < 0.0001$). Although we did not detect regression of myocardial fibrosis in these mice, both cardiomyocyte contractility and profibrotic gene expression were normalized (Fig. 4C), indicating that reduction in sarcomere power in the prehypertrophic and overt HCM hearts promoted maintenance or restoration of normal transcriptional pathways.

Because LV hypertrophy has been linked with inefficient energy utilization (28), we also compared gene expression for 1158 genes (29) that encode proteins localized to mitochondria (fig. S8A) in WT and HCM mice (R403Q or R453C). In untreated HCM mice, we observed dysregulated expression in 19.7% (228 genes; R403Q) and 28.7% (332 genes; R453C) of genes encoding mitochondrial proteins, as compared with WT levels ($P = 0.01$) (fig. S8B). Early treatment with MYK-461 reduced the percentage of dysregulated gene expression to 4.2% (49 genes; R403Q) and 7.5% (87 genes; R453C) ($P < 0.01$ versus untreated). These data are consistent with an altered metabolic state in HCM that is normalized by treatment with MYK-461.

Fig. 4. MYK-461 suppresses hypertrophic and profibrotic gene programs in mouse models of HCM.

(A) Heat map illustrating levels of gene expression in WT and treated and untreated HCM mice for 200 genes that are highly differentially regulated in HCM mice compared with WT mice. Genes are divided according to the cell type in which they are expressed (myocytes, fibroblasts, or both). Treatment with MYK-461 (2.5 mg/kg per day) began either before overt hypertrophy (early Rx) or after the development of hypertrophy (late Rx). (B) Heat map showing Pearson correlations between mouse genetic backgrounds and MYK-461 treatment regimens for 200 genes differentially regulated in untreated HCM mice. Statistical comparisons were performed between the Pearson correlations for WT animals or untreated mutants and each treatment condition for that mutant. Significance was assessed by Fisher r -to- z transformation ($*P < 0.0001$). (C) Fold change in gene expression levels (as compared with WT animals) for selected genes expressed in myocytes, fibroblasts, or both across MYK-461 treatment regimens in R453C mice (top) and R403Q mice (bottom; $*P < 0.05$).



In summary, our data demonstrate that a small-molecule inhibitor of sarcomere power administered early in the course of disease can attenuate the development and progression of the morphologic, histopathologic, and molecular changes that characterize HCM. Our findings support a mechanistic model for HCM in which sarcomere mutations lead to increased molecular power output, hyperdynamic contraction, and ultimately, pathologic remodeling of the heart. We suggest that analyses from reconstituted systems (18, 21) have not consistently validated this model because key components (e.g., MYBPC or titin) are missing and/or important parameters for power production have not been examined (30). Nevertheless, our *in vivo* results indicate that reduction of sarcomere power output by direct manipulation of their biomechanical properties—with a small molecule that targets cardiac myosin—may present a therapeutic approach to HCM.

As other heritable cardiomyopathies are associated with mutations that disrupt physiologic power production by the sarcomere (31), the salutary effects of inhibiting myosin power in HCM suggest a more general paradigm for treating genetic cardiomyopathies: pharmacologic normalization of underlying biomechanical defects by either increasing or decreasing sarcomere power (22). Small molecules that augment myosin power have already been identified and are in clinical trials for patients with heart failure (32, 33). Further elucidation of the biochemical and biophysical consequences of human mutations on cardiac function can form the basis for

future efforts to treat these diseases at their mechanistic source.

REFERENCES AND NOTES

- B. J. Maron *et al.*, *Circulation* **92**, 785–789 (1995).
- M. D. Klein, F. J. Lane, R. Gorlin, *Am. J. Cardiol.* **15**, 773–781 (1965).
- W. S. Wilson, J. M. Criley, R. S. Ross, *Am. Heart J.* **73**, 4–16 (1967).
- S. Stewart, D. T. Mason, E. Braunwald, *Circulation* **37**, 8–14 (1968).
- B. J. Maron *et al.*, *JAMA* **281**, 650–655 (1999).
- B. J. Maron, M. S. Maron, *Lancet* **381**, 242–255 (2013).
- R. Spoladore, M. S. Maron, R. D'Amato, P. G. Camici, I. Olivetto, *Eur. Heart J.* **33**, 1724–1733 (2012).
- A. A. Alfares *et al.*, *Genet. Med.* **17**, 880–888 (2015).
- J. M. Bos *et al.*, *Mayo Clin. Proc.* **89**, 727–737 (2014).
- J. R. Moore, L. Leinwand, D. M. Warshaw, *Circ. Res.* **111**, 375–385 (2012).
- C. Y. Ho *et al.*, *Circulation* **105**, 2992–2997 (2002).
- J. Forsey, L. Benson, E. Rozenblyum, M. K. Friedberg, L. Mertens, *J. Am. Soc. Echocardiogr.* **27**, 215–221 (2014).
- I. K. Rüssel *et al.*, *J. Cardiovasc. Magn. Reson.* **13**, 3 (2011).
- A. A. Geisterfer-Lowrance *et al.*, *Science* **272**, 731–734 (1996).
- D. Georgakopoulos *et al.*, *Nat. Med.* **5**, 327–330 (1999).
- P. Teekakirikul *et al.*, *J. Clin. Invest.* **120**, 3520–3529 (2010).
- B. M. Palmer *et al.*, *Am. J. Physiol. Heart Circ. Physiol.* **287**, H91–H99 (2004).
- R. F. Sommese *et al.*, *Proc. Natl. Acad. Sci. U.S.A.* **110**, 12607–12612 (2013).
- C. Ruwhof, A. E. van Wamel, J. M. Egas, A. van der Laarse, *Mol. Cell. Biochem.* **208**, 89–98 (2000).
- D. V. Abramochkin, I. T. Lozinsky, A. Kamkin, *J. Mol. Cell. Cardiol.* **70**, 27–36 (2014).
- S. Nag *et al.*, *Sci. Adv.* **1**, e1500511 (2015).
- J. A. Spudich, *Biophys. J.* **106**, 1236–1249 (2014).
- A. M. Lompré, B. Nadal-Ginard, V. Mahdavi, *J. Biol. Chem.* **259**, 6437–6446 (1984).
- P. Cummins, S. J. Lambert, *Circ. Res.* **58**, 846–858 (1986).
- A. M. Varnava, P. M. Elliott, N. Mahon, M. J. Davies, W. J. McKenna, *Am. J. Cardiol.* **88**, 275–279 (2001).
- W. Wan, J. B. Dixon, R. L. Gleason Jr., *Biophys. J.* **102**, 2916–2925 (2012).
- C. P. Ng, B. Hinz, M. A. Swartz, *J. Cell Sci.* **118**, 4731–4739 (2005).
- H. Ashrafian, C. Redwood, E. Blair, H. Watkins, *Trends Genet.* **19**, 263–268 (2003).
- S. E. Calvo, K. R. Clauser, V. K. Mootha, *Nucleic Acids Res.* **44**, D1251–D1257 (2016).
- J. A. Spudich, *Biochem. Soc. Trans.* **43**, 64–72 (2015).
- T. Aksel, E. Choe Yu, S. Sutton, K. M. Ruppel, J. A. Spudich, *Cell Reports* **11**, 910–920 (2015).
- F. I. Malik *et al.*, *Science* **331**, 1439–1443 (2011).
- J. G. F. Cleland *et al.*, *Lancet* **378**, 676–683 (2011).

ACKNOWLEDGMENTS

We thank C. Homcy, J. Fox, K. Ruppel, S. Ingle, and A. Pollen for advice; H. Ghermazien, M. Lun, S. Markova, A. Sran, and C. Zambataro for technical assistance; and J. Hartman, J. Schaletzky, P. Lu, L. Ashcroft, and others from Cytokinetics for assistance during the early stages of this work. E.M.G., R.L.A., M.J.E., M.H., R.K., J.D.O., H.M.R., Y.S., and R.S.M. are employees and own shares of MyoKardia, a biotechnology company developing small molecules that target the sarcomere for treatment of inherited cardiomyopathy. L.A.L., J.A.S., J.G.S., and C.E.S. are founders and own shares of MyoKardia. MyoKardia holds the rights to published patents on MYK-461 (U.S. Pat. Nos. 20140378464 and 20140378491). MYK-461 is available from MyoKardia under a material transfer agreement. Support for these studies was provided by MyoKardia. B.C.H. was supported by NIH grant 5K01AR055676.

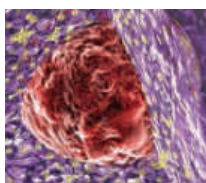
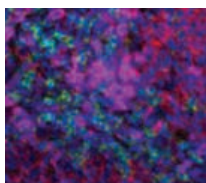
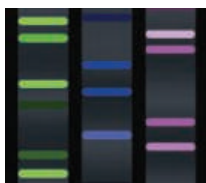
SUPPLEMENTARY MATERIALS

www.sciencemag.org/content/351/6273/617/suppl/DC1
Materials and Methods
Figs. S1 to S8
Tables S1 and S2
References (34–38)

1 September 2015; accepted 20 December 2015
10.1126/science.aad3456

want new technologies?

antibodies
apoptosis
biomarkers
cancer
cytometry
data
diseases
DNA
epigenetics
genomics
immunotherapies
medicine
microbiomics
microfluidics
microscopy
neuroscience
proteomics
sequencing
toxicology
transcriptomics



watch our **webinars**

Learn about the latest breakthroughs, new technologies, and ground-breaking research in a variety of fields. Our expert speakers explain their quality research to you and answer questions submitted by live viewers.

VIEW NOW!

webinar.sciencemag.org

Science



Brought to you by the *Science*/AAAS
Custom Publishing Office



@SciMagWebinars

WE'VE GOT A **MATERIAL** INTEREST IN YOU



Time sequence of buckling silicon microwires.

**Publish in our Special Series, Materials By Design.
We'll waive all APCs. Use code: ADVSSMBD**

Science Advances, the new, open-access journal from AAAS, is publishing interdisciplinary research that advances the frontiers of science and technology. We're now preparing an exciting Special Series, Materials By Design, showcasing important work in material science and engineering with potential global impact.

You're invited to submit your research to the series, and if our guest editors select your manuscript for publication, we'll waive all APCs. *Science Advances* offers expert editing, rapid publication, and all the marketing clout you'd expect from the publisher of *Science*.

**Submit your research at
ScienceAdvances.org**

ScienceAdvances | 
SIGNIFICANT RESEARCH, GLOBAL IMPACT

Chiral Column

The Amylose-1 chiral stationary phase has been added to the high-efficiency Lux polysaccharide chiral column line. The affordable Amylose-1 adds valuable enantioselectivity to the Lux column family with the chiral selector amylose tris (3,5-dimethylphenylcarbamate) and is a guaranteed alternative to other phases with the same chiral selector. Offered in 5- μm particles, the new media is available in analytical columns and Phenomenex-patented Axia preparative column hardware, both of which are stable in normal phase, reversed phase, polar organic, and supercritical fluid (SFC) conditions. The Phenomenex Axia preparative format delivers longer column lifetime, higher efficiencies, improved performance, and high reproducibility, compared with conventionally packed columns for lab-scale preparative high-performance liquid chromatography (HPLC) and SFC chromatography. The expanded Phenomenex Lux chiral column line of six amylose and cellulose chiral selectors comprises an affordable and complementary kit for chiral separations, featuring high efficiency, excellent loading capacity, and pressure stability up to 300 bar in a wide range of conditions.

Phenomenex

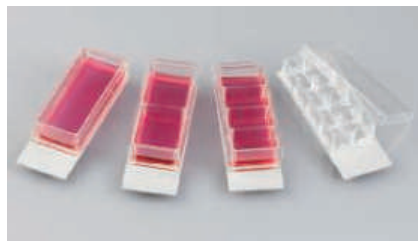
For info: 310-212-0555
www.phenomenex.com

PCR Kits

My PCR Kits contain all the necessary components for polymerase chain reaction (PCR) and are designed for convenient use. The kits come in three packs with different combinations of reagents. My PCR Kit 1 contains 2X *Taq* master mix with *Taq* DNA polymerase, deoxynucleotide triphosphates (dNTPs), MgCl_2 , 50mM MgCl_2 , 6X loading dye, nuclease-free water, and buffer. My PCR Kit 2 offers Chromo *Taq* DNA polymerase, 2mM dNTPs mix, 50mM MgCl_2 , and buffers. Finally, My PCR Kit 3 is a standard pack offering great value and convenience with *Taq* DNA polymerase, 2mM dNTPs mix, 6X loading dye, 50mM MgCl_2 , and buffers. All Vivantis products derive from in-house research to provide integrated solutions to life science researchers worldwide.

Vivantis

For info: +603-8025-1603
www.vivanttechnologies.com



Cell Culture Chambers

The new lumox x-well cell culture chambers are available with a 50 μm ultrathin, gas-permeable film base that combines excellent imaging with superior cell growth. Compared to plastic or glass bases, the gas-permeable lumox film provides more effective gas exchange and homogeneous cell growth. Lumox film shows virtually no autofluorescence and higher light transmission for consistently high assay sensitivity and excellent microscopy and fluorescence-based imaging. Lumox film is chemically resistant to a multitude of fixatives and stains and can be easily cut for cell isolation or storage after fixation and staining. Lumox x-well cell culture chambers are available in 1-, 2-, 4-, and 8-well configurations with a standard adherent cell culture surface. Chambers can be detached from the slide frames easily without tools or adhesive residues. The culture chamber slides are conveniently sold per sterile tray of six.

Sarstedt

For info: 800-257-5101
www.sarstedt.com

Neuron Cryopreservation Kit

The NeuroFreeze kit utilizes a unique, straightforward, and effective method for cryopreserving primary neurons from mice and rats. Neurons frozen in this cutting-edge media can be stored for 12 months and will retain up to 90% viability upon thawing. NeuroFreeze has an easy-to-follow freezing procedure that does not require multiple stepwise reductions in temperature. Thawed neurons show all the expected characteristics of primary neurons, including appropriate morphology and expression of neuronal and synaptic markers. The NeuroFreeze kit is advantageous for researchers using rodent models of disease or genetically engineered strains. The availability of this media will enable investigators to freeze primary neurons and thaw them as necessary, without having to harvest neuronal cells for each investigation. Researchers with the means to conduct studies on neurons from the same cellular source and origin will have more consistent results and decrease the need for repeated experiments.

MD Biosciences

For info: 888-876-3246
www.mdbiosciences.com

Mounting System

McPherson introduces a new line of mechanical positioning systems with high load capacity and stiffness. This strut-based mounting system minimizes vibration and allows easy and precise

position adjustment of a wide variety of hardware. It can even work inside high vacuum or ultrahigh vacuum (UHV) systems. The six struts provide very solid (seismically adequate) support. When submillimeter alignment is required, the six-strut system is a proven way of rigidly supporting instruments and fixtures with precise adjustability. Even the smallest designs support 200 lbs. The strut mechanical positioner has up to six degrees of freedom—translational: X, Y, Z; and angular: pitch, roll, and yaw. It consists of a support system made up of adjustable struts and provides support without adding stress or distortion. The struts have ball joint ends and an orthogonal arrangement to simplify position adjustments. The result is a strong, rigid system that allows easy positioning of even heavy equipment in all six degrees of freedom.

McPherson

For info: 978-256-4512
www.mcphersoninc.com

Electronically submit your new product description or product literature information! Go to www.sciencemag.org/products/newproducts.dtl for more information.

Newly offered instrumentation, apparatus, and laboratory materials of interest to researchers in all disciplines in academic, industrial, and governmental organizations are featured in this space. Emphasis is given to purpose, chief characteristics, and availability of products and materials. Endorsement by *Science* or AAAS of any products or materials mentioned is not implied. Additional information may be obtained from the manufacturer or supplier.



Join the Conversation!

Twitter is a great way to connect with AAAS members and staff about the issues that matter to you most. Be a part of the discussion while staying up-to-date on the latest news and information about your personal member benefits.

Follow us @AAASmember and join the conversation with #AAAS



MemberCentral.aaas.org



Join AAAS. Get instant access to *Science*. Support all of the sciences.

When you subscribe to *Science*, you become part of the American Association for the Advancement of Science (AAAS), a nonprofit community of more than 100,000 members worldwide who believe in the power of science to make the world a better place. AAAS is hard at work promoting science in government, schools, and in the public commons around the globe.


AAAS's award-winning journal *Science* offers the top peer-reviewed research across multiple disciplines. With your subscription, you'll get:

- 51 weeks of home delivery of *Science*
- Instant online retrieval of every *Science* article ever published, dating back to 1880
- Full access to the *Science* mobile site and apps
- Career advice, webinars, blogs and fascinating features exclusively for AAAS members
- Members-only newsletters, and much more

With increasing public skepticism about science—and public funding for research more uncertain than ever—our work has never been more important. Join hands with us today!

Visit promo.aaas.org/joinaaas. Together, we can make a difference.

Science
AAAS



Call for entries:
a global award in
stem cells and
regenerative medicine

BOYALIFE
& Science
Science Translational Medicine
Award in
Stem Cells
and Regenerative
Medicine

Stem cells and regenerative medicine
is the new frontier in life sciences.

Boyalife, Science and Science Translational
Medicine jointly establish a global award to
recognize significant contributions in advancing
basic science to clinical applications in this field.

The award is to recognize and reward scientists in the fields of stem cells and/or regenerative medicine with a focus on developing cell-based treatments for cancer, degenerative disorders, immunotherapy and stem cells transplantation.

You could be next to win this prize and to receive

- ★ A Grand Prize of **\$25,000** and a Runner-Up Prize of **\$5,000** will be awarded.
- ★ The Grand Prize Winning Essay will be published in Science; a brief abstract of the Runner-Up Essay will be published in Science.

The 2016 Award is now open. The deadline for submissions is March 1, 2016
For more information, please visit: <http://www.sciencemag.org/prizes/boyalife>



SCIENCE'S 2016 INFORMATION FOR AUTHORS

This is an abbreviated version of *Science's* Information for Authors. Complete Information for Authors is available at www.sciencemag.org/authors/science-information-authors

PEER-REVIEWED MANUSCRIPTS

Research Articles present a major scientific advance, and those articles whose significance can be demonstrated in 4500 words and 6 figures or tables will be published in print and online. Often, Research Articles require additional text and figures to adequately document the findings. Articles that need more than 4500 words and 6 figures or tables will be published in full online with only an extended abstract in print. Requests for the longer online format should provide justification for the additional presentation length. All Research Articles include an abstract, an introduction, and sections with brief subheads.

Reports present new research results of broad significance and include an abstract and introductory paragraph. Reports should have approximately 2500 words, about 30 references, and up to 4 figures or tables. Reports are published in full online and in print.

For Research Articles and Reports, other information needed to support the conclusions should be presented as supplementary materials.

Reviews (6000 words, 4 to 6 figures or tables, and up to 100 references) are now published online with an extended abstract in print. Reviews describe new developments of interdisciplinary significance and highlight unresolved questions and future directions. Most Reviews are solicited by the editors, but unsolicited submissions are considered occasionally.

INSIGHTS

Science's Insights section presents analysis by scientists and other experts on issues of interest to *Science* readers.

Perspectives (1000 to 1500 words, 1 to 2 figures, up to 15 references) can either (i) analyze recent research developments or (ii) present issues at the intersection between science and society that have policy implications. Research-related Perspectives should not primarily discuss the author's own work. Essays on science education and its practice, from preschool to postgraduate education, will also be considered.

Books et al. (up to 1000 words) present reviews of current books, multimedia, exhibitions, and films.

Books *et al.* reviews and Perspectives are frequently solicited by the editors, but unsolicited contributions will be considered.

Letters (up to 300 words) discuss material published in *Science* in the last 3 months or issues of general interest. Letters are edited for clarity and space.

COMMENTS

Technical Comments (up to 1000 words, 2 figures or tables, and 15 references) are published online and discuss the core conclusions and/or methodology of research published in *Science* within the previous 3 months. A brief abstract is included in the Letters section of the print edition. Technical Comments should not present new data or other previously unpublished work nor be based on new findings or concepts that would not have been accessible to the authors when the target paper was written. Pertinent comments on noncentral aspects of a paper should be submitted as E-letters.

Authors of Technical Comments should contact the authors of the target paper before submitting their manuscript, and should submit to *Science* evidence of any correspondence. Technical Comments may be peer-reviewed. We post accepted Technical Comments promptly online along with a formal reply from the authors of the original paper.

E-letters. Brief online comments can be posted on papers or news stories from the full-text view on *Science's* website. Authors are identified and must agree to our terms and conditions.

MANUSCRIPT SELECTION

We are committed to the prompt evaluation and publication of submitted papers through our fully electronic submission and review process. Papers are assigned to a staff editor who has knowledge of the field(s) discussed in the manuscript. Most

Science Contact Information

Phone: (1)-202-326-6550 (USA)
(44)-1223-326500 (UK)

E-mail: science_editors@aaas.org (USA)
science@science-int.co.uk (Europe)

submitted papers are rated for suitability by members of the Board of Reviewing Editors (see the masthead). The editors at *Science* consider their advice in selecting papers for in-depth review. Authors of papers that are not highly rated are notified by e-mail within 2 weeks. Membership in AAAS is not a factor in selection.

Papers selected for in-depth review are reviewed by at least two anonymous referees. Reviewers are contacted before being sent a paper and are asked to return comments within 2 weeks. We are able to expedite the review process for papers that require rapid assessment. Papers selected for publication are edited to improve accuracy and clarity and to shorten, if necessary. Most papers are published 4 to 8 weeks after acceptance. The accepted versions of selected papers are made available through online publication prior to the final copy-edited version appearing in a print issue.

Papers cannot be resubmitted over a disagreement on interest or relative merit. If a paper was rejected on the basis of serious reviewer error, resubmission may be considered. Papers submitted to *Science* but not accepted for publication may be eligible for publication in *Science Signaling*, *Science Translational Medicine*, or *Science Advances*.

SUBMISSION REQUIREMENTS

Authorship. All authors must agree to be so listed and must have seen and approved the manuscript and its submission to *Science*. Any changes in authorship must be approved in writing by all the original authors. Submission of a paper that has not been approved by all authors will result in immediate rejection without appeal.

Prior publication. *Science* will not consider any paper or component of a paper that has been published or is under consideration elsewhere. Distribution on the Internet may be considered prior publication and may compromise the originality of the paper. Reporting the main findings

Submitting a Manuscript or Letter

Manuscripts and letters should be submitted through our submission website, <https://cts.sciencemag.org/scc/login.html>. For details, see www.sciencemag.org/authors/science-information-authors. We are not able to accept submissions by e-mail. Your submission should include a cover letter containing a statement of the paper's main point and any information needed to ensure a fair review process.

of a paper in the mass media may compromise the novelty of the work and thus its appropriateness for *Science*. Please contact the editors with questions regarding these policies.

Human studies. Informed consent must have been obtained for studies on humans after the nature and possible consequences of the studies were explained. All research on humans must have approval from the author's institutional review board (IRB) or equivalent body.

Animal care. Care of experimental animals must be in accordance with the author's institutional guidelines.

Preclinical studies. Authors must indicate whether there was a pre-experimental plan for data handling, whether they conducted a sample size estimation, whether samples were treated randomly, and whether the experimenter was blind to the conduct of the experiment.

Related papers. Copies of papers submitted to other journals by any of the authors that relate to the paper submitted to *Science* must be included with the submission.

Unpublished data and personal communications. Citations to unpublished data, in-press papers, and personal communications cannot be used to support claims in the paper.

Dual use. Authors and reviewers are expected to notify editors if a manuscript could be considered to report dual-use research of concern. Papers identified as such will be brought to the attention of the Editor-in-Chief for further evaluation. If necessary, outside reviewers with expertise in the area will be consulted.

CONDITIONS OF ACCEPTANCE

Authorship, funding, and conflict of interest. All authors must disclose all affiliations, funding sources, and financial or management relationships related to a paper, including those that could be perceived as potential sources of bias, before acceptance. *Science* now requires all authors of accepted papers to affirm their contribution to a paper and agree to our policies on data and materials availability. The senior author from each group is required to have examined the raw data that his/her group has produced.

Data deposition. Before publication, large data sets—including but not limited to microarray data, protein or DNA sequences, and atomic coordinates and structure factors for macromolecular or chemical structures—must be deposited in an approved database, an accession number must be included in the published paper, and the deposited information must

Manuscript Preparation

Titles should be no more than 96 characters for Reports, Research Articles, and Reviews.

One-sentence summaries should be submitted for all papers.

Abstracts explain to the general reader why the research was done and why the results are important. The abstract should present, in no more than 125 words, background information to convey the context of the research, describe the results, and draw general conclusions.

Text starts with a brief introduction describing the paper's significance, which should be intelligible to readers in other disciplines. Technical terms should be defined. Symbols, abbreviations, and acronyms should be defined the first time they are used. All tables and figures should be cited in numerical order.

References and notes are numbered in the order in which they are cited, first through the text, then through the text of the references, then through the figure and table legends, and finally through the supplementary materials. Each reference should have a unique number; do not combine references or embed references in notes. Do not use *op. cit.* or *ibid.* Include titles in references. They will be included in the online version. There should be only one reference list, containing all of the citations in the paper and in the supplementary materials.

Acknowledgments, including complete funding information; a statement indicating the availability of data, including accession numbers; and any

(See www.sciencemag.org/authors for more information.)

be released at the time of publication. Electron micrograph maps must also be deposited. Approved databases are listed online. Large data sets with no appropriate repository must be housed as part of the supplementary materials at *Science*, or when this is not possible, on the author's website, provided that a copy of the data is held in escrow at *Science* to ensure availability to readers.

Data availability and materials sharing. After publication, all data and computer codes necessary to understand, assess, and extend the conclusions of the manuscript must be available to any reader of *Science*, and all reasonable requests for materials must be fulfilled. Before acceptance, *Science* must be informed of any restrictions on sharing of materials (materials transfer agreements or patents, for example) applying to materials used in the reported research.

License and access policies. Authors retain copyright but must agree to grant to *Science* an exclusive license to publish the paper in print and online. Any author whose university or institution has poli-

information related to authorship conflict of interest should be gathered into an unnumbered note at the end of the references.

Tables should be included at the end of the references and should supplement, not duplicate, the text. The first sentence of the table legend should be a brief descriptive title. Every vertical column should have a heading, consisting of a title with the unit of measure in parentheses. Units should not change within a column.

Figure legends should be double-spaced and in numerical order. The figure title should be given as the first line of the legend. No single legend should be longer than ~200 words. Nomenclature, abbreviations, symbols, and units used in a figure should match those used in the text. Units should be metric and follow SI conventions.

Supplementary materials are posted permanently at the *Science* website, are linked to the manuscript, and are freely available. Files can include materials and methods, figures, tables, and video or audio clips that are important for the integrity of the paper, but not further discussion.

Figures should be submitted as part of the online submission or, if necessary for large files only, on a CD or DVD. No part of a figure may be selectively manipulated. When figures are assembled from multiple gels or micrographs, a line or space should indicate the border between two original images. See our online Information for Authors for information on preparing art.

cies or other restrictions limiting their ability to assign exclusive publication rights (such as Harvard, MIT, or Open University) must apply for a waiver or other exclusion from that policy or those restrictions. After publication, authors may post the accepted version of the paper on their personal website and are provided one referrer link that can be posted on a personal or institutional web page, through which users can freely access the published paper on *Science's* online site. *Science* allows deposition of accepted papers into repositories if mandated by funders with a release 6 months after publication and provided that a link to the final version published in *Science* is included. Original research papers are freely accessible with registration on *Science's* website 12 months after publication.

Press coverage. The paper should remain a privileged document and should not be released to the press or the public before publication. Questions should be referred to the AAAS Office of Public Programs (phone 202-326-6440).



There's only one **Science**

Science Careers Advertising

For full advertising details, go to ScienceCareers.org and click For Employers, or call one of our representatives.

Tracy Holmes

Worldwide Associate Director
Science Careers
Phone: +44 (0) 1223 326525

THE AMERICAS

E-mail: advertise@sciencecareers.org

Fax: +1 (202) 289 6742

Tina Burks

Phone: +1 (202) 326 6577

Nancy Toema

Phone: +1 (202) 326 6578

Online Job Posting Questions

Phone: +1 (202) 312 6375

EUROPE / INDIA / AUSTRALIA / NEW ZEALAND / REST OF WORLD

E-mail: ads@science-int.co.uk

Fax: +44 (0) 1223 326532

Sarah Lelarge

Phone: +44 (0) 1223 326527

Kelly Grace

Phone: +44 (0) 1223 326528

Online Job Posting Questions

Phone: +44 (0) 1223 326528

JAPAN

Katsuyoshi Fukamizu (Tokyo)

E-mail: kfukamizu@aaas.org

Phone: +81 3 3219 5777

Hiroyuki Mashiki (Kyoto)

E-mail: hmashiki@aaas.org

Phone: +81 75 823 1109

CHINA / KOREA / SINGAPORE / TAIWAN / THAILAND

Ruolei Wu

Phone: +86 186 0082 9345

E-mail: rwu@aaas.org

All ads submitted for publication must comply with applicable U.S. and non-U.S. laws. *Science* reserves the right to refuse any advertisement at its sole discretion for any reason, including without limitation for offensive language or inappropriate content, and all advertising is subject to publisher approval. *Science* encourages our readers to alert us to any ads that they feel may be discriminatory or offensive.

Science Careers

FROM THE JOURNAL SCIENCE AAAS

ScienceCareers.org



Research Assistant Professor Position University of Pittsburgh School of Medicine Department of Pharmacology & Chemical Biology

Applications are invited for a Research Assistant Professor level faculty position in the Department of Pharmacology & Chemical Biology. Candidates who have a PhD, MD or preferably both, or equivalent graduate degrees are being recruited to expand a program in Nrf2 signaling networks. The University of Pittsburgh School of Medicine and the Department of Pharmacology & Chemical Biology consistently rank among the top 10 by NIH funding.

The successful candidate will be expected to: have excellent communication skills, both oral and written, and to have a strong record of scholarly publications. While all strong applicants will be considered, research interests that complement laboratory interests in Nrf2, Notch1 signaling, metabolic disease and carcinogenesis will be especially competitive.

Applicants should mail by **1 March 2016** a one-page statement of research objectives, curriculum vitae, and contact information for three references to: **Dr. Thomas W. Kensler, PhD, Professor of Pharmacology & Chemical Biology, Department of Pharmacology & Chemical Biology, University of Pittsburgh, School of Medicine, E1352 Biomedical Science Tower, Pittsburgh, PA 15261; <http://www.pharmacology.us>**

The University of Pittsburgh is an Affirmative Action/Equal Opportunity Employer Minorities/ Women/Vets/Disabled.



Memorial Sloan-Kettering Cancer Center

Postdoctoral Research Fellow

A post doctoral research position is available immediately to join the newly established laboratory of Dr. Anas Younes, within the Lymphoma Service at Memorial Sloan Kettering Cancer Center (MSKCC).

The major focus of the laboratory is the development of novel targeted therapy and mechanism-based novel combination regimens for the treatment of lymphoma. The lab is actively investigating genetic and molecular biomarkers for predicting treatment response, and identifying negative feedback loops that may facilitate the design of combination strategies. Highly motivated individuals (Ph.D. or M.D.) with outstanding training in cell biology, cell signaling, cancer genetics, or related areas, are encouraged to apply.

Interested candidates should email CV and contact information for three references to:

Anas Younes, M.D.
Chief, Lymphoma Service, MSKCC
email: younesa@mskcc.org

Download the Science Careers Job App

SEARCH JOBS ON THE GO!

apps.sciencemag.org



Faculty Position in Tumor Immunology

Department of Microbiology/Immunology
Northwestern University Feinberg School of
Medicine and Robert H. Lurie Comprehensive
Cancer Center of Northwestern University

The Department of Microbiology/Immunology and the Robert H. Lurie Comprehensive Cancer Center at the Feinberg School of Medicine, Northwestern University are seeking a top level scientist to expand the research program in Tumor Immunology. We are looking for a researcher excited to join our effort to find novel insights into cancer therapy and prevention by harnessing the immune system. The position is at the level of Assistant Professor, Associate Professor, or Professor in the University Tenure Line. The successful candidate will be an accomplished investigator with a demonstrated record of achievement as evidenced by research funding and publications in leading journals.

Applicants must apply online. Applications will be reviewed as received, but to receive full consideration, must be received by **April 15, 2016**. Please submit a complete curriculum vitae, a concise research statement/plan, and the names and contact information for at least three letters of reference to: tumorimmunology@northwestern.edu.

Northwestern University is an Equal Opportunity, Affirmative Action Employer of all protected classes, including veterans and individuals with disabilities. Women and minorities are encouraged to apply. Hiring is contingent upon eligibility to work in the United States.



Director, Cancer Genomics Associate Director, Translational Genomics Laboratory

The Ontario Institute for Cancer Research (OICR) is seeking a Director of Cancer Genomics to develop an innovative research program in cancer genomics.

The Director will join OICR's senior management team which oversees OICR's research plan. The Director will devote at least 50% of time to oversee technology development within the Translational Genomics Laboratory, a new partnership between the Princess Margaret Cancer Centre and OICR.

OICR was created by the Government of Ontario to enhance cancer research, particularly translation of new discoveries into effective interventions that impact cancer and promote knowledge-based industries in Ontario.

Qualifications: • PhD and/or MD with a proven track record in cancer genomics, next generation sequencing and technology development; • A relevant international reputation and strong publication record; • Proven leadership, management experience and communications skills; • Previous experience in leading multidisciplinary, multi-institutional teams; • Excellent and broad understanding of the field of genomics, epigenomics and informatics in oncology; • Eligible to hold the rank of associate or full professor at an Ontario university.

Conditions of Employment: The position will be based at OICR's core laboratories in the MaRS Centre in Toronto. An academic appointment may be obtained at the University of Toronto. The initial appointment is for five years, renewable pending satisfactory review. A competitive salary and benefits package will be negotiated.

Application Process: Candidates are invited to submit a curriculum vitae, a vision statement on the opportunities for OICR to play a lead role in cancer genomics and in the translation of genome technologies and science in the health care system, and names of three references, electronically to search@oicr.on.ca. For more information about OICR please visit the website at www.oicr.on.ca.

The position will remain open until a suitable candidate is found, however applications are preferred by **March 15, 2016**.



WE BELIEVE GRAND CHALLENGES

REQUIRE BOLD ACTIONS.

We believe in the relentless pursuit of big ideas. In thinking ahead of the curve. We believe in individual strength and the power of collaboration. And in making tomorrow what we dream it can be. We believe in advancing the common good with uncommon will.

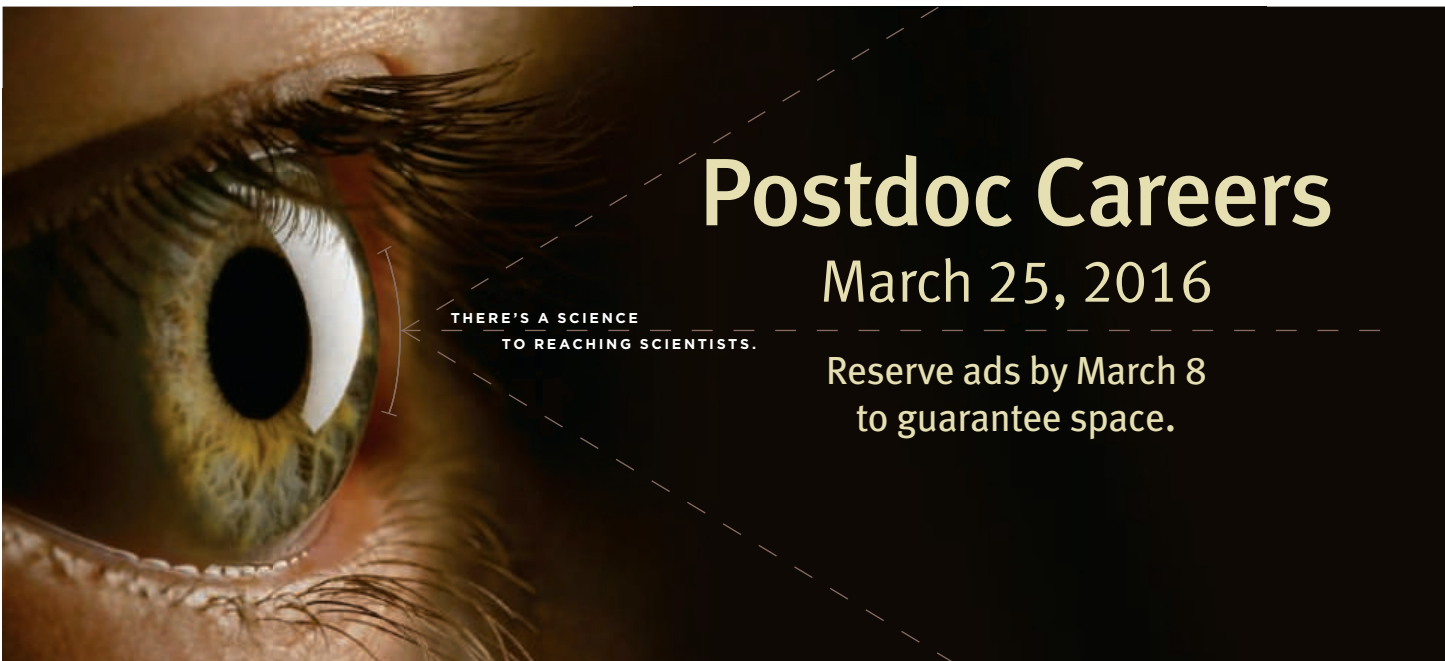
MSU's Global Impact Initiative is a bold endeavor designed to accelerate the pace of discovery through the creation of more than 100 new faculty positions in some of the most promising—and critical—fields of research, including energy, health, education, the environment, national security, and global development. **Join us.**

SPARTANS WILL.

msu.edu/globalimpact



MICHIGAN STATE
UNIVERSITY



Postdoc Careers

March 25, 2016

Reserve ads by March 8 to guarantee space.

THERE'S A SCIENCE TO REACHING SCIENTISTS.

For recruitment in science, there's only one

Science

Fantastic Recruiting Opportunity!

POSTDOC CAREERS | March 25, 2016

Be sure to promote your openings to the thousands of scientists who will be reading *Science* to find out about the latest postdoc opportunities.

Reserve ads by March 8 to guarantee space.



Produced by the *Science*/AAAS Custom Publishing Office.

SCIENCECAREERS.ORG

Science Careers

FROM THE JOURNAL SCIENCE AAAS

To book your ad: advertise@sciencecareers.org

The Americas
+202-326-6582

Japan
+81-3-3219-5777

Europe/RoW
+44 (0) 1223-326500

China/Korea/Singapore/Taiwan
+86-186-0082 9345

Sêr Cymru II – Building Research Capacity in Wales

The Sêr Cymru programme is a £100 million strategy to produce a step change in research capacity in Wales. Sêr Cymru II is the latest round of funding and is a collaboration between Welsh Government, Higher Education Funding Council Wales (HEFCW) and Welsh Universities.

The Sêr Cymru II scheme is looking for high-calibre candidates to work with stellar researchers in STEMM (Science, Technology, Engineering, Maths and Medicine) and relevant areas of Applied Social Science in Wales. The fellowships available include:

- **Rising Star fellowships₁**. Up to 26 five-year fellowships for the very best 'rising stars' of academic research.
- **Marie Skłodowska-Curie Actions Strengthening International Research Capacity in Wales (SIRCIW) Fellowships₂**. - Up to 90 three year fellowships for researchers from outside of the UK to come to work in a Welsh University.
- **Early Career Fellowships₁**. Around 30 three-year fellowships for stellar candidates, to be recruited from anywhere in the world to come to work in Wales.
- **Recapturing Research Talent₁**. Approximately 12 fellowships for talented researchers returning to work following a career break or who have left the scientific world.

The first deadline for applications is **17:00 UK time, Tuesday 1st March** but further funding rounds will be announced soon.

1. The project has been part funded by the European Regional Development Fund through the Welsh Government.
2. This project has received funding from the European Union's Horizon 2020 research and innovation programme under the Marie Skłodowska-Curie grant agreement No 663830.

For more information, please see the Expertise Wales website:
<http://expertisewales.com/support-and-funding-researchers> or contact the Management Team via SERCYMRUII@wales.gsi.gov.uk



Llywodraeth Cymru
Welsh Government

www.llyw.cymru
www.gov.wales



UNIOB EYRACHYDD
EUROPEAN UNION



Llywodraeth Cymru
Welsh Government

**Cronfa Datblygu
Rhanbarthol Ewrop
European Regional
Development Fund**



myIDP:
A career plan customized
for you, by you.



For your career in science, there's only one **Science**



Recommended by
leading professional
societies and the NIH

Features in myIDP include:

- Exercises to help you examine your skills, interests, and values
- A list of 20 scientific career paths with a prediction of which ones best fit your skills and interests
- A tool for setting strategic goals for the coming year, with optional reminders to keep you on track
- Articles and resources to guide you through the process
- Options to save materials online and print them for further review and discussion
- Ability to select which portion of your IDP you wish to share with advisors, mentors, or others
- A certificate of completion for users that finish myIDP.

Visit the website and start planning today!
myIDP.sciencecareers.org

ScienceCareers In partnership with:



By Rima Wilkes

Retire the letter of reference

Each year, I write letters of reference for undergraduate students applying to master's and Ph.D. programs; law school; and programs in social work, architecture, and medicine. I write letters to help them win awards, internships, and placements in study abroad programs. I write letters for graduate students trying to win fellowships, find postdoc appointments, and secure tenure-track positions. I write letters for faculty members submitting applications for prizes, as well as for those coming up for tenure and promotion appraisals. Suffice it to say, I spend a lot of time writing letters.

Maybe I should feel good about this—after all, I am helping a lot of people achieve their dreams—but I don't. It isn't that I don't wish the people I am writing for well—I do. They often succeed in their applications, and I like to think that my letters play an important part in this. However, I am beginning to question the value of all this letter writing. I certainly don't mean to sound ungracious. Yes, many people have written letters on my behalf. Yes, without these letters I wouldn't be where I am today. But I became an academic to be a scholar and a teacher. I didn't sign up to be a letter writer.

Even as I am sometimes exasperated with my own letter-writing load, I was surprised to learn that, compared with other colleagues I have talked to, the 50 or so letters I am now writing each year is probably average. One colleague told me that he knows someone who routinely writes several hundred letters each year. Others probably write more. This is work we in the academy all feel obliged to do—but lately, as I serve on more of the hiring and award committees that request all these letters, I find myself wondering whether they are losing value.

In the past, there were fewer universities than today, and networks were smaller. A letter of reference mattered because it was written by someone the letter reader knew. Now, we are reading hundreds of letters of reference, most by people we don't know. Maybe we have heard of the letter writer's research and have met once or twice at a conference, but still, we often have no sense of what a letter from that individual means. Is "good" high or faint praise? When is "brilliant" honest and when is it hyperbole? Is this a form letter? Does the fact that a letter was written by a big-name scholar employed at a big-name school indicate that the subject of the letter is doing quality work or merely that they are well connected? And should we discount a letter if there



“We need to write fewer letters.”

are typos or grammatical mistakes? In the end, a strong letter can simply mean a strong letter writer.

Indeed, now that I have served on committees faced with hundreds of letters, each describing said candidate as “outstanding” or some other superlative, I find myself paying less and less attention to them. Although we used to look to letters to get a sense of someone's scholarly promise, in today's competitive academic arena, promise is no longer enough. Instead, we end up relying on markers of achievement—CV, transcript, proposal, scholarly output—as do the writers of all those letters.

Last month, Roger Day wrote on this page that some academics need

to stop using others to ghostwrite their letters. (You can read that story at <http://scim.ag/RogerDayWL>.) But we don't just need more diligent letter writers or more honesty about who is doing the letter writing. We need to write fewer letters. I think it's time we consider retiring the letter of reference. Professors' labor isn't free; our time must be allocated and paid for, to say nothing of the time spent by contingent faculty members who are asked to write letters on their own dime. Although the price of a single letter may seem low, the cost of the time faculty members are spending reading and writing all these letters probably amounts to hundreds of millions of dollars a year.

Yes, it would be nice to have highly insightful letters that provide valuable information about a candidate beyond what comes through from a CV or written work. But if you are on a committee that does admissions or any other form of adjudication and you request letters, ask yourself this: Will the decision you make be that much better? ■

Rima Wilkes is a professor of sociology at the University of British Columbia, Vancouver, in Canada. Send your story to SciCareerEditor@aaas.org.